



# **V $\gamma$ 9V $\delta$ 2TCR and Beyond:**

Novel Insights and Strategies  
for Advanced T cell-based  
Immunotherapies

**Astrid Cleven**



**V $\gamma$ 9V $\delta$ 2TCR and Beyond:  
Novel Insights and  
Strategies for Advanced T  
cell-based  
Immunotherapies**

**Astrid Cleven**

ISBN: 978-94-6483-948-7

Cover Design & Layout: Astrid Cleven

Print: Ridderprint – [www.ridderprint.nl](http://www.ridderprint.nl)

©Copyright 2024: Astrid Cleven, Utrecht, The Netherlands

All rights reserved. No part of this publication may be reproduced, stored in a retrieval system, or transmitted in any form or by any means, electronic, mechanical, by photocopying, recording, or otherwise, without the prior written permission of the author.

Printing of this thesis was financially supported by Infection & Immunity Utrecht.

# **V $\gamma$ 9V $\delta$ 2TCR and Beyond: Novel Insights and Strategies for Advanced T cell-based Immunotherapies**

**V $\gamma$ 9V $\delta$ 2TCR en meer: nieuwe inzichten en strategieën voor  
immunotherapieën met T-cellen**

(met een samenvatting in het Nederlands)

## **Proefschrift**

ter verkrijging van de graad van doctor aan de  
Universiteit Utrecht  
op gezag van de  
rector magnificus, prof. dr. H.R.B.M. Kummeling,  
ingevolge het besluit van het college voor promoties  
in het openbaar te verdedigen op

woensdag 24 april 2024 te 2.15 uur

door  
Astrid Cleven

geboren op 22 juni 1990  
te Geldern, Duitsland

## **Promotor:**

Prof. dr. J.H.E. Kuball

## **Copromotoren:**

Dr. Z. Sebestyen

Dr. G.C.M. Straetemans

## **Beoordelingscommissie:**

prof. dr. A.P. Kater

prof. dr. J.H.W. Leusen

prof. dr. M.C. Minnema

prof. dr. P.A.J.T. Robe (voorzitter)

prof. dr. E.J.H.J. Wiertz

# Content

|                   |   |     |
|-------------------|---|-----|
| <b>Chapter 1</b>  | General Introduction. Strategies to improve $\gamma\delta$ TCRs engineered T-cell therapies for the treatment of solid malignancies<br><br><i>Frontiers in Immunology, 2023</i>   | 7   |
| <b>Chapter 2</b>  | Thesis outline  | 23  |
| <b>Chapter 3</b>  | PI3K-AKT1-mTOR activity and BTN3A1 phosphorylation are required for early cancer immune surveillance via V $\gamma$ 9V $\delta$ 2TCR T cells<br><br><i>Manuscript in preparation</i><br>Patent application: P36295EP00 submitted 2023 (A. Cleven co-inventor) | 27  |
| <b>Chapter 4</b>  | Uncovering the mode of action of engineered T cells in patient cancer organoids<br><br><i>Nature Biotechnology, 2023</i>  | 63  |
| <b>Chapter 5</b>  | Efficacy of $\alpha\beta$ T cell based immunotherapies relies on CCR5 expression in both CD4+ and CD8+ $\alpha\beta$ T cells<br><br><i>Manuscript in preparation</i>  | 105 |
| <b>Chapter 6</b>  | Unlocking Immunomodulation: Mesenchymal Stem Cells Explored In 3D Co-Culture Modeling<br><br><i>Manuscript in preparation</i>   | 129 |
| <b>Chapter 7</b>  | Summarizing Discussion  | 163 |
| <b>Appendices</b> | Nederlandse Samenvatting  | 178 |
|                   | Acknowledgement   | 181 |
|                   | List of publications  | 186 |
|                   | Curriculum vitae  | 188 |





# CHAPTER

# 1

## General Introduction

### Strategies to improve $\gamma\delta$ TCRs engineered T-cell therapies for the treatment of solid malignancies

A. D. Meringa<sup>1†</sup>, P. Hernández-López<sup>1†</sup>, A. Cleven<sup>1†</sup>,  
M. de Witte<sup>1,2</sup>, T. Straetemans<sup>1,2</sup>,  
J. Kuball<sup>1,2</sup>, D. X. Beringer<sup>1</sup>, Z. Sebestyen<sup>1</sup>

† Equally contributed

<sup>1</sup>Center for Translational Immunology, University Medical Center Utrecht,  
Utrecht University, Utrecht, Netherlands

<sup>2</sup>Department of Hematology, University Medical Center Utrecht, Utrecht  
University, Utrecht, Netherlands

*Frontiers in Immunology, 2023*

## Introduction

After the overwhelming clinical success of targeting hematological malignancies with CAR-T cells<sup>1</sup>, the first signals of treatment are seen for solid tumors targeted by engineered immune cells<sup>2</sup>. However, targeting solid tumors with this kind of immunotherapy still remains a challenge<sup>3,4</sup>. There are multiple mechanisms that make it difficult for adoptive cellular therapies to effectively target solid tumors.

First, most solid tumors lack homogeneous expression of a tumor-specific antigen making it difficult to find appropriate receptors to target them<sup>5</sup>. The selection of targetable tumor antigens needs careful consideration to avoid targeting of healthy tissue, especially when considering engineered cellular therapies against solid cancers, where potent and safe antigens are rare<sup>6</sup>. Additionally, the microenvironment of solid tumors holds unique features such as expression of immunosuppressive molecules and hypoxia that have a huge impact on T cell fitness<sup>4,7,8</sup>. Finally, a combination of extracellular matrix deposition and anti-inflammatory signals, like attracting mesenchymal derived suppressor cells (MDSCs), prevent effective infiltration of T cells towards the tumor site<sup>9</sup>.

In this article we will further discuss the roadblocks facing successful implementation of T cell therapies for the treatment of solid malignancies focusing on  $\gamma\delta$ T cells and their receptors since they provide a new avenue to target novel tumor antigens. Characterization of these cells and their receptors holds the potential to generate novel strategies for targeting cancer and provide new engineering strategies to potentially overcome these hurdles.

## Gamma delta T cells as source of novel tumor-targeting receptors

The infiltration of  $\gamma\delta$ T cell in tumors has been associated in many studies to have a favorable impact on patient survival<sup>10-16</sup>, while some other studies made in murine models report that interleukin-17 (IL-17) producing  $\gamma\delta$ T cells are tumor promoting<sup>17, 18</sup>. While these data are very insightful, it has to be carefully handled when translating it to human clinical practices given that human and mouse  $\gamma\delta$ T cell repertoires and functions are not fully compatible. Regardless of the ultimate effector function, activation of  $\gamma\delta$ T cells is contingent upon the engagement of their surface receptors with antigens on the tumor cell.  $\gamma\delta$  T cells can be divided into two groups,  $V\delta 2+$  and  $V\delta 2-$ , with  $V\delta 1$  forming the majority of  $V\delta 2-$  T-cells.  $V\delta 2-$  T cells are predominantly found in peripheral tissue and have also been shown to be enriched in carcinomas<sup>11, 19-21</sup>. Multiple studies

reported a correlating favorable clinical outcome either with the presence of V $\delta$ 2<sup>-</sup> T-cells<sup>12, 13</sup> or with  $\gamma\delta$ T in general<sup>22</sup>. This tissue-association might be advantageous for targeting and infiltrating solid tumors when using V $\delta$ 1TCR T cells as effector cells. V $\delta$ 2-TCRs can recognize a wide variety of ligands that are expressed on infected and malignant cells<sup>23</sup>. A large number of studies have shown that numerous V $\delta$ 2-TCRs can recognize nonpolymorphic MHC I-like molecules MR1 and CD1<sup>24, 25</sup>. Most CD1 isoforms, CD1a, CD1b, and CD1c, are mainly found on cells of hematological origin and declassify them as potential ligands for solid tumors<sup>26</sup>, but both MR1 as CD1d have been found to be expressed on solid tumors<sup>26, 27</sup>. Other  $\gamma\delta$ TCR ligands expressed on solid tumors and are recognized by specific V $\delta$ 2<sup>-</sup> TCR clones are endothelial protein C receptor (EPCR)<sup>28</sup>, Annexin A2<sup>29</sup>, and EphA2<sup>30</sup>. Based on the wide breath of ligands recognized by V $\delta$ 2<sup>-</sup>TCRs<sup>23</sup>, it is to be expected that many more ligands for this subset will be identified in the future. While many of these V $\delta$ 2<sup>-</sup> TCR ligands are also expressed on the surface healthy cells, such as EPCR on endothelial cells<sup>31</sup> and CD1d on APCs<sup>32</sup>, no major safety concerns have been reported. For example, a study demonstrating that while an EPCR reactive V $\delta$ 2<sup>-</sup> TCR clone recognized cytomegalovirus (CMV)-infected or malignant endothelial cells it was not reactive against normal endothelial cells, due to increased expression of immune modulating molecules such as CD54 and CD58<sup>28</sup>. Additionally, to avoid toxicity towards healthy, antigen presenting cells (APCs), lipid-specific CD1d reactive V $\delta$ 2<sup>-</sup> TCRs can be used<sup>33</sup>.

Unlike above discussed V $\delta$ 2<sup>-</sup> T cells, V $\delta$ 2<sup>+</sup> T cells, also referred as V $\gamma$ 9V $\delta$ 2 T cells are mainly present in blood and their role of cancer immune surveillance have been studied the most among all  $\gamma\delta$ T cells<sup>34</sup>. The process of identifying the ligand complex for the invariant V $\gamma$ 9V $\delta$ 2 TCRs has been a long and winding path, that started with the identification of phosphoantigens<sup>35</sup> that are bound by the intracellular domain of butrophilin 3A1 (BTN3A1)<sup>36</sup>. This process leads to a re-localization of BTN3A1 to the cell surface<sup>37, 38</sup>, where it can form a complex with BTN2A1<sup>39-41</sup>. Only when this phosphoantigen driven complex of BTN3A1 and BTN2A1 is formed on the plasma membrane, V $\gamma$ 9V $\delta$ 2 TCRs can be activated. This multistep ligand complex formation serves a safety threshold that prevents V $\gamma$ 9V $\delta$ 2 TCR mediated toxicity towards healthy tissue but enables the eradication of tumors in many preclinical models<sup>42-44</sup>.

While  $\gamma\delta$ T cells have their natural potential to target cancer, as described above, the most clinical trials to date, that have assessed the efficacy and safety of  $\gamma\delta$ T cells as adoptive cellular therapy did show moderate clinical efficacy<sup>45-48</sup> where only incidentally e.g. prolonged survival of patients has been reported<sup>47</sup>. However, the potential of natural, tumor infiltrating  $\gamma\delta$ T cells has recently been demonstrated in colorectal cancer<sup>10</sup> and kidney cancer<sup>16</sup>, supporting the idea to further investigate the details of receptors present on  $\gamma\delta$ T cells for the treatment of cancer. While providing an emerging

universe of tumor specific receptors, one has to carefully assess possible toxicity against healthy tissues in advanced 3-dimensional preclinical models<sup>42, 43, 49</sup> that resemble the homeostatic environment of the human body.

## Improving T-cell fitness for durable tumor control

T cell dysfunction has been one of the major causes of failure of CAR-T cell treatments as it results in poor T cell expansion and short-term persistence resulting in reduced anti-tumor efficacy<sup>8, 50</sup>. Despite efforts to improve CAR designs, CAR-T cell exhaustion remains one of the main limitations of this kind of therapy<sup>51-53</sup>. Thus, although CAR-T field has significantly growth in the last years, some studies advocate for the use of natural TCR signaling to reduce exhaustion of T cells<sup>54, 55</sup>. The main reason for this is that CAR's artificial design accelerates exhaustion of T cells when compared to TCR based therapies, mostly due to the described tonic signaling in the absence of antigen<sup>55-57</sup>. In this line, several designs have been explored to make CAR more TCR-like, such as HLA-independent TCR (HIT) or synthetic TCR and antigen receptor (STAR)<sup>58, 59</sup>. The CAR scFv sequence in these receptors is fused to the constant domains of an  $\alpha\beta$ TCR, thereby preserving TCR signaling while using the CAR's ability to recognize tumors in an HLA independent way. An elegant alternative to these designs is engineering  $\alpha\beta$  T cells to express tumor-reactive V $\gamma$ 9V $\delta$ 2 TCRs (called TEGs)<sup>42, 60</sup>. In this way, the use of  $\gamma\delta$ TCRs in T cell therapy appear to be advantageous when compared with CARs or  $\alpha\beta$ TCRs, as they supply T cells with natural TCR signaling while preserving the ability of recognize tumors in an HLA-independent way<sup>45</sup>.

Optimal co-stimulation has been described as key to overcome exhaustion and improve T cell fitness and persistence in the context of cancer<sup>61-63</sup>. Therefore, as costimulatory signals are highly involved in T cell metabolic reprogramming<sup>64, 65</sup> and T cell exhaustion is closely related with metabolic dysfunction, manipulation of co-stimulation in T cell therapies will result in improved metabolic T cell fitness, which is key to achieve robust anti-tumor responses<sup>64</sup>. One example is the addition of co-stimulatory domains to the first generation of CARs, which has shown to improve persistence of these cells<sup>66, 67</sup>. This led to the development of second and third generation of CARs with improved proliferation ability. Therefore, combining natural TCR signaling properties, by using  $\gamma\delta$ TCRs to target tumors, with improved co-stimulation might be the answer to CAR-T limitations.

One way to improve the co-stimulation of T cells can be achieved by expressing chimeric costimulatory receptors (CCRs) in combination with a CAR or a TCR<sup>68-71</sup>. These receptors preserve the structure of conventional second-generation CARs but lack the CD3 $\zeta$  domain, therefore providing only costimulatory signals to the T cell. Uncoupling of signal

1 (CD3 signal) and signal 2 (co-stimulation) by this dual targeting has been shown to be beneficial<sup>72-74</sup> as T cells will only activate once synergistic signals are delivered upon encounter of both antigens. While these receptors improve T cell proliferation, they also reduce exhaustion<sup>72</sup> thereby improving T cell persistence in the tumor niche and leading to an improved therapeutic effect<sup>72, 75</sup>.

A type of CCRs are the so-called switch chimeric co-receptors<sup>76-79</sup>, which use the extracellular domain of a described inhibitory receptor (such as PD-1 or TIGIT) and link it to the intracellular domain of activating costimulatory receptors (such as CD28 or 4-1BB) or eventually DAP10, when expressed in  $\gamma\delta$ T cells<sup>71</sup>. Thus, these receptors turn inhibitory signals, that would normally induce exhaustion of T cells, into activating signals. This strategy improves not only T cell fitness, by improving co-stimulation, but also makes engineered T cells resistant to tumor microenvironment immunosuppressive factors.

Finally, it is important to further investigate the mechanisms that impact T cell fitness as not all the T cells subsets respond equal to the same stimulus. For example, TGF- $\beta$  has been shown to improve cytotoxic activity of V $\delta$ 2<sup>+</sup> T cells<sup>80</sup> while it is been described to suppress  $\alpha\beta$  T cells function<sup>81</sup>. Furthermore, IL-15 has been shown to improve tumor killing capacity of  $\gamma\delta$ T cells isolated from AML patients<sup>82</sup>. Therefore, comprehensive studies and rational engineering it is key to develop effective therapies. In conclusion, to achieve durable anti-tumor responses the next generation of T cell-based immunotherapies should include fine-tuning of co-stimulation, to preserve T cell fitness, ensure persistence, and skew the T cells to the most potent phenotype.

## Tackling the tumor microenvironment

The lack of efficacy observed for different T cell treatments targeting various antigens in solid tumors suggest the presence of general barriers that inhibit the efficacy of these immunotherapies. The cellular and extra-cellular composition of the tumor microenvironment can influence the tumor biology and response to immune therapy<sup>83</sup>. The dense extracellular matrix (ECM) of solid tumors is a physical barrier for T cells to penetrate leading to low numbers of infiltrating, endogenous T cells in solid tumors<sup>4</sup>. Meanwhile, immunosuppressive cells such as myeloid-derived suppressive cells and regulatory T cells in the tumor microenvironment (TME) inhibit antitumor activity of T cells that do infiltrate in the TME<sup>84</sup>. Different engineering strategies are being developed to overcome these general barriers of T-cell therapies in solid malignancies.

Modulation of the chemokine signaling of the tumor-reactive T cells can lead to improved T cell infiltration by increasing chemotaxis towards the tumor site. For

example, expression of the colony stimulating factor receptor (CSF-R) in CAR-T cells improved migration towards solid tumor models producing CSF<sup>85</sup>. Arming T cells with other chemokine receptors have shown similar results where CCR4, CCR2b and CXCR3 overexpression in the T cell products led to increased infiltration in the TME and thereby increased tumor targeting<sup>86-88</sup>.

Upon infiltration of immune cells in the TME, multiple mechanisms can render the T cells inactive via expression of immunosuppressive molecules. Well-known checkpoint molecules such as PD-1 and TIM3 are not only affecting  $\alpha\beta$  T cells but also act on  $\gamma\delta$  T cells as has been recently shown<sup>10</sup> in colorectal cancer. However,  $\gamma\delta$  T cells are also often regulated by unique sets of inhibitory natural killer (NK) receptors: for example, tumor and stromal cells can express ligands for immune checkpoints in T cells like HLA-E binding NKG2A on  $\gamma\delta$  tumor infiltrating lymphocytes (TILs)<sup>89</sup>. To overcome this, numerous cytokines have been tested to make armed CAR-T cells also known as T cell redirected for antigen-unrestricted cytokine-initiated killing (TRUCKs)<sup>90</sup>. CAR-T cells targeting different solid tumor models were shown to improve their anti-tumor activity, increase their resistance to regulatory T cell signaling and improve local proliferation upon arming the T cells with IL-12 expression<sup>91-93</sup>. Expression of other cytokines such as IL-7, IL-15 and IL-18 have shown to provide similar results by increasing therapy efficacy via increasing local inflammation in the TME<sup>93-95</sup>. Chemokine and cytokine arming of  $\gamma\delta$ TCR based T cell therapies could increase efficacy since other T cell engineering approaches for CAR-T cells.

Additionally, CAR-T cells can be engineered to express ECM-modifying enzymes to facilitate better penetration to the tumor site. Heparinase expressing GD2 CAR-T cells improved their infiltrating capacity in solid tumor models compared to CAR-T cells lacking heparin expression<sup>96,97</sup>. Arming CAR-T cell with prolyl endopeptidase is another approach for targeting the ECM in the TME<sup>98</sup>. Expression of prolyl endopeptidase in CAR-T cells improved their anti-tumor activity, however some toxicity towards healthy tissue was observed with both ECM targeting approaches. Introducing these types of modifications could be very promising for improving the therapeutic effect of  $\gamma\delta$ TCR T cells in solid tumors.

## Future Perspectives

Current developments in the field of engineered adoptive cellular therapies, especially CAR-T cell therapies show promising results in the treatment of haematological malignancies; more specifically B cell-derived tumors. However, adapting these T cells therapies to solid tumor treatments options requires overcoming certain impediments posed by solid malignancies and their TME (**Figure 1**). Fortunately, these T cells-based

therapies allow for *ex vivo* modifications of the treatment to address these tumor-specific challenges posed in the TME of solid tumors where lesson learned from tumor specific  $\gamma\delta$ T may provide a possible solution.

Selection of the tumor-reactive receptor and the tumor specific/associated antigen remains the first important step in optimizing T cell therapies in solid tumors. To this end,  $\gamma\delta$ TCRs are an interesting option due to their unique recognition patterns. Secondly, the addition of a co-stimulatory signal, especially in combination with a naturally low affinity  $\gamma\delta$ TCR can help improve T cell fitness via either one of the three suggested signalling approaches. Expressing a chimeric costimulatory receptor to mimic signal 2 will help the T cells to retain their anti-tumor activity upon prolonged exposure in the TME. Furthermore, the induction of inflammation via secretion of cytokines such as at the tumor site can help the tumor infiltrating  $\gamma\delta$ TCR T cells to overcome the immunosuppressive signals present in the TME. Finally, expression of chemokine(receptors) or ECM modifying molecules can help increase T cell infiltration in the solid tumor microenvironment.

In conclusion, promising approaches for improving the efficacy and scope of T cell therapies are being developed to overcome the current roadblocks in the treatment of solid malignancies. Using  $\gamma\delta$ TCRs as tumor-reactive receptors, and combining these with appropriate co-stimulation via expression of additional chimeric costimulatory receptor to improve fitness and providing additional mechanisms to improve  $\gamma\delta$ TCR T-cell infiltration like boosting chemotaxis, will be key assets to enhance efficacy of T cell therapies for solid malignancies. While further modifying the T cells does contain risks, these solutions will help to optimize efficacy of engineered T cell therapies and introduce this technology for a more widespread use in anticancer therapy.

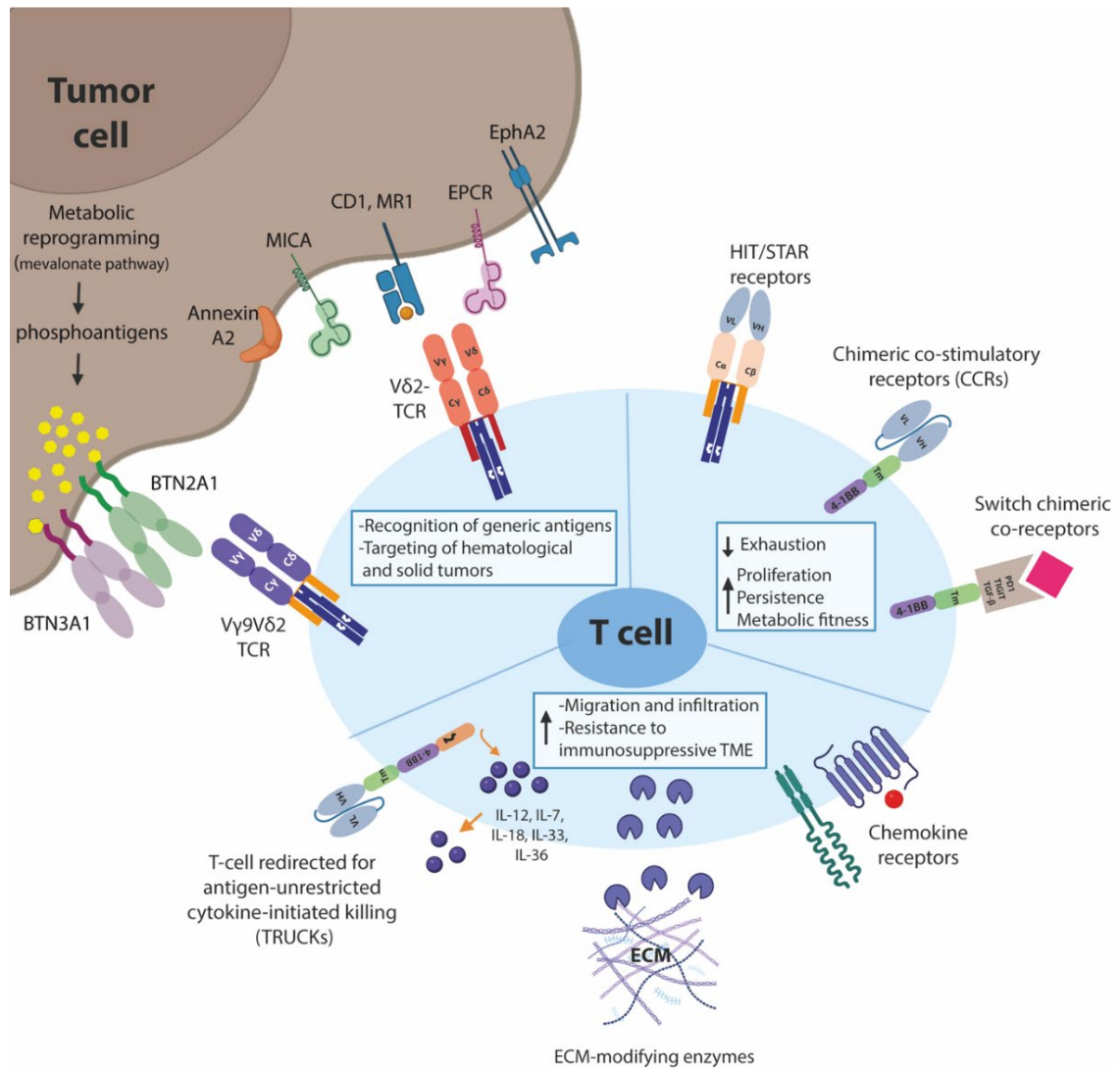


**Figure 1. Schematic representation of T-cell engineering approaches.** Biological mechanisms that prevent effective adoption of gd T-cell therapies for the treatment of solid malignancies and suggested engineering strategies to overcome these hurdles are shown



## **Author contributions**

All authors listed have made a substantial, direct, and intellectual contribution to the work and approved it for publication.

## **Funding**

This work was supported by grants KWF 11979, KWF 11393, KWF 12586, KWF 13043, KWF 13493 to authors JK, ZS and DB from the Dutch Cancer Society KWF

## **Conflict of interest**

JK, ZS and DB are inventors on various patents regarding T cell immune therapies, JK is shareholder at Gadeta BV. The remaining authors declare that the research was conducted in the absence of any commercial or financial relationships that could be construed as a potential conflict of interest.

## References

1. Roschewski, M., D.L. Longo, and W.H. Wilson, *CAR T-Cell Therapy for Large B-Cell Lymphoma - Who, When, and How?* N Engl J Med, 2022. **386**(7): p. 692-696.
2. Majzner, R.G., et al., *GD2-CAR T cell therapy for H3K27M-mutated diffuse midline gliomas*. Nature, 2022. **603**(7903): p. 934-941.
3. Marofi, F., et al., *CAR T cells in solid tumors: challenges and opportunities*. Stem Cell Res Ther, 2021. **12**(1): p. 81.
4. Hou, A.J., L.C. Chen, and Y.Y. Chen, *Navigating CAR-T cells through the solid-tumour microenvironment*. Nat Rev Drug Discov, 2021. **20**(7): p. 531-550.
5. Wagner, J., et al., *CAR T Cell Therapy for Solid Tumors: Bright Future or Dark Reality?* Mol Ther, 2020. **28**(11): p. 2320-2339.
6. Bailey, S.R., et al., *Four challenges to CAR T cells breaking the glass ceiling*. Eur J Immunol, 2022: p. e2250039.
7. Gao, T.A. and Y.Y. Chen, *Engineering Next-Generation CAR-T Cells: Overcoming Tumor Hypoxia and Metabolism*. Annu Rev Chem Biomol Eng, 2022. **13**: p. 193-216.
8. Gumber, D. and L.D. Wang, *Improving CAR-T immunotherapy: Overcoming the challenges of T cell exhaustion*. EBioMedicine, 2022. **77**: p. 103941.
9. Lanitis, E., et al., *Mechanisms regulating T-cell infiltration and activity in solid tumors*. Ann Oncol, 2017. **28**(suppl\_12): p. xii18-xii32.
10. de Vries, N.L., et al., *gammadelta T cells are effectors of immunotherapy in cancers with HLA class I defects*. Nature, 2023. **613**(7945): p. 743-750.
11. Gherardin, N.A., et al., *gammadelta T Cells in Merkel Cell Carcinomas Have a Proinflammatory Profile Prognostic of Patient Survival*. Cancer Immunol Res, 2021. **9**(6): p. 612-623.
12. Donia, M., et al., *Analysis of Vdelta1 T cells in clinical grade melanoma-infiltrating lymphocytes*. Oncoimmunology, 2012. **1**(8): p. 1297-1304.
13. Gentles, A.J., et al., *The prognostic landscape of genes and infiltrating immune cells across human cancers*. Nat Med, 2015. **21**(8): p. 938-945.
14. Zakeri, N., et al., *Characterisation and induction of tissue-resident gamma delta T-cells to target hepatocellular carcinoma*. Nat Commun, 2022. **13**(1): p. 1372.
15. Rosso, D.A., et al., *Glioblastoma cells potentiate the induction of the Th1-like profile in phosphoantigen-stimulated gammadelta T lymphocytes*. J Neurooncol, 2021. **153**(3): p. 403-415.
16. Rancan, C., et al., *Exhausted intratumoral Vdelta2(-) gammadelta T cells in human kidney cancer retain effector function*. Nat Immunol, 2023.
17. Coffelt, S.B., et al., *IL-17-producing gammadelta T cells and neutrophils conspire to promote breast cancer metastasis*. Nature, 2015. **522**(7556): p. 345-348.
18. Lo Presti, E., et al., *Squamous Cell Tumors Recruit gammadelta T Cells Producing either IL17 or IFNgamma Depending on the Tumor Stage*. Cancer Immunol Res, 2017. **5**(5): p. 397-407.
19. Hidalgo, J.V., et al., *Histological Analysis of gammadelta T Lymphocytes Infiltrating Human Triple-Negative Breast Carcinomas*. Front Immunol, 2014. **5**: p. 632.

20. Dadi, S., et al., *Cancer Immunosurveillance by Tissue-Resident Innate Lymphoid Cells and Innate-like T Cells*. Cell, 2016. **164**(3): p. 365-77.
21. Janssen, A., et al., *gammadelta T-cell Receptors Derived from Breast Cancer-Infiltrating T Lymphocytes Mediate Antitumor Reactivity*. Cancer Immunol Res, 2020. **8**(4): p. 530-543.
22. Gentles, A.J., et al., *The prognostic landscape of genes and infiltrating immune cells across human cancers*. Nat Med, 2015. **21**(8): p. 938-45.
23. Willcox, B.E. and C.R. Willcox, *gammadelta TCR ligands: the quest to solve a 500-million-year-old mystery*. Nat Immunol, 2019. **20**(2): p. 121-128.
24. Van Rhijn, I. and J. Le Nours, *CD1 and MR1 recognition by human gammadelta T cells*. Mol Immunol, 2021. **133**: p. 95-100.
25. Castro, C.D., et al., *Diversity in recognition and function of human gammadelta T cells*. Immunol Rev, 2020. **298**(1): p. 134-152.
26. Consonni, M., P. Dellabona, and G. Casorati, *Potential advantages of CD1-restricted T cell immunotherapy in cancer*. Mol Immunol, 2018. **103**: p. 200-208.
27. Crowther, M.D., et al., *Genome-wide CRISPR-Cas9 screening reveals ubiquitous T cell cancer targeting via the monomorphic MHC class I-related protein MR1*. Nat Immunol, 2020. **21**(2): p. 178-185.
28. Willcox, C.R., et al., *Cytomegalovirus and tumor stress surveillance by binding of a human gammadelta T cell antigen receptor to endothelial protein C receptor*. Nat Immunol, 2012. **13**(9): p. 872-9.
29. Marlin, R., et al., *Sensing of cell stress by human gammadelta TCR-dependent recognition of annexin A2*. Proc Natl Acad Sci U S A, 2017. **114**(12): p. 3163-3168.
30. Harly, C., et al., *Human gammadelta T cell sensing of AMPK-dependent metabolic tumor reprogramming through TCR recognition of EphA2*. Sci Immunol, 2021. **6**(61).
31. Laszik, Z., et al., *Human protein C receptor is present primarily on endothelium of large blood vessels: implications for the control of the protein C pathway*. Circulation, 1997. **96**(10): p. 3633-40.
32. Brigl, M. and M.B. Brenner, *CD1: antigen presentation and T cell function*. Annu Rev Immunol, 2004. **22**: p. 817-90.
33. Luoma, A.M., et al., *Crystal structure of Vdelta1 T cell receptor in complex with CD1d-sulfatide shows MHC-like recognition of a self-lipid by human gammadelta T cells*. Immunity, 2013. **39**(6): p. 1032-42.
34. Sebestyen, Z., et al., *Translating gammadelta (gammadelta) T cells and their receptors into cancer cell therapies*. Nat Rev Drug Discov, 2020. **19**(3): p. 169-184.
35. Tanaka, Y., et al., *Natural and synthetic non-peptide antigens recognized by human gamma delta T cells*. Nature, 1995. **375**(6527): p. 155-8.
36. Harly, C., et al., *Key implication of CD277/butyrophilin-3 (BTN3A) in cellular stress sensing by a major human gammadelta T-cell subset*. Blood, 2012. **120**(11): p. 2269-79.
37. Vantourout, P., et al., *Heteromeric interactions regulate butyrophilin (BTN) and BTN-like molecules governing gammadelta T cell biology*. Proc Natl Acad Sci U S A, 2018. **115**(5): p. 1039-1044.

38. Vyborova, A., et al., *gamma9delta2T cell diversity and the receptor interface with tumor cells*. J Clin Invest, 2020. **130**(9): p. 4637-4651.
39. Rigau, M., et al., *Butyrophilin 2A1 is essential for phosphoantigen reactivity by gammadelta T cells*. Science, 2020. **367**(6478).
40. Karunakaran, M.M., et al., *Butyrophilin-2A1 Directly Binds Germline-Encoded Regions of the Vgamma9Vdelta2 TCR and Is Essential for Phosphoantigen Sensing*. Immunity, 2020. **52**(3): p. 487-498 e6.
41. Hsiao, C.C., et al., *Ligand-induced interactions between butyrophilin 2A1 and 3A1 internal domains in the HMBPP receptor complex*. Cell Chem Biol, 2022. **29**(6): p. 985-995 e5.
42. Johanna, I., et al., *Evaluating in vivo efficacy - toxicity profile of TEG001 in humanized mice xenografts against primary human AML disease and healthy hematopoietic cells*. J Immunother Cancer, 2019. **7**(1): p. 69.
43. van Diest, E., et al., *Gamma delta TCR anti-CD3 bispecific molecules (GABs) as novel immunotherapeutic compounds*. J Immunother Cancer, 2021. **9**(11).
44. De Gassart, A., et al., *Development of ICT01, a first-in-class, anti-BTN3A antibody for activating Vgamma9Vdelta2 T cell-mediated antitumor immune response*. Sci Transl Med, 2021. **13**(616): p. eabj0835.
45. Sebestyen, Z., et al., *Translating gammadelta ( $\gamma\delta$ ) T cells and their receptors into cancer cell therapies*. Nat Rev Drug Discov, 2020. **19**(3): p. 169-184.
46. Mensurado, S., R. Blanco-Dominguez, and B. Silva-Santos, *The emerging roles of gammadelta T cells in cancer immunotherapy*. Nat Rev Clin Oncol, 2023.
47. Xu, Y., et al., *Allogeneic Vgamma9Vdelta2 T-cell immunotherapy exhibits promising clinical safety and prolongs the survival of patients with late-stage lung or liver cancer*. Cell Mol Immunol, 2021. **18**(2): p. 427-439.
48. Fournie, J.J., et al., *What lessons can be learned from gammadelta T cell-based cancer immunotherapy trials?* Cell Mol Immunol, 2013. **10**(1): p. 35-41.
49. Braham, M.V.J., et al., *Cellular immunotherapy on primary multiple myeloma expanded in a 3D bone marrow niche model*. Oncoimmunology, 2018. **7**(6): p. e1434465.
50. Fraietta, J.A., et al., *Determinants of response and resistance to CD19 chimeric antigen receptor (CAR) T cell therapy of chronic lymphocytic leukemia*. Nat Med, 2018. **24**(5): p. 563-571.
51. Kouro, T., H. Himuro, and T. Sasada, *Exhaustion of CAR T cells: potential causes and solutions*. J Transl Med, 2022. **20**(1): p. 239.
52. Wherry, E.J. and M. Kurachi, *Molecular and cellular insights into T cell exhaustion*. Nat Rev Immunol, 2015. **15**(8): p. 486-99.
53. Poorebrahim, M., et al., *Counteracting CAR T cell dysfunction*. Oncogene, 2021. **40**(2): p. 421-435.
54. Salter, A.I., et al., *Comparative analysis of TCR and CAR signaling informs CAR designs with superior antigen sensitivity and in vivo function*. Sci Signal, 2021. **14**(697).
55. Wachsmann, T.L.A., et al., *Comparing CAR and TCR engineered T cell performance as a function of tumor cell exposure*. Oncoimmunology, 2022. **11**(1): p. 2033528.

56. Calderon, H., M. Mamonkin, and S. Guedan, *Analysis of CAR-Mediated Tonic Signaling*. *Methods Mol Biol*, 2020. **2086**: p. 223-236.
57. Gomes-Silva, D., et al., *Tonic 4-1BB Costimulation in Chimeric Antigen Receptors Impedes T Cell Survival and Is Vector-Dependent*. *Cell Rep*, 2017. **21**(1): p. 17-26.
58. Mansilla-Soto, J., et al., *HLA-independent T cell receptors for targeting tumors with low antigen density*. *Nat Med*, 2022. **28**(2): p. 345-352.
59. Liu, Y., et al., *Chimeric STAR receptors using TCR machinery mediate robust responses against solid tumors*. *Sci Transl Med*, 2021. **13**(586).
60. Marcu-Malina, V., et al., *Redirecting alphabeta T cells against cancer cells by transfer of a broadly tumor-reactive gammadeltaT-cell receptor*. *Blood*, 2011. **118**(1): p. 50-9.
61. Long, A.H., et al., *4-1BB costimulation ameliorates T cell exhaustion induced by tonic signaling of chimeric antigen receptors*. *Nat Med*, 2015. **21**(6): p. 581-90.
62. Guedan, S., et al., *Enhancing CAR T cell persistence through ICOS and 4-1BB costimulation*. *JCI Insight*, 2018. **3**(1).
63. Kowolik, C.M., et al., *CD28 costimulation provided through a CD19-specific chimeric antigen receptor enhances in vivo persistence and antitumor efficacy of adoptively transferred T cells*. *Cancer Res*, 2006. **66**(22): p. 10995-1004.
64. Pellegrino, M., et al., *Manipulating the Metabolism to Improve the Efficacy of CAR T-Cell Immunotherapy*. *Cells*, 2020. **10**(1).
65. Kawalekar, O.U., et al., *Distinct Signaling of Coreceptors Regulates Specific Metabolism Pathways and Impacts Memory Development in CAR T Cells*. *Immunity*, 2016. **44**(2): p. 380-90.
66. Tokarew, N., et al., *Teaching an old dog new tricks: next-generation CAR T cells*. *Br J Cancer*, 2019. **120**(1): p. 26-37.
67. Imai, C., et al., *Chimeric receptors with 4-1BB signaling capacity provoke potent cytotoxicity against acute lymphoblastic leukemia*. *Leukemia*, 2004. **18**(4): p. 676-84.
68. Katsarou, A., et al., *Combining a CAR and a chimeric costimulatory receptor enhances T cell sensitivity to low antigen density and promotes persistence*. *Sci Transl Med*, 2021. **13**(623): p. eabh1962.
69. Krause, A., et al., *Antigen-dependent CD28 signaling selectively enhances survival and proliferation in genetically modified activated human primary T lymphocytes*. *J Exp Med*, 1998. **188**(4): p. 619-26.
70. Sadelain, M., R. Brentjens, and I. Rivière, *The basic principles of chimeric antigen receptor design*. *Cancer Discov*, 2013. **3**(4): p. 388-98.
71. Fisher, J., et al., *Engineering gammadeltaT cells limits tonic signaling associated with chimeric antigen receptors*. *Sci Signal*, 2019. **12**(598).
72. Wilkie, S., et al., *Dual targeting of ErbB2 and MUC1 in breast cancer using chimeric antigen receptors engineered to provide complementary signaling*. *J Clin Immunol*, 2012. **32**(5): p. 1059-70.
73. Liao, Q., et al., *PD-L1 chimeric costimulatory receptor improves the efficacy of CAR-T cells for PD-L1-positive solid tumors and reduces toxicity in vivo*. *Biomark Res*, 2020. **8**(1): p. 57.

74. Lanitis, E., et al., *Chimeric antigen receptor T Cells with dissociated signaling domains exhibit focused antitumor activity with reduced potential for toxicity in vivo*. *Cancer Immunol Res*, 2013. **1**(1): p. 43-53.
75. Halim, L., et al., *Engineering of an Avidity-Optimized CD19-Specific Parallel Chimeric Antigen Receptor That Delivers Dual CD28 and 4-1BB Co-Stimulation*. *Front Immunol*, 2022. **13**: p. 836549.
76. Vienot, A., et al., *Chemokine switch regulated by TGF- $\beta$ 1 in cancer-associated fibroblast subsets determines the efficacy of chemo-immunotherapy*. *Oncoimmunology*, 2022. **11**(1): p. 2144669.
77. Supimon, K., et al., *Cytotoxic activity of anti-mucin 1 chimeric antigen receptor T cells expressing PD-1-CD28 switch receptor against cholangiocarcinoma cells*. *Cytotherapy*, 2022.
78. Chen, C., et al., *Construction of PD1/CD28 chimeric-switch receptor enhances anti-tumor ability of c-Met CAR-T in gastric cancer*. *Oncoimmunology*, 2021. **10**(1): p. 1901434.
79. Hoogi, S., et al., *A TIGIT-based chimeric co-stimulatory switch receptor improves T-cell anti-tumor function*. *J Immunother Cancer*, 2019. **7**(1): p. 243.
80. Peters, C., et al., *TGF- $\beta$  enhances the cytotoxic activity of V $\delta$ 2 T cells*. *Oncoimmunology*, 2019. **8**(1): p. e1522471.
81. Dahmani, A. and J.S. Delisle, *TGF- $\beta$  in T Cell Biology: Implications for Cancer Immunotherapy*. *Cancers (Basel)*, 2018. **10**(6).
82. Van Acker, H.H., et al., *Interleukin-15 enhances the proliferation, stimulatory phenotype, and antitumor effector functions of human gamma delta T cells*. *J Hematol Oncol*, 2016. **9**(1): p. 101.
83. Junttila, M.R. and F.J. de Sauvage, *Influence of tumour micro-environment heterogeneity on therapeutic response*. *Nature*, 2013. **501**(7467): p. 346-54.
84. Verma, N.K., et al., *Obstacles for T-lymphocytes in the tumour microenvironment: Therapeutic challenges, advances and opportunities beyond immune checkpoint*. *EBioMedicine*, 2022. **83**: p. 104216.
85. Lo, A.S., et al., *Harnessing the tumour-derived cytokine, CSF-1, to co-stimulate T-cell growth and activation*. *Mol Immunol*, 2008. **45**(5): p. 1276-87.
86. Di Stasi, A., et al., *T lymphocytes coexpressing CCR4 and a chimeric antigen receptor targeting CD30 have improved homing and antitumor activity in a Hodgkin tumor model*. *Blood*, 2009. **113**(25): p. 6392-402.
87. Nagarsheth, N., M.S. Wicha, and W. Zou, *Chemokines in the cancer microenvironment and their relevance in cancer immunotherapy*. *Nat Rev Immunol*, 2017. **17**(9): p. 559-572.
88. Craddock, J.A., et al., *Enhanced tumor trafficking of GD2 chimeric antigen receptor T cells by expression of the chemokine receptor CCR2b*. *J Immunother*, 2010. **33**(8): p. 780-8.
89. Cazzetta, V., et al., *NKG2A expression identifies a subset of human Vdelta2 T cells exerting the highest antitumor effector functions*. *Cell Rep*, 2021. **37**(3): p. 109871.
90. Chmielewski, M., A.A. Hombach, and H. Abken, *Of CARs and TRUCKs: chimeric antigen receptor (CAR) T cells engineered with an inducible cytokine to modulate the tumor stroma*. *Immunol Rev*, 2014. **257**(1): p. 83-90.

91. Pegram, H.J., et al., *Tumor-targeted T cells modified to secrete IL-12 eradicate systemic tumors without need for prior conditioning*. *Blood*, 2012. **119**(18): p. 4133-41.
92. Koneru, M., et al., *IL-12 secreting tumor-targeted chimeric antigen receptor T cells eradicate ovarian tumors in vivo*. *Oncoimmunology*, 2015. **4**(3): p. e994446.
93. Yeku, O.O., et al., *Armored CAR T cells enhance antitumor efficacy and overcome the tumor microenvironment*. *Sci Rep*, 2017. **7**(1): p. 10541.
94. Hoyos, V., et al., *Engineering CD19-specific T lymphocytes with interleukin-15 and a suicide gene to enhance their anti-lymphoma/leukemia effects and safety*. *Leukemia*, 2010. **24**(6): p. 1160-70.
95. Chmielewski, M. and H. Abken, *CAR T Cells Releasing IL-18 Convert to T-Bet(high) FoxO1(low) Effectors that Exhibit Augmented Activity against Advanced Solid Tumors*. *Cell Rep*, 2017. **21**(11): p. 3205-3219.
96. Caruana, I., et al., *Heparanase promotes tumor infiltration and antitumor activity of CAR-redirectioned T lymphocytes*. *Nat Med*, 2015. **21**(5): p. 524-9.
97. Mardomi, A. and S. Abediankenari, *Matrix Metalloproteinase 8: Could it Benefit the CAR-T Cell Therapy of Solid Tumors?- a- Commentary on Therapeutic Potential*. *Cancer Microenviron*, 2018. **11**(1): p. 93-96.
98. Tran, E., et al., *Immune targeting of fibroblast activation protein triggers recognition of multipotent bone marrow stromal cells and cachexia*. *J Exp Med*, 2013. **210**(6): p. 1125-35.





The background is an abstract, textured composition of warm, earthy tones. It features a mix of light beige, cream, and golden-brown hues, with darker, more saturated brown and grey tones appearing in the lower half. The texture is reminiscent of layered paint or aged paper, with visible brushstrokes and a sense of depth. The overall effect is organic and artistic.

**CHAPTER**

**2**

**Thesis Outline**

Immunotherapy in general and CAR-T cell therapy in particular have emerged as groundbreaking approaches in the way we treat cancer by harnessing the power of the human immune system. In **Chapter 1** we review current challenges in treating solid malignancies with adoptive immunotherapy and how they might be overcome by using  $\gamma\delta$ TCRs. In this thesis we aim to improve engineered T cell therapies, with a focus on **T cells** engineered to express a defined  **$\gamma\delta$**  TCR (TEGs), more specifically TEG-Cl5 (V $\gamma$ 9V $\delta$ 2 TCR), by tackling from various sites: Improving pre-treatment patient screening (**chapter 3**), identifying potent subsets of engineered T cells (**chapter 4**), and modifying T cells for improved migration to the tumor site, and tumor infiltration of the immunosuppressive tumor microenvironment and tumor killing (**chapters 5 and 6**). **Chapter 7** summarizes and discusses the findings of this thesis in the context of recent literature on V $\gamma$ 9V $\delta$ 2TCR targeting and improvement of engineered T cell therapy.

**Chapter 3** focusses on elucidating the unknown mechanisms of transformation in malignant cells by which V $\gamma$ 9V $\delta$ 2TCRs recognize and target tumor cells. We demonstrated in two independent human genetically engineered step-wise tumor mutagenesis models of colorectal and breast cancer that single oncogenic mutations allow for targeting by V $\gamma$ 9V $\delta$ 2TCR T cells. We have established that surface expression of the butyrophilin BTN2A1, the direct ligand of the gamma chain of V $\gamma$ 9V $\delta$ 2T cell receptor, is a direct consequence of these earliest PI3K/AKT/mTOR activating mutations. Although these hallmarks of V $\gamma$ 9V $\delta$ 2 targeting were already present in the absence of aminobisphosphonates (ABP), full activation required elevated phosphoantigen levels. We could link this to two novel ABP-dependent phosphorylation sites in the juxtamembrane region of BTN3A1, impacting the regulation of BTN2A1 and BTN3A1 surface expression. Finally, we applied an ABP-dependent protein interactome analysis pipeline and identified an interactome of BTN3A1-proximate proteins, and established an influence on targeting by V $\gamma$ 9V $\delta$ 2T cells for three of them, namely PHLDB2, SYNJ2 and CARMIL1.

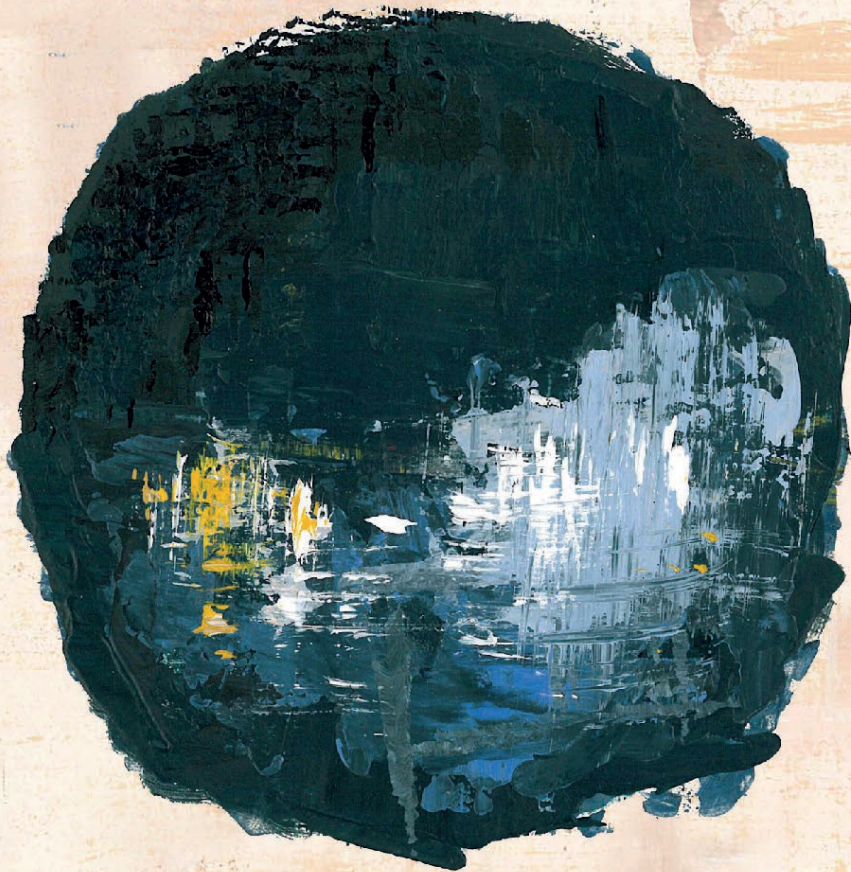
In **Chapter 4** we introduced a 3D-live-imaging platform, BEHAV3D, which allows live-tracking and characterization of T cells and their dynamic interactions with patient-derived organoids (PDO). In this system we described how this characterization can improve cellular anticancer immunotherapies by identification of different behavioral types of T cells that differ among different PDOs with the potential to enrich for a certain potent transcriptomic signature in effector cells.

In **Chapter 5** we aimed to improve migration of cytotoxic CD8+ engineered T cells to the tumor site and infiltration of the tumor microenvironment (TME) by harnessing a natural occurring chemokine gradient (CCL4-CCR5). Armoring of engineered T cells with the chemokine receptor CCR5 enhanced active migration of the T cells as well as tumor

infiltration and killing in a 3D multicellular tumor model, consisting of patient-derived organoids (PDOs) of colorectal and breast cancer.

In **Chapter 6** we strived to better understand and overcome the hostile environment of the TME by applying a complex *in vitro* 3D multicellular screening pipeline combined with transcriptomic analyses. Investigation of the influence of various patient-derived mesenchymal stromal cells (MSCs) revealed vastly heterogenous, donor-dependent responses of T lymphocytes regarding their ability to successfully target tumor cells, with some MSCs suppressing the cytotoxic abilities of the T cells. Transcriptomic analyses of both, mono- and multi-cellular systems, revealed distinctive gene signatures of immunosuppressive and immunopermissive MSCs, and identified differences in collagen expression as potential point of intervention. Finally, we confirmed the role of MSCs in the formation of an immunosuppressive collagen matrix in the TME and showed that blockade of the immune inhibitory collagen-receptor LAIR-1 on T cells led to enhanced tumor infiltration in the presence of immunosuppressive MSCs.

**Chapter 7** summarizes and discusses the findings of the abovementioned chapters in the context of recent literature within the field of V $\gamma$ 9V $\delta$ 2T cell biology and engineering of adoptive T cell immunotherapies.



*<sup>1</sup> Center for Translational Immunology, University Medical Center Utrecht, Utrecht University, Utrecht, The Netherlands*

*<sup>2</sup> Department of Hematology, University Medical Center Utrecht, Utrecht University, Utrecht, The Netherlands*

*<sup>3</sup> Biomolecular Mass Spectrometry and Proteomics, Bijvoet Center for Biomolecular Research and Utrecht Institute for Pharmaceutical Sciences, Utrecht University, Utrecht, The Netherlands.*

*<sup>4</sup> Netherlands Proteomics Centre, Utrecht, The Netherlands.*

*<sup>5</sup> Facultad de Ciencias Biomédicas y Salud, Universidad Europea, Madrid, Spain*

*<sup>6</sup> Hubrecht Institute, Royal Netherlands Academy of Arts and Sciences (KNAW), University Medical Centre Utrecht, Utrecht The Netherlands*

*<sup>7</sup> Oncode Institute, Hubrecht Institute, Utrecht The Netherlands,*

*<sup>8</sup> Department of Medical Oncology, University Medical Center Utrecht, Utrecht University, Utrecht, The Netherlands*

*<sup>9</sup> Princess Máxima Center for Pediatric Oncology, Oncode Institute, Utrecht, The Netherlands*

*<sup>10</sup> Department of Pathology, University Medical Center Utrecht, Utrecht, The Netherlands.*

# CHAPTER | 3

## **PI3K-AKT1-mTOR activity and BTN3A1 phosphorylation are required for early cancer immune surveillance via V $\gamma$ 9V $\delta$ 2TCR T cells**

Astrid Cleven<sup>1\*</sup>, Angelo D. Meringa<sup>1\*</sup>, Domenico Fasci<sup>1</sup>, Thijs Koorman<sup>10</sup>, Peter Brazda<sup>1</sup>, Tineke Aarts<sup>1</sup>, Inez Johanna<sup>1</sup>, Dennis X Beringer<sup>1</sup>, Patricia Hernandez-Lopez<sup>1</sup>, Sabine Heijhuurs<sup>1</sup>, Tomohiro Mizutani<sup>6</sup>, Sangho Lim<sup>6</sup>, Maarten Huismans<sup>8</sup>, Jochem Bernink<sup>6</sup>, David Vargas Dias<sup>3,4</sup>, Wei Wu<sup>3,4</sup>, Esther San Jose<sup>5</sup>, Jelle Schipper<sup>1</sup>, Nikos Tskakirakis<sup>1</sup>, Lauren Hoorens van Heyningen<sup>1</sup>, Annick Nouwens<sup>10</sup>, Lucrezia Gatti<sup>1</sup>, Trudy Straetemans<sup>1,2</sup>, Hugo Snippert<sup>8</sup>, Jeanine Roodhart<sup>8</sup>, Patrick Derksen<sup>10</sup>, Jarno Drost<sup>9</sup>, Maarten Altelaar<sup>3,4</sup>, Albert Heck<sup>3,4</sup>, Hans Clevers<sup>6,7</sup>, Juergen Kuball<sup>1,2#</sup>, Zsolt Sebestyen<sup>1#</sup>

\*authors contributed equally  
#Shared senior authorship

*Manuscript in preparation*  
**Patent application: P36295EP00 submitted 2023**  
**(A. Cleven co-inventor)**

## Abstract

Although tumor infiltrating V $\gamma$ 9V $\delta$ 2T cells often have a good prognostic value, their role in cancer immune surveillance remains to be defined. We employed two independent human genetically engineered step-wise mutagenesis models of colorectal and breast cancer to demonstrate that a single oncogenic mutation which led to enhanced PI3K activity introduced into healthy cells or organoids is sufficient to upregulate surface expressed BTN2A1, a known ligand of V $\gamma$ 9V $\delta$ 2TCR on tumor cells. Full activation of T cells through a V $\gamma$ 9V $\delta$ 2TCR required phosphorylation of JTM amino acids of BTN3A1 leading to the activating heterodimerization of BTN2A1 and 3A1. Using a novel protein interactome mapping pipeline, we identified PHLDB2, SYNJ2 and CARMIL1 as key players in controlling surface dynamics of BTN2A1 and 3A1 during early transformation. This mode of action allowed V $\gamma$ 9V $\delta$ 2TCR T cells to control tumors in vitro and in vivo emphasizing the crucial role of these molecules from early mutagenesis to advanced cancer stages and the therapeutic potential of a V $\gamma$ 9V $\delta$ 2TCR.

## Introduction

Increasing evidence show that human  $\gamma\delta$ T cells have an essential role in cellular stress sensing and immune surveillance for both microbial and autologous stress (e.g. tumorigenesis)<sup>1</sup>. Infiltration of  $\gamma\delta$ T cells in various tumors has been shown to have a favorable prognostic value<sup>2</sup> and play an important role in the immunosurveillance of early tumor development in mice<sup>3</sup>, putting V $\gamma$ 9V $\delta$ 2T cells most likely at the first line of defense during transformational processes of a healthy to a cancer cell, however it remains unclear which process triggers  $\gamma\delta$ T cells during early transformation even though the anti-tumor role of  $\gamma\delta$ T cells has been implicated in various tumor models with established tumors<sup>4-7</sup>. V $\gamma$ 9V $\delta$ 2T cells, which are considered the most innate-like subset of gamma delta T cells in general<sup>1</sup>, are activated by intermediate metabolites of the isoprenoid/mevalonate pathway, such as isopentenyl-5-pyrophosphate (IPP)<sup>8</sup>, also referred to as phosphoantigens (pAgs) which can build up in cancerous- or virally-infected cells due to disruption of the mevalonate pathway. Aminobiphosphonate (ABP) drugs, such as pamidronate (PAM), can also further increase cellular pAg levels, by inhibiting farnesyl diphosphate synthase (FPPS), an essential enzyme in this pathway<sup>9</sup>. Because of the broad-, but tumor-specific recognition of malignantly-transformed cells, and the lack of MHC-restriction, V $\gamma$ 9V $\delta$ 2T cells harbor great clinical potential as an immunotherapy for cancer<sup>10-12</sup>. Even though it is well-established that the  $\gamma\delta$ TCR itself is essential for recognition of pAgs, the exact mechanism of ligand-receptor interaction has not been found yet, intracellular pAgs are bound to the B30.2 domain of butyrophilin-3 isoform A1 (BTN3A1) which leads to complex formation with BTN2A1<sup>11,13-15</sup>. BTN2A1 has emerged as key protein for recognition of tumor cells by V $\gamma$ 9V $\delta$ 2-T cells<sup>14</sup> where it is directly bound by the gamma chain of V $\gamma$ 9V $\delta$ 2TCR. The role of the small GTPase RHOB, was previously demonstrated by our group to relocalize to the membrane and interact with BTN3A1 upon pAg build-up<sup>16</sup>. This is associated with cytoskeletal changes and reduced mobility of BTN3A1 in the membrane, implying a sort of “membrane trapping” mechanism. It is thought that direct binding of pAgs to the intracellular B30.2 domain enables heterodimerization of BTN3A1 with BTN2A1. The subsequently induced joint conformational and spatial changes stabilize BTN2A1-homodimers, which are then available for interaction with the  $\gamma\delta$ -TCR<sup>16-18</sup>.

Even with the identification of BTN2A1<sup>11,13,14</sup>, the understanding of BTN3A1 regulation through RHOB<sup>11,16</sup>, and the most recent observation that pAgs glue BTN3A1 and BTN2A1<sup>18</sup>, it is not fully elucidated how this mechanism is regulated. Recently, it has been shown to be partially controlled by the AMPK pathway, and activation of this pathway led to increased transcription of both molecules, BTN3A and BTN2A1, followed by enhanced activation of V $\gamma$ 9V $\delta$ 2T cells<sup>19</sup>. Although, these new insights defined a signature which is predictive for recognition of tumors in cancer patients<sup>19</sup>, the signature

could not elucidate at which stage of transformation from a healthy cell to a cancer cell the BTN-pathway is turned on. We used therefore a step wise mutagenesis model for colon cancer, which remodels different steps during mutagenesis in order to characterize expression patterns of BTN2A1, BTN3A1 and RHOB during transformation and hunt for novel players regulating in particular the heavily orchestrated BTN3A1 molecule by an innovative proximity proteomics approach. To properly analyze recognition of a tumor cell through V $\gamma$ 9V $\delta$ 2TCR and overcome diversity in innate receptor expression and diversity in function of natural V $\gamma$ 9V $\delta$ 2 T cells we used soluble V $\gamma$ 9V $\delta$ 2TCR formats<sup>11,12</sup> as well as  $\alpha\beta$ T cells expressing a high affinity V $\gamma$ 9V $\delta$ 2 TCR20-22. This strategy allowed to characterize the orchestration of BTN2A1 and BTN3A1 during early transformation and late-stage cancers where BTN2A1 traffics early during mutagenesis to the cell membrane in close proximity to BTN3A1, a process heavily regulated by PHLDB2, SYNJ2 and CARMIL1.

## Results

### V $\gamma$ 9V $\delta$ 2TCR T cells target early transformation events in colorectal cancer (CRC) which features are preserved in late CRC stages to enable targeting by V $\gamma$ 9V $\delta$ 2TCR T cells

Screening for tumor recognition of V $\gamma$ 9V $\delta$ 2TCR expressing T cells in CRC showed IFN $\gamma$  production by the T-cells upon co-culture with different CRC cell lines and importantly, also when using patient derived CRC organoids indicating that fully differentiated CRC cells and organoids can be recognized by the V $\gamma$ 9V $\delta$ 2TCR (**Figure 1A**), however, only in the presence of pamidronate (PAM). To assess at which stage of malignant transformation can be sensed by V $\gamma$ 9V $\delta$ 2TCRs we made use of a step-wise mutagenesis colon organoid model, where the introduction of single mutations of *APC* (*APC*<sup>KO</sup>), *KRAS* (*KRAS*<sup>G12D</sup>), *TP53* (*p53*<sup>KO</sup>) and *SMAD* (*SMAD*<sup>KO</sup>) into normal (healthy) colon organoids represents models for pre-cancerous lesions while the combination all four mutations (later referred as AKPS mutant) was used as model for fully developed CRC<sup>23</sup>. After co-incubation of T cells engineered to express a defined V $\gamma$ 9V $\delta$ 2TCR with organoids treated with/without PAM, a single gene mutation introduced in the normal (healthy) colon was already able to induce IFN $\gamma$  production through T cells harbouring a V $\gamma$ 9V $\delta$ 2TCR, while the matching normal colon organoids (healthy) did not (**Figure 1B and Supplementary Figure 1A**). We chose *APC*<sup>KO</sup> and AKPS mutant CRC organoids to represent very early and late stages of CRC development, respectively, to further characterize the capacity of a V $\gamma$ 9V $\delta$ 2TCR to sense early or late-stage cancer development.



APC and AKPS mutant CRC organoids both induced cytotoxic degranulation of V $\gamma$ 9V $\delta$ 2TCR T cells on a PAM-dependent manner after co-culture (**Supplementary Figure 1B**), confirming that a V $\gamma$ 9V $\delta$ 2TCR has the potential to sense early metabolic changes which are also preserved in fully developed CRC. Furthermore, V $\gamma$ 9V $\delta$ 2TCR T cells were also able to control CRC outgrowth for at least 43 days after tumor injection (**Figure 1C**) *in vivo* and improve overall survival of mice (**Supplementary Figure 1C**) when NSG-mice were engrafted with APKS mutant CRC organoids which is the only mutant that engrafts in mice<sup>23</sup>.

Recognition of late-stage tumors through a V $\gamma$ 9V $\delta$ 2TCR critically depends on the surface expression of BTN2A1, a complex regulation of BTN3A1<sup>13,14</sup> and hallmarked by changes in RhoB intracellular re-localisation<sup>16</sup>, however it is not known what role they play during early to late-stage cancer development. We found that these hallmarks are already present in the early, pre-cancerous stage as well as in fully developed CRC while lacking in normal (healthy) colon organoids as determined by using V $\gamma$ 9V $\delta$ 2TCR-coated beads to quantify surface-expressed BTN2A1<sup>11</sup> or by determining RhoB intracellular distribution using confocal microscopy<sup>11,16</sup> (**Figure 1D and E**). At the same time, we found that total expression of these essential ligands was similar among all tested organoids (**Figure 1F**).

The regulation of the intracellular storage pool of BTN2A1 that involves complex orchestration of other molecules in tumor cells including BTN3A1<sup>11,13,14,16</sup> and the intracellular re-localization of RhoB can be used as a hallmark of tumor cell recognition by V $\gamma$ 9V $\delta$ 2TCR<sup>16</sup>. In particular this process has been described to depend on PAM modulation<sup>11,16</sup>. This altogether suggests that early onset of transformation including single mutations in oncogenes is not only accompanied with BTN2A1 surface expression but also modulation in the BTN3A1-RHOB axis, though the later one depends on PAM.

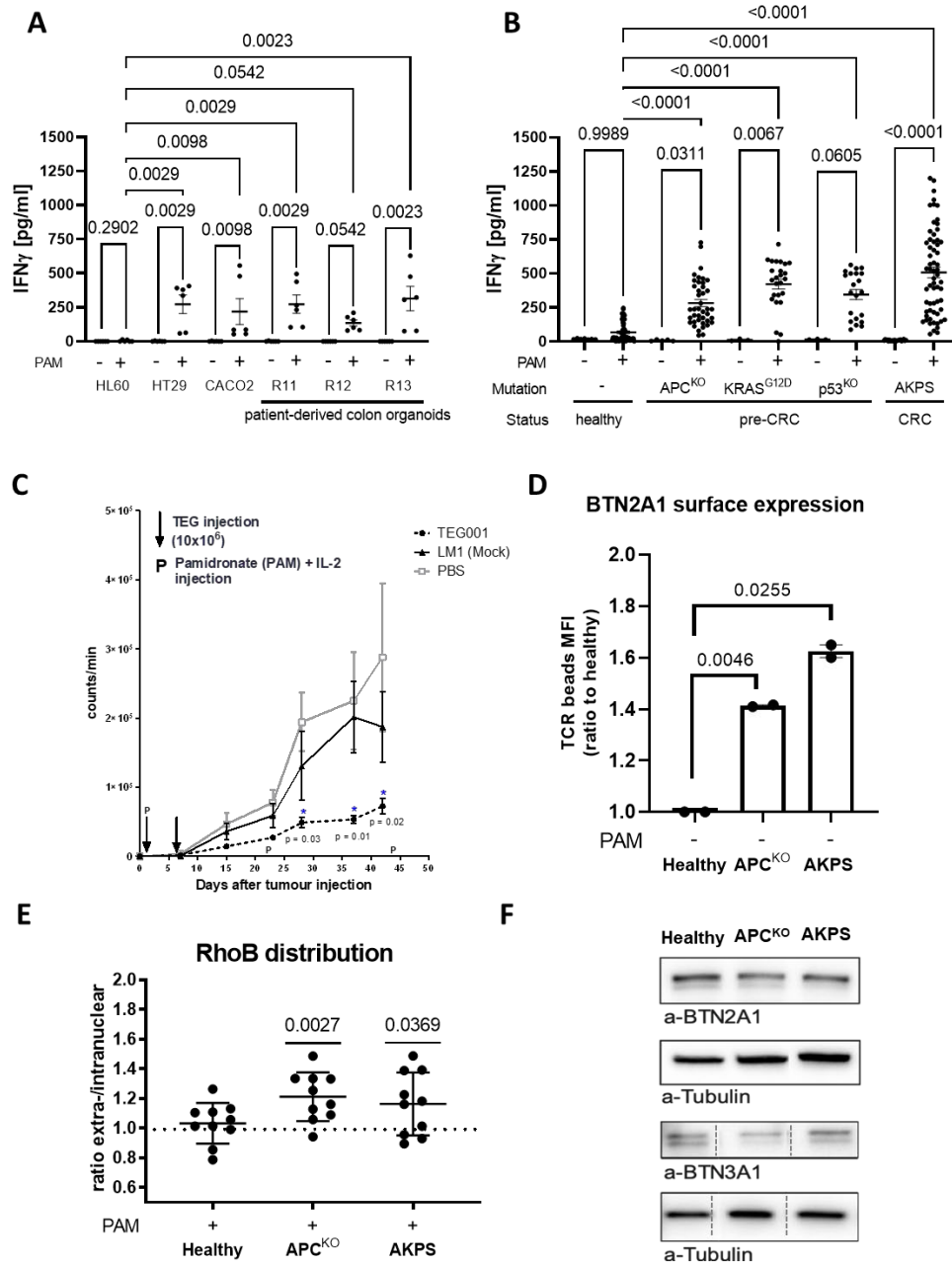


**Figure 1. V $\gamma$ 9V $\delta$ 2 TCR T cells recognize early transformed CRC organoids. (A)** Patient derived CRC organoids (PDO) were co-cultured with V $\gamma$ 9V $\delta$ 2TCR T cells in the presence of PAM and IFN $\gamma$  release of T cells was determined by ELISA. **(B)** IFN $\gamma$  production by V $\gamma$ 9V $\delta$ 2TCR T cells after co-culture with either healthy colon organoids (wt) or CRC organoids mutated for APC, p53, KRAS or the combination (AKPS) in the presence of 100uM PAM. **(C)** In vivo efficacy of V $\gamma$ 9V $\delta$ 2TCR T cells against AKPS CRC organoids in the presence of PAM. Mice were treated with either PBS, T cells expressing a non-functional V $\gamma$ 9V $\delta$ 2TCR (LM1) or a high affinity V $\gamma$ 9V $\delta$ 2TCR (TEG001). Tumor burden of AKPS CRC organoids assessed by in vivo bioluminescence imaging (BLI) measuring integrated density per entire tumor area of mice. Statistical significances were calculated by mixed-effects model with repeated measures; \*, P < 0.05; \*\*\*, P < 0.001. **(D)** Healthy colon organoids (WT), CRC organoids mutated for APCKO or AKPS mutant CRC were stained with microbeads coated with either non-functional LM1 soluble V $\gamma$ 9V $\delta$ 2TCR (LM1) or with high affinity soluble V $\gamma$ 9V $\delta$ 2TCR (CI5) in the absence of PAM. Data show MFI of bead binding. **(E)** RhoB intracellular distribution after PAM treatment in wt, APCKO or AKPS mutant CRC organoids, measured by confocal microscopy. **(F)** Total BTN2A1 and BTN3A1 expression of wt, APCKO and AKPS mutant CRC organoids in the absence of PAM was determined by western blot.

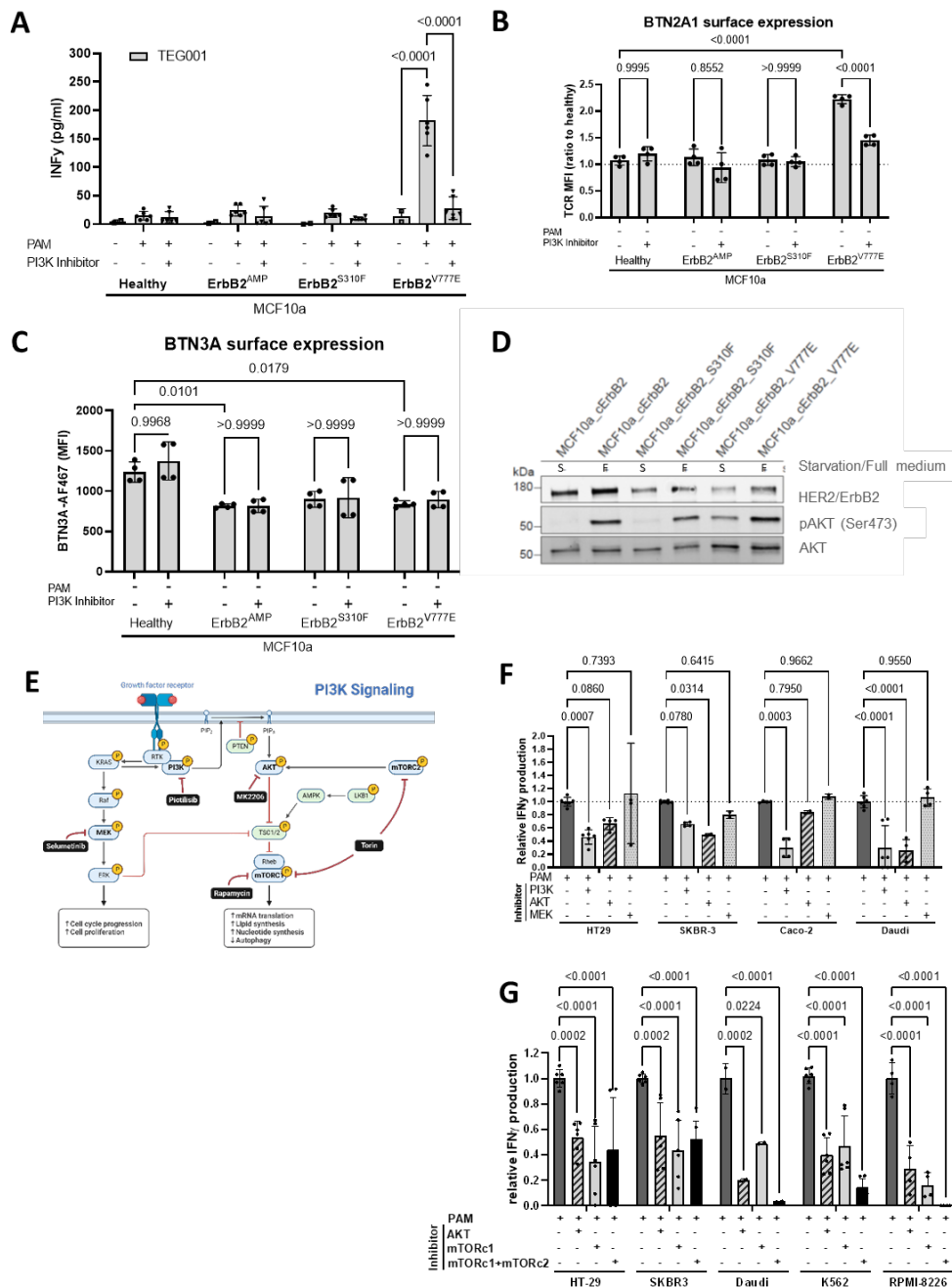


**Figure 2. Transformed cells upregulate BTN2A1 surface expression via PI3K kinase activity.** (A) MCF10a cells were transduced with different ErbB2 variants and co-cultured with either V $\gamma$ 9V $\delta$ 2TCR or HER2-CAR transduced T cells. Tumor cells were pre-treated with the PI3K kinase inhibitor Pictilisib at 2 $\mu$ M overnight. After an overnight co-culture, supernatant was used to determine IFN $\gamma$  production by the V $\gamma$ 9V $\delta$ 2TCR T cells. (B) Furthermore, tumor cells were isolated and stained for BTN2A1 via TCR tetramer staining and (C) BTN3A cell surface expression. (D) Protein expression of HER2, phosphorylated AKT (pAKT) and total AKT in MCF10a mutant lines cultured for 24h in full culture medium (F) or medium without additional growth factors (S). (E) Schematic of receptor tyrosine kinase activation pathway and common inhibitors. (F) Multiple tumor cell lines were co-cultured with V $\gamma$ 9V $\delta$ 2TCR T-cells after pre-treatment with either the PI3K kinase inhibitor, AKT inhibitor or MEK inhibitor. After an overnight co-culture, supernatant was used to determine IFN $\gamma$  production by the V $\gamma$ 9V $\delta$ 2TCR T cells. (G) Multiple tumor cell lines were pre-treated with either PI3K kinase inhibitor, AKT inhibitor, mTOR inhibitor Rapamycin or mTOR inhibitor Torin1 and subsequently co-cultured with V $\gamma$ 9V $\delta$ 2TCR T cells. After an overnight co-culture, supernatant was used to determine IFN $\gamma$  production by the V $\gamma$ 9V $\delta$ 2TCR T cells.

### Phosphoinositide 3-kinase/AKT1 activity during early transformation is a prerequisite of V $\gamma$ 9V $\delta$ 2TCR activation

In order to confirm that single oncogenic mutations generally trigger V $\gamma$ 9V $\delta$ 2TCR activation, we tested the effect of single ErbB2 mutations and overexpression in breast tissue<sup>24-26</sup>. MCF10a benign breast tissue cell line was engineered to mimic various oncogenic ErbB2 gene related mutations such as overexpression of HER2 (ErbB2<sup>AMP</sup>), a single mutation in the extracellular domain (ErbB2<sup>S310F</sup>) or amplified kinase activity mutant (ErbB2<sup>V777E</sup>). Curiously, only MCF10a cells expressing kinase mutant HER2 variant (ErbB2<sup>V777E</sup>) triggered IFN $\gamma$  production of V $\gamma$ 9V $\delta$ 2TCR T cells in the presence of PAM (**Figure 2A**) while benign cells and the two other oncogenic variants remained unrecognized. Moreover, pre-treating MFC10a ErbB2<sup>V777E</sup> tumor cells with PI3K inhibitor Pictilisib led to significant reduction of IFN $\gamma$  production of V $\gamma$ 9V $\delta$ 2TCR T cells upon co-culture while HER2 CAR-T cell reactivity remained unaffected (**Supplementary Figure 2A**). Importantly, surface expression of the primary V $\gamma$ 9V $\delta$ 2TCR ligand, BTN2A1 was significantly increased upon ErbB2<sup>V777E</sup> mutation, and this increase was dependent of PI3 kinase activity in MCF10a cells, since pan PI3K inhibition depleted BTN2A1 surface expression, independently of the presence of PAM (**Figure 2B**). BTN3A surface expression however did not change either upon ErbB2<sup>V777E</sup> mutation or PI3K inhibition but it significantly reduced upon any oncogenic mutations induced into benign cells (**Figure 2C**).

We could confirm the dependency of BTN2A1 and independency of BTN3A1, respectively, on PI3K signalling in multiple targeted cell lines (**Supplementary Figures 2B and C**). When analyzing phosphorylation of AKT in MCF10a HER2 mutants, we found that while AKT was phosphorylated on position Ser473 in all lines in the presence of full culture medium containing growth factors, only a mutation in position V777E showed phosphorylation already in the absence of growth factors (**Figure 2D**), confirming the special role of this mutation. To further clarify the signalling cascade downstream of PI3K necessary for activation of V $\gamma$ 9V $\delta$ 2TCR T cells, we blocked various key kinases that might be activated by PI3K (**Figure 2E**) in the subsequent experiments. First, we confirmed the observed reliance of V $\gamma$ 9V $\delta$ 2TCR activation on PI3K activity in a panel of well-targeted tumor cell lines and confirmed AKT as preferred downstream target. In all tumor cell lines inhibition of both, PI3K and AKT1 significantly reduced V $\gamma$ 9V $\delta$ 2TCR activity, while specific MEK inhibitors did not alter recognition of the tumor cells (**Figure 2F**). Finally, pretreatment of tumor cell lines with blocking reagents of mTOR reduced recognition significantly, in a similar or even higher potency as inhibiting AKT activity (**Figure 2G**). Strikingly, inhibition of both mTOR-involved complexes, mTORC1 and mTORC2, by inhibitor Torin1 was superior in reducing activation of V $\gamma$ 9V $\delta$ 2TCR T cells compared to inhibition of only mTOR complex 1 (mTORC1) by Rapamycin. Furthermore,

hematological malignancies showed higher dependency on PI3K, AKT and mTOR compared to CRC tumor lines. These data together indicate that PI3K/AKT1/mTOR activity in the early onset of malignant transformation drives BTN2A1 surface upregulation on tumor cells therefore makes them susceptible for V $\gamma$ 9V $\delta$ 2TCR targeting.

### **BTN3A1 phosphorylation affects surface expression of BTN3A1 and BTN2A1**

Although we have shown that transformation induced AKT/mTOR activity bringing BTN2A1 to the cell surface is a prerequisite for V $\gamma$ 9V $\delta$ 2TCR binding in a PAM-independent manner, this only leads to full activation of  $\gamma\delta$ TCR T cells following PAM treatment. In order to better understand how PAM-induced cellular processes are separated from those induced by malignant transformation, we revisited previously generated mass spectrometry data 11, where PAM-induced changes in protein composition were studied. This analysis identified two potential phospho-sites on the juxtamembrane (JTM) region of the BTN3A1 molecule; the residues S296 and T297 that were shown to be phosphorylated upon PAM (**Figure 3A**) and which were previously suggested to be involved in pAg binding<sup>27</sup>.

To dissect PAM-induced phosphorylation on BTN3A1 from phosphorylation events induced by endogenous phosphoantigen (pAg) levels, we constructed modified versions of the BTN3A1 sequence that mimic protein conformation of either a phosphorylated (phospho-mimic variant) or an unphosphorylated state (phospho-deficient variant). These phospho-variants were developed by substituting residues S296 and T297 with aspartic acid which is known to function similarly to phosphorylated serine and threonine (D, phospho-mimic) or alanine which is employed regularly to inhibit residue phosphorylation (A, phospho-deficient). When reconstituting these BTN3A1-variants in HEK293FT-BTN3A1KO cells at comparable total expression (**Supplementary Figure 3**), we found that phospho-mimic BTN3A1 results in lower surface expression compared to phospho-deficient BTN3A1 (**Figure 3B**) which at the same time led to higher surface expression of BTN2A1 on these cells on a PAM-independent way (**Figure 3C**) while total expression of these proteins remained unchanged.

Importantly, the introduction of phospho-mimic BTN3A1 variant ultimately also resulted in a significantly higher activation of V $\gamma$ 9V $\delta$ 2TCR T cells upon PAM (**Figure 3D and 3E**). It has been shown that RhoB intracellular interaction and BTN2A1 heterodimerization in the cell membrane with BTN3A1 is a crucial spatial orchestration step in tumor cells that enable V $\gamma$ 9V $\delta$ 2TCR full activation upon pAg accumulation<sup>16,28</sup>. In order to understand whether phosphorylation mimicking of here-investigated residues is required for BTN3A1 membrane orchestration, we performed FRET measurements that showed that phospho-deficient BTN3A1 is unable to interact with both BTN2A1 and RhoB (**Figure 3F**)

suggesting an important role of JTM phosphorylation of BTN3A1 in enabling V $\gamma$ 9V $\delta$ 2TCR full activation.

### **Interactome platform identifies potential BTN3A1-proximate proteins involved in V $\gamma$ 9V $\delta$ 2TCR-induced tumor targeting**

Since PAM-dependent spatial changes in BTN3A1 are a hallmark for tumor recognition by V $\gamma$ 9V $\delta$ 2TCR, we further looked now at which PAM-induced spatial changes of protein complexes can be identified in the close proximity of BTN3A1. We set up an interactome pipeline to identify PAM-induced molecular complexes in the proximity of BTN3A1 that are exclusively related to V $\gamma$ 9V $\delta$ 2TCR activation (**Figure 4A**). As first step, we made use of Proximity-dependent biotin identification (BioID) approach<sup>29</sup> by overexpressing BTN3A1 fused to bacterial biotin ligase BirA\* to its the C-terminus in HEK293F cells. Cells were treated with 100  $\mu$ M PAM and 50  $\mu$ M biotin for 24h, which led to biotinylation of BTN3A1-close proteins (**Supplementary Figure 4A and B**), after which cells were lysed and biotinylated proteins were pulled down using streptavidin beads. Identification of proteins was done by mass spectrometry analyzing quadruplicate samples, which resulted in a list of 60 candidate proteins including 31 hits under no treatment, 19 upon PAM treatment and 10 hits that occurred upon both conditions (**Supplementary Figure 4C**).

In order to determine if candidate proteins play a physiological role in tumor targeting by V $\gamma$ 9V $\delta$ 2TCR T cells, we knocked down each candidate protein in HEK293F cells using siRNAs and used these cells as target against V $\gamma$ 9V $\delta$ 2TCR T cells in the presence of PAM (**Supplementary Figure 5A**). We used the same target cells also against Wilms tumor 1 specific (WT-1)  $\alpha\beta$ TCR T cells after loading with WT-1 peptide in order to exclude that candidate proteins are not involved in general T cell-target cell interactions (**Supplementary Figure 5B**). The effect of individual siRNA knock-down of candidate proteins was also confirmed in renal cell carcinoma cell line MZ1851RC (**Supplementary Figure 5C**). The summary of these knock-down experiments is shown in **Figure 4B**, which suggested that 5 candidate proteins, including PHLDB2, PKP2, SYNJ2, CARMIL1 and PA2G4 may play a role in the PAM-dependent activation of V $\gamma$ 9V $\delta$ 2TCR T cells, as additional modulators of the BTN3A1-RhoB axis.

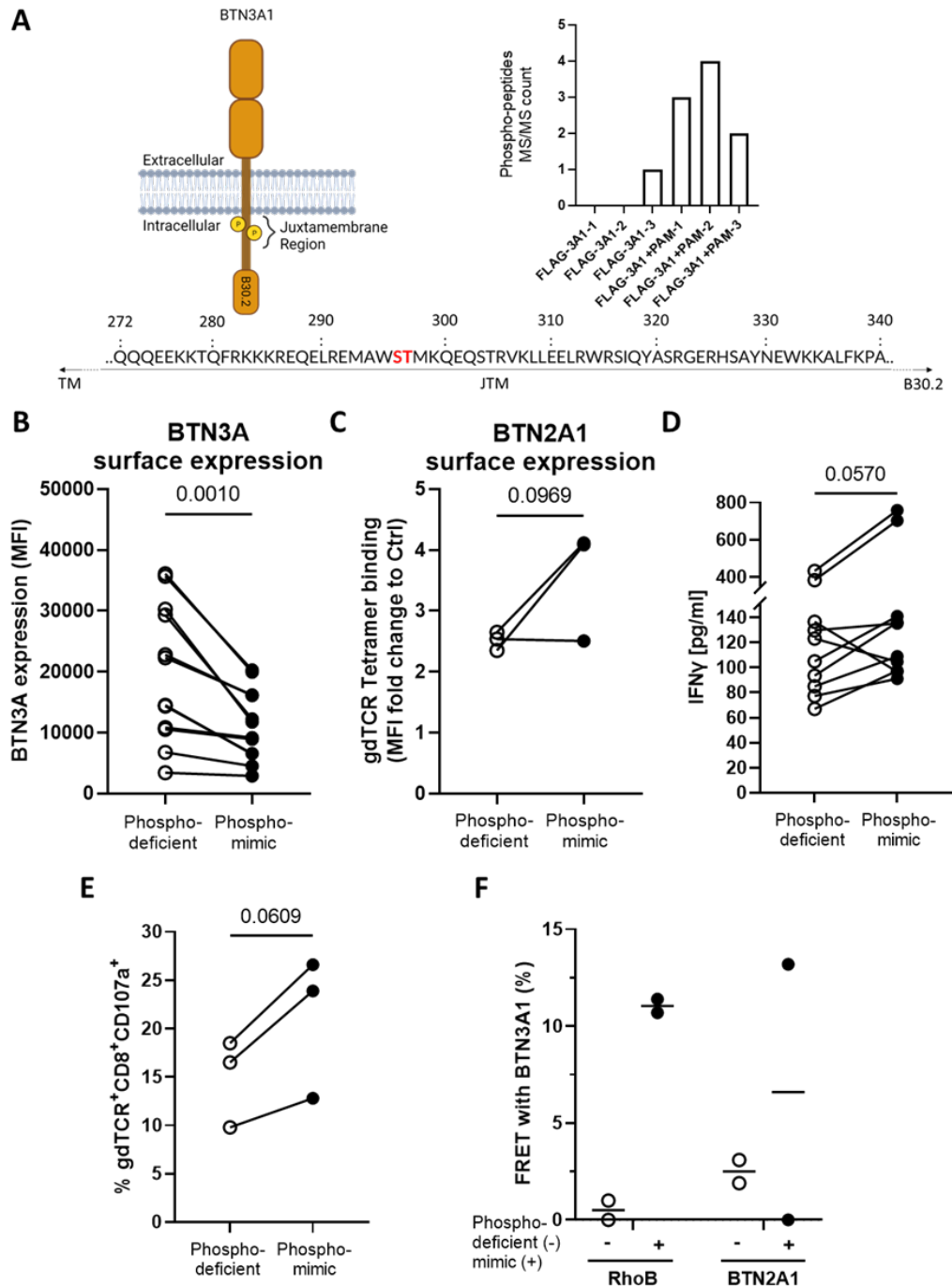


**Figure 3. Phosphosites of juxtamembrane region of BTN3A1 affect V $\gamma$ 9V $\delta$ 2TCR T cells target recognition.** (A) Previously published proteomic data including phospho-S/T/Y as variable modification on lysine identifies potential BTN3A1 phospho-sites enriched after PAM treatment. (B) Phospho-deficient and phospho-mimic mutated of S296 and T297 are reconstituted in BTN3A deficient HEK293FT cells together with wt BTN3A2. Surface expression of BTN3A1 was measured by using an anti-CD277 antibody. (C) BTN2A1 surface expression was determined using V $\gamma$ 9V $\delta$ 2TCR-tetramer binding. (D) IFN $\gamma$  production of V $\gamma$ 9V $\delta$ 2TCR T cells was measured upon co-culture with either the Phospho-deficient or the phospho-mimic mutated HEK293FT cells. (E) CD107a degranulation of V $\gamma$ 9V $\delta$ 2TCR T cells was measured upon co-culture with either the Phospho-deficient or the phospho-mimic mutated HEK293FT cells. (F) FRET measurement was performed between phospho-mutated variants of BTN3A1 and both, RHOB and BTN2A1-HA

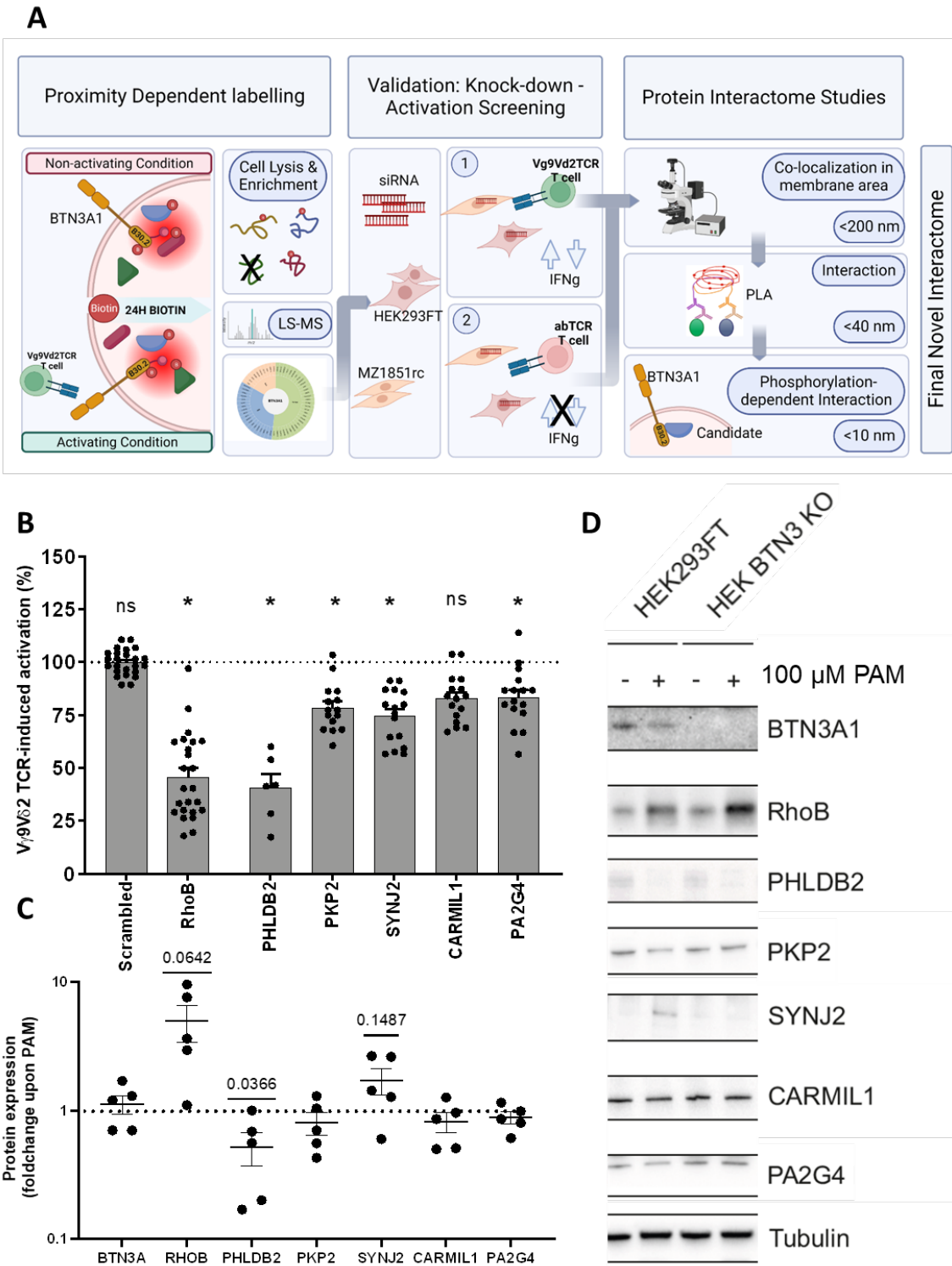


**Figure 4. BioID identifies BTN3A-interacting proteins involved in T-cell tumor targeting.** (A) Schematic representation of the BTN3A1 proteome characterization pipeline. (B) Genes as indicated have been transiently knocked-down using siRNA. After 48h V $\gamma$ 9V $\delta$ 2TCR T cells and 100  $\mu$ M PAM were added. After overnight co-culture IFN $\gamma$  production of V $\gamma$ 9V $\delta$ 2TCR T cells was measured. (C) Protein expression on 5 different targeted tumor cell lines was determined in the absence and presence of PAM by Western Blot, expression differences (PAM vs no PAM) as ratio are depicted in the figure. (D) Protein expression was determined using western blot analysis on either wild type HEK293 cells or HEK293 BTN3A-KO cells in the presence or absence of 100  $\mu$ M PAM.



## Novel protein interactome linked to BTN3A1 and RHOB in PAM-treated tumor cells

We wondered if PAM-induced spatial rearrangements of BTN3A1-related proteins as observed with BioID-tagging could partially be the result of post-transcriptional or post-translational regulation of proteins in tumor cells. Therefore, we assessed changes in protein expression upon PAM treatment in a panel of V $\gamma$ 9V $\delta$ 2TCR-activating tumor cell lines including breast cancer line MDA-MB 231, HEK293FT, renal cell carcinoma cell line MZ1851rc and head and neck cancer cell line SCC9 by performing Western blot analysis. We found that PAM treatment induced a significant increase of RhoB and SYNJ2 expression and decrease of PHLDB2 protein expression in all tested cell lines in the presence of PAM (**Figure 4C and Supplementary Figure 5D**). While BTN3A1 does not serve as direct ligand to V $\gamma$ 9V $\delta$ 2TCR but its knock-out in tumor cells abolishes V $\gamma$ 9V $\delta$ 2TCR activation<sup>30</sup>, we wondered if the expression of these proteins are dependent on expression of BTN3A. We compared protein expression in HEK293FT wt and HEK BTN3 KO cells in the presence and absence of PAM of the newly identified proteins and observed partial loss of expression of SYNJ2, suggesting its expression is partially co-regulated with BTN3A1 (**Figure 4D**).

To further map how BTN3A interaction dynamics occur with candidate proteins in a PAM-dependent manner, we analyzed co-localization between BTN3A membrane clusters and each of the candidate proteins using confocal microscopy in MZ1851rc cells. Examples of the region of interest selections and representative images are shown in (**Supplementary Figure 6A and B**). We found that while PHLDB2 moves out of, SYNJ2 and CARMIL1 moves into BTN3A membrane clusters upon PAM treatment within the range of approximately 200 nm, while CARMIL1 remains highly enriched in these BTN3A membrane clusters with or without PAM (**Figure 5A**). For the rest of the analysis, we narrowed down our focus on PHLDB2, SYNJ2 and CARMIL1 for two reasons: 1) the expression and cellular localization of PHLDB2 and SYNJ2 correlated significantly with that of BTN3A and 2) CARMIL1 gene is situated on chromosome 6 in close proximity to the BTN genes. To confirm if PHLDB2, SYNJ2 and CARMIL1 truly interact with BTN3A1 in tumor cell membranes we studied interaction at higher resolution measured by Proximity ligation assay (PLA) which is able to visualize protein interactions within approximately 40 nm. Similarly to the previously described small GTPase RHOB<sup>16</sup>, SYNJ2 showed a significant PAM-dependent interaction with BTN3A1. PHLDB2 showed no significant interaction with BTN3A1 while CARMIL1 showed a tendency to interact with BTN3A1 only upon PAM treatment (**Figure 5B and Supplementary Figure 6C**). This suggests that PHLDB2, SYNJ2 and CARMIL1 are next to RHOB involved in orchestrating PAM-induced cytoskeletal rearrangements in tumor cells that is a prerequisite for spatial and conformational changes in BTN3A1 leading to V $\gamma$ 9V $\delta$ 2TCR T cell activation.

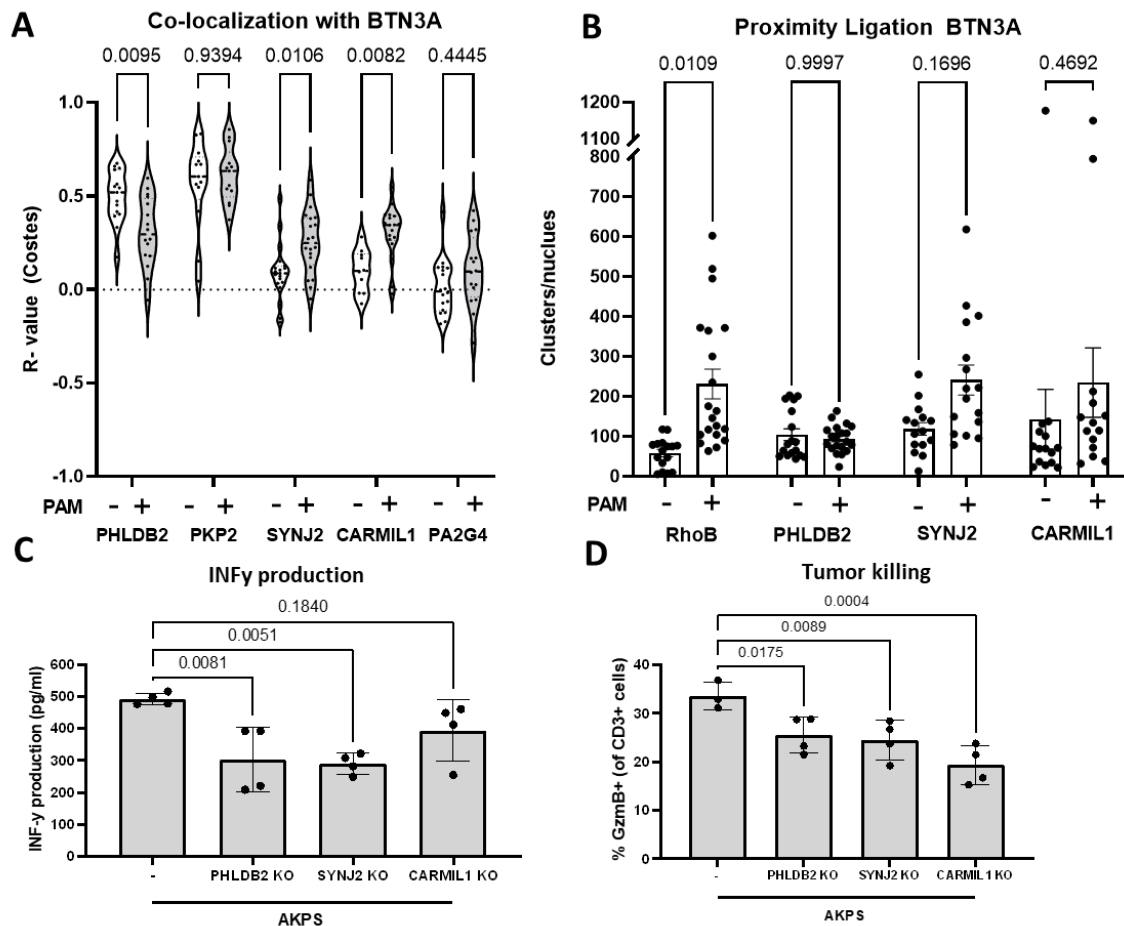


**Figure 5. Candidate proteins differentially colocalize with BTN3A in membrane clusters. (A)** MZ1851rc cells were treated overnight with either 0 $\mu$ M or 100 $\mu$ M PAM. Afterwards, cells were fixed, permeabilized, and stained for all of the indicated candidate interacting proteins and BTN3A1. Bars indicate mean  $\pm$  SEM. Statistical significance of differences between no PAM and PAM conditions were determined using unpaired parametric T-tests. All analyses were performed blinded to sample conditions. **(B)** MZ1851rc cells were either treated overnight with 100 $\mu$ M PAM or left untreated. Subsequently, cells were fixed and permeabilized. A DuoLink<sup>TM</sup> proximity ligation assay (PLA) was performed to assess interaction between CD277 and either PHLDB2, SYNJ2, or CARMIL1 respectively. Each condition was paired with a technical control (C) constituted by leaving out one of the primary antibodies. All the technical control samples were pulled together to form the control condition. Multiplicity adjusted P-values were calculated using a two-way ANOVA with Tukey's multiple comparison test. Bars indicate mean  $\pm$  SEM. **(C)** INF $\gamma$  production of V $\gamma$ 9V $\delta$ 2TCR T cells after co-culture with AKPS CRC organoids knocked out for PHLDB2, SYNJ2 and CARMIL1, respectively in the presence of 100  $\mu$ M PAM. **(D)** Granzyme B production of V $\gamma$ 9V $\delta$ 2TCR T cells after co-culture with KO-variants of AKPS mutant organoids knocked out for PHLDB2, SYNJ2 and CARMIL1 with the presence of 100  $\mu$ M PAM.

### PHLDB2, CARMIL1 and SYNJ2 affect V $\gamma$ 9V $\delta$ 2TCR targeting in CRC

In order to demonstrate that the here-identified BTN3A1-network is significant for the immunosurveillance of V $\gamma$ 9V $\delta$ 2TCR T cells in a clinically more relevant setting, we knocked out the individual candidate genes in AKPS mutant organoids using CRISPR/Cas system and tested V $\gamma$ 9V $\delta$ 2TCR T cells reactivity against them. KO of each individual genes similarly reduced both IFN $\gamma$  production and direct tumor killing of V $\gamma$ 9V $\delta$ 2TCR T cells in response to AKPS mutant organoids (**Figure 5C and D**).

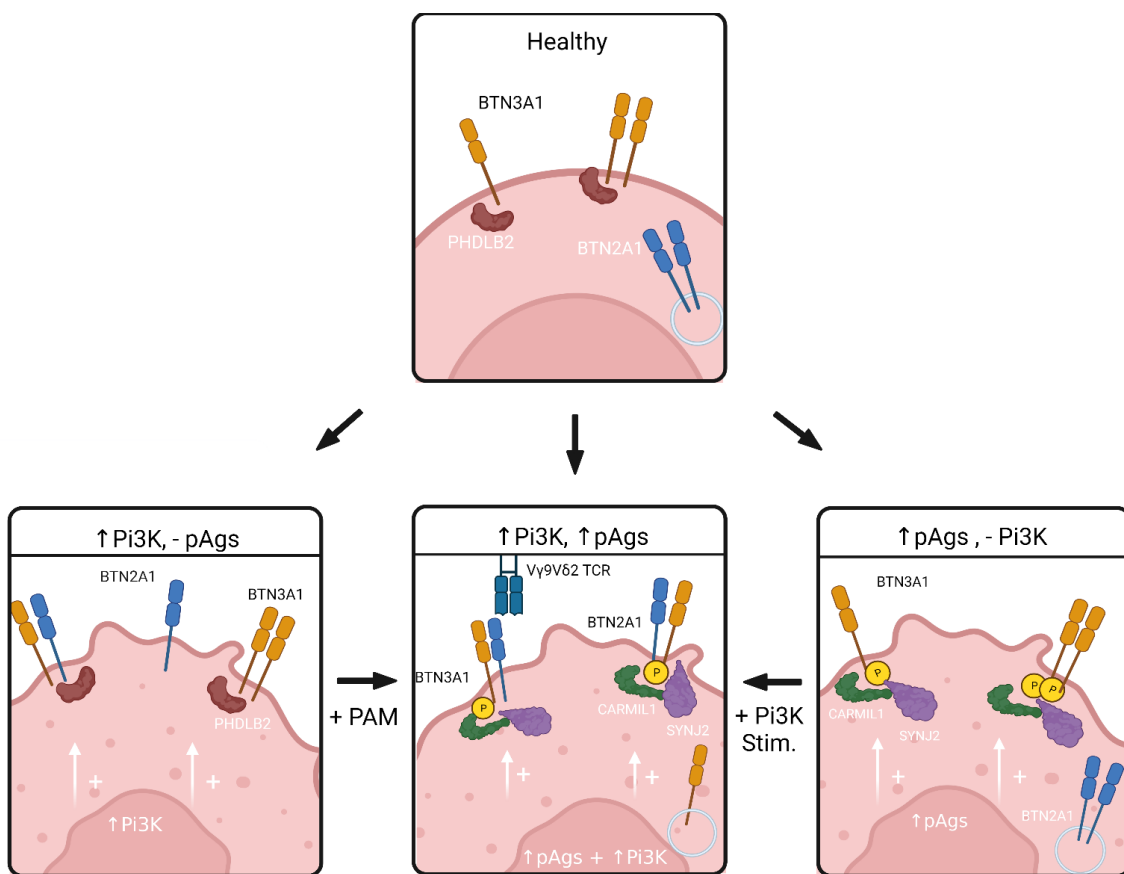


Figure 6. Graphical Abstract

## Discussion

Despite the growing interest in V $\gamma$ 9V $\delta$ 2T cells and their anti-tumor potential and the research aiming to resolve the unknown mechanisms of induction and regulation of this anti-tumor effect, there are still many mysteries to resolve. One of them being how tumor recognition is being triggered, and another how it is exactly regulated.

Here, we have demonstrated that V $\gamma$ 9V $\delta$ 2TCR T cells can sense earliest transformational alternations in cells that are driven by single mutations of a variety of oncogenes. We show that AKT phosphorylation and mTOR activity via enhanced PI3K activity in transformed cells results in enhanced BTN2A1 surface expression, a known ligand for the gamma chain of V $\gamma$ 9V $\delta$ 2TCR<sup>14,28</sup>, and thereby making early transformed cells susceptible for V $\gamma$ 9V $\delta$ 2TCR recognition. However, we show that in order to achieve full activation of T cells via the V $\gamma$ 9V $\delta$ 2TCR, an additional, parallel step is required that involves increased levels of intracellular phosphoantigens, which can be induced by aminobisphosphonates, like Pamidronate (PAM). We could link this to phosphorylation of the juxtamembrane (JTM) region of BTN3A1. These steps together result in a tightly regulated composition of membrane expressed BTN2A1 and BTN3A1 which is fed by a constant intracellular protein pool. While intracellular pAg-induced changes in total expression of BTN proteins were minimal, we found a series of spatial rearrangements directly related to BTN3A1, a crucial yet controversial player in V $\gamma$ 9V $\delta$ 2TCR immunity. Through mapping of the BTN3A1-RHOB axis we identified three novel functionally relevant proteins that showed PAM-dependent spatial dynamics, CARMIL1, SYNJ2, and PHLDB2.

Our data, in line with previous findings<sup>11,13,28</sup> imply that BTN2A1 and BTN3A1 membrane expression dynamics are tightly regulated together in human cells. It has been previously suggested that various pathways including AMPK<sup>19</sup> or EBV-induced activation of JNK<sup>31</sup> can influence BTN surface expression by enhancing transcription of BTN2A1 and BTN3A1. In contrary, we found the total BTN2A1 protein pool does not differ between healthy and transformed cells, however, in healthy cells we found no or low surface expression. And despite the contribution of these studies to better understand regulation of V $\gamma$ 9V $\delta$ 2T cell targeting, it is still unknown at what stage of tumorigenesis exactly V $\gamma$ 9V $\delta$ 2T cells begin to recognize and eliminate transformed cells.

In this study, we show that single mutations that induces higher PI3K activity were sufficient to allow expression of BTN2A1 at the cell membrane and to enable binding of the gamma chain of the V $\gamma$ 9V $\delta$ 2TCR. BTN2A1 surface expression was solely dependent on the onset of the PI3K pathway and was also not lost during later cancer stages suggesting that V $\gamma$ 9V $\delta$ 2TCR-based therapies would preferentially target tumors with

oncogenic mutations promoting PI3K activity, even at very early stages of malignant transformation.

While PI3K activity directly affects re-localization of BTN2A1 to the cell membrane, BTN3A1 surface expression remained unaffected by this oncogenic offset. However, we show that the upregulation of BTN2A1 on the cell surface is insufficient to fully activate V $\gamma$ 9V $\delta$ 2TCR T cells, but that accumulation of intracellular pAg are required. Dysregulation of the mevalonate pathway, a frequent hallmark of malignant transformation<sup>32</sup> leads to this accumulation, and it can be further boosted by the administration of aminobisphosphonates (ABP), like Pamidronate (PAM). Therefore, the oncogenic-regulated translocation of BTN2A1 to the cell surface and subsequent binding of pAg to the B30.2 domain of BTN3A1 upon ABP treatment, eventually leads to heterodimerization of BTN2A1 and BTN3A1 and ultimately to TCR binding and activation. Interestingly, in contrast to the previously mentioned JNK pathway, which is a downstream signaling pathway of PI3K/AKT<sup>33</sup>, AMPK and AKT are often seen to act as antagonists in regulating autophagy and apoptosis<sup>34,35</sup>, however, it has been shown that under certain conditions, e.g. cancer, activation of AMPK, especially via AMPK-activator AICAR, can also activate AKT<sup>36,37</sup> and mTORC2<sup>38</sup>, and vice versa, inhibition of AMPK via compound C reduced AKT activity<sup>36</sup>. It is also possible, that for the initial trigger, BTN2A1 surface expression, an oncogenic PI3K-activating mutation is necessary, but that further regulation and enhancement can be achieved by other pathways, such as AMPK.

The fact that not only artificial organoids mutated for all tumor associated genes, but also patient derived colorectal organoids are recognized by V $\gamma$ 9V $\delta$ 2TCR cells shows that these molecular rearrangements are preserved during tumor development. Since we show that depletion of PI3 kinase activity and in particular AKT phosphorylation and mTOR activity in tumor cells impairs V $\gamma$ 9V $\delta$ 2TCR reactivity implies that targeted therapies acting on the PI3K pathway should be carefully designed as they might interfere with endogenous innate responses against the tumor. On the other hand, PI3K activation in cancer patients, next to PAM treatment, might provide a new avenue to possibly sensitize tumors for V $\gamma$ 9V $\delta$ 2TCR-driven attack. When combining the knowledge from these studies with next generation engineering strategies such as TEGs<sup>20,22</sup> and Gamma delta TCR anti-CD3 bispecific molecules (GABs)<sup>12</sup> might employ full potential of how to maximize targeting potential via V $\gamma$ 9V $\delta$ 2TCRs.

We now propose that BTN2A1/BTN3A1 surface dynamics are regulated by spatial rearrangements of so-far unknown intracellular modulators of V $\gamma$ 9V $\delta$ 2TCR targeting. In this study we established a detailed ABP-dependent interactome of BTN3A1-related proteins using various protein proximity techniques that resolved spatial interaction hierarchies among the studied proteins. Out of 60 proteins, three showed a PAM-

dependent, differential co-localization pattern with BTN3A1 and were shown to directly modulate activation of V $\gamma$ 9V $\delta$ 2TCR T cells. PHLDB2 was found, as the only protein of all candidates to occupy BTN3A1-proximity membrane clusters without showing detectable direct close interaction with BTN3A1. Furthermore, it dissociates from these clusters once PAM is present, suggesting a complementary role in regulating the formation of PAM-induced protein aggregations, with PHLDB2 at low intracellular pAg levels possibly preventing the accumulation of BTN protein membrane clusters as also suggested by others<sup>39,40</sup>.

During early transformation events such as single mutations in oncogenes, rise of intracellular pAg levels leads to activations of the small GTPase RHOB. Active RHOB relocates to the cell membrane in the vicinity of BTN3A1 dimers as we have shown before<sup>16</sup>. Similarly to Rac1, another small GTPase closely linked to RHOB, active RhoB might cause relocalization of SYNJ2 from the cytosol to the cell membrane upon PAM stimulation<sup>41</sup>. SYNJ2, being enriched in larger size clusters but also in direct interaction with BTN3A1 in the presence of PAM leading to a PAM-induced protein aggregation close to BTN3A1. The phosphoinositide-5 phosphatase SYNJ2 has been shown to be involved in actin-based cytoskeleton dynamics<sup>42,43</sup> and furthermore has also been implicated in vesicle trafficking<sup>44</sup>, suggesting a role in BTN3A1 recycling<sup>11</sup>.

Like SYNJ2 and PHLDB2, also CARMIL1 most likely accommodates the formation of cytoskeletal rearrangement<sup>45</sup> and might altogether enable stabilized BTN2A1-BTN3A1 dimers in an immunological synapse on the tumor cell surface. While we found prove on multiple levels for co-localization or interaction with BTN3A1 in a PAM-dependent manner with CARMIL1, SYNJ2 and PHLDB2, their relationship to BTN2A1 remains unclear. Like AKT1, PHLDB2 contains a PH-domain, which has a high affinity to membrane-bound PIP3<sup>39</sup>, an oncogenic product by PI3K<sup>46</sup>. Therefore, a role of PHLDB2 in recruitment of BTN proteins to the cell membrane is not excluded and needs to be further investigated.

However, refining cytoskeletal rearrangements and regulating the surface expression dynamics of BTN2A1 and BTN3A1 to allow early formation of proper immunological synapses might be their most important role in V $\gamma$ 9V $\delta$ 2T cell activation. Importantly, these events are activated at very early stages of tumor formation and therefore sensed by V $\gamma$ 9V $\delta$ 2TCR T cells, indicating, that V $\gamma$ 9V $\delta$ 2T cells could play a crucial role in recognizing very subtle changes in normal tissue, that later possibly leads to tumor formation. Regardless of the physiological implication during early tumor development and cancer immune surveillance, this mechanism is independent on high mutational tumor load and would, once combined with phosphoantigens, open a novel avenue

towards treating many tumors where current immune therapies fail and have major implication for all V $\gamma$ 9V $\delta$ 2TCR based immune therapies.

Recently, pAg were shown to act as glue between BTN molecules BTN2A1 and BTN3A1 to activate V $\gamma$ 9V $\delta$ 2T cells<sup>18</sup>, and previously, the juxtamembrane (JTM) region have been identified as being sensitive for translating pAg-induced inside-out-signaling<sup>17,47</sup>. We have now identified two amino acids that are likely to be phosphorylated specifically upon PAM treatment. Phosphorylation of these sites led to lower BTN3A and higher BTN2A1 surface expression and was associated with higher IFN $\gamma$  production by V $\gamma$ 9V $\delta$ 2TCR T cells upon co-culture. Furthermore, our data suggests that phosphorylation of JTM BTN3A1 sites promotes interaction with RhoB and heterodimerization of BTN3A1 and BTN2A1 which will ultimately stabilize BTN2A1 at the cell surface and further increase in membrane surface clusters that altogether will form immunological synapses that enable proper T cell activation. These events are not only present in very early transformation events but likely also preserved in late stages of tumors, since colorectal organoids mutated for all four colon cancer associated oncogenes are equally recognized by V $\gamma$ 9V $\delta$ 2TCR T cells as single APC mutated ones.

In summary, we show that during early mutagenesis hallmarks for the recognition of a cell through V $\gamma$ 9V $\delta$ 2TCR are induced such as BTN2A1 surface upregulation and RhoB relocalization. We found activated PI3K pathway in single oncogene mutated tumors and phosphorylation of BTN3A1 JTM region as two independent mechanism that drive immunogenicity of V $\gamma$ 9V $\delta$ 2TCRs. We identified three novel key players that affect BTN2A1 surface expression and directly regulates BTN3A1 dynamics on the cell surface. These findings do not only shed light in the role of V $\gamma$ 9V $\delta$ 2T cells during early cancer immune surveillance but have also great implication for all V $\gamma$ 9V $\delta$ 2T cell based immune therapies.

## Methods

**Antibodies.** The following antibodies were used: Anti-CD277/BTN3A Alexa Fluor 647 (FAB7316R, Clone 849203), Anti-CD277/BTN3A PE MAb (FAB7316P, Clone 849203), anti-CD277/BTN3A (clone 20.1, LSC106569), pan- $\gamma\delta$ TCR PE (IMMU510, B49176), Granzyme B APC (QA16A02, 372204), CD107a PE (H4A3), CD8a PerCP-Cy5.5 (RPA-T8, 301032), anti-RhoB mouse monoclonal (C-5, sc-8048), anti-RhoB rabbit polyclonal (abcam, ab170611), anti-CD3 (clone: OKT3), Goat-anti-Rabbit AF488 IgG (H+L), anti-Rabbit AF488 Fab fragment, Goat-anti-Mouse AF488 IgG (H+L), anti-LRRC16A/CARMIL1 Rabbit polyclonal IgG (NBP1-91221), anti-PHLDB2 Rabbit polyclonal IgG (NBP2-38238), anti-CASKIN1 Rabbit polyclonal IgG (HPA055990), anti-HNRNPC mouse monoclonal IgG (AMAb91010), anti-PKP2 Rabbit polyclonal IgG (PA553144), anti-ANKRD26 Rabbit polyclonal IgG (PA559240), anti-VPS13A Rabbit polyclonal IgG (PA554483), anti-TANC1 Rabbit polyclonal IgG (PA557797), anti-SDK2 Rabbit polyclonal IgG (ABIN1386438), anti-NBEA rabbit Polyclonal IgG (HPA040385), anti-PA2G4 Mouse monoclonal IgG (ABIN518579), anti-SYNJ2 Rabbit polyclonal IgG (PA556784). Rabbit mAb ERBB2 (29D8) (1:1,000; #2165; Cell Signaling Technology), rabbit mAb AKT (1:1,000; #9272; Cell Signaling Technology), rabbit Phospho-AKT Ser473 (1:1,000; #9272; Cell Signaling Technology), rabbit mAb Phospho-AKT Thr308 (D25E6) (1:1,000; #13038; Cell Signaling Technology), Rabbit mAb P44/42 MAPK (Erk 1/2) (137F5) (1:1,000; #4695; Cell Signaling Technology), rabbit mAb Phospho-MAPK (Erk 1/2 Thr202/Tyr204) (D13.14.4E) (1:1,000; #4370; Cell Signaling Technology), mouse mAb GAPDH (1:5000, G8795, MERCK/Sigma-Aldrich).

**Cell and patient derived organoid culture.** HEK293FT, MDA-MB-231, MZ1851rc, HT29, SKBR-3, Caco-2, HL-60, Phoenix-ampho and MCF10a cells lines were cultured in DMEM+GlutaMAX with 10% fetal calf serum (FCS) and 1% Penicillin-Streptomycin. Daudi cells were cultured in in RPMI-GlutaMAX with 1% Pen/Strep and 10% FCS. MCF10A cells were cultured in DMEM/Ham's F-12 (Gibco) supplemented with, 1% Penicillin/Streptomycin (Gibco), Ala-Gln (Ultra-Glutamine) (Gibco), 5% heat-inactivated horse serum (Lonza), 0.01 mg/ml insulin (Gibco), 500 ng/ml hydrocortisone (Sigma), 100ng/ml cholera toxin (Sigma), 20 ng/ml epidermal growth factor (EGF) (Peprotech). Cell lines were routinely tested for mycoplasma and STR type verified by eurofins. PBMCs were isolated from buffy coats using ficoll-paque obtained from the Blood bank Sanquin. Colon organoids were established and cultured as previously described<sup>48</sup>. Before co-cultures, organoids were recovered from the BME using TrypLE express.

**Generation of engineered T-cells.**  $\gamma\delta$ TCR and HER2 CAR T-cells were generated as previously published<sup>22</sup>. In short, Phoenix-ampho cells were transfected with env (COLT-GALV), gag-pol (HIT60) and pBullet retrovirus constructs containing either both TCR chains or the HER2 CAR sequence. Pre-activated T-cells were subsequently transduced



twice with the viral supernatant of these cells with polybrene. Transduced T-cells were isolated and expanded using a rapid expansion protocol.

**Viral transduction MCF10a.** pBABE-Puro retroviral vector (EV) and pBABE-Puro vectors carrying ERBB2 wild-type and mutants were co-transfected independently with pUMVC (Addgene #8449) and VSV-G (Addgene #8454) retroviral packaging plasmids into HEK-293T cells using PEI-transfection. Medium was refreshed after 24hrs and viral supernatant was collected 48hrs and 72hrs after transfection. Viral particles were added to low passage MCF10A cells and incubated overnight. Twenty-four hours following transduction, MCF10A cells were selected using 2  $\mu$ g/ml Puromycin (Gibco) for two days. Gene transduction and protein expression were validated using western analysis. Established cell lines were immediately expanded and cryopreserved in low passage aliquots.

**Plasmids.** Retroviral pBabe-Puro plasmids were purchased from Addgene: ERBB2 (#40978), ERBB2::S310F (#40991), and ERBB2:: A775\_G775insV, G776C (V777E) (#40979). All plasmids and mutations were verified by Sanger Sequencing.

**BioID.** pcDNA3.1 MCS-BirA(R118G)-HA was a gift from Kyle Roux (Addgene plasmid # 36047; <http://n2t.net/addgene:36047>; RRID:Addgene\_36047). The DNA sequence of BTN3A1-BirA(R118G)-HA has been subcloned into pBullet retrovirus constructs. Phoenix-ampho cells were transfected with env (COLT-GALV), gag-pol (HIT60) and pBullet retrovirus constructs containing BTN3A1-BirA(R118G)-HA constructs. HEK293FT cells were subsequently transduced twice with the viral supernatant of these cells with polybrene. Transduced cells were selected using 2,5 mg/ml G418. Expression was confirmed by confocal microscopy. The preparation of the samples for analysis by LS-MS followed the protocol by Roux et al 29,49. In short, HEK293FT WT or BTN3A1-BirA(R118G)-HA expressing cells were 50  $\mu$ M Biotin alone or 50  $\mu$ M Biotin and 100  $\mu$ M Pamidronate. Cells were lysed and sonicated to generate whole cell lysates. Biotinylated proteins were pulled down using streptavidin-magnetic beads and samples were then analyzed by LS-MS. Each condition was prepared as quadruplicate.

**Western Blot.** Cell lines were seeded in a 10 cm dish overnight to confluency. Cells were rinsed with ice cold PBS and lysed with lysis buffer containing 1% NP-40, 150 mM NaCl, 20 mM Tris HCl pH 7,6 and protease inhibitors (complete, Roche, #11873580001). Protein concentration was determined using Pierce BCA Protein Assay Kit - Rapid Gold (Fisher Scientific, #15776178) and 5  $\mu$ g total protein was loaded on each lane of a Mini Protean TGX Gel (BioRad, #4561093) together with a standard (WesternC, BioRad, #1610376) and run at 140V. The protein was then transferred to a 0.2  $\mu$ m nitrocellulose membrane (BioRad, #1704158) using Trans-Blot Turbo System. The membrane was incubated in blocking buffer (PBS-T + 5% BSA for 1h at RT, washed three times with PBS-

T (0,1% Tween) and incubated overnight on a rotator with the respective primary antibodies as indicated. After three times washing with PBS-T at RT, membranes were incubated with the respective secondary antibodies for 1h at RT on a rotator. After final washings, membranes were developed using the ECL Kit and measured.

**Inhibitors.** The following inhibitors were used in this study; PI3K inhibitor GDC-0941 (Pictilisib) (SelleckChem, #S1065), pan-AKT inhibitor MK2206 (SelleckChem, #S1078), MEK inhibitor AZD6244 (Selumetinib) (SelleckChem, #S1008), mTORC 1 inhibitor Rapamycin (Sirolimus) (SelleckChem, #S1039), mTORC 1 / 2 inhibitor Torin 1 (SelleckChem, #S2827).

**Stimulation assays.** 50.000 tumor cells were co-cultured overnight at 37°C in a round-bottom 96-well plate (Nunc, Thermo-Fisher Scientific) with 50.000 Vγ9Vδ2-expressing T cells (TEGs) or HER2 CAR expressing T cells in RPMI-GlutaMAX medium, containing pamidronate as indicated. Furthermore, for the inhibitor experiments tumor cells were pre-treated overnight with either PI3K (Pictilisib, GDC-0941), AKT (MK2206), MEK (Selumetinib, AZD6244) inhibitors, Rapamycin or Torin. Before co-culture cells were washed twice with fresh RPMI medium and afterwards adjusted to 50.000 cells in 100 μL RPMI culture medium. After co-culture, 100μL supernatant was used for INF-γ detection using the Invitrogen™ eBioscience™ human IFN-γ ELISA kit ready-set-go by following the manufactures protocol<sup>42</sup>.

**Flow Cytometry.** Cells were counted and 200.000 per condition were put in a FACS tube, after which 1mL FACS buffer (PBS, 1% Na-azide) was added and tubes spun down at 1500RPM for 5 min. Supernatant was discarded and, for the tetramer and bead stainings with soluble TCRs, cells were incubated with tetramer/bead solution for 30 minutes at RT. Cells are washed with PBS and subsequently, 20μL of the antibody mixture in FACS buffer was added to each well, after which cells were resuspended and incubated for 30min at RT. 1mL FACS buffer was added to each well and cells were spun down at 1500RPM for 5 min, supernatant removed and resuspended in 1mL FACS buffer and spun down again at 1500RPM for 5 min. Finally, supernatant was removed and 150μL 1% PFA was added. Samples were measured on a FACSCanto 2 (BD bioscience) using FACSDiva software.

**Intracellular staining and colocalization analysis.** MZ1851rc cells were seeded in a 16-well Nunc Lab-Tek™ chamber at 1500 cells per well in 200μL cDMEM and cultured for 76h at 37°C, 5% CO<sub>2</sub> in a wet chamber (petri dish + wet paper cloth). Medium was removed and 200μL cDMEM with 100μM pamidronate (PAM) (where indicated) was added to the wells. After 24h incubation, cells were washed with PBS and subsequently fixed with 4% paraformaldehyde (PFA) for 15min at RT. Cells were permeabilized for 10min using either 100% ice-cold methanol, 0.3% Triton X100 in PBS, or 0.1% saponin in

PBS (changed protocol over time, saponin seems to work best) at RT. Sample blocking was performed by incubating wells for 1h at RT with blocking solution (PBS, 5% Pooled human serum (HuS), 1% BSA, 1% Na-azide + either 0.3% Triton X-100 or 0.1% saponin). Primary antibodies diluted in antibody dilution buffer (PBS, 1% BSA, 1% Na-azide + either 0.3% Triton X-100 or 0.1% saponin) were added to the wells and were incubated either 1h at RT, or overnight at 4°C. Cells were washed 3x with PBS and secondary antibody diluted in antibody dilution buffer was added and incubated either 1h at RT, or overnight at 4°C. Finally, the chamber gasket and any glue residue was removed from the well chamber using a sterile tweezer and surgical blade, some Prolong Diamond Antifade mountant with DAPI was added and a coverglass applied. Before imaging, any leftover residue was removed with a Kimwipe and slide was kept in a dark place for at least 30min. Imaging was performed on a Zeiss LSM710 confocal laser scanning microscope using a 63x 1.40 oil immersion objective. Analysis of pictures was done blinded to conditions using Volocity™ image analysis software (PerkinElmer) by selecting areas of interest on membrane clusters of BTN3A, and determining the Pearson's correlation coefficient. Representative images were made using ImageJ software (NIH).

**Animal models.** NSG mice were administered total body irradiation of 1.65 Gy on day -1. AKPS mutated PDOs were injected subcutaneously in the right flank on day 0. On day 1 and 7, 10<sup>7</sup> TEG-001 or TEG-LM1 cells were administered intravenously in pamidronate (10 mg/kg body weight). Next to T-cell administration, 0.6 × 10<sup>6</sup> IU of IL-2 in incomplete Freund's adjuvant was injected subcutaneously at day 1 as described in<sup>50</sup>. Bioluminescence was used to weekly monitor PDO outgrowth over time.

**Proximity ligation assays.** Duolink™ PLA Fluorescence protocol was followed.<sup>41</sup> Duolink Plus and minus probes and detection reagents orange were obtained from Merck. MZ1851rc cells were seeded in a 16-well Nunc Lab-Tek™ chamber (Thermo-Fisher Scientific, Nunc) at 15000 per well per 200 $\mu$ L cDMEM and cultured for 76h. afterwards, medium was gently removed and 100 $\mu$ M pamidronate in cDMEM was added where indicated and incubated overnight. Wells were washed 1x with PBS and fixed with 4% PFA for 15min at RT. Wells were washed 3x with PBS and permeabilized using 0.1% saponin in PBS for 15min at RT. Wells were blocked using Duolink blocking buffer and primary antibodies diluted in Duolink PLA diluent were added to the wells and incubated for 1h at RT in a humidity chamber (empty pipette tip box with elevated plateau covered in parafilm for slide to sit on, water around it). Wells were washed 2x with 1x wash buffer A (Merck) and incubated for 1 hour at 37°C in a wet chamber with 35 $\mu$ L/well of Duolink min/plus PLA probe mix (anti-mouse-plus, anti-rabbit-minus). Wells were washed 2x with 1x wash buffer A and incubated with 35 $\mu$ L/well Duolink ligation buffer with 1:40 Ligase enzyme added from freezing block and incubated for 30 min at 37°C in a wet chamber. Wells were washed 2x with 1x wash buffer A again and incubated with Duolink

Orange amplification buffer with 1:80 polymerase enzyme added from freezing block and incubated for 100min at 37°C. Finally, wells were washed 2x with 1x wash buffer B (Merck) for 10min and 1x with 0.01x wash buffer B for 1 min. All remaining buffer was discarded and further preparation of the slide was done in the same way as described for intracellular staining. Imaging was performed on a Zeiss LSM710 confocal laser scanning microscope using both a 20x objective or a 63x 1.40 oil immersion objective. PLA clusters per image and number of nuclei were determined using Volocity™ image analysis software (PelkinElmer).

**Fluorescence Resonance Energy Transfer (FRET).** To study direct interaction between proteins upon phosphoantigen accumulation, HEK293T cells expressing phospho-variants of BTN3A1 were first dissociated using Trypsin-EDTA, transferred into a FACS tube and resuspended in complete DMEM. The cells were then treated with 100 μM PAM for 1 hour at 37°C and washed with FACS buffer (PBS, 1% Na-azide). After that, the cells were blocked with PBS containing 5% BSA for 15 minutes and then incubated for 30 minutes at room temperature with an antibody conjugated with the donor fluorochrome at 100μl staining volume. Cells were washed once and then split into two samples: donor and donor+acceptor. Donor samples were incubated with FACS buffer and donor+acceptor samples were incubated for 30 minutes at room temperature with an antibody conjugated with the acceptor fluorochrome at 50μl staining volume. After washing with FACS buffer twice, samples were fixed with 1% PFA. The donor fluorescence was measured using a FACS Canto-II flow cytometer (BD Biosciences) where donor fluorescence of the donor+acceptor (double stained) samples was compared with the one of the samples labeled only with donor antibody. FRET efficiency was calculated from the fractional decrease of the donor fluorescence in the presence of the acceptor. Background noise in the donor fluorescent channel due to spectral overlap with different fluorescence channels was excluded from the calculations, by subtracting the measured mean fluorescence intensity (MFI) on unlabeled and single stained samples from the MFI of the donor and donor+acceptor samples respectively. The centrifugation steps during washes were done at 1500RPM for 5 minutes and the antibodies were diluted in FACS buffer. The samples stained with antibodies conjugated to Alexa Fluor 594 were validated for proper staining by remeasurement using an LSR Fortessa cell analyzer (BD Biosciences).

**Generation of HEK-293FT phospho-variants.** For the generation of the cell lines stably expressing BTN3A1 phospho-variants and BTN3A2, the BTN3A1-Flag as well as the BTN3A2 sequence were codon optimized, custom synthesized and cloned in pBullet-IRES-puro plasmid vectors. The retroviral particles produced by transfection in Phoenix amphi cells were generated with the same procedure used to generate TEGs. The viral supernatant from the Phoenix amphi cells was used to transduce the HEK 293T BTN3KO

cell line. 48 hours post-transduction 1.5  $\mu$ g/mL of puromycin was supplemented to the culture medium for antibiotic selection and it was carried out until the control (untransduced) cell line died completely.

**Software used.** Office 2016 (Microsoft), Illustrator CS6 / Illustrator 2019 (Adobe systems), Zen 2009 / 2012 (Zeiss), ImageJ (NiH), Volocity image analysis software (PerkinElmer), GraphPad Prism 8, Microplate Manager (Bio-Rad), FACSDiva (BD Biosciences).

## Acknowledgements

We thank the staff of the Flow Core Facility at the UMC Utrecht. We kindly thank Prof. Erin Adams (The University of Chicago) for providing the CD277 KO HEK293T cell line and Halvard Boenig (Institute for Transfusion Medicine and Immunohematology, Goethe University, Frankfurt a. M., Germany) for providing feeder cells. We also thank the Snippert Group of the Center for Molecular Medicine in the UMC Utrecht for providing the colon cancer PDOs under the RASTRIC protocol. Funding for this study was provided by ZonMW 43400003 and VIDI-ZonMW 917.11.337, UU 2013-6426, UU 2014-6790 and UU 2015-7601 and Gadeta to J.K., UU 2018-11393 to Z.S. and J.K., Marie Curie 749010 to D.X.B. DF acknowledge financial support from the NWO funded Netherlands Proteomics Centre through the National Road Map for Large-scale Infrastructures program X- Omics (Project 184.034.019).

## Contributions

A.C., A.D.M., D.F., T.K., P.B., I.J., D.X.B., P.H.L., S.H., L.G., T.M., S.L., M.H., J.B., D.V.D., E.S.J., J.S., N.T., L.H.H., A.N. and T.A. performed the experiments and analyzed data, W.W., T.S., H.S., J.R., P.D., J.D., A.H., H.C., J.K. and Z.S. supervised the study, J.K. and Z.S. designed the study, A.C. and A.D.M. wrote the paper together with Z.S. and J.K.

## Conflict of interest:

Z.S., J.K., D.X.B., T.S., A.C., A.D.M., P.H.L., T.K. and P.D. are inventors on different patents with  $\gamma\delta$ TCR sequences, recognition mechanisms and isolation strategies. J.K. is scientific advisor and shareholder of Gadeta ([www.gadeta.nl](http://www.gadeta.nl)).

## References

- 1 Hayday, A. C. Gammadelta T cells and the lymphoid stress-surveillance response. *Immunity* **31**, 184-196, doi:10.1016/j.immuni.2009.08.006 (2009).
- 2 Gentles, A. J. *et al.* The prognostic landscape of genes and infiltrating immune cells across human cancers. *Nat Med* **21**, 938-945, doi:10.1038/nm.3909 (2015).
- 3 Dadi, S. *et al.* Cancer Immunosurveillance by Tissue-Resident Innate Lymphoid Cells and Innate-like T Cells. *Cell* **164**, 365-377, doi:10.1016/j.cell.2016.01.002 (2016).
- 4 Street, S. E. *et al.* Innate immune surveillance of spontaneous B cell lymphomas by natural killer cells and gammadelta T cells. *J Exp Med* **199**, 879-884, doi:10.1084/jem.20031981 (2004).
- 5 Liu, Z. *et al.* Protective immunosurveillance and therapeutic antitumor activity of gammadelta T cells demonstrated in a mouse model of prostate cancer. *J Immunol* **180**, 6044-6053, doi:10.4049/jimmunol.180.9.6044 (2008).
- 6 He, W. *et al.* Naturally activated V gamma 4 gamma delta T cells play a protective role in tumor immunity through expression of eomesodermin. *J Immunol* **185**, 126-133, doi:10.4049/jimmunol.0903767 (2010).
- 7 Chauvin, C. *et al.* NKG2D Controls Natural Reactivity of Vgamma9Vdelta2 T Lymphocytes against Mesenchymal Glioblastoma Cells. *Clin Cancer Res* **25**, 7218-7228, doi:10.1158/1078-0432.CCR-19-0375 (2019).
- 8 Tanaka, Y. *et al.* Natural and synthetic non-peptide antigens recognized by human gamma delta T cells. *Nature* **375**, 155-158, doi:10.1038/375155a0 (1995).
- 9 Kunzmann, V. *et al.* Stimulation of gammadelta T cells by aminobisphosphonates and induction of antiplasma cell activity in multiple myeloma. *Blood* **96**, 384-392 (2000).
- 10 Sebestyen, Z., Prinz, I., Dechanet-Merville, J., Silva-Santos, B. & Kuball, J. Translating gammadelta (gammadelta) T cells and their receptors into cancer cell therapies. *Nat Rev Drug Discov* **19**, 169-184, doi:10.1038/s41573-019-0038-z (2020).
- 11 Vyborova, A. *et al.* gamma9delta2T cell diversity and the receptor interface with tumor cells. *J Clin Invest* **130**, 4637-4651, doi:10.1172/JCI132489 (2020).
- 12 van Diest, E. *et al.* Gamma delta TCR anti-CD3 bispecific molecules (GABs) as novel immunotherapeutic compounds. *J Immunother Cancer* **9**, doi:10.1136/jitc-2021-003850 (2021).
- 13 Cano, C. E. *et al.* BTN2A1, an immune checkpoint targeting Vgamma9Vdelta2 T cell cytotoxicity against malignant cells. *Cell Rep* **36**, 109359, doi:10.1016/j.celrep.2021.109359 (2021).
- 14 Rigau, M. *et al.* Butyrophilin 2A1 is essential for phosphoantigen reactivity by gammadelta T cells. *Science* **367**, doi:10.1126/science.aay5516 (2020).
- 15 Hsiao, C. C., Nguyen, K., Jin, Y., Vinogradova, O. & Wiemer, A. J. Ligand-induced interactions between butyrophilin 2A1 and 3A1 internal domains in the HMBPP receptor complex. *Cell Chem Biol* **29**, 985-995 e985, doi:10.1016/j.chembiol.2022.01.004 (2022).

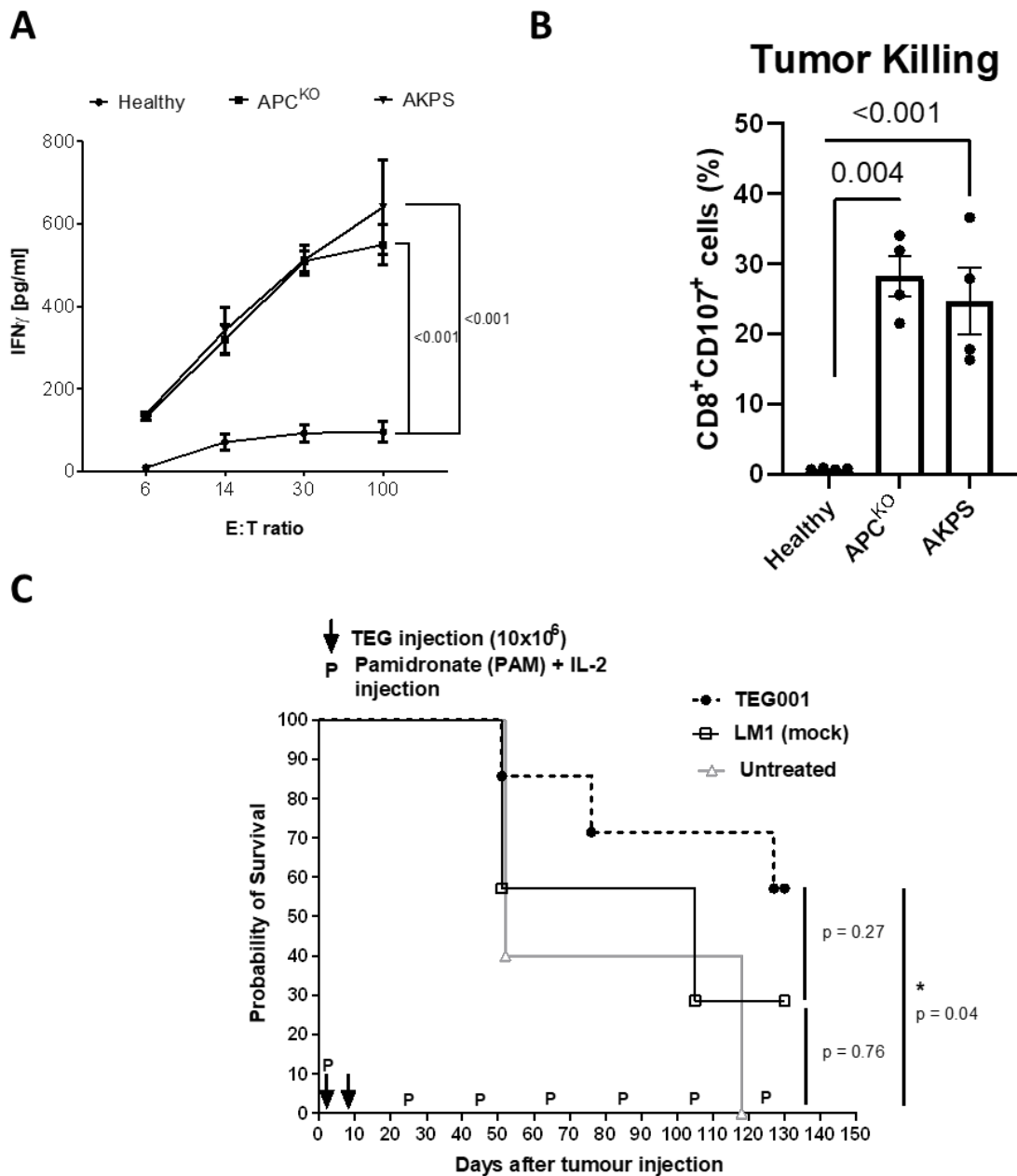
- 16 Sebestyen, Z. *et al.* RhoB Mediates Phosphoantigen Recognition by Vgamma9Vdelta2 T Cell Receptor. *Cell Rep* **15**, 1973-1985, doi:10.1016/j.celrep.2016.04.081 (2016).
- 17 Sandstrom, A. *et al.* The intracellular B30.2 domain of butyrophilin 3A1 binds phosphoantigens to mediate activation of human Vgamma9Vdelta2 T cells. *Immunity* **40**, 490-500, doi:10.1016/j.immuni.2014.03.003 (2014).
- 18 Yuan, L. *et al.* Phosphoantigens glue butyrophilin 3A1 and 2A1 to activate Vgamma9Vdelta2 T cells. *Nature*, doi:10.1038/s41586-023-06525-3 (2023).
- 19 Mamedov, M. R. *et al.* CRISPR screens decode cancer cell pathways that trigger gammadelta T cell detection. *Nature* **621**, 188-195, doi:10.1038/s41586-023-06482-x (2023).
- 20 Grunder, C. *et al.* gamma9 and delta2CDR3 domains regulate functional avidity of T cells harboring gamma9delta2TCRs. *Blood* **120**, 5153-5162, doi:10.1182/blood-2012-05-432427 (2012).
- 21 Scheper, W. *et al.* gammadeltaT cells elicited by CMV reactivation after allo-SCT cross-recognize CMV and leukemia. *Leukemia* **27**, 1328-1338, doi:10.1038/leu.2012.374 (2013).
- 22 Marcu-Malina, V. *et al.* Redirecting alphabeta T cells against cancer cells by transfer of a broadly tumor-reactive gammadeltaT-cell receptor. *Blood* **118**, 50-59, doi:10.1182/blood-2010-12-325993 (2011).
- 23 Drost, J. *et al.* Sequential cancer mutations in cultured human intestinal stem cells. *Nature* **521**, 43-47, doi:10.1038/nature14415 (2015).
- 24 Yi, Z. *et al.* Molecular landscape and efficacy of HER2-targeted therapy in patients with HER2-mutated metastatic breast cancer. *NPJ Breast Cancer* **6**, 59, doi:10.1038/s41523-020-00201-9 (2020).
- 25 Di Fiore, P. P. *et al.* erbB-2 is a potent oncogene when overexpressed in NIH/3T3 cells. *Science* **237**, 178-182, doi:10.1126/science.2885917 (1987).
- 26 Muller, W. J., Sinn, E., Pattengale, P. K., Wallace, R. & Leder, P. Single-step induction of mammary adenocarcinoma in transgenic mice bearing the activated c-neu oncogene. *Cell* **54**, 105-115, doi:10.1016/0092-8674(88)90184-5 (1988).
- 27 Peigne, C. M. *et al.* The Juxtamembrane Domain of Butyrophilin BTN3A1 Controls Phosphoantigen-Mediated Activation of Human Vgamma9Vdelta2 T Cells. *J Immunol* **198**, 4228-4234, doi:10.4049/jimmunol.1601910 (2017).
- 28 Karunakaran, M. M. *et al.* Butyrophilin-2A1 Directly Binds Germline-Encoded Regions of the Vgamma9Vdelta2 TCR and Is Essential for Phosphoantigen Sensing. *Immunity* **52**, 487-498 e486, doi:10.1016/j.immuni.2020.02.014 (2020).
- 29 Roux, K. J., Kim, D. I., Burke, B. & May, D. G. BioID: A Screen for Protein-Protein Interactions. *Curr Protoc Protein Sci* **91**, 19 23 11-19 23 15, doi:10.1002/cpps.51 (2018).
- 30 Gu, S., Nawrocka, W. & Adams, E. J. Sensing of Pyrophosphate Metabolites by Vgamma9Vdelta2 T Cells. *Front Immunol* **5**, 688, doi:10.3389/fimmu.2014.00688 (2014).
- 31 Liu, Y. *et al.* EBV latent membrane protein 1 augments gammadelta T cell cytotoxicity against nasopharyngeal carcinoma by induction of butyrophilin molecules. *Theranostics* **13**, 458-471, doi:10.7150/thno.78395 (2023).

- 32 Clendening, J. W. *et al.* Dysregulation of the mevalonate pathway promotes transformation. *Proc Natl Acad Sci U S A* **107**, 15051-15056, doi:10.1073/pnas.0910258107 (2010).
- 33 Zhao, H. F., Wang, J. & Tony To, S. S. The phosphatidylinositol 3-kinase/Akt and c-Jun N-terminal kinase signaling in cancer: Alliance or contradiction? (Review). *Int J Oncol* **47**, 429-436, doi:10.3892/ijo.2015.3052 (2015).
- 34 Kovacic, S. *et al.* Akt activity negatively regulates phosphorylation of AMP-activated protein kinase in the heart. *J Biol Chem* **278**, 39422-39427, doi:10.1074/jbc.M305371200 (2003).
- 35 Zhao, Y. *et al.* ROS signaling under metabolic stress: cross-talk between AMPK and AKT pathway. *Mol Cancer* **16**, 79, doi:10.1186/s12943-017-0648-1 (2017).
- 36 Leclerc, G. M., Leclerc, G. J., Fu, G. & Barredo, J. C. AMPK-induced activation of Akt by AICAR is mediated by IGF-1R dependent and independent mechanisms in acute lymphoblastic leukemia. *J Mol Signal* **5**, 15, doi:10.1186/1750-2187-5-15 (2010).
- 37 Tao, R. *et al.* AMPK exerts dual regulatory effects on the PI3K pathway. *J Mol Signal* **5**, 1, doi:10.1186/1750-2187-5-1 (2010).
- 38 Kazyken, D. *et al.* AMPK directly activates mTORC2 to promote cell survival during acute energetic stress. *Sci Signal* **12**, doi:10.1126/scisignal.aav3249 (2019).
- 39 Xie, M. J. *et al.* PIP3-Phldb2 is crucial for LTP regulating synaptic NMDA and AMPA receptor density and PSD95 turnover. *Sci Rep* **9**, 4305, doi:10.1038/s41598-019-40838-6 (2019).
- 40 Lim, B. C. *et al.* Prickle1 promotes focal adhesion disassembly in cooperation with the CLASP-LL5beta complex in migrating cells. *J Cell Sci* **129**, 3115-3129, doi:10.1242/jcs.185439 (2016).
- 41 Malecz, N. *et al.* Synaptojanin 2, a novel Rac1 effector that regulates clathrin-mediated endocytosis. *Curr Biol* **10**, 1383-1386, doi:10.1016/s0960-9822(00)00778-8 (2000).
- 42 Ramos, A. R., Ghosh, S. & Erneux, C. The impact of phosphoinositide 5-phosphatases on phosphoinositides in cell function and human disease. *J Lipid Res* **60**, 276-286, doi:10.1194/jlr.R087908 (2019).
- 43 Ben-Chetrit, N. *et al.* Synaptojanin 2 is a druggable mediator of metastasis and the gene is overexpressed and amplified in breast cancer. *Sci Signal* **8**, ra7, doi:10.1126/scisignal.2005537 (2015).
- 44 Geng, J., Wang, L., Lee, J. Y., Chen, C. K. & Chang, K. T. Phosphorylation of Synaptojanin Differentially Regulates Endocytosis of Functionally Distinct Synaptic Vesicle Pools. *J Neurosci* **36**, 8882-8894, doi:10.1523/JNEUROSCI.1470-16.2016 (2016).
- 45 Edwards, M. *et al.* Capping protein regulators fine-tune actin assembly dynamics. *Nat Rev Mol Cell Biol* **15**, 677-689, doi:10.1038/nrm3869 (2014).
- 46 Denley, A., Gymnopoulos, M., Kang, S., Mitchell, C. & Vogt, P. K. Requirement of phosphatidylinositol(3,4,5)trisphosphate in phosphatidylinositol 3-kinase-induced oncogenic transformation. *Mol Cancer Res* **7**, 1132-1138, doi:10.1158/1541-7786.MCR-09-0068 (2009).

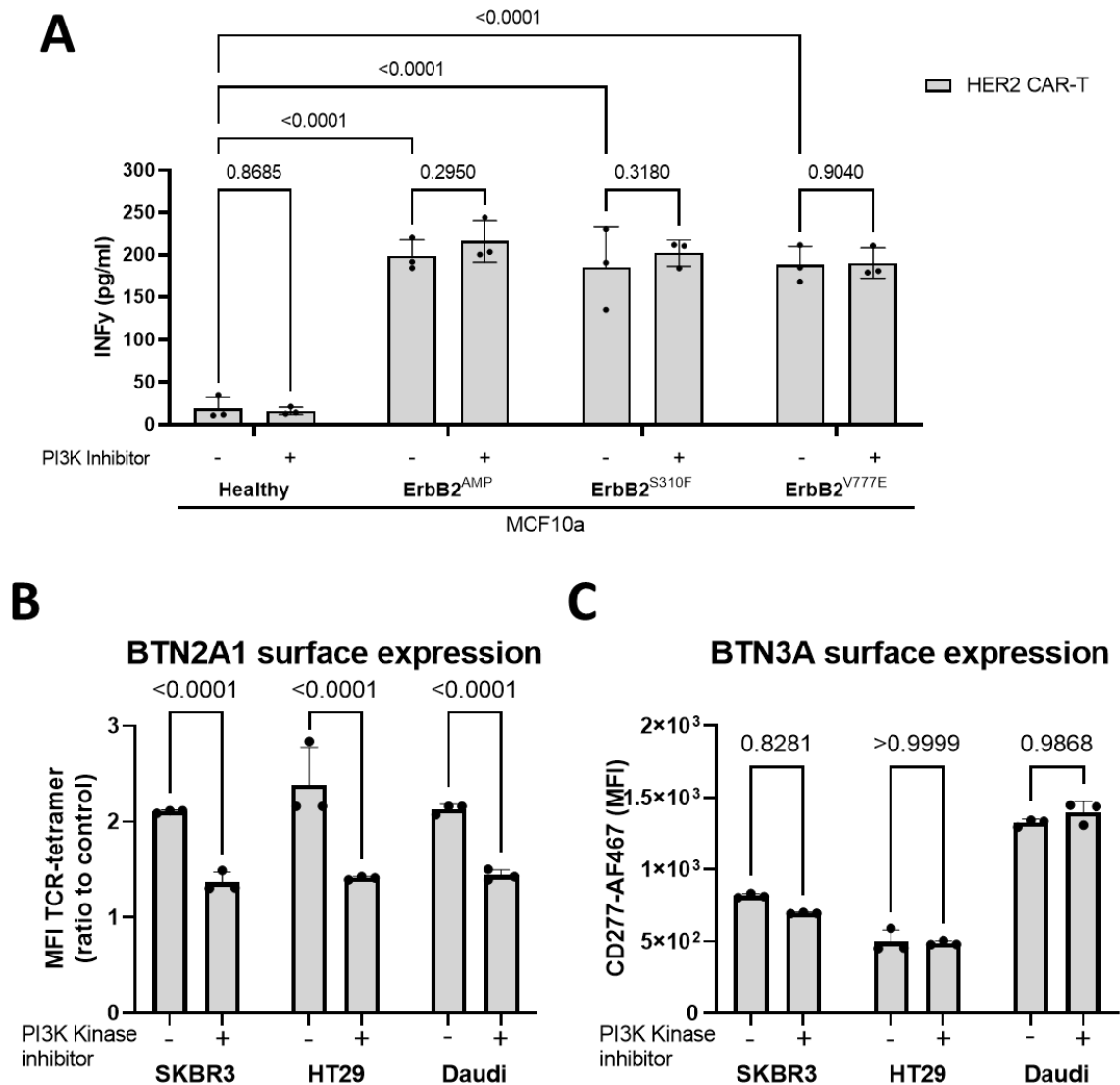


- 47 Nguyen, K. *et al.* The butyrophilin 3A1 intracellular domain undergoes a conformational change involving the juxtamembrane region. *FASEB J*, doi:10.1096/fj.201601370RR (2017).
- 48 Driehuis, E., Kretzschmar, K. & Clevers, H. Establishment of patient-derived cancer organoids for drug-screening applications. *Nat Protoc* **15**, 3380-3409, doi:10.1038/s41596-020-0379-4 (2020).
- 49 Roux, K. J., Kim, D. I., Raida, M. & Burke, B. A promiscuous biotin ligase fusion protein identifies proximal and interacting proteins in mammalian cells. *J Cell Biol* **196**, 801-810, doi:10.1083/jcb.201112098 (2012).
- 50 Johanna, I. *et al.* Evaluating in vivo efficacy - toxicity profile of TEG001 in humanized mice xenografts against primary human AML disease and healthy hematopoietic cells. *J Immunother Cancer* **7**, 69, doi:10.1186/s40425-019-0558-4 (2019).

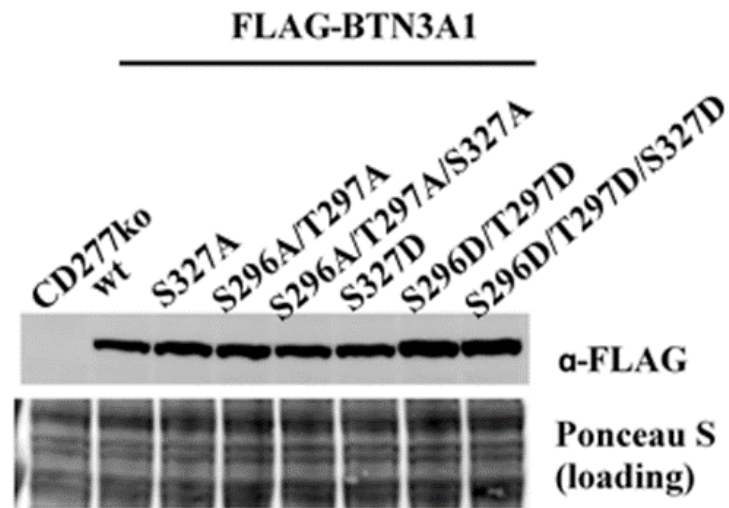
## Supplementary Data



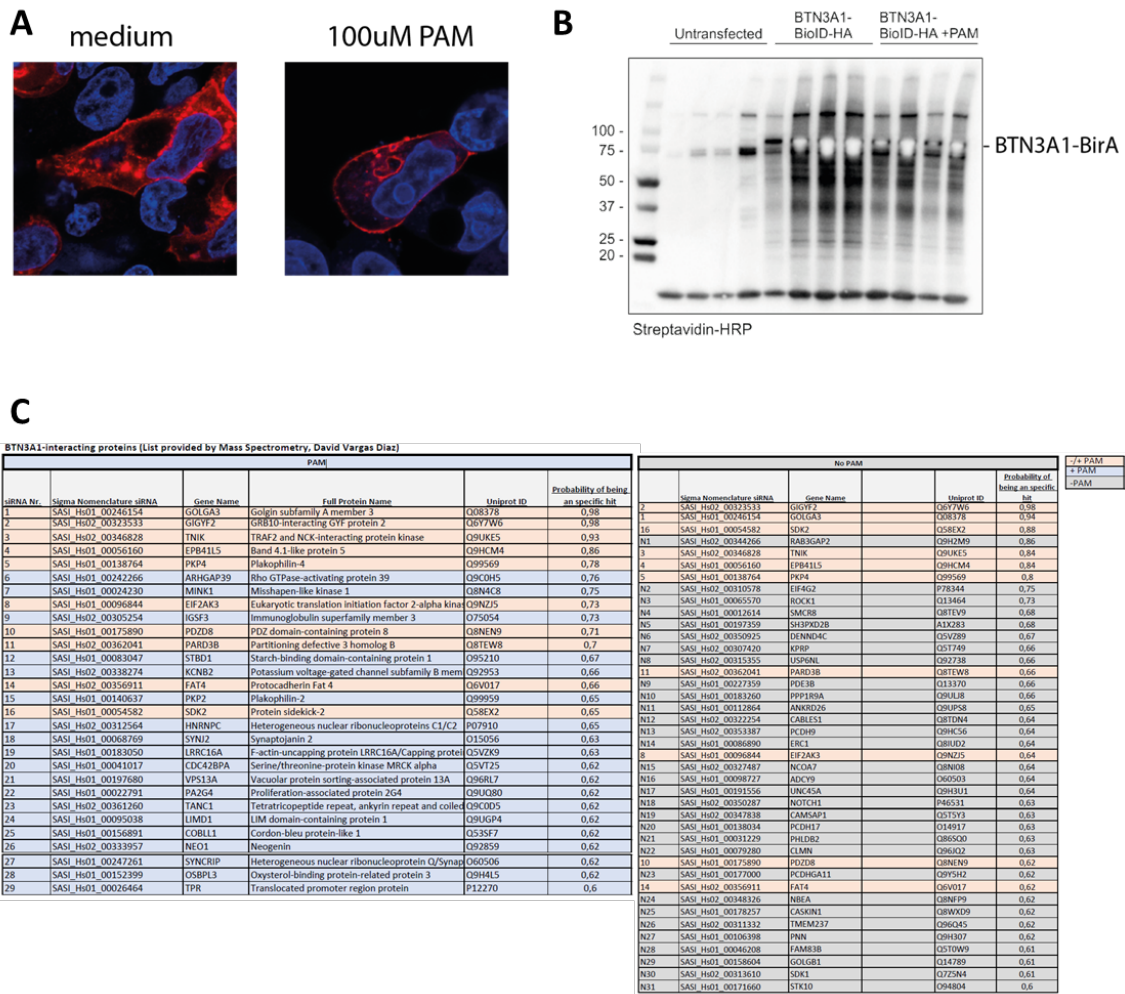
**Supplementary Figure 1. TEG targeting of APC and AKPS. (A)** IFN $\gamma$  production by V $\gamma$ 9V $\delta$ 2TCR T cells after co-culture with wt, APC and AKPS CRC organoids at various target:effector ratios in the presence of 100uM PAM. **(B)** CD107 degranulation of V $\gamma$ 9V $\delta$ 2TCR T cells after co-culture with wt, APC and AKPS CRC organoids at various PAM concentrations. **(C)** NOD.Cg-Prkdcscid Il2rgtm1Wjl/SzJ (NSG) mice were injected subcutaneously in right-flank with 250,000 cells AKPS CRC organoid (suspended in culture media and Matrigel with 1:1 ratio) on Day 0 followed by intravenous injection of either PBS (untreated control),  $10^7$  TEG001 or TEG-LM1 cells on Day 1 and 6 (n = 7 mice; indicated by arrows). Overall survival of tumor-bearing mice was recorded for 130 days. Statistical significance was calculated by log-rank (Mantel-Cox) test, \* P < 0,05.



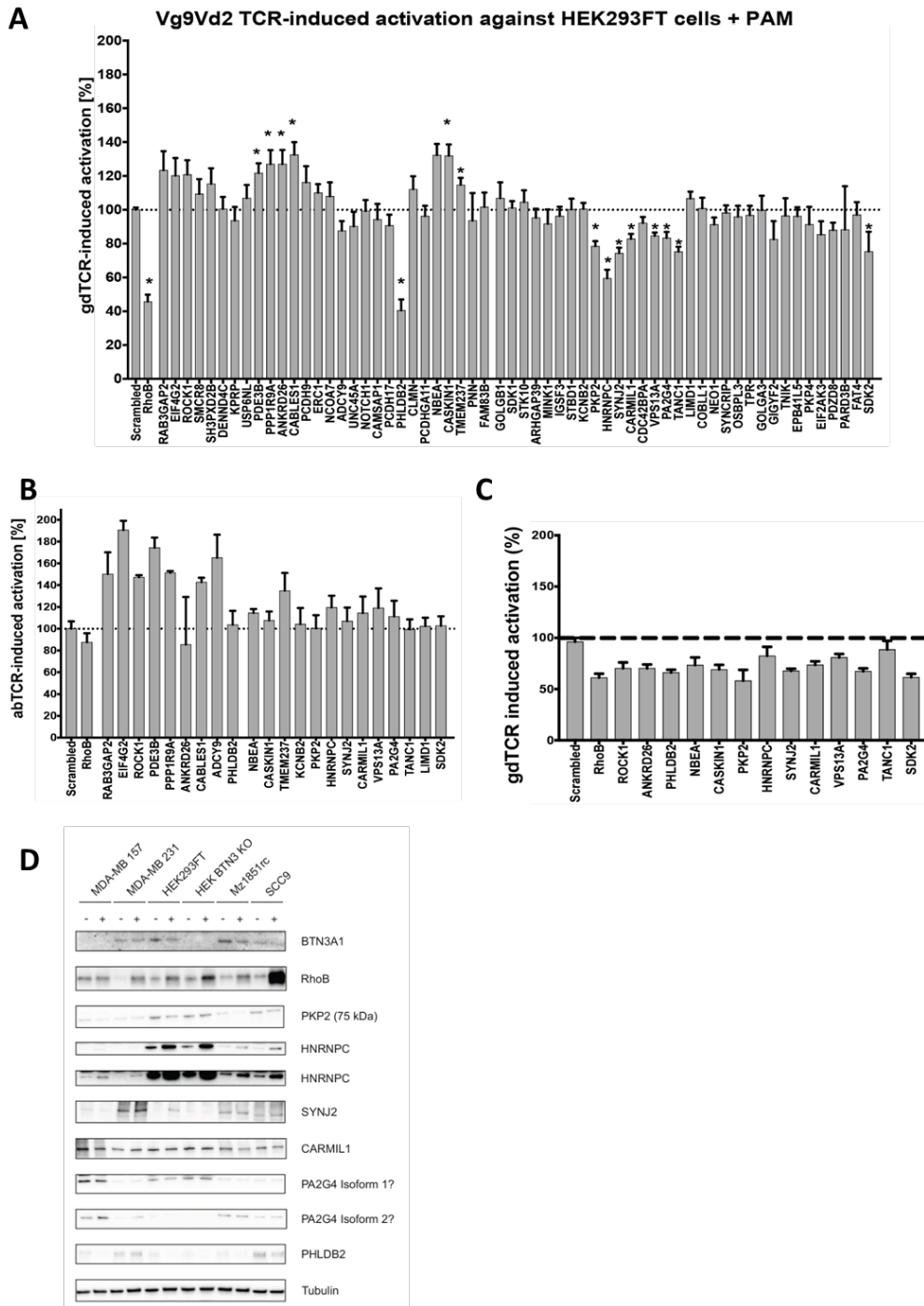
**Supplementary Figure 2. Addition of PI3K inhibitor consistently reduces BTN2A1 surface expression, but not BTN3A surface expression, in various tumor cell lines. (A)** MCF10a wt (healthy) and ErbB2/HER2 mutants were co-cultured overnight with HER2 CAR-T cells. IFN $\gamma$  expression was evaluated with IFN $\gamma$  ELISA. **(B)** BTN2A1 surface expression was determined by V $\gamma$ 9V $\delta$ 2TCR-tetramer binding relative to control-tetramer binding after pre-incubation with PI3K inhibitor. **(C)** BTN3A surface expression was measured using a CD277-AF467 antibody after pre-incubation with PI3K inhibitor.



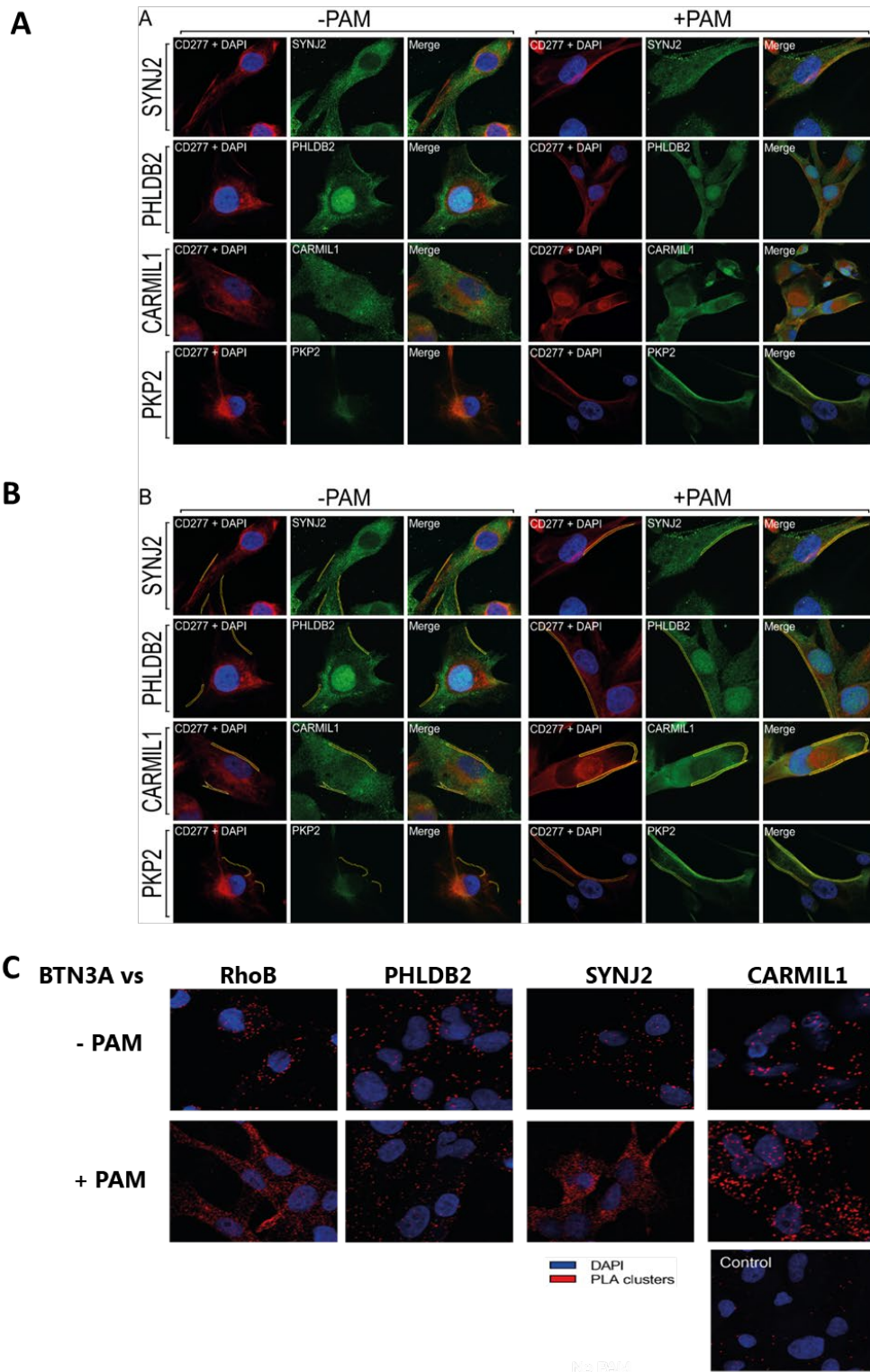
**Supplementary Figure 3. Total expression of BTN3A1 phospho-variants.** Western blot analysis of HEK-293 BTN3A1 KO cells reconstituted with either wt BTN3A1 or with phospho-variants of BTN3A1 using anti-FLAG antibody.



**Supplementary Figure 4. Expression of BTN3A1-BirA\* of candidate protein.** (A) Representation of differentially expressed genes between AKPS CRC organoids incubated either with or without 100uM PAM. (A) HEK-293F cells were transfected with BTN3A1-BirA fusion plasmid and biotinylating pattern of fusion protein was controlled after adding biotin. Biotinylation was visualized by adding streptavidin-APC (red) and DAPI (blue) for nuclear staining. (B) cellular expression of the fusion protein was controlled by western blot. (C) List of BTN3A1-BioID biotinylated proteins identified by mass spectrometry with a > 0,6 probability being a specific hit. Colours indicate in which condition the proteins were found under various conditions (green = no PAM, blue = PAM, orange = both).



**Supplementary Figure 5. siRNA screening of protein candidates.** (A) HEK-293FT cells were transfected with siRNAs against candidate proteins and cells were used as targets against Vγ9Vδ2TCR T cells in the presence of 100 μM PAM and IFNγ release of T cells upon activations was measured by ELISA. Knock-down effect was determined by comparing IFNγ levels to scrambled RNA conditions. (B) Target cells used in A were loaded with 50uM WT-1 peptide and used as targets against WT-1 TCR T cells, knock down effect was determined by comparing IFNγ levels to that of scrambled RNA conditions. (C) MZ1851rc renal cell carcinoma cell line was transfected with siRNAs against target proteins and used as target against Vγ9Vδ2TCR T cells and IFNγ was measured for activation. (D) Cell lysates MDA-MB157 and MDA-MB231, HEK293FT wt or HEK BTN3AKO, MZ1851rc and SCC9 were cultured in the presence or absence of 100 μM PAM for 24h, lysed and Western blots were probed with antibodies against candidates.



**Supplementary Figure 6. Representative images for colocalization analysis. (A)** Raw representative images for the colocalization analyses of SYNJ2, PHLDB2, CARMIL1, and PKP2 with BTN3A. **(B)** Representative images for the colocalization analyses of SYNJ2, PHLDB2, CARMIL1, and PKP2 with BTN3A with the region of interest (ROI) in yellow around the BTN3A membrane clusters. **(C)** Representative images for each of the PLA conditions are shown.

3



<sup>1</sup> Hubrecht Institute, Royal Netherlands Academy of Arts and Sciences and University Medical Center Utrecht, Utrecht, the Netherlands.

<sup>2</sup> Princess Máxima Center for Pediatric Oncology, Utrecht, the Netherlands.

<sup>3</sup> Oncode Institute, Utrecht, the Netherlands.

<sup>4</sup> Center for Translational Immunology, University Medical Center Utrecht, Utrecht University, Utrecht, the Netherlands.

<sup>5</sup> Microbiome and Cancer Division, German Cancer Research Center, Heidelberg, Germany.

<sup>6</sup> Department of Hematology, University Medical Center Utrecht, Utrecht University, Utrecht, the Netherlands.

<sup>7</sup> Mildred Scheel Early Career Center for Cancer Research Würzburg, University Hospital Würzburg, MSNZ/IZKF, Würzburg, Germany.

<sup>8</sup> University Medical Center Utrecht, Utrecht, the Netherlands.

<sup>9</sup> Comprehensive Cancer Center München, Munich, Germany.

<sup>10</sup> Pharma, Research and Early Development, F. Hoffmann-La Roche Ltd, Basel, Switzerland.



# CHAPTER

# 4

## Uncovering the mode of action of engineered T cells in patient cancer organoids

Johanna F. Dekkers<sup>1,2,3\*</sup>, Maria Alieva<sup>2,3\*</sup>, Astrid Cleven<sup>4</sup>, Farid Keramati<sup>2</sup>, Amber K. L. Wezenaar<sup>2,3</sup>, Esmée J. van Vliet<sup>2,3</sup>, Jens Puschhof<sup>1,3,5</sup>, Peter Brazda<sup>2</sup>, Inez Johanna<sup>4</sup>, Angelo D. Meringa<sup>4</sup>, Heggert G. Rebel<sup>2,3</sup>, Maj-Britt Buchholz<sup>2,3</sup>, Mario Barrera Román<sup>2,3</sup>, Amber L. Zeeman<sup>2,3</sup>, Sam de Blank<sup>2,3</sup>, Domenico Fasci<sup>4</sup>, Maarten H. Geurts<sup>1,3</sup>, Annelisa M. Cornel<sup>2,4</sup>, Else Driehuis<sup>1,3</sup>, Rosemary Millen<sup>1,3</sup>, Trudy Straetemans<sup>4,6</sup>, Mara J. T. Nicolassen<sup>4</sup>, Tineke Aarts-Riemens<sup>4</sup>, Hendrikus C. R. Ariese<sup>2,3</sup>, Hannah R. Johnson<sup>2,3</sup>, Ravian L. van Ineveld<sup>2,3</sup>, Froso Karaiskaki<sup>4</sup>, Oded Kopper<sup>1,3</sup>, Yotam E. Bar-Ephraim<sup>1,3</sup>, Kai Kretschmar<sup>1,3,7</sup>, Alexander M. M. Eggermont<sup>2,8,9</sup>, Stefan Nierkens<sup>2,4</sup>, Ellen J. Wehrens<sup>2,3</sup>, Henk G. Stunnenberg<sup>2</sup>, Hans Clevers<sup>1,2,3,10#</sup>, Jürgen Kuball<sup>4,6#</sup>, Zsolt Sebestyen<sup>4#</sup> and Anne C. Rios<sup>2,3#</sup>

\*These authors contributed equally  
#These authors jointly supervised this work

*Nature Biotechnology*, 2023

## Abstract

Extending the success of cellular immunotherapies against blood cancers to the realm of solid tumors will require improved in vitro models that reveal therapeutic modes of action at the molecular level. Here we describe a system, called BEHAV3D, developed to study the dynamic interactions of immune cells and patient cancer organoids by means of imaging and transcriptomics. We apply BEHAV3D to live-track >150,000 engineered T cells cultured with patient-derived, solid-tumor organoids, identifying a ‘super engager’ behavioral cluster comprising T cells with potent serial killing capacity. Among other T cell concepts we also study cancer metabolome-sensing engineered T cells (TEGs) and detect behavior-specific gene signatures that include a group of 27 genes with no previously described T cell function that are expressed by super engager killer TEGs. We further show that type I interferon can prime resistant organoids for TEG-mediated killing. BEHAV3D is a promising tool for the characterization of behavioral-phenotypic heterogeneity of cellular immunotherapies and may support the optimization of personalized solid-tumor-targeting cell therapies.

## Introduction

Single-cell analyses are providing unprecedented opportunities to analyze the complexity of biological systems<sup>1</sup>. However, they are restricted to providing a snapshot of cellular processes, lacking analysis of dynamic behavior inherent to cell function. Therefore, the development of technologies that address individual cell dynamics will be essential for understanding cellular behavior and how it relates to function. Immune cells engineered to kill tumor cells represent such dynamic cell populations with increasing clinical importance<sup>2</sup>. Successes of Tcell therapies for hematological malignancies have sparked efforts for translation to solid tumors, but efficacy has so far been limited<sup>3</sup>. This poses a clear need for better understanding of the mechanism of action of cellular therapies to optimize treatment design.

Various T cell therapy concepts are being developed to target cancer, including chimeric antigen receptor (CAR)<sup>4</sup> and conventional Tcell receptor (TCR)<sup>5</sup> Tcell therapies, as well as  $\alpha\beta$  Tcells engineered to express a  $\gamma\delta$  TCR (TEGs)<sup>6-10</sup>, endowing cancer-recognizing properties through metabolic sensing<sup>10-12</sup>. Because of their ability to recapitulate important characteristics of the original tumor specimen<sup>13</sup>, including patient-specific responses to treatment<sup>14-18</sup>, there is a growing interest in the use of patient-derived organoids (PDOs) to model immunotherapy function<sup>19-23</sup>. At the same time, imaging has proved a powerful approach to characterization of the spatial cellular organization and tissue dynamics in these three-dimensional (3D) structures<sup>24-28</sup>, including CAR Tcell treatment efficacy in immuno-organoid cocultures<sup>23</sup>. However, imaging has not yet been used to probe in depth the solid-tumor-targeting dynamics of cellular immunotherapy with PDOs, which could generate critical insight into their mode of action in a patient-specific manner that could be exploited towards improved therapy design. Therefore, here we combined organoid and 3D imaging technology for the analysis of functional single-cell behavior integrated with transcriptomic profiling, to decipher and manipulate the solid-tumor-targeting strategy of engineered immune cells **(Supplementary Video 1)**.

## Results

### 3D live-tracked TEG targeting efficacy

We devised BEHAV3D, a multispectral, 3D image-based platform, to live-track the efficacy and mode of action of cellular immunotherapy for ~60 human cancer organoid cultures simultaneously (**Fig. 1a–c, Supplementary Video 1, Extended Data Fig. 1a–c and Methods**). Applied to an extensive and well-characterized breast cancer (BC) PDO biobank<sup>29</sup> and cancer metabolome-sensing TEGs, we detected a high variation of TEG-mediated killing efficacy in cultures derived from 14 patients with BC (**Fig. 1d and Supplementary Table 1**) and different targeting kinetics over time (**Fig. 1e,f and Extended Data Fig. 1d–f**), with percentages of dying PDOs ranging from near 0 (for example, 34T) to 100 (for example, 13T) (**Fig. 1f**). This variation in PDO killing kinetics was also observed between single organoids in the same PDO culture (**Extended Data Fig. 1f**), and we show that this is not related to differences in organoid size at the start of coculture (**Extended Data Fig. 1g**). Instead, by subcloning of 10T PDOs, we demonstrate that each clone displayed an individual level of targeting that was stably maintained over multiple passages (**Extended Data Fig. 1h**), suggesting an intrinsic biological diversity in sensitivity. This, furthermore, demonstrates that BEHAV3D can adequately capture such functional heterogeneity within PDO cultures, as well as between patients. Pearson correlation analysis between imaging data and a commonly used cell viability assay (**Extended Data Fig. 1i,j**) or interferon gamma (IFN- $\gamma$ ) secretion (**Extended Data Fig. 1k,l**), confirmed the robustness of our imaging quantification method. Among the six highest TEG-sensitive BC PDO cultures (>50% dying organoids; **Fig. 1f**), we noted cultures derived from primary BC of distinct subtypes, as well as a metastasis-derived sample (**Fig. 1d,f**). In addition, TEGs controlled the growth of PDO-derived breast tumor in vivo in mouse xenograft models (**Fig. 1g**). Together, this provides evidence in favor of the clinical potential of TEG against solid tumors and, specifically, pan-targeting of BC, albeit with variation in responsiveness among individual donors.

### PDO inflammatory features are associated with TEG sensitivity

Bulk RNA sequencing (RNA-seq) of BC PDOs revealed differentially expressed genes (DEGs) between the six lowest versus the six highest TEG-sensitive PDO cultures (**Supplementary Table 2**), related to upregulated cadherin signaling and steroid biosynthesis pathways in TEG-insensitive cultures, whereas both cytokine signaling and extracellular matrix (ECM) organization, correlated with high sensitivity to TEG therapy (**Fig. 1h and Extended Data Fig. 2a–c**). The highest association was found between TEG killing and type1 interferon (IFN-I) signaling genes, including MX1, IFIT1, OASL and XAF1, which were highly expressed, especially in the two highest TEG-sensitive PDO cultures, 14T and 13T (**Fig. 1h and Extended Data Fig. 2c**). Thus, PDOs maintain tumor-specific

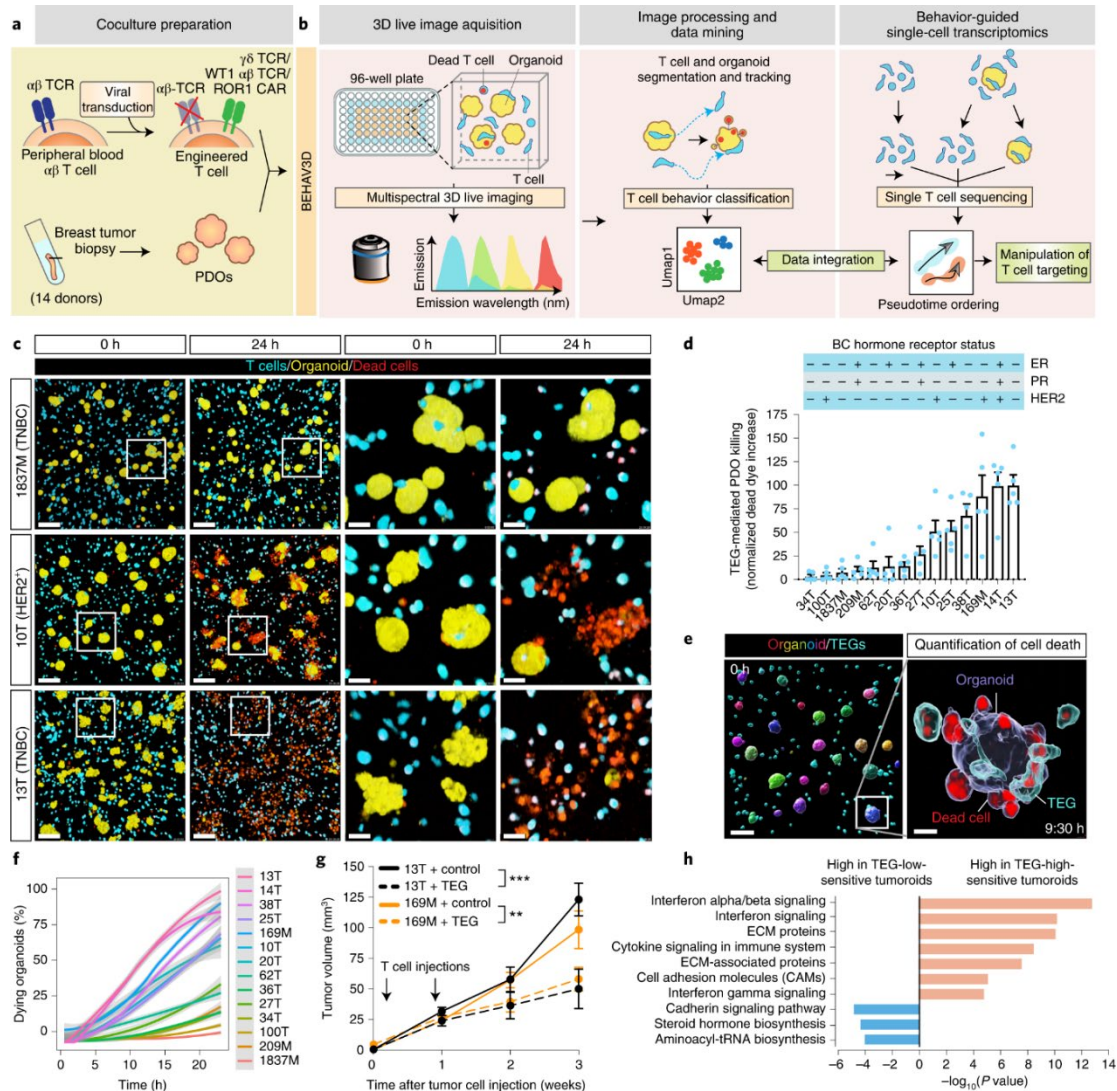


**Figure 1. TEG efficacy across organoids of multiple BC subtypes detected by multispectral 3D live imaging and in vivo TEG targeting.** **a,b**, Schematic representation of TEG generation and coculture with PDOs (**a**) and of the BEHAV3D platform (**b**). Cocultures of organoids and TEGs were imaged using 3D microscopy, followed by segmentation and tracking of organoids and T cells and subsequent behavior classification. Pseudotime ordering was used to integrate behavioral data. **c**, 3D multispectral images of breast PDO cultures (yellow) showing low (1837M), intermediate (10T) and high (13T) killing by TEGs (blue) at the indicated time points of imaging. Scale bars, 100  $\mu$ m (two left-hand columns) and 30  $\mu$ m (two right-hand columns). **d**, Quantification of killing of organoids derived from 14 patients with BC following 24-h coculture with TEGs, by 3D live-cell imaging. Data were corrected for control LM1 T cell responses ( $n=4$  independent experiments, mean  $\pm$  s.e.m.). TNBC, triple-negative breast cancer; ER, estrogen receptor; PR, progesterone receptor. **e**, 3D image of organoids and T cells; enlarged section showing the presence of dead cell dye (red) in a single organoid (transparent purple rendering) and TEGs (transparent blue rendering) at the indicated time of coculture. Scale bars, 100  $\mu$ m (left) and 30  $\mu$ m (right). **f**, Quantification of the percentage of dying single organoids (of total) over time for each PDO cocultured with TEGs ( $n=4$  independent experiments, mean  $\pm$  s.e.m.). **g**, Quantification of tumor volume over time generated by subcutaneous transplantation of cell 13T (black) or 169M organoids (orange). Animals received two injections of either TEGs (dashed line) or control TEG011 cells (control, solid line) at the indicated time points ( $n=10$  mice for 13T and  $n=15$  for 169M, mean  $\pm$  s.e.m.). Two-way ANOVA with repeated measures: 13T/TEG versus 13T/control,  $P < 0.0001$  (\*\*\*) ; 169M/TEG versus 169M/control,  $P = 0.0016$  (\*\*). **h**, Gene Ontology (GO) enrichment analysis of DEGs between the six highest versus six lowest TEG-sensitive organoid cultures from **d**. **c,e**, Images representative of  $n=4$  independent experiments.

inflammatory features in culture, highlighting their utility for modeling cellular immunotherapy responses in a patient-specific manner.

### TEGs display high diversity in behavior and killing potential

BEHAV3D implements single-immune cell tracking in a 3D space over time and behavioral classification (**Figs 1b and 2a and Supplementary Video 1**), revealing that, when exposed to BC PDOs, TEGs could be separated into nine subpopulations with unique behavioral patterns (**Fig. 2b–d and Extended Data Fig. 3a,b**). Patterns varied from inactive behaviors (dying, static and lazy) to active motility (slow scanner, medium scanner and super scanner) and organoid engagement (tickler, engager and super engager), thus demonstrating a high level of behavioral heterogeneity. We captured this behavioral single-cell landscape in a classifier (**Extended Data Fig. 3c–e**), allowing us to interrogate and predict engineered Tcell behavior under other coculture conditions by tracking >150,000 Tcells in total. First, we investigated targeting of different solid-tumor subtypes beyond BC and detected TEG targeting of PDOs from head and neck cancer (3/4 PDOs killed with 50–90% killing efficacy), as well as in patients with diffuse midline glioma (DMG) (4/4 PDOs killed with 20–90% killing efficacy; **Extended Data Fig. 3f–h**). We observed comparable behavioral diversity of TEGs, as seen for BC targeting, including static and super engager behavior (**Extended Data Fig. 3i,j**). This not only further supports the broad solid-tumor-targeting efficacy of TEGs, but also shows that extensive behavioral heterogeneity of TEGs is universally present among different solid-tumor PDO cocultures. Next we used our behavioral classifier (**Extended Data Fig. 3c–e**) to predict TEG behavior when cocultured with BC PDOs showing varying TEG sensitivity (34T, 100T, 27T, 10T or 13T; **Fig. 1f**), as well as an organoid culture derived from normal breast tissue showing only minimal death when cultured with TEGs (**Fig. 2e**). For each PDO culture, TEGs displayed unique distributions of behavioral signatures (**Fig. 2e**) and higher organoid killing associated with an increase in tumor engagement (tickler, engager and super engager), while static, lazy and medium scanner behavior decreased (**Fig. 2f**). Correlation between single-organoid dying dynamics and TEG engagement over time revealed that organoids contacted by super engagers, as compared with other organoid-engaging clusters, had the highest chance of being killed (**Fig. 2g and Extended Data Fig. 3k**). This indicates that effective killing by TEGs relies on prolonged organoid contact, a key feature of super engagers ( $48 \pm 8 \text{ min h}^{-1}$ ; mean  $\pm$  s.d.).

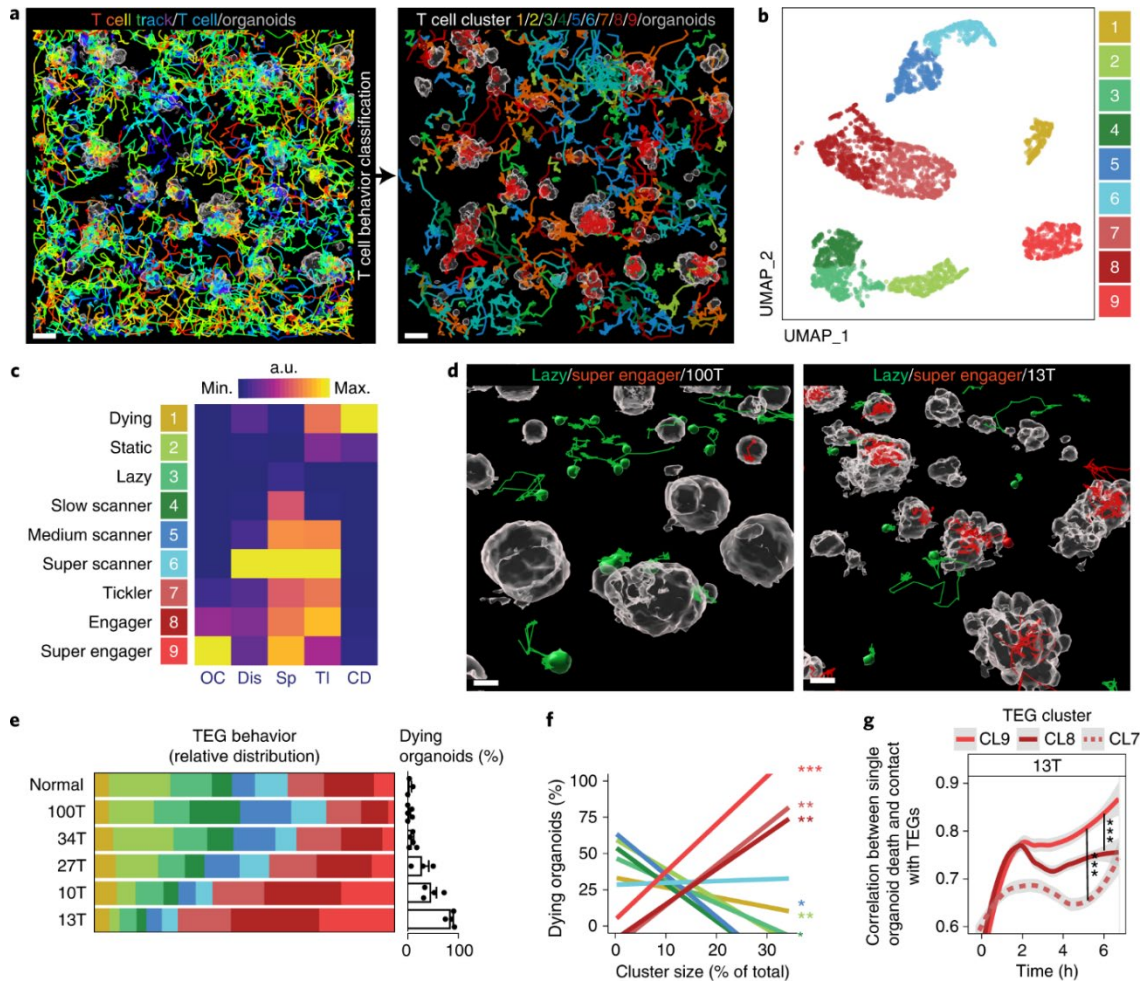


**Figure 2. TEGs exposed to PDOs display high diversity in their behavior with distinct killing potential. a**, Image of automated tracking of each TEG (left, 10-h tracks are rainbow colored for time). Tracks were classified according to TEG behavior and back-projected in the image (right, color coded by cluster). Scale bars, 50  $\mu\text{m}$ . Representative of  $n=11$  independent experiments. **b**, UMAP plot showing nine color-coded clusters identified by unbiased multivariate time series dynamic time-warping analysis. Each data point represents one T cell track of 3.3 h. See Supplementary Table 8 for conditions and replicates included. **c**, Heatmap depicting relative values of T cell features indicated for each cluster, named according to their most distinct characteristics. a.u., Arbitrary units in respect to maximal and minimal values for each feature. OC, organoid contact; Dis, square displacement; Sp, speed; TI, T cell interactions; CD, cell death. **d**, 3D-rendered images of 100T (low-targeting, left) and 13T (high-targeting, right) organoids (gray) and TEGs, with 3.3-h tracks belonging to lazy (green) and super engager (red) clusters. Scale bars, 20  $\mu\text{m}$ . Representative of  $n=5$  independent experiments. **e**, Behavioral cluster distribution of TEGs cocultured with the indicated PDOs and a normal organoid culture (left), in relation to their killing capacity (right, bar graph), represented as the percentage of dying organoids (percentage of total);  $n \geq 3$  independent experiments, mean  $\pm$  s.e.m. X2-test,  $P=1.132 \times 10^{-8}$ . **f**, Pearson correlation between behavior cluster (CL) size and percentage of dying organoids represented in **d**. CL9,  $P=0.00006$  (\*\*\*) ; CL8,  $P=0.009$  (\*\*); CL7,  $P=0.006$  (\*\*); CL5,  $P=0.014$  (\*) ; CL4,  $P=0.022$  (\*) ; CL2,  $P=0.0019$  (\*\*) (mean). See Supplementary Table 8 for test statistics and replicates included. **g**, Change in correlation between 13T organoid death dynamics (measured as increase in dead cell dye) and cumulative contact with TEGs (from CL7–9). Data presented as mean correlation per time point of all single organoids ( $n=4$  independent experiments). Linear mixed model fitting with each experimental replicate as a random effect: C9 versus C8,  $P=5.19 \times 10^{-6}$  (\*\*\*) ; C9 versus C7,  $P < 2 \times 10^{-16}$  (\*\*\*) .

## Behavioral differences detected between engineered Tcell therapie

We next applied BEHAV3D to evaluate two alternative Tcell immunotherapy concepts: (1) Tcells engineered with a conventional  $\alpha\beta$  TCR that targets tumor cells through recognition of the cancer-specific Wilms tumor antigen-1 (WT1) peptide presented on HLA-A\*0201 (ref. <sup>30</sup>), and (2) Tcells engineered to express a CAR targeting the tumor-expressed receptor tyrosine kinase-like orphan receptor 1 (ROR1) antigen<sup>4</sup>. We found that WT1 and ROR1 CAR Tcells effectively killed various BC PDOs (**Fig. 3a–d**) while, as expected, a HLA-A\*0201<sup>-</sup> (10T) and ROR1<sup>-</sup> line (34T) (**Fig. 3e**) were not killed. Tcell behavioral analysis showed similar detection of nine behavioral clusters, as identified for TEGs (**Fig. 3f,g**), and a substantial larger proportion of the super engager cluster in (highly) targeted PDOs compared with nontargeted PDOs (**Fig. 3h,i and Supplementary Video 1**). Finally, by comparing therapies that killed certain PDOs at similar efficacy, BEHAV3D uncovered behavioral differences between the different engineered Tcells (**Figs. 1d and 3a,b**). CAR Tcells were enriched in active behaviors, including super engager behavior, while showing an increased death rate compared with both WT1 Tcells and TEGs (**Fig. 3j**). Together, these data demonstrate the broad applicability of the BEHAV3D pipeline to various cellular immunotherapies, with the important opportunity to compare and correlate Tcell behavior to tumor targeting for identification of the most potent engineered Tcells.

## Serial killing capability of super engager CD8+ TEGs

To link tumor-targeting behavior to population phenotypes, we next differentially labelled CD4<sup>+</sup> and CD8<sup>+</sup> TEGs in BC PDO cocultures (**Fig. 4a and Extended Data Fig. 4a**). This revealed that prolonged organoid contact and super engager behavior was a preferred feature of CD8<sup>+</sup> TEGs, whereas CD4<sup>+</sup> TEGs showed a higher proportion of lazy cells, slow scanners, medium scanners, super scanners and ticklers (**Fig. 4a–c**) characteristic of high movement and short organoid contact (**Fig. 2c**). Furthermore, long-term behavior classification and back-projection of cells classified in the live-tracked imaging dataset (**Extended Data Fig. 4b,c**) showed that single CD8<sup>+</sup> TEGs, once engaged with an organoid, most often killed multiple cells consecutively (serial killing) (**Fig. 4d,e, Extended Data Fig. 5a,b and Supplementary Video 1**), a preferred feature of engineered Tcells<sup>31–33</sup>. By contrast, CD4<sup>+</sup> TEGs often moved away after organoid engagement without killing but occasionally targeted individual cells in different organoids (**Fig. 4d,e and Extended Data Figs. 4d and 5a**), thereby showing slower killing rates (**Extended Data Fig. 5c**).



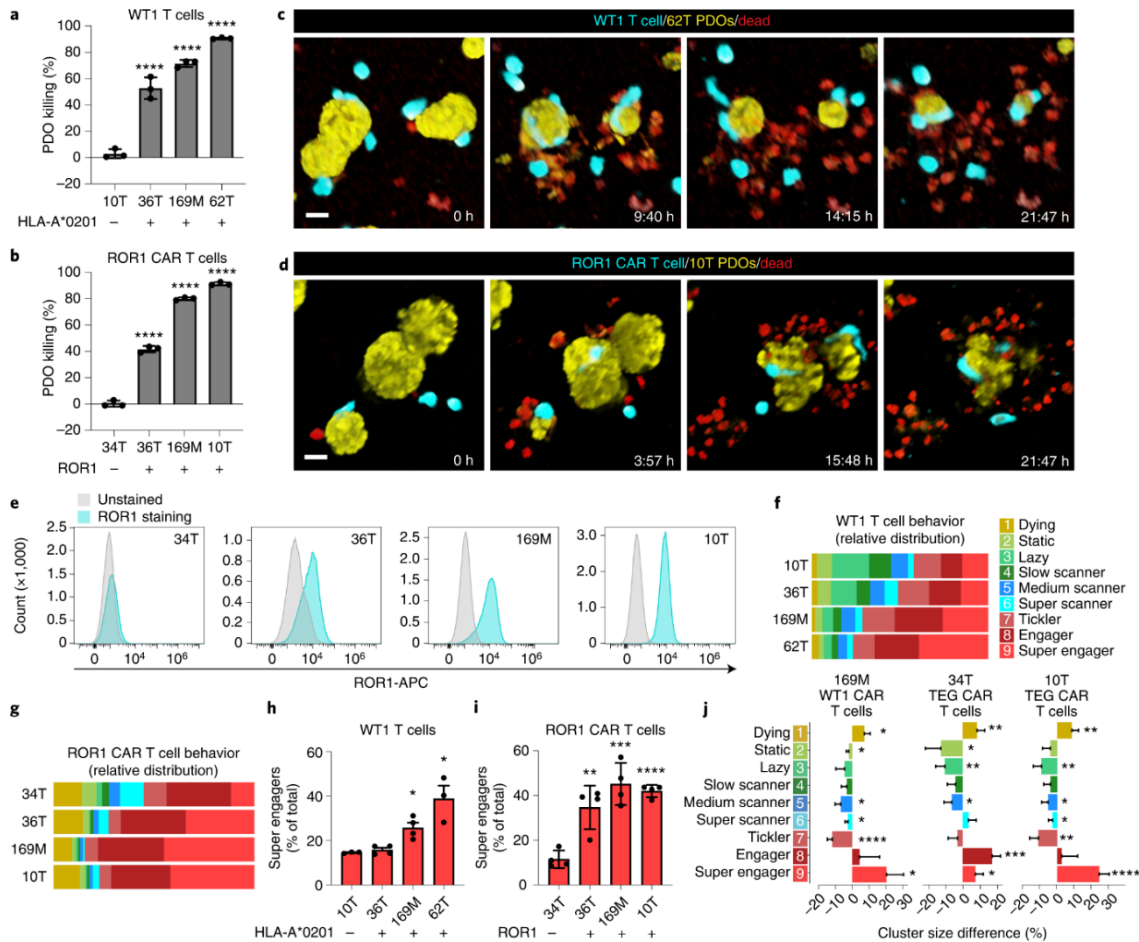


**Figure 3. Behavioral heterogeneity of TCR and CAR T cell therapies targeting BC PDOs.** **a,b**, Quantification of BC PDO viability using CellTiter-Glo following overnight coculture of PDOs with WT1 T cells (**a**) or ROR1 CAR T cells (**b**). **a,b**, One-way ANOVA followed by Dunnett's correction: 10T versus 36T,  $P < 0.0001$  (\*\*\*\*); 10T versus 169M,  $P < 0.0001$  (\*\*\*\*); 10T versus 62T,  $P < 0.0001$  (\*\*\*\*) (**a**); 34T versus 36T,  $P < 0.0001$  (\*\*\*\*); 34T versus 169M,  $P < 0.0001$  (\*\*\*\*); 34T versus 10T,  $P < 0.0001$  (\*\*\*\*) (**b**). Data corrected for untransduced T cell responses (mean  $\pm$  s.d.). **c,d**, 3D multispectral images of BC PDO cultures (yellow) showing killing by WT1 T cells (blue, **c**) or ROR1 CAR T cells (blue, **d**) at the indicated time points of imaging. Dead cells depicted in red. Scale bars, 30  $\mu$ m. **e**, FACS histogram plots showing ROR1 expression in the indicated breast cancer PDO cultures (blue) compared with unstained control (gray). **f,g**, Behavioral cluster distribution of WT1 T cells (**f**) and ROR1 CAR T cells (**g**) cocultured with the indicated BC PDOs (mean  $\pm$  s.e.m.).  $\chi^2$ -test,  $P < 0.0001$ . **h,i**, Super engager (CL9) cluster size (%) of total for WT1 T cells (**h**) and ROR1 CAR T cells (**i**). **h**, One-way ANOVA with Dunnett's correction: 10T versus 169M,  $P = 0.0501$ ; 10T versus 62T,  $P = 0.0006$ ; 34T versus 36T,  $P = 0.0018$ ; 34T versus 169M,  $P < 0.0001$ ; 34T versus 10T,  $P = 0.0002$  (mean  $\pm$  s.d.). **j**, Behavioral cluster size difference (%) between TEGs and CAR T cells cocultured with 34T (middle) or 10T (right), or between WT1 T cells and CAR T cells cocultured with 169M PDOs (left) (mean  $\pm$  s.d.). Welch's two-sided  $t$ -test: 169M: CL1,  $P = 0.015$ ; CL2,  $P = 0.041$ ; CL5,  $P = 0.023$ ; CL6,  $P = 0.047$ ; CL7,  $P = 9.94 \times 10^{-4}$ ; CL9,  $P = 0.012$ . 34T: CL1,  $P = 0.004$ ; CL2,  $P = 0.016$ ; CL3,  $P = 0.003$ ; CL5,  $P = 0.012$ ; CL8,  $P = 0.0004$ ; CL9,  $P = 0.037$ . 10T: CL1,  $P = 0.0014$ ; CL3,  $P = 0.0045$ ; CL5,  $P = 0.014$ ; CL6,  $P = 0.025$ ; CL7,  $P = 0.001$ ; CL9,  $P = 1.16 \times 10^{-5}$ . **a-e**, Representative of  $n = 3$  independent experiments; **f-j**,  $n = 3-6$  independent experiments; see Supplementary Table 8 for value of  $n$  per condition.

Thus, compared with CD4<sup>+</sup> TEGs, CD8<sup>+</sup> TEGs were shown to be more potent tumor-targeting cells with profound serial killing capacity. Serial killing by super engager CD8<sup>+</sup> TEGs was characterized by attachment to PDOs using a defined anchor point from which surrounding cells were killed via long protrusions, intercalating between epithelial cells and extending their initial size up to fivefold (**Fig. 4d and Extended Data Fig. 4e,f**). We confirmed morphological plasticity and serial killing potential also for WT1 Tcells and ROR1 CAR Tcells analyzed through BEHAV3D (**Fig. 3c,d and Supplementary Video 1**). Remarkably, single CD8<sup>+</sup> TEGs were able to kill entire organoids (up to 18cells in 11h; **Fig. 4d, Extended Data Fig. 5b and Supplementary Video 1**). This extent of serial killing and morphological plasticity of super engager CD8<sup>+</sup> TEGs was uniquely revealed by the high spatiotemporal resolution character of BEHAV3D.

4

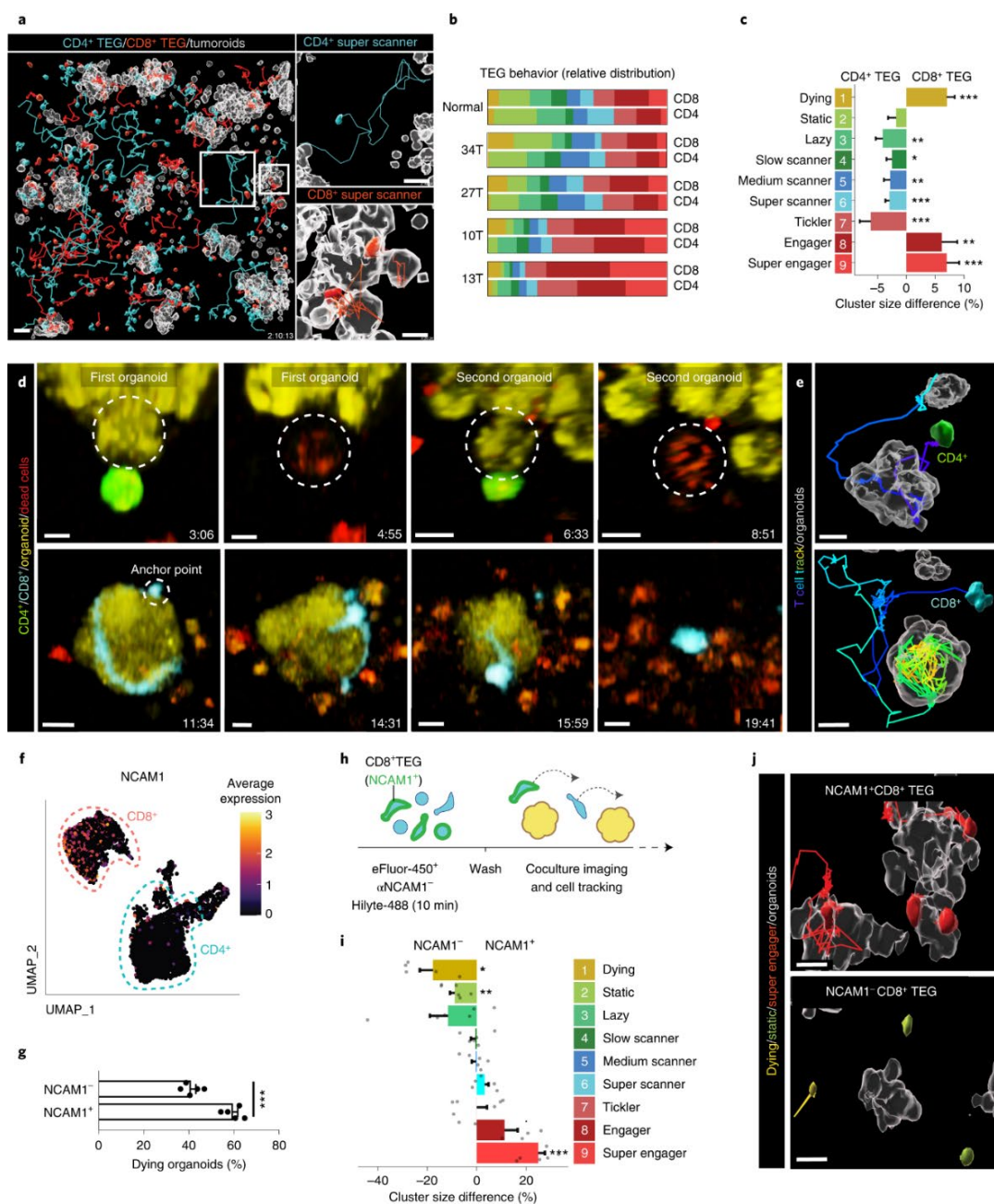


**Figure 4. Unique targeting features of TEG subpopulations and serial killer potential.** **a**, Images of CD4+ (blue) and CD8+ (red) TEGs and their full tracks (up to 10 h) cocultured with 13T organoids (gray surface rendering at  $t=0$ ). Scale bars, 50  $\mu\text{m}$  (main image), 30  $\mu\text{m}$  (zoomed-in images). **b**, Relative behavioral cluster distribution of TEGs cocultured with various organoids. **c**, Behavioral cluster size difference (%) between CD4+ and CD8+ TEGs cocultured with the indicated organoid cultures from **b** ( $n=33$  wells pooled from the five organoid cultures shown in **b**; see Supplementary Table 8 for replicate specifics; mean  $\pm$  s.e.m.). Linear regression model fitting with each well as a random effect: CL9,  $P=7.52 \times 10^{-6}$  (\*\*\*) ; CL8,  $P=0.0034$  (\*\*); CL7,  $P=0.00018$  (\*\*\*) ; CL6,  $P=0.000023$  (\*\*\*) ; CL5,  $P=0.0062$  (\*\*); CL4,  $P=0.01$  (\*); CL3,  $P=0.001$  (\*\*); CL1,  $P=3.01 \times 10^{-6}$  (\*\*\*) . **d**, A CD4+ TEG killing a 13T tumor cell in a first organoid and a second tumor cell in a neighboring organoid (upper), and a CD8+ TEG killing a complete 13T organoid over 11 h (lower). Scale bars, 30  $\mu\text{m}$ ; time, **h**. **e**, Processed images from **d** showing 3D-rendered organoids (gray) at  $t=0$  and the CD4+ TEG or CD8+ TEG with their full track. Scale bars, 10  $\mu\text{m}$ . **f**, UMAP embedding showing expression levels of NCAM1. Color gradient represents  $\log_2$ -transformed normalized counts of genes. **g**, Quantification of the percentage of dying 13T organoids (of total) after 10 h of coculture with either sorted NCAM1<sup>-</sup> CD8+ TEGs or NCAM1+CD8+ TEGs ( $n=5$  independent experiments, mean  $\pm$  s.e.m.). Two-tailed unpaired  $t$ -test,  $P=0.0001036$ . **h**, Schematic representation of fluorescent labelling strategy for CD8+ TEGs. **i**, Behavioral cluster difference (%) between NCAM1<sup>-</sup> CD8+ TEGs and NCAM1+CD8+TEGs cocultured with 13T organoids ( $n=6$  independent experiments, mean  $\pm$  s.e.m.). Linear regression model fitting with each experimental replicate as a random effect: CL9,  $P=0.0002$  (\*\*\*) ; CL8,  $P=0.07$  (-) ; CL2,  $P=0.005$  (\*\*); CL1,  $P=0.02$  (\*). **j**, Images of 13T organoids (gray) with NCAM+ super engager CD8+TEGs (top) and NCAM<sup>-</sup> lazy and dying CD8+TEGs (bottom). Scale bars, 10  $\mu\text{m}$ . **a,d,j**, Representative of  $n=5$ , 3 and 5 independent experiments, respectively).

## Neural cell adhesion molecule 1 is associated with super engager behavior

Through single-cell RNA sequencing (scRNA-seq), we observed differential expression of neural cell adhesion molecule 1 (NCAM1) in CD8<sup>+</sup> TEGs (**Fig. 4f**, **Extended Data Fig. 4g,h** and **Supplementary Table 3**). Although linked to cytotoxicity in both  $\alpha\beta$  and  $\gamma\delta$  Tcells<sup>34</sup>, this surface marker has not been examined in the context of cellular immunotherapy. Making use of this differential NCAM1 expression, we provided proof of concept for engineered Tcell functional selection by showing that sorted NCAM1<sup>+</sup>CD8<sup>+</sup> TEGs have a greater capacity to kill various BC PDOs compared with NCAM1<sup>-</sup>CD8<sup>+</sup> TEGs (**Fig. 4g** and **Extended Data Fig. 4i**). To identify behavioral mechanisms underlying this high killing potential, we prelabelled CD8<sup>+</sup> TEGs with NCAM1 nanobodies (**Fig. 4h**) for direct comparison of NCAM1-positive and -negative populations within the same environment. NCAM1<sup>+</sup>CD8<sup>+</sup> TEGs showed reduced dying and static behavior (**Fig. 4i,j** and **Extended Data Fig. 4j**), supporting a higher in vitro persistence. Strikingly, NCAM1<sup>+</sup>CD8<sup>+</sup> TEGs additionally showed a significant increase in super engager behavior compared with NCAM1<sup>-</sup> CD8<sup>+</sup> TEGs (**Fig. 4i,j**). Thus, surface marker expression can be linked to engineered Tcell behavior, offering the opportunity to enrich for potent effector behaviors through cell selection. Functional skewing during engineered Tcell production might also be feasible, because TEGs expanded in the presence of IL-15 expressed higher levels of NCAM1 (**Extended Data Fig. 4k**), in line with a role for IL-15 in NCAM1 induction<sup>34</sup>.

## Behavioral-transcriptomic profiling of TEGs

To generate insight into the transcriptional programs that underlie tumor-targeting dynamics revealed by BEHAV3D, we next performed single-cell transcriptomic profiling of TEG populations enriched for different behavioral signatures following coculture with BC PDOs, including a TEG population containing >90% super engagers (**Fig. 5a,b, Extended Data Fig. 6a and Supplementary Video 1**). For each main TEG subset identified, effector CD8<sup>+</sup> (CD8<sup>eff</sup>), effector CD4<sup>+</sup> (CD4<sup>eff</sup>) and memory CD4<sup>+</sup> (CD4<sup>mem</sup>), profound transcriptional changes were observed following 6h of coculture with highly targeted 13T organoids as compared with baseline (no-target control) (**Fig. 5c–e**), showing that dynamic interplay with PDOs shapes the TEG transcriptomic profile. We developed a method of behavioral probability mapping inferred from pseudotemporal ordering (**Extended Data Fig. 6b**) of the sequenced TEG populations (**Fig. 5f**), allowing us to pinpoint gene programs in TEGs regulated by environmental stimuli, short PDO engagement and prolonged PDO engagement (**Fig. 5f,g**). This revealed dynamic transcriptional programs highly conserved between CD8<sup>eff</sup>, CD4<sup>eff</sup> and CD4<sup>mem</sup> TEGs (**Fig. 5g**; gene clusters 1–3, 85% of genes; **Supplementary Table 4**). These programs included genes either downregulated (CL1) or upregulated (CL3) by environmental stimuli or engagement with PDOs, as well as those transiently expressed (CL2) along the pseudotime trajectory (**Fig. 5g**; GO terms per cluster shown in **Extended Data Fig. 6c**). This differential dynamic expression matched with known gene function, confirming robust ordering of TEGs as shown by genes related to the CD3 signaling complex (LCK, SOS1, CD3E, CD3G, CL1; GO term ‘Tcell activation’) known to be downregulated following Tcell activation<sup>35</sup> in CL1 (**Fig. 5h**). NF-κB signaling, critical for tumor control<sup>36</sup>, and effector molecules, including FASLG, IFNG, GZMB and TNF, were found in CL3, with NF-κB signaling induced by environmental stimuli reaching maximum expression following prolonged PDO engagement, while effector molecules appeared upon engagement (**Fig. 5i**). In addition, CL3 contained genes related to ribosomal RNA processing that increased only following prolonged engagement with organoids (**Fig. 5h**), consistent with accelerated protein production in Tcells following TCR engagement<sup>37,38</sup>. Finally, CL2 contained the early activation markers CD69 and EGR1 with peak expression following short organoid engagement, in line with IL-2 (CL3), known to be induced by EGR1 (ref. <sup>39</sup>), upregulated towards the end of the trajectory (**Fig. 5i**). Thus, through our behavior-guided transcriptomics approach we robustly identified dynamic gene orchestration of TEGs during tumor targeting.

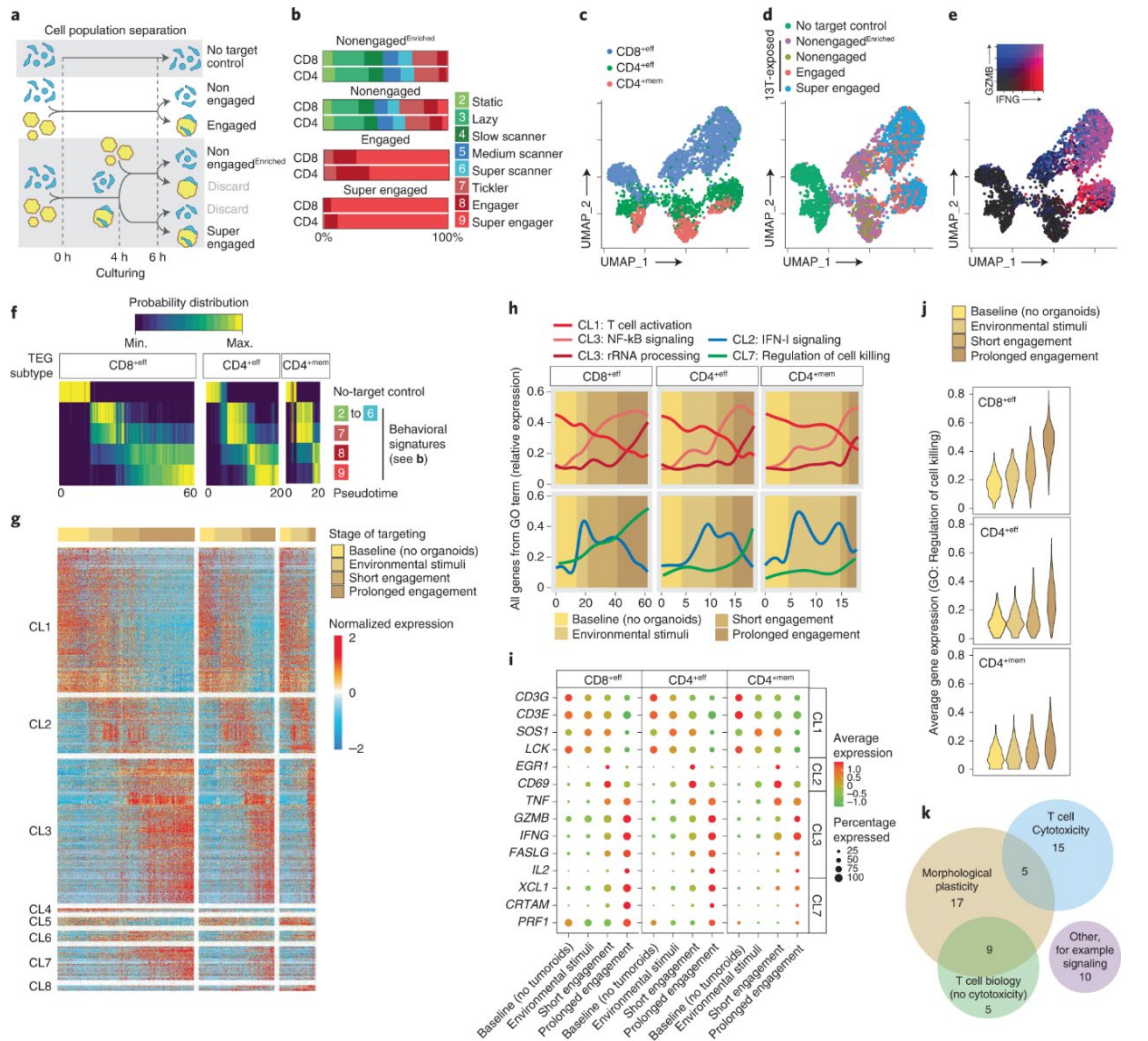


**Figure 5. Behavioral-transcriptomic profiling of TEGs following PDO exposure, engagement and killing.** **a**, Schematic representation of cell population separation for isolation and sequencing of super engaged, engaged, nonengaged, nonengaged<sup>Enriched</sup> and no-target control TEGs. **b**, Distribution of the nine behavioral signatures described in Fig. 2b,c of the indicated behavior-enriched TEG populations isolated after 6 h of coculture with 13T PDOs.  $n=6$  independent experiments. **c–e**, UMAP embedding of pooled scRNA-seq profiles showing distribution of CD8<sup>eff</sup>, CD4<sup>eff</sup> and CD4<sup>mem</sup> TEGs (**c**), the five behavior-enriched TEG populations described in **a** (**d**) and normalized gene expression of IFNG and GZMB (**e**). Colors represent log<sub>2</sub>-transformed normalized counts of genes. **f**, Heatmap representing the probability distribution of different behavioral signatures and no-target control over pseudotime for CD8<sup>eff</sup>, CD4<sup>eff</sup> and CD4<sup>mem</sup> TEGs. Colors represent the scaled probability for each behavioral group. **g**, Heatmap showing normalized gene expression dynamics of TEGs following exposure to and engagement with 13T PDOs. Columns represent T cells ordered in pseudotime, rows represent gene expression grouped based on similarity, resulting in eight gene clusters. CLs 1–3 represent gene expression patterns shared among TEG subsets; CLs 4–8 show different expression dynamics between TEG subsets. Horizontal color bar (top) represents the corresponding stage of targeting based on data in **f**. **h**, Averaged gene expression over pseudotime for all genes from indicated GO terms for the indicated TEG subtypes. Background color shading represents the corresponding stage of targeting; line colors indicate GO terms. **i**, Gene expression dot plot for a curated subset of genes at different stages of targeting. Rows depict genes, dot color gradient indicates average expression while dot size reflects the proportion of cells expressing a particular gene (%). **j**, Violin plots for different TEG subtypes showing averaged expression of genes related to GO term 'Regulation of cell killing' enriched in CL7 from **g**. Colors indicate different stages of targeting. **k**, Venn diagram depicting common and unique functions from 61 conserved genes comprising a (serial) killer gene signature. **b–d**, T cells pooled from two independent experiments).

## Gene signature related to (serial) killing super engager TEGs

Of those gene sets regulated in a TEG subset-specific manner (CL4–8, 15% of genes), CL7 contained genes mainly induced following prolonged organoid engagement, including cytotoxic genes (for example, PRF1, CRTAM, XCL1; **Fig. 5h,i**; GO: Regulation of cell killing). This cluster of genes was specifically induced in super engager CD8<sup>eff</sup> and, to a lesser extent, in CD4<sup>eff</sup> TEGs but was almost absent in CD4<sup>mem</sup> TEGs (**Fig. 5j**), associating this gene cluster with potent (serial) killing Tcells (**Fig. 4d–g**). Analysis of TEGs derived from a different donor and cocultured with another BC PDO (10T) confirmed that 61 out of the 83 genes of CL7 represent a conserved ‘killer’ gene signature (**Supplementary Table 5**). Of these, we identified 20 genes related to Tcell activation and cytotoxicity and 14 related to other Tcell functions (**Fig. 5k and Extended Data Fig. 6d**). However, we found 27 genes with no previously described Tcell function (**Fig. 5k and Extended Data Fig. 6d**). Overall, half of all conserved signature genes (31/61) and 17 out of the 27 genes were related to morphological plasticity processes including motility, cytoskeleton remodeling and adhesion (**Extended Data Fig. 6d**). Given that morphological plasticity is a key determinant of cell migration, many of the identified genes were found to have a role in promotion of tumor cell migration and invasion, including ECM production and mesenchymal state induction (HEG1, BZW2, DCAF13, SQLE, PKIA). For some of these genes, such as CCT3 or AFAP1L2, the mechanism promoting migration is yet to be described. In line with the prolonged organoid engagement behavioral feature of super engager TEGs (**Fig. 2c**), we also found various genes related to cell adhesion including NCEH1, BYSL and EMP1. Finally, some genes had an additional function related to neurite outgrowth and dendritic pruning (SERPINE2, CHD4, NRTK1), potentially matching the long protrusion that was observed to occur in these serial killing TEGs (**Fig. 4e, Extended Data Fig. 4e,f and Supplementary Video 1**). Thus, the behavioral-transcriptomics module of BEHAV3D identified a specific gene signature induced in (serial) killing super engager TEGs. To provide some context as to how induced gene signatures in TEGs relate to in vivo tumor targeting, we compared our behavior-guided transcriptomics results with two published scRNA-seq datasets on tumor-infiltrating lymphocytes (TILs) obtained from patients with breast cancer<sup>40,41</sup>. Both datasets identified a potent CD8<sup>+</sup> Tcell population defined by a cytotoxic gene signature (310 (ref. <sup>41</sup>) and 533 genes<sup>40</sup>) and prognostic value for patient survival (**Extended Data Fig. 7a–d and Supplementary Table 6**). When comparing the gene profiles of these in-vivo-identified cytotoxic CD8<sup>+</sup> TILs with our data, we observed a substantial overlap with the gene signature of CD8<sup>+</sup> TEGs that were selected based on super engager behavior (**Extended Data Fig. 7e**). The highest relative expression of the cytotoxic gene signatures from both datasets above<sup>41,40</sup> was observed in CD8<sup>eff</sup> TEGs after prolonged organoid engagement (**Extended Data Fig. 7f**). These data thereby demonstrate that the gene signatures related to potent tumor targeting in vivo of patients with breast cancer

overlap with that of super engager TEGs, supporting the in vivo relevance of our approach.

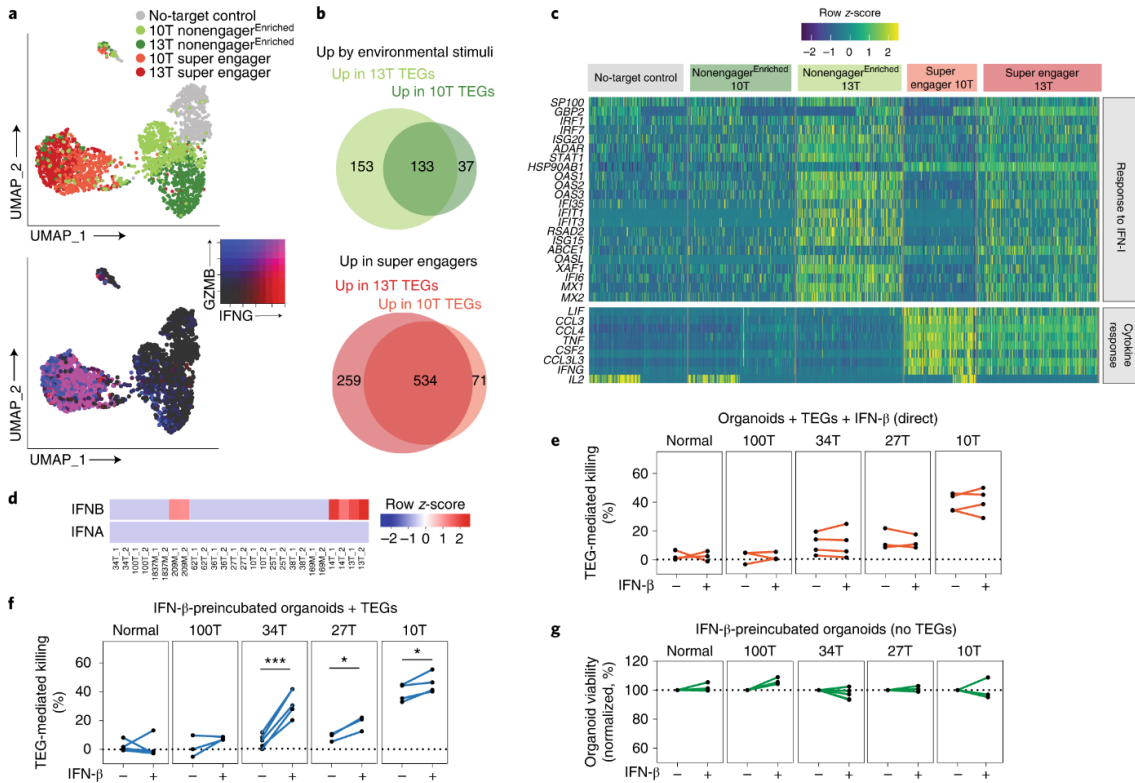


**Figure 6. IFN-I signaling in PDOs primes TEG efficacy.** **a**, Top: UMAP embedding of pooled scRNA-seq profiles from super engaged and nonengager<sup>Enriched</sup> TEG populations cocultured with either 13T or 10T PDOs, and from no-target control T cells. TEGs are colored according to experimental condition. Bottom: UMAP plot showing expression levels of *IFNG* and *GZMB*. Colors represent  $\log_2$ -transformed normalized counts of genes. **b**, Venn diagrams depicting common and unique genes upregulated (up) in TEGs following 13T and 10T organoid exposure (top, environmental stimuli) or prolonged engagement (bottom, super engagers). **c**, Heatmap of gene expression for genes involved in functional annotations of interest in response to IFN-I, cytokine response), grouped according to TEG populations. **d**, *IFNA* and *IFNB* expression in PDOs from the BC panel in Fig. 1d. 1 and 2 indicate different experimental replicates. **e-g**, Quantification of dying single organoids in the presence or absence of recombinant IFN- $\beta$  for the following conditions: organoids cocultured with TEGs with direct addition of IFN- $\beta$ , corrected for responses of LM1 control T cells (**e**); organoids preincubated with IFN- $\beta$  for 24 h before coculture with TEGs, corrected for responses of LM1 control T cells (**f**); and organoids preincubated with IFN- $\beta$  for 24 h and cultured in the absence of TEGs (**g**). Lines connect experimental replicates. **f**, Statistical analysis was performed by paired *t*-test: 34T IFN- $\beta$  versus 34T control,  $P < 0.0006$  (\*\*\*) ; 27T IFN- $\beta$  versus 27T control,  $P < 0.0216$  (\*) ; 10T IFN- $\beta$  versus 10T control,  $P < 0.0402$  (\*). See Supplementary Table 8 for summary of replicates in **e-g**.

## PDOs shape the dynamic gene signature of TEG during tumor targeting

To further explore our behaviorally guided transcriptomics approach, we next compared behavior-enriched TEG populations cocultured with either highly sensitive (13T) or intermediately targeted (10T) BC PDOs. Distinct uniform manifold approximation and projection (UMAP) embedding of different TEG populations (**Fig. 6a**) indicated that patient-specific organoid exposure influences the dynamic TEG transcriptional profile—41 and 61%, respectively, of upregulated genes by environmental stimuli or following prolonged PDO engagement in super engagers were common between 10T- and 13T-cocultured TEGs (**Fig. 6b, Extended Data Fig. 8a,b and Supplementary Table 7**). Common super-engager-related gene signatures included rRNA processing, NF- $\kappa$ B signaling and cytokine signaling (**Extended Data Fig. 8b**), and matched CL3 gene signatures (**Extended Data Fig. 6c**). However, 10T-cocultured TEGs were characterized by induction of high cytokine expression following prolonged PDO engagement, including TNF, IFNG and IL2, whereas IFN-I signaling genes were uniquely induced in TEGs cocultured with highly sensitive 13T (**Fig. 6c and Extended Data Fig. 8c**).

## IFN- $\beta$ primes PDOs for TEG-mediated killing

IFN-I signaling plays fundamental roles in antitumor immunity, but with diverse and sometimes opposing functions reported for both tumor and immune cells, thereby making it difficult to fully comprehend and therapeutically exploit these effects<sup>42</sup>. IFN-I signaling was detected in 13T BC PDOs (**Extended Data Fig. 2c**), which most prominently showed increased RNA levels of the upstream mediator IFN- $\beta$ , but not IFN- $\alpha$ , among our collection of PDOs (**Fig. 6d**). Secretion of IFN- $\beta$  was confirmed by Luminex (**Extended Data Fig. 8d**), implying that IFN- $\beta$  was the main mediator of IFN-I signaling observed in 13T. Interestingly, peak induction of IFN-I signaling in 13T-cocultured TEGs was detected in nonorganoid-engaging TEGs (from static to super scanner behavior), in line with a secreted source of IFN- $\beta$ , while the pathway was shut down in super engager TEGs, suggesting a limited role of IFN-I signaling in direct killing behavior (**Fig. 5f–h**). The addition of recombinant IFN- $\beta$  to cocultures of TEGs with various BC PDOs showing low to medium sensitivity to TEG therapy (100T, 34T, 27T and 10T) indeed did not affect TEG targeting efficacy (**Fig. 6e**). However, 34T, 27T and 10T organoids pretreated with IFN- $\beta$  showed increased TEG-mediated killing while IFN- $\beta$  treatment did not impact organoid viability by itself (**Fig. 6f,g**). These data support the premise that IFN- $\beta$  has limited impact on the killing capacity of super engager TEGs, confirming that dynamic IFN-I signaling is mainly associated with static to scanner behavior. However, IFN-I signaling increases the sensitivity of BC PDOs to TEG therapy. Thus, behavior-guided TEG transcriptomics in relation to the type of organoid exposure shows that IFN- $\beta$  primes PDOs for targeting by TEGs. This illustrates the potential of BEHAV3D to improve understanding and guide combinatory treatment approaches in a patient-specific manner.



## Discussion

Here we provide an organoid-based, 3D imaging-transcriptomic platform, BEHAV3D, for understanding the mode of action of cellular anticancer immunotherapies in a patient-specific manner and apply it to diverse solid-tumor PDO models and multiple engineered Tcell products. With BEHAV3D we have demonstrated differences in behavior between various engineered Tcell products, uncovered the gene signature associated with serial killing, designed an optimal sequence of Tcell combination therapy and provided proof of concept for a cell selection strategy to enrich for potent tumor-targeting behavior (**Supplementary Discussion**). Thus, BEHAV3D integrates multiple single-cell readouts (**Supplementary Video 1**) to offer a comprehensive platform with potential for broadening the implementation of cellular immunotherapy for solid tumors.

## References

1. van der Leun, A. M., Tommen, D. S. & Schumacher, T. N. CD8(+) T cell states in human cancer: insights from single-cell analysis. *Nat. Rev. Cancer* 20, 218–232 (2020).
2. June, C. H. & Sadelain, M. Chimeric antigen receptor therapy. *N. Engl. J. Med.* 379, 64–73 (2018).
3. Chen, D. S. & Mellman, I. Elements of cancer immunity and the cancer-immune set point. *Nature* 541, 321–330 (2017).
4. Wallstabe, L. et al. ROR1-CAR T cells are effective against lung and breast cancer in advanced microphysiologic 3D tumor models. *JCI Insight* 4, e126345 (2019).
5. Chapuis, A. G. et al. T cell receptor gene therapy targeting WT1 prevents acute myeloid leukemia relapse post-transplant. *Nat. Med.* 25, 1064–1072 (2019).
6. Grunder, C. et al. gamma9 and delta2CDR3 domains regulate functional avidity of T cells harboring gamma9delta2TCRs. *Blood* 120, 5153–5162 (2012).
7. Johanna, I. et al. Evaluating in vivo efficacy – toxicity profile of TEG001 in humanized mice xenografts against primary human AML disease and healthy hematopoietic cells. *J. Immunother. Cancer* 7, 69 (2019).
8. Marcu-Malina, V. et al. Redirecting alphabeta T cells against cancer cells by transfer of a broadly tumor-reactive gammadeltaT-cell receptor. *Blood* 118, 50–59 (2011).
9. Sebestyen, Z., Prinz, I., Dechanet-Merville, J., Silva-Santos, B. & Kuball, J. Translating gammadelta ( $\gamma\delta$ ) T cells and their receptors into cancer cell therapies. *Nat. Rev. Drug Discov.* 19, 169–184 (2019).
10. Vyborova, A. et al. gamma9delta2T cell diversity and the receptor interface with tumor cells. *J. Clin. Invest.* 130, 4637–4651 (2020).
11. Rigau, M. et al. Butyrophilin 2A1 is essential for phosphoantigen reactivity by gammadelta T cells. *Science* 367, eaay5516 (2020).
12. Sebestyen, Z. et al. RhoB mediates phosphoantigen recognition by Vgamma9Vdelta2 T cell receptor. *Cell Rep.* 15, 1973–1985 (2016).
13. Tuveson, D. & Clevers, H. Cancer modeling meets human organoid technology. *Science* 364, 952–955 (2019).
14. Ganesh, K. et al. A rectal cancer organoid platform to study individual responses to chemoradiation. *Nat. Med.* 25, 1607–1614 (2019).
15. Oof, S. N. et al. Patient-derived organoids can predict response to chemotherapy in metastatic colorectal cancer patients. *Sci. Transl. Med.* 11, eaay2574 (2019).
16. Tiriác, H. et al. Organoid profiling identifies common responders to chemotherapy in pancreatic cancer. *Cancer Discov.* 8, 1112–1129 (2018).
17. Vlachogiannis, G. et al. Patient-derived organoids model treatment response of metastatic gastrointestinal cancers. *Science* 359, 920–926 (2018).
18. Yao, Y. et al. Patient-derived organoids predict chemoradiation responses of locally advanced rectal cancer. *Cell Stem Cell* 26, 17–26 (2020).
19. Bar-Ephraim, Y. E., Kretzschmar, K. & Clevers, H. Organoids in immunological research. *Nat. Rev. Immunol.* 20, 279–293 (2019).
20. Cattaneo, C. M. et al. Tumor organoid-T-cell coculture systems. *Nat. Protoc.* 15, 15–39 (2020).
21. Dijkstra, K. K. et al. Generation of tumor-reactive T cells by co-culture of peripheral blood lymphocytes and tumor organoids. *Cell* 174, 1586–1598 (2018).
22. Neal, J. T. et al. Organoid modeling of the tumor immune microenvironment. *Cell* 175, 1972–1988 (2018).

23. Schnalzger, T. E. et al. 3D model for CAR-mediated cytotoxicity using patient-derived colorectal cancer organoids. *EMBO J.* 38, e100928 (2019).
24. Dekkers, J. F. et al. High-resolution 3D imaging of fixed and cleared organoids. *Nat. Protoc.* 14, 1756–1771 (2019).
25. Lukonin, I. et al. Phenotypic landscape of intestinal organoid regeneration. *Nature* 586, 275–280 (2020).
26. Rios, A. C. et al. Intracлонаl plasticity in mammary tumors revealed through large-scale single-cell resolution 3D imaging. *Cancer Cell* 35, 618–632 (2019).
27. Rios, A. C. & Clevers, H. Imaging organoids: a bright future ahead. *Nat. Methods* 15, 24–26 (2018).
28. Serra, D. et al. Self-organization and symmetry breaking in intestinal organoid development. *Nature* 569, 66–72 (2019).
29. Sachs, N. et al. A living biobank of breast cancer organoids captures disease heterogeneity. *Cell* 172, 373–386 (2018).
30. Kuball, J. et al. Facilitating matched pairing and expression of TCR chains introduced into human T cells. *Blood* 109, 2331–2338 (2007).
31. Cazaux, M. et al. Single-cell imaging of CAR T cell activity in vivo reveals extensive functional and anatomical heterogeneity. *J. Exp. Med.* 216, 1038–1049 (2019).
32. Halle, S. et al. In vivo killing capacity of cytotoxic T cells is limited and involves dynamic interactions and T cell cooperativity. *Immunity* 44, 233–245 (2016).
33. Weigelin, B. et al. Cytotoxic T cells are able to efficiently eliminate cancer cells by additive cytotoxicity. *Nat. Commun.* 12, 5217 (2021).
34. Van Acker, H. H., Capsomidis, A., Smits, E. L. & Van Tendeloo, V. F. CD56 in the immune system: more than a marker for cytotoxicity? *Front. Immunol.* 8, 892 (2017).
35. Liu, H., Rhodes, M., Wiest, D. L. & Vignali, D. A. On the dynamics of TCR:CD3 complex cell surface expression and downmodulation. *Immunity* 13, 665–675 (2000).
36. Barnes, S. E. et al. T cell-NF-kappaB activation is required for tumor control in vivo. *J. Immunother. Cancer* 3, 1 (2015).
37. Asmal, M. et al. Production of ribosome components in effector CD4+ T cells is accelerated by TCR stimulation and coordinated by ERK-MAPK. *Immunity* 19, 535–548 (2003).
38. Tan, T. C. J. et al. Suboptimal T-cell receptor signaling compromises protein translation, ribosome biogenesis, and proliferation of mouse CD8 T cells. *Proc. Natl Acad. Sci. USA* 114, E6117–E6126 (2017).
39. Collins, S., Wolfrain, L. A., Drake, C. G., Horton, M. R. & Powell, J. D. Cutting edge: TCR-induced NAB2 enhances T cell function by coactivating IL-2 transcription. *J. Immunol.* 177, 8301–8305 (2006).
40. Azizi, E. et al. Single-cell map of diverse immune phenotypes in the breast tumor microenvironment. *Cell* 174, 1293–1308 (2018).
41. Savas, P. et al. Single-cell profiling of breast cancer T cells reveals a tissue-resident memory subset associated with improved prognosis. *Nat. Med.* 24, 986–993 (2018).
42. Boukhaled, G. M., Harding, S. & Brooks, D. G. Opposing roles of type I interferons in cancer immunity. *Annu. Rev. Pathol.* 16, 167–198 (2021).

## Methods

### Human material

All human BC and head and neck PDO samples were retrieved from a biobank through the Hubrecht Organoid Technology (HUB; [www.hub4organoids.nl](http://www.hub4organoids.nl)). Authorizations were obtained by the medical ethical committee and biobank research ethics committee of UMC Utrecht (UMCU) at the request of HUB, to ensure compliance with the Dutch Medical Research Involving Human Subjects Act. Normal breast organoids were generated from milk obtained via the Moedermelkbank Amsterdam (Amsterdam UMC). Primary patient-derived DMG cultures (no. DMG-VI/SU-DIPG-VI) were kindly provided by M. Monje (Stanford University), M. Vinci (Ospedale Pediatrico Bambino Gesù, nos. DMG002/OPBG-DIPG-002 and DMG-004/OPBG-DIPG-004-aa) and A. M. Carcaboso (Hospital San Juan de Dios, no. DMG-007/HSJD-DIPG-007). For TEG and WT1 T cell generation, peripheral blood of anonymous healthy donors was purchased from the Dutch blood bank (Sanquin). For CAR Tcell generation, cord blood was collected with approval from the Ethical Committee of UMCU. Informed consent was obtained from all donors.

### Animal material

NOD.Cg-Prkdcscidll2rgtm1Wjl/SzJ (NSG) mice were purchased from Charles River Laboratories. Experiments were conducted with permission from the Animal Welfare Body Utrecht (nos. 4288-1-08 and 4288-1-09) as per current Dutch laws on animal experimentation. Mice were housed under 45–65% humidity and a daily 12/12-h light/dark regime, in sterile conditions using an individually ventilated cage system and fed with sterile food and water. Irradiated mice were given sterile water with antibiotic ciproxin for the duration of the experiment. Mice were randomized with equal distribution by age and initial weight measured on day 0 and divided into groups of ten (13T) or 15 (169M).

### Organoid culture

Breast cancer and normal breast organoids were seeded in basement membrane extract (BME, Cultrex) in uncoated 12-well plates (Greiner Bio-one) and cultured as described previously<sup>29,43</sup>. Briefly, Advanced DMEM/F12 was supplemented with penicillin/streptomycin (pen/strep), 10mM HEPES, GlutaMAX (adDMEM/F12+++), 1×B27 (all Thermo Fisher), 1.25 mM N-acetyl-l-cysteine (Sigma-Aldrich), 10mM nicotinamide (Sigma-Aldrich), 5μM Y-27632 (Abmole), 5nM Heregulin β-1 (Peprotech), 500nM A83-01 (Tocris), 5 ng ml<sup>-1</sup> epidermal growth factor (Peprotech), 20 ng ml<sup>-1</sup> human fibroblast growth factor (FGF)-10 (Peprotech), 10% Noggin-conditioned

medium<sup>20</sup>, 10% Rspo1-conditioned medium<sup>44</sup> and 0.1 mg ml<sup>-1</sup> primocin (Thermo Fisher); and, in addition, with 1 μM SB202190 (Sigma-Aldrich) and 5 ng ml<sup>-1</sup> FGF-7 (Peprotech) for PDO propagation (type 1 culture medium<sup>43</sup>), or with 20% Wnt3a-conditioned medium<sup>44</sup>, 0.5 μg ml<sup>-1</sup> hydrocortisone (Sigma-Aldrich), 100 μM β-estradiol (Sigma-Aldrich) and 10 mM forskolin (Sigma-Aldrich) for normal organoid propagation (type 2 culture medium<sup>43</sup>). Organoids from passages 5–30 after cell isolation were used for T cell coculture. For T cell coculture, organoids were recovered from the BME by resuspension in TrypLE Express and collected in adDMEM/F12+++ (BC and head and neck cancer PDOs) or resuspended and collected in adDMEM/F12+++ (DMG PDOs). Organoid suspensions were filtered through a 70-μm strainer (Greiner) to remove large organoids and pelleted before coculture.

### T cells engineered to express a γδ TCR (TEGs and LM1s)

TEG001 (T cells engineered to express a highly tumor-reactive Vγ9Vδ2 TCR)<sup>6,45,46</sup>, LM1s (mock T cells engineered to express a mutant Vγ9/Vδ2 TCR with abrogated function)<sup>8</sup> and TEG011 (mock T cells engineered to express HLA-A\*24:02-restricted Vγ5/Vδ1 TCR, used as control for in vivo studies)<sup>47,48</sup> were produced as previously described<sup>8</sup>. Briefly, packaging cells (Phoenix-Ampho) were transfected with helper constructs gag-pol (pHIT60), env (pCOLT-GALV) and pMP71 retroviral vectors containing both Vγ9/Vδ2 TCR chains separated by a ribosomal-skipping T2A sequence, using FugeneHD reagent (Promega). Human peripheral blood mononuclear cells (PBMCs) from healthy donors were preactivated with anti-CD3 (30 ng ml<sup>-1</sup>; Orthoclone OKT3, Janssen-Cilag) and IL-2 (50 IU ml<sup>-1</sup>; Proleukin, Novartis) and subsequently transduced twice with viral supernatant within 48 h in the presence of 50 IU ml<sup>-1</sup> IL-2 and 6 mg ml<sup>-1</sup> polybrene (Sigma-Aldrich). TCR-transduced T cells were expanded by stimulation with anti-CD3/CD28 Dynabeads (500,000 beads 10<sup>-6</sup> cells; Life Technologies) and IL-2 (50 IU ml<sup>-1</sup>). Thereafter, TCR-transduced T cells were depleted of nonengineered T cells by magnetic-activated cell sorting (MACS) as previously described<sup>8</sup>. This depletion protocol establishes a predominantly αβ TCR<sup>-</sup> population (Extended Data Fig. 4a), which has been shown to result in complete loss of alloreactivity (Extended Data Fig. 1e)<sup>45</sup>. To separate CD4<sup>+</sup> and CD8<sup>+</sup> TEGs and LM1s, we performed positive selection using either CD4 or CD8 Microbeads (Miltenyi Biotech) following the manufacturer's instructions. After incubation with magnetic microbeads, cells were applied to LS columns and CD4<sup>+</sup> or CD8<sup>+</sup> TEGs or LM1s were selected by MACS. After the MACS selection procedure, Vγ9/Vδ2 TCR<sup>+</sup> CD4<sup>+</sup> or Vγ9/Vδ2 TCR<sup>+</sup> CD8<sup>+</sup> subsets of TEGs were stimulated every 2 weeks using a rapid expansion protocol<sup>8</sup> where TEGs were cultured in 'T cell culture medium' (RPMI-GlutaMAX supplemented with 2.5–10% human serum (Sanquin), 1% pen/strep and 0.5 M beta-2-mercaptoethanol) on a feeder cell mixture comprising sublethally irradiated allogenic PBMCs, Daudi and LCL-TM in the presence of IL-2

(50Uml<sup>-1</sup>), IL-15 (5 ng ml<sup>-1</sup>; both R&D Systems) and PHA-L (1 µg ml<sup>-1</sup>; Sigma-Aldrich). To monitor the purity of CD4<sup>+</sup> and CD8<sup>+</sup> TEGs, as well as the absence of allogenic irradiated feeder PBMCs, cells were analyzed weekly by flow cytometry before functional assays using the antibodies anti-pan γδTCR-PE (Beckman Coulter), anti-αβTCR-FITC (eBioscience) anti-CD8-PerCP-Cy5.5 (Biolegend) and anti-CD4-APC (Biolegend). TEGs of purity <90% were reselected as described above. TEGs were used for coculture assays 4–5 days after the last IL2/IL15/PHA-L stimulation.

### Live-cell imaging of T cells and organoid cocultures

Engineered T cells (20,000) were cocultured with normal organoids, PDOs or control cell lines (Daudi or HL-60) in an effector/tumor cell (E:T) ratio of 1:30 or 1:25 (only for Fig. 4d,e and Extended Data Fig. 5a). CD4<sup>+</sup> and CD8<sup>+</sup> TEGs were mixed in a 1:1 ratio immediately before plating. Cells were incubated in 96-well, glass-bottom SensoPlates (Greiner) in 200 µl of 'coculture medium': 50% type 1 organoid culture medium, 50% 'TEG assay medium' (RPMI-GlutaMAX supplemented with 10% fetal calf serum and 1% pen/strep), 2.5% BME and pamidronate for the accumulation of the phosphoantigen IPP to stimulate tumor cell recognition<sup>8</sup> (1:2,000). Coculture medium was supplemented with both NucRed Dead647 (two drops ml<sup>-1</sup>; Thermo Fisher) and TO-PRO-3 (1:3,000; Thermo Fisher) for fluorescent labelling of living and dead cells ('Imaging medium'). The combination of NucRed Dead647 and TO-PRO-3 labels dead cells when excited with a 633-nm laser and living cells with a 561-nm laser (Extended Data Fig. 1a,b). Both were combined to achieve the optimal fluorescent intensity ratio between dead and living cells for live-cell imaging. Before coculture, TEGs were incubated with eBioscience Cell Proliferation Dye eFluor 450 (referred to as eFluor-450; 1:4,000; Thermo Fisher) in PBS for 10min at 37 °C to fluorescently label all Tcells. When CD4<sup>+</sup> and CD8<sup>+</sup>TEGs were simultaneously imaged, both eFluor-450 and Calcein AM (1:4,000; Thermo Fisher) were used to label the different TEG subsets in PBS for 10min at 37 °C. For NCAM1 prelabelling experiments, a combination of eFluor-450 (1:4,000; Thermo Fisher) and Hilyte-488-conjugated NCAM1 nanobodies (1:400; QVQ) was used to label CD8<sup>+</sup> TEGs in PBS for 20min at 37 °C before coculture. The plate was placed in a LSM880 (Zeiss Zen Black Edition v.2.3) microscope containing an incubation chamber (37 °C, 5% CO<sub>2</sub>) and incubated for 30min to ensure settling of TEGs and organoids at the bottom of the well. The plate was imaged for up to 24h with a Plan-Apochromat ×20/0.8 numerical aperture dry objective with the following settings: online fingerprinting mode, bidirectional scanning, optimal Z-stack step size, Z-stack of 60µm in total and time series with either a 30-min interval (up to 60 conditions simultaneously; resolution 512×512) or a 2-min interval (up to four or ten conditions simultaneously; resolution 512×512 and 200×200, respectively). To minimize photobleaching of NCAM1-prelabelled TEGs, the 488-nm laser was activated during only one Z-stack each hour within the first few hours of

imaging. Directly after imaging, production of IFN- $\gamma$  in the supernatant was quantitated using an ELISA-ready-go! Kit (eBioscience) and cell pellets were used to measure organoid viability with the CellTiter-Glo Luminescent Cell Viability Assay (Promega).

### IFN- $\beta$ stimulations

PDOs were harvested as described above and incubated in 96-well, round-bottom culture plates (Thermo Fisher) in 100  $\mu$ l of type 1 organoid culture medium, supplemented with 2.5% BME and with or without the presence of 100  $\text{pg ml}^{-1}$  recombinant human IFN- $\beta$  (Peprotech). After 24h of incubation (37 °C, 5% CO<sub>2</sub>), TEGs or LM1s were added to either IFN- $\beta$ -preincubated or unstimulated organoids (E:T ratio 1:30) in 100  $\mu$ l of TEG assay medium, supplemented with 2.5% BME and pamidronate (1:1,000) and with or without the presence of 100  $\text{pg ml}^{-1}$  recombinant human IFN- $\beta$  (Peprotech). Medium without Tcells was added for 'organoid only' controls. After 16h of incubation (37 °C, 5% CO<sub>2</sub>), plates were used to measure organoid viability using the CellTiter-Glo Luminescent Cell Viability Assay.

### In vivo targeting by TEGs

Adult female NSG mice (15–16weeks old) received sublethal total body irradiation (1.75Gy) and subcutaneous implantation of a  $\beta$ -estradiol pellet (Innovative Research of America) on day -1. On day 0, PDOs ( $1 \times 10^6$  13T or  $0.5 \times 10^6$  169M organoid cells in 100 $\mu$ l of BME per mouse) were prepared as described previously<sup>43</sup> for subcutaneous injection in the right flank on day 0, and mice received two injections of 107TEGs or TEG011 mock cells on days 1 and 6 in pamidronate (10mg  $\text{kg}^{-1}$  body weight) as previously reported<sup>7</sup>. On day 1, together with the first Tcell injection, all mice also received  $0.6 \times 10^6$  IU of IL-2 (Proleukin, Novartis) in incomplete Freund's adjuvant (IFA; MD Bioproducts) subcutaneously. Tumor volume was measured once per week using a digital caliper and calculated by the following formula:  $0.4 \times (\text{length} \times \text{width}^2)$ . Mice were monitored at least twice per week for weight loss and clinical appearance scoring (scoring parameters included hunched appearance, activity, fur texture, piloerection and respiratory/breathing problem). Humane endpoint was reached either when mice experienced 20% weight loss from initial weight, tumor volume reached 2  $\text{cm}^3$  or when a clinical appearance score of 2 was reached for an individual parameter or an overall score of 4. In no case was the tumor burden exceeded.

### Image processing

For 3D visualization, cell segmentation, extraction of statistics and time-lapse videos were processed with Imaris (Oxford Instruments) v.9.2–9.5. The Channel Arithmetics Xtension was used to create new channels for specific identification of organoids (live and dead) and eFluor-450-labelled or calcein AM-labelled Tcells (live and dead) and to

exclude cell debris. The Surface and ImarisTrack modules were used for object detection and automated tracking of both Tcells (autoregressive motion) and organoids ('connected components' or no tracking). The Distance Transformation Xtension was used to measure the distance between TEGs and organoids, with thresholds for defining organoid–Tcell interactions visually determined. For tracked TEGs, time-lapse data containing the coordinates of each cell, the values of cell speed, mean square displacement, distance to organoids and dead cell dye channel intensity were exported. For experiments with NCAM1 prelabelling, the mean intensities of the NCAM1 channel per Tcell were exported. For tracked organoids, time-lapse data containing the coordinates of each organoid, the surface area, volume and mean dead cell dye channel intensity were exported.

### **PDO killing dynamics**

To quantify the cell death dynamics of PDO cultures, >5,000 single organoids were analyzed at each time point (48 in total). The mean dead cell dye intensity within single organoid surfaces was quantified and rescaled to a range between 0 and 100 per experiment to normalize for variation in absolute dead cell dye intensity. To analyze whether organoid sensitivity to TEGs was dependent on initial organoid size, we compared the initial area (0h) of organoids killed by TEGs at 10h compared with the area of TEGs remaining alive at 10h.

### **T cell dynamics analysis and multivariate time series clustering**

For the analysis of TEG behavior over time, the following parameters were used: Tcell death, contact with organoids, speed, square displacement and interaction with other Tcells. For each Tcell time series, linear interpolation was used to estimate the values in several cases of missing time points. To compare time series independently of their length, cell tracks were cut to a length of 3.3h. Similarity between distinct cell tracks was measured using a strategy that allows for best alignment between time series, previously applied for mitotic kinetics<sup>49</sup> or temporal module dynamics comparisons<sup>50</sup>. A cross-distance matrix based on multivariate time series data was computed using the dynamic time-warping algorithm. To visualize distinct cell behaviors in two dimensions, dimensionality reduction on the multidimensional feature count table was performed by the UMAP method<sup>51,52</sup>. Clustering was performed using the k-means clustering algorithm with outlier detection. To confirm the identity of each cluster, Tcell cluster assignments were back-projected to visualize the surfaces and tracks of particular Tcell populations in the imaging dataset (Fig. 2a and Extended Data Figs. 3a,b and 4b).



## Cell behavior classification using a random forest classifier

For standardized integration of new experiments, we used a random forest classification approach<sup>53</sup> to relate cell behavior to the nine behavioral signatures that we found in our global TEG behavior atlas (Fig. 2b). To allow for inclusion of experiments with a low E:T ratio of 1:25, where the parameter of Tcell interaction would be influenced as compared with the standard E:T ratio of 1:30, the following parameters were used: Tcell death, organoid contact, speed and square displacement. The reference dataset used to build the global TEG behavior atlas was split into cell tracks for use as either a training dataset (95%) or a test dataset (5%). To reduce dimensionality, for each cell track four time series descriptive statistics were quantified and used to train the classifier. For numeric variables, the following measures were computed for each cell track: mean, median, the top 90% of the distribution and standard deviation. For binary values, such as contact with organoids, the mean was calculated as well as the mean and maximum of cumulative interaction. The random forest classifier was trained using 100 trees on the above-mentioned variables using the nine behavioral signatures as labels (Extended Data Fig. 3c,d). The test dataset was used to assess accuracy of the classifier and to determine in which behavioral signatures the errors occurred (Extended Data Fig. 3e). A slightly updated version of the classifier was used in Fig. 3

## Correlation between TEG behavior and organoid killing dynamics

To estimate the correlation between onset of death in individual organoids and engagement with Tcells belonging to the engaging clusters (CL7–9), we implemented a technique of sliding window correlation analysis previously used for functional brain connectivity<sup>54</sup> and genome analysis<sup>55</sup>. We calculated the Pearson correlation coefficient between the cumulative number of organoid contacts with TEGs from each cluster and the increase in dead cell dye intensity in each over a sliding window of 3h (Fig. 2f and Extended Data Fig. 3k).

## NCAM1 prelabelling quantification using 3D imaging data

Behavioral classification of NCAM1-prelabelled TEGs was performed as described above, by prediction of behavioral signatures with the random forest classifier. NCAM1<sup>+/-</sup> TEGs were identified based on an NCAM1 intensity threshold in individual TEGs, visually defined at the time points where the 488-nm laser was turned on. To ensure inclusion of true NCAM1<sup>-</sup> or NCAM1<sup>+</sup> TEGs, two intensity thresholds were defined.

## Pseudotime trajectory inference

Two experimental SORT-seq replicates of TEGs cocultured with 13T PDOs, generated as described above, were used for trajectory inference (Extended Data Fig. 6b).

Proliferating Tcells were excluded from the analysis because they did not show any dynamic inflammatory genes during analysis. Afterwards, the gene expression table was log normalized with a 10,000 scaling factor. Shared nearest-neighbor, graph-based clustering was done as described above at a resolution of 2. Based on marker gene expression of CD8, CD4 and IL17RB<sup>56</sup>, TEGs were subclustered into three subtypes: IL17RB<sup>-</sup>CD8<sup>+eff</sup>, IL17RB<sup>-</sup>CD4<sup>+eff</sup> and IL17RB<sup>+</sup>CD4<sup>+mem</sup>. Downstream analyses were performed on each subset separately and compared with each other where mentioned. The RunFastMNN function from the SeuratWrappers package was utilized to correct for batch effects between the two SORT-seq replicates. We used the package Monocle3 (ref.<sup>57</sup>) to infer the pseudotime trajectory and significantly dynamic genes for each Tcell subtype. For each cell subtype, either no-target control or nonengaged<sup>Enriched</sup> TEGs were designated as the root of the trajectory. To acquire comparable results from both Seurat and Monocle3 packages, the FastMNN batch-corrected UMAP coordinates were imported and used throughout the trajectory analysis in Monocle3. In IL17RB<sup>-</sup>CD4<sup>+eff</sup> and IL17RB<sup>+</sup>CD4<sup>+mem</sup> subtypes, Monocle identified no-target control cells as a separate partition. To have all cells along with a single pseudotime spectrum, we added maximum pseudotime values of no-target control Tcells to pseudotime values of remaining cells in that subtype. For all TEG subtypes, significant dynamic genes along with the pseudotime trajectory were calculated and identified using Monocle3's graph\_test function, with  $1 \times 10^{-20}$  *q*-value as the significance cutoff. Afterwards, using both k-means clustering and visual inspection of gene behavior over the pseudotime, TEGs were clustered into subclusters of similar pattern (CL1–8; Fig. 5g). The expression profile of the genes, along with the pseudotime trajectory, was plotted using the package pheatmap<sup>58</sup> using row-scaled (z-score) expression values. Smoothed gene behavior was calculated and visualized recruiting the gam smoothing function in the ggplot2 package<sup>59</sup>.

### Behavior signature inference over pseudotime

To align pseudotime inference with the different behavioral signatures that we identified with BEHAV3D, we built a probability map distribution for different behavioral signatures over the pseudotime based on the fundamental principle of transitivity of probabilistic distribution (Fig. 5f). We defined three states of cells quantified by different methods:

Behavioral\_signatures ( $B_{sig}$ ): (Static, Lazy, Medium scanner, Scanner, Super scanner, Tickler, Engager, Super engager). Behavioral signatures of cells identified by imaging (Fig. 5b).

- Experimental\_engagement\_state ( $Exp_{eng}$ ): (No-target control, Nonengaged, Nonengaged<sup>enriched</sup>, Engaged, Super engager). Cell distribution among different experimental conditions (Fig. 5a).

- UMAP\_cluster ( $U_{cl}$ ): (1...X). Cell assignment to distinct clusters grouping cells of similar gene expression. Shared nearest-neighbor, graph-based clustering was repeated several times using the Seurat package FindNeighbors and FindClusters functions with resolution in the range 1–7. From these three different cell states, the following information was quantified:

- $p(B_{sig}|Exp_{eng})$ : for each Experimental\_engagement\_state we quantified the probability distribution of each Behavioral\_signature (Fig. 5f). This was achieved by reproducing the Experimental\_engagement\_states in silico on our imaging data. These values were calculated separately for CD4<sup>+</sup> and CD8<sup>+</sup> TEGs.

- $p(Exp_{eng}|U_{cl})$ : for each UMAP\_cluster, we quantified the probability of each Experimental\_engagement\_state belonging to this cluster.

Given these probabilities, we then quantified for each Tcell the probability distribution of each unique Behavioral\_signature in each UMAP\_cluster using the equation:

$$p(B_{sig}|U_{cl}) = \sum_{Exp_{eng}} p(B_{sig}|Exp_{eng}) \times p(Exp_{eng}|U_{cl})$$

As a result, each cell was assigned a certain probability distribution for different behavioral signatures. To refine the probability map, the same process was repeated for seven runs with different cluster sizes and final probability distributions were averaged per cell. Note that, for cells belonging to the No-target control Experimental\_engagement\_state, a Behavioral\_signature called No-target control was assumed. Given that the nonengaged behavioral signatures (Static, Lazy, Slow scanner, Medium scanner, Super scanner) exhibited an identical probability map, their values were plotted together. For visualization purpose, extreme outlier values of skewed distributions were transformed to a maximal cutoff value. Based on the probability distribution of different behavioral signatures, pseudotime was divided into four stages—Baseline (no organoids), Environmental stimuli, Short engagement and Prolonged engagement—for each TEG subtype (CD8<sup>eff</sup>, CD4<sup>eff</sup> and CD4<sup>mem</sup>).

### Serial killer gene signature analysis

Genes of CL7 (Fig. 5g and Supplementary Tables 4 and 5) were analyzed to identify a unique signature for killer TEGs. Sixty-one of 83 genes comprising this cluster were common to TEGs incubated with 13T and 10T organoids and underwent extensive literature curation to identify those with a known role in Tcell cytotoxicity, Tcell biology (not related to cytotoxicity), morphological plasticity or other processes such as GTPase signaling, ribogenesis and transcriptional regulation.

## Cytotoxic in vivo T cell signature definition and projection on TEGs

To generate a signature gene set for cytotoxic CD8<sup>+</sup> T cells in samples from patients with BC, we downloaded two publicly available datasets from GEO (accession nos. GSE114724 (ref.<sup>40</sup>) and GSE110686 (ref.<sup>41</sup>)). Raw data were downloaded and analyzed with Seurat, using the same procedure utilized for TEG data processing. Clusters were identified and named using the marker genes defined in the study of Savas et al.<sup>41</sup>. From the study of Azizi et al.<sup>40</sup>, only TILs were used for analysis. Clusters were generated with a resolution of 0.9. For the Azizi and Savas studies, two marker gene lists were identified for cytotoxic CD8<sup>+</sup> T cells (based on the 2,000 variable features and an average log(fold change) cut off of 0.3; Supplementary Table 6). The overall enrichment of the identified gene sets for each study was calculated using VISION60 and visualized on top of UMAP cell embeddings for each study. In addition, the overall enrichment of in vivo identified gene sets was projected on the UMAP of TEGs. For the following methods we refer to Supplementary Protocols: primary DMG patient-derived lines and head and neck cancer PDO cultures, cell lines, WT1 T cells, ROR1 CAR T cells, flow cytometry analysis of NCAM1 and ROR1 expression, sorting of NCAM1<sup>-/+</sup> TEGs, T cell serial killing capacity analysis, PDO bulk RNA-seq, SORT-seq sample preparation, SORT-seq library preparation and sequencing, mapping and quantification of SORT-seq data, SORT-seq and 10X Genomics data integration and TEG subpopulation analysis, differential gene expression analysis of TEGs cocultured with distinct PDO cultures and gene set enrichment analysis.

### Statistics and reproducibility

Statistical analysis was performed using either R or Prism v.7 software (GraphPad), and results are represented as mean ± s.e.m. unless indicated otherwise; *n* represents independent biological replicates. Two-tailed unpaired *t*-tests were performed between two groups unless indicated otherwise. Pearson correlation was used for paired comparison among three different readouts (IFN- $\gamma$  production, cell viability and live imaging). For live-cell imaging, the increase in dead cell dye between the first and last time points was used as a measure. To compare tumor volumes in mice treated with TEGs or TEG001 mock cells, two-way analysis of variance (ANOVA) with repeated measures was performed. To compare frequencies of different behavioral signatures among PDOs, a Pearson's chi-squared test was applied. To compare the percentage of dead organoids when TEGs were cocultured with different PDOs, one-way ANOVA followed by Bonferroni correction was performed. To estimate the change in correlation between PDO death dynamics and cumulative contact with TEGs for different behavioral signatures, data were fitted to a linear mixed model with experimental replicate as the random effect to account for variation between them. For cell type enrichment analysis of TEG first and second action after engagement, a hypergeometric test was used (Fisher's exact test). For comparisons of percentages of distinct TEG subtypes in the

same well (CD4<sup>+</sup> versus CD8<sup>+</sup> or NCAM<sup>+</sup> versus NCAM), for each behavioral signature data were fitted to a linear regression model with each individual replicate set as the random effect to account for variation between them. For comparisons of percentages between different Tcell lines (different wells), the standard deviation of the difference between mean cluster percentages for pairs of Tcell lines was calculated by taking the square root of the sum of the variances of both separate distributions (Fig. 3j). For each fitted model, ANOVA was computed with an F-test. For comparison of IFN- $\beta$  treatment, paired *t*-tests were performed. To ensure global TEG behavior atlas (Fig. 2a,b) reproducibility, we pooled 22 different imaging datasets comprising TEGs and LM1 cells cocultured with 13T or 100T organoids. Supplementary Table 8 summarizes the value of *n* per condition for Figs. 2b, 3f–j and 6e–g and includes statistical test details from Fig. 2f.

### Reporting summary

Further information on research design is available in the Nature Research Reporting Summary linked to this article.

### Data availability

RNA-seq data of this study have been deposited in the Gene Expression Omnibus under accession no. GSE172325 (<https://www.ncbi.nlm.nih.gov/ezproxy.u-pec.fr/geo/query/acc.cgi?acc=GSE172325>). Imaging data used for the behavioral reference map have been deposited in the BioImage Archive under accession no. S-BIAD448 (<https://www.ebi.ac.uk/biostudies/studies/s-biad448>).

### Code availability

We provide the BEHAV3D framework as a compilation of Rscripts on github (<https://github.com/alievakrash/BEHAV3D>).

### Online content

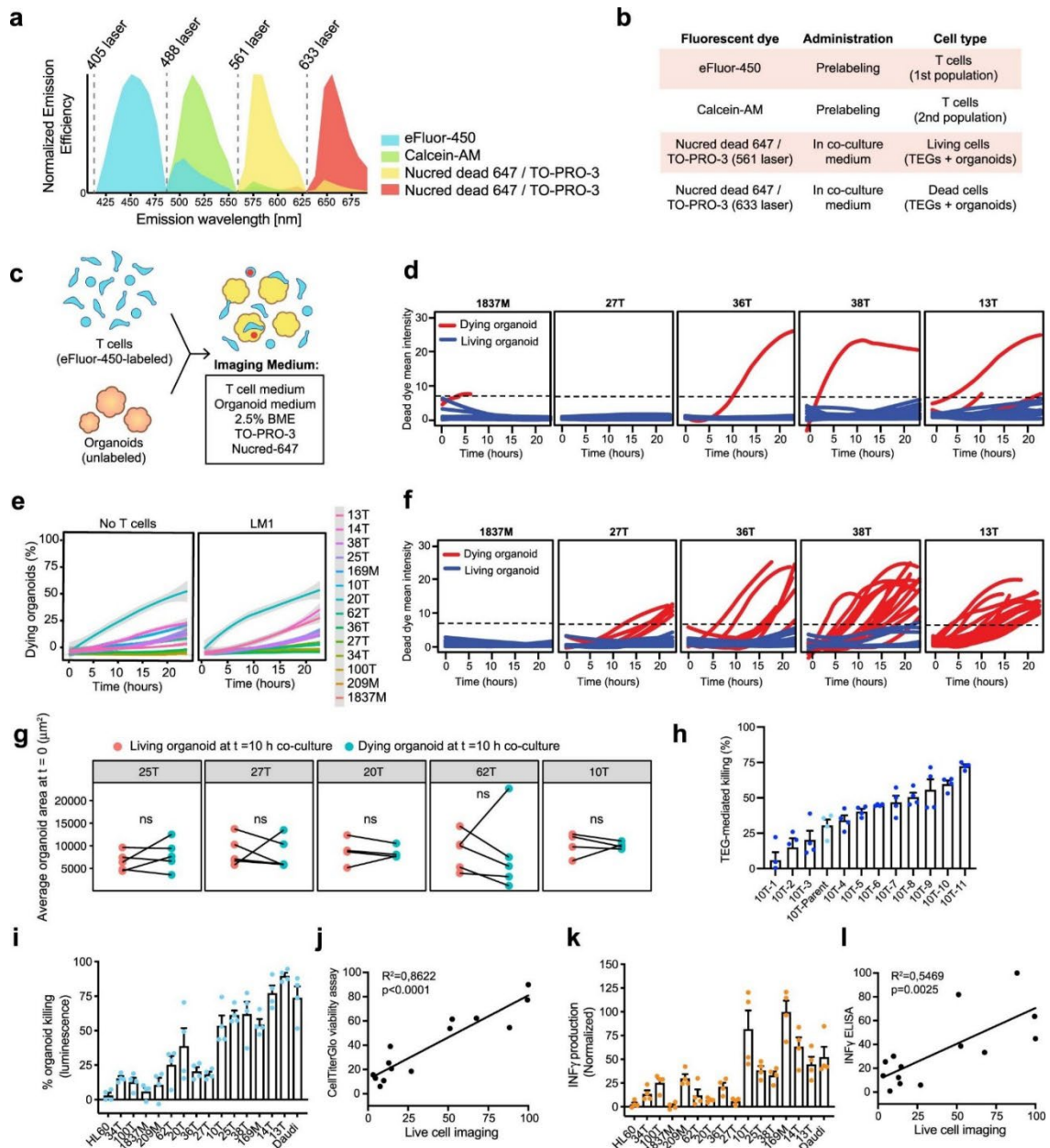
Any methods, additional references, Nature Research reporting summaries, source data, extended data, supplementary information, acknowledgements, peer review information; details of author contributions and competing interests; and statements of data and code availability are available at <https://doi.org/10.1038/s41587-022-01397-w>.

**Received: 26 May 2021; Accepted: 14 June 2022; Published online: 25 July 2022**

## References

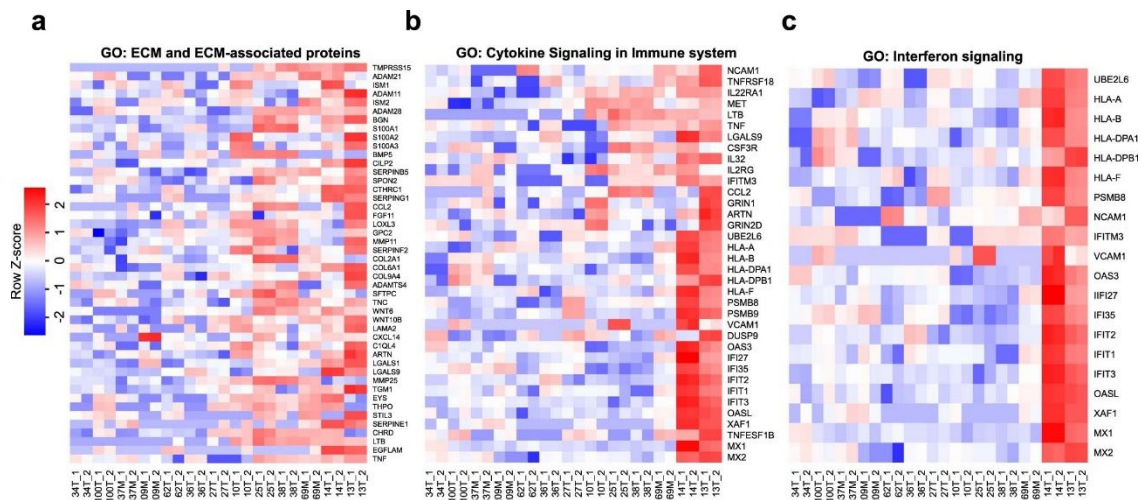
43. Dekkers, J. F. et al. Long-term culture, genetic manipulation and xenotransplantation of human normal and breast cancer organoids. *Nat. Protoc.* 16, 1936–1965 (2021).
44. Broutier, L. et al. Culture and establishment of self-renewing human and mouse adult liver and pancreas 3D organoids and their genetic manipulation. *Nat. Protoc.* 11, 1724–1743 (2016).
45. Straetemans, T. et al. Untouched GMP-ready purified engineered immune cells to treat cancer. *Clin. Cancer Res.* 21, 3957–3968 (2015).
46. Straetemans, T. et al. GMP-grade manufacturing of T cells engineered to express a defined gammadelta TCR. *Front. Immunol.* 9, 1062 (2018).
47. Kierkels, G. J. J. et al. Identification of a tumor-specific allo-HLA-restricted gammadeltaTCR. *Blood Adv.* 3, 2870–2882 (2019).
48. Scheper, W., Grunder, C., Straetemans, T., Sebestyén, Z. & Kuball, J. Hunting for clinical translation with innate-like immune cells and their receptors. *Leukemia* 28, 1181–1190 (2014).
49. Cai, Y. et al. Experimental and computational framework for a dynamic protein atlas of human cell division. *Nature* 561, 411–415 (2018).
50. Schafer, S. T. et al. Pathological priming causes developmental gene network heterochronicity in autistic subject-derived neurons. *Nat. Neurosci.* 22, 243–255 (2019).
51. Ali, M. J., Xianghua, W. & Williams, X. M. TimeCluster: dimension reduction applied to temporal data for visual analytics. *Vis. Comput.* 35, 1013–1026 (2019).
52. Becht, E. et al. Dimensionality reduction for visualizing single-cell data using UMAP. *Nat. Biotechnol.* 37, 38–44 (2018).
53. Breiman, L. Random forests. *Mach. Learn.* 45, 5–32 (2001).
54. Preti, M. G., Bolton, T. A. & Van De Ville, D. The dynamic functional connectome: state-of-the-art and perspectives. *Neuroimage* 160, 41–54 (2017).
55. Burke, M. K. et al. Genome-wide analysis of a long-term evolution experiment with *Drosophila*. *Nature* 467, 587–590 (2010).
56. Terrier, B. et al. Interleukin-25: a cytokine linking eosinophils and adaptive immunity in Churg–Strauss syndrome. *Blood* 116, 4523–4531 (2010).
57. Cao, J. et al. The single-cell transcriptional landscape of mammalian organogenesis. *Nature* 566, 496–502 (2019).
58. Kolde, R. Package ‘pheatmap’.  
<https://mran.microsoft.com/snapshot/2015-09-04/web/packages/pheatmap/pheatmap.pdf> (2015).
59. Wickham, H. *ggplot2: Elegant Graphics for Data Analysis* (Springer, 2016).
60. DeTomaso, D. et al. Functional interpretation of single cell similarity maps. *Nat. Commun.* 10, 4376 (2019).

## Extended Data



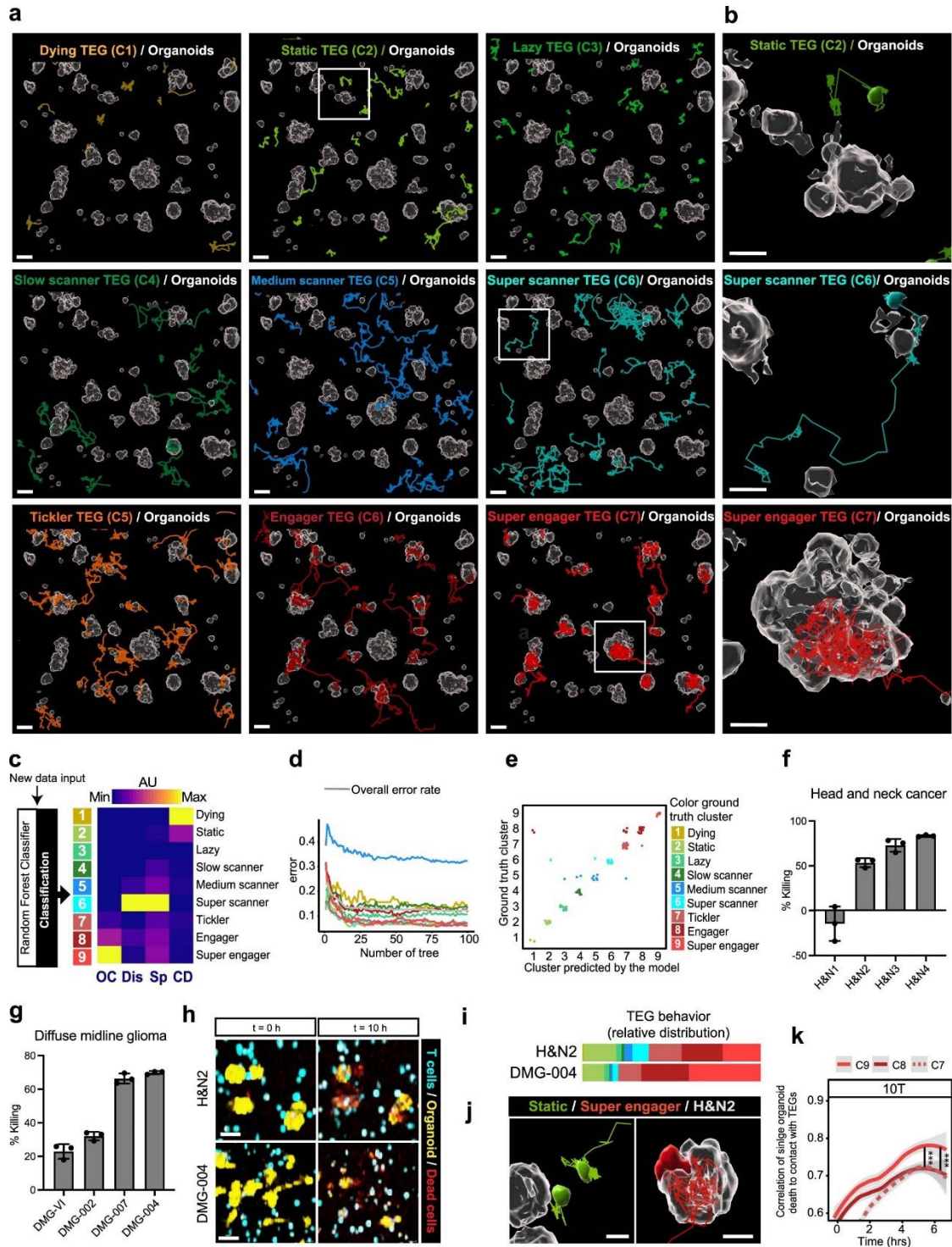
**Extended Data Figure 1. Multi-spectral 3D imaging quantification of organoid killing.** (a) Emission spectra of the indicated fluorescent real-time cell dyes separately imaged by multispectral imaging with the lambda mode using the indicated lasers. (b) Overview of fluorescent real-time cell dyes for labelling the indicated cell types. (c) Schematic representation of the co-culture setup. (d) Quantification of death of individual PDOs in the presence of control TEGs expressing a mutated V $\psi$ 9/V82 TCR (LM1s). (e) Quantification of the percentage of dying single organoids (% of total) over time for each PDO co-cultured with LM1 control TEGs (right panel) or in the absence of T cells (left panel) ( $n=4$  independent experiments; mean). (f) Quantification of death of individual PDOs in the presence of TEGs. (g) Comparison of average size of PDOs ( $t=0$  of TEG co-culture) that were either dying or alive at 10 h of co-culture with TEGs for the indicated PDO lines. Data corrected for control LM1 T cell responses.  $n=4$  (20 T and 10 T) or 5 (25 T, 27 T, 62 T) independent experiments. Two-tailed unpaired  $t$  test: NS =  $p > 0.05$ . (h) Quantification of killing of 11 10 T PDO clonal lines as well as the parental culture using a CellTiter-Glo<sup>®</sup> viability assay, upon overnight co-culture of organoids with TEGs in the presence of pamidronate, ( $n=3$  (10T-1 and 10T-2) or 4 (all other clones) independent experiments; mean  $\pm$  s.e.m.). (i-l) Quantification of

PDO targeting using a CellTiter-Glo® viability assay (i) or INF $\psi$  ELISA assay (k), upon 24 h co-culture of organoids with TEGs in the presence of pamidronate, and Pearson correlation plots between the outcomes of live cell imaging compared to CellTiter-Glo® measured viability (j). ( $F = 75.05$ ,  $DFn=1$ ,  $DFd=12$ ,  $95\% \text{ CI } [0.5184, 0.8668]$ ,  $p < 0.0001$ ) and INF $\psi$  ELISA (l) ( $F = 14.49$ ,  $DFn=1$ ,  $DFd=12$ ,  $95\% \text{ CI } [0.257, 0.9452]$ ,  $p = 0.0025$ ). Data corrected for control LM1 T cell responses. ( $n = 4$  independent experiments; mean  $\pm$  s.e.m.). (d,f: Single organoids that crossed the mean dead cell dye intensity threshold of 7 (dashed lines) are considered dying (red lines)).

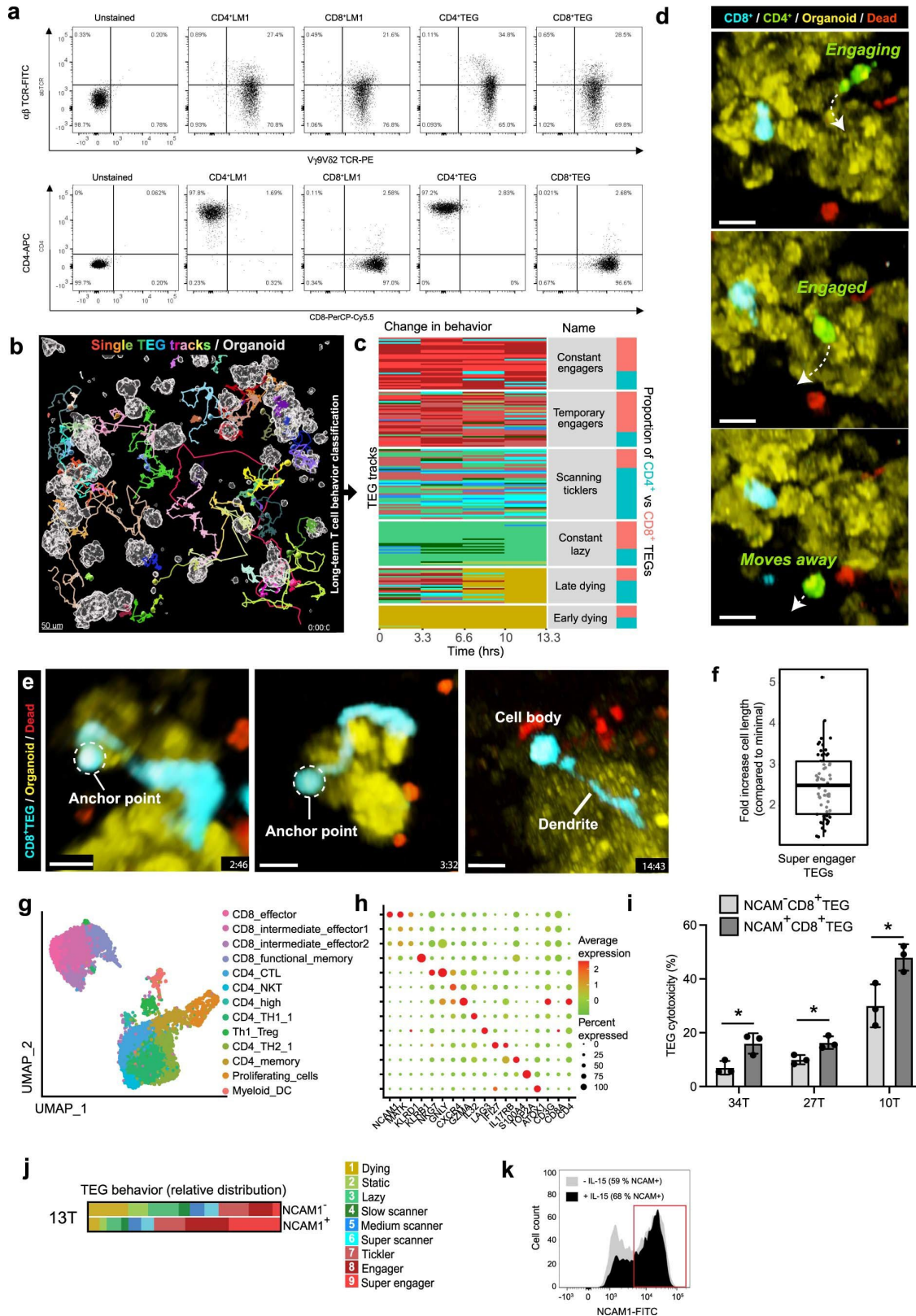


**Extended Data Figure 2. GO terms associating with PDO sensitivity to TEGs.** (a-c) Heatmap showing normalized gene expression (Row Z-score) for the indicated PDOs harvested at two different time points in culture (experimental replicates ‘\_1’ and ‘\_2’). GO terms ‘extracellular matrix (ECM) and ECM-associated proteins’ (a), ‘cytokines signaling in immune system’ (b) and ‘interferon signaling’ (c) are presented, which were identified in the gene ontology enrichment analysis of differentially expressed genes between the six highest versus six lowest TEG-sensitive organoid cultures from Fig. 1h.





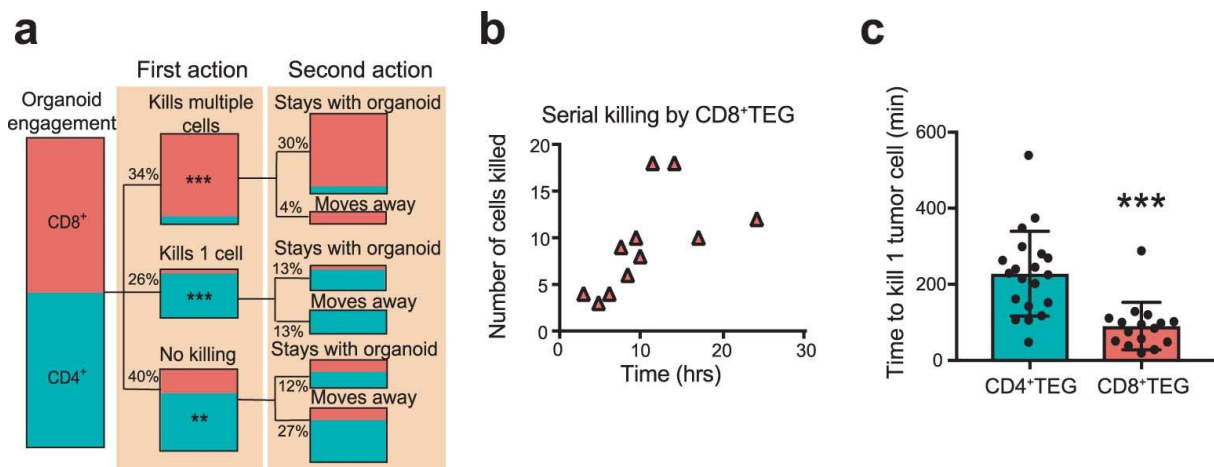
**Extended Data Figure 3. Properties of the 9 TEG behavioral clusters, random forest classification and head and neck cancer and diffuse midline glioma PDO targeting.** (a,b) Representative multispectral overview images (a; scale bars, 50  $\mu\text{m}$ ) and enlarged sections for clusters of interest (b; scale bars, 20  $\mu\text{m}$ ) of 13 T organoids co-cultured with TEGs classified into 9 different behavioral clusters.  $n = 11$  independent experiments. (c) Schematic representation of the Random Forest classification pipeline and the resulting heatmap showing relative intensity values of T cell features indicated for each cluster resulting from the classification of the experiment in Fig. 2c. (OC, organoid contact; Dis, square displacement; Sp, speed; TI, T-cell interaction; CD, cell death) (d,e) Error rate of the training data per cluster and overall for all trees (d) and correlation plot between ground truth cluster classification and predicted cluster classification (e). Color represents ground truth cluster. (f,g) Quantification of head and neck cancer (H&N) PDO (f) or diffuse midline glioma (DMG) PDO (g) targeting using a CellTiter-Glo<sup>®</sup> viability assay upon overnight co-culture with TEGs in the presence of pamidronate. Data corrected for control LM1 T cell responses. ( $n = 3$  independent wells, representative graph of  $n = 3$  independent experiments; mean  $\pm$  s.d.). (h) Images of H&N cancer & DMG PDO cultures (yellow) showing killing by TEGs (blue) at the indicated time points of imaging. Dead cells in red. Scale bars, 50  $\mu\text{m}$ . (i) Behavioral cluster distribution of TEGs co-cultured with the indicated PDOs.  $\chi^2$  test;  $p = 1.132\text{e-}08$ . (j) Representative multispectral images of H&N2 PDOs (rendered in grey) co-cultured with TEGs classified as static (C2; green) or super engager (C9; red), Scale bars, 15  $\mu\text{m}$ . (k) Change in correlation between 10 T organoid death dynamics (measured as increase in dead cell dye) and cumulative contact with TEGs (from behavior clusters 7-9). Data is represented as mean correlation per timepoint of all single organoids ( $n = 4$  independent experiments). Linear mixed model fitting with each experimental replicate as a random effect: C9 vs C8,  $p < 2\text{e-}16$ ; C9 vs C7,  $p < 2\text{e-}16$ . (h-j: representative data of  $n = 3$  independent experiments).



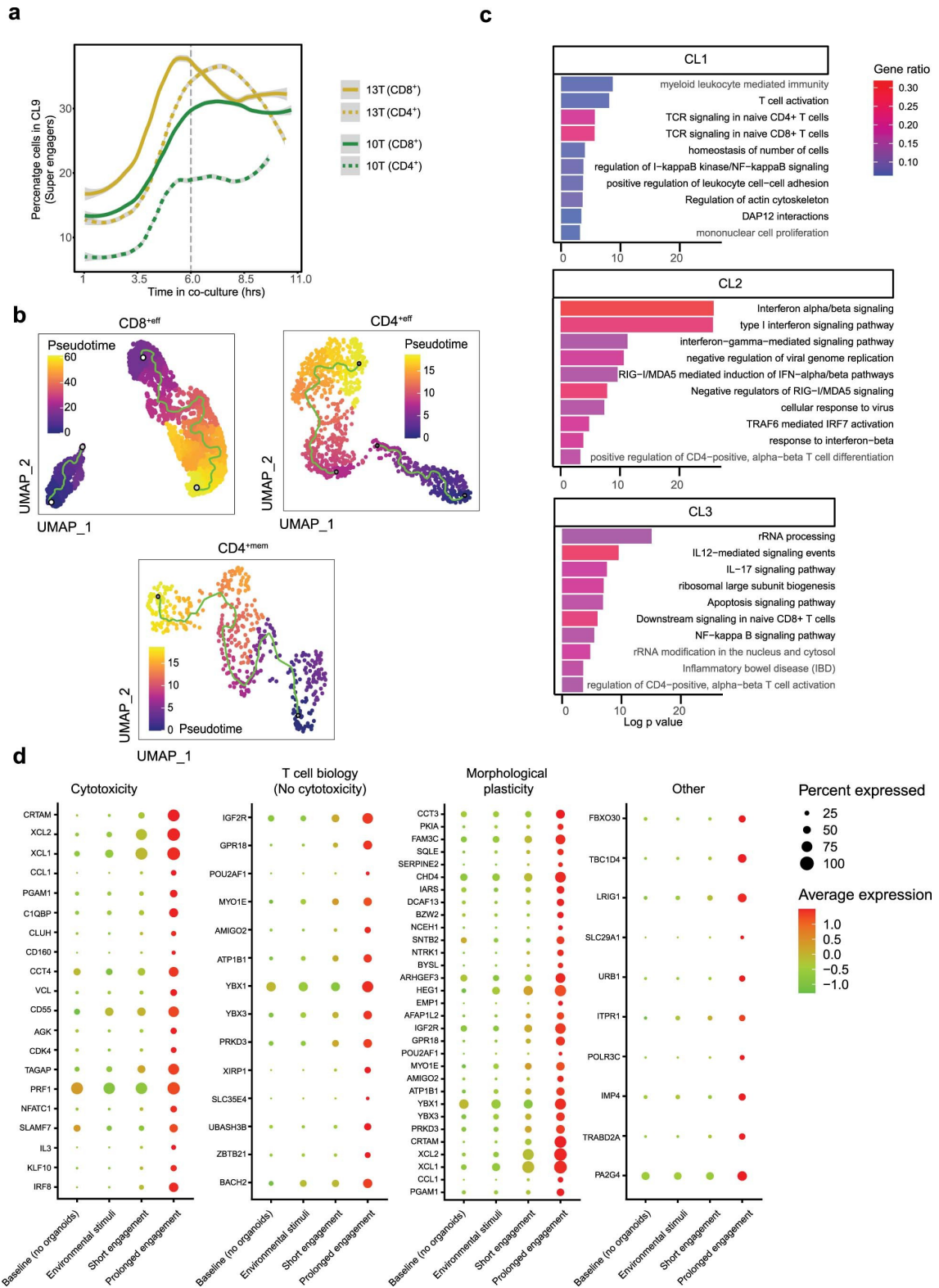
4

**Extended Data Figure 4. Unique targeting features of CD4<sup>+</sup> and CD8<sup>+</sup> TEGs and behavioral signatures in relation to NCAM1 expression.** (a) Representative FACS plots showing CD4, CD8,  $\alpha\beta$  TCR and V $\psi$ 9/V82 TCR expression for cultured CD4<sup>+</sup> and CD8<sup>+</sup> LM1s or TEGs. (b) Representative image of long-term tracking of TEGs in co-culture with 13 T organoids (grey surface rendering at t = 0) showing full tracks (up to 20 hrs);

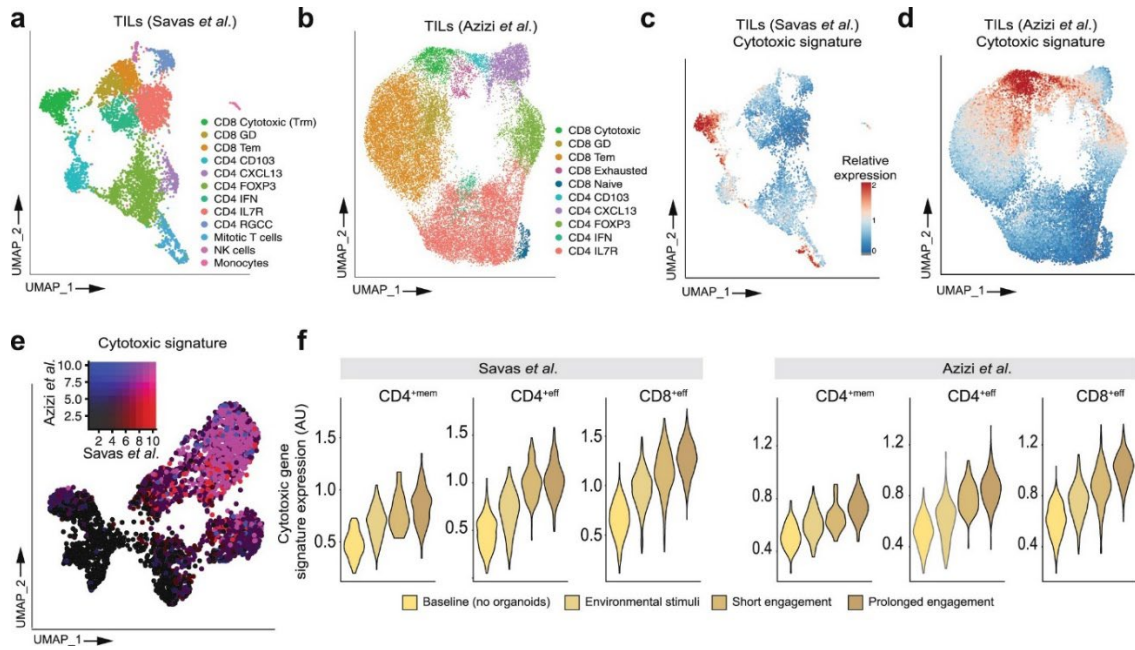
rainbow-colored). Scale bar, 50  $\mu\text{m}$ . (c) Time series color plot showing long-term tracks of TEGs (co-cultured with 13 T) and how they change their behavioral signature overtime for each time interval. (0-3.3 hrs; 3.3-6.6 hrs; 6.6-10 hrs; 10-13.3 hrs). Colors indicate cluster identity for each TEG (see j). Tracks were classified into 6 different groups (named according to their most distinct behavior) and the proportion of CD4<sup>+</sup>TEG and CD8<sup>+</sup>TEG is indicated per group. TEGs were pooled from 3 independent experiments. (d) CD4<sup>+</sup> TEG moving away from a 13 T organoid without killing. Scale bars, 20  $\mu\text{m}$ . (e) Images showing 13 T organoids and CD8<sup>+</sup> TEGs with defined anchor points. Scale bars, 10  $\mu\text{m}$ . (f) Quantification of fold increase in cell length. Individual cells pooled from 6 independent experiments. Boxplot depicts the median, first and third quartiles, whiskers extend 1.5 times from the interquartile range. (g) UMAP plot shows distinct TEGs subsets unexposed to PDOs, pooled from three independent experiments. (h) Gene-expression dot plot of a curated set of differentially expressed genes in each cell subpopulation. Rows depict cell subpopulations as in g, while columns depict genes. (i) Quantification of breast cancer PDO targeting using a CellTiter-Glo<sup>®</sup> viability assay upon overnight co-culture with sorted NCAM1<sup>-</sup>CD8<sup>+</sup>TEGs or NCAM1<sup>+</sup>CD8<sup>+</sup>TEGs. Data corrected for organoid only responses. Unpaired T test: 34 T  $p = 0,0263$ ; 27 T  $p = 0,0198$ ; 10 T  $p = 0,0289$ . (n = 3 individual wells, representative data of 3 independent experiments; mean  $\pm$  s.d.). (j) Relative behavioral cluster distribution of NCAM1<sup>-</sup>CD8<sup>+</sup> TEGs or NCAM1<sup>+</sup>CD8<sup>+</sup> TEGs co-cultured with 13 T PDOs. (k) FACS histogram plots showing NCAM1 expression in TEGs that were cultured in the absence (grey) or presence of IL-15 (black) for 10 days. (Representative data of 3 (b,d,e,k) or 4 (a) independent experiments).



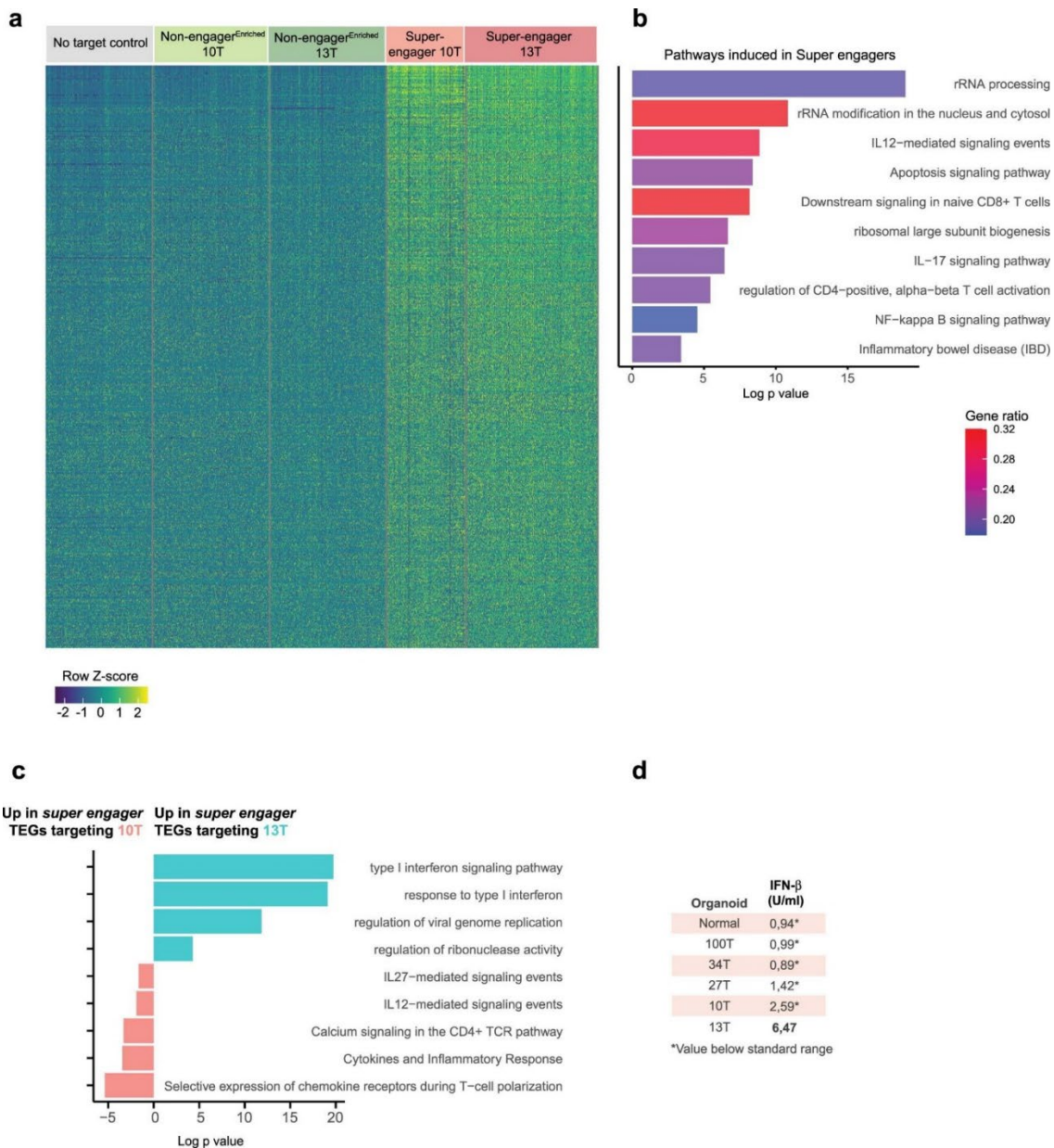
**Extended Data Figure 5. Analysis of TEG behavior and killing properties.** (a) Quantification of the first action and second action of CD4<sup>+</sup> and CD8<sup>+</sup> TEGs after they engaged with an organoid. (n = 3 independent experiments). Hypergeometric test was used to analyze cell type enrichment in each category. ‘Kills multiple cells’  $p < 0.0001$ ; ‘Kills one cell’  $p = 0.000015$ ; ‘No killing’  $p = 0.0018$ . (b) Quantification of the number of cells killed in a sequence by CD8<sup>+</sup>TEGs in time. (n=3 independent experiments). (c) Quantification of the time it takes to kill one 13 T tumor cell for CD4<sup>+</sup>TEGs and CD8<sup>+</sup>TEGs (n = 3 independent experiments).



**Extended Data Figure 6: Behavior-guided transcriptomics of TEGs co-cultured with 13T organoids. (a)** Dynamic change of the percentage of TEGs exhibiting *super engager* behavior (C9) over time in co-culture. Color denotes TEGs co-cultured with 13 T or 10 T organoids and line type CD4<sup>+</sup> (dashed) or CD8<sup>+</sup> (solid) TEGs. The 6 hrs time point was selected for single cell TEG sequencing (dashed grey line). **(b)** Separate UMAP embeddings showing inferred pseudo-time trajectory of CD8<sup>eff</sup>, CD4<sup>eff</sup> and CD4<sup>mem</sup> TEGs. Color scale represents the inferred pseudotime. **(c)** Functional enrichment analysis for biological processes and pathways from gene clusters (CL) that are downregulated (CL1), upregulated (CL3) or transiently expressed (CL2) over the pseudotime trajectory of TEGs targeting 13 T organoids. CL1-3 are represented in Fig. 5g. **(d)** Gene- expression dot plot of the 61 conserved genes composing the (serial) killer gene signature separated by function. Rows depict genes, while columns depict stage of targeting. Dot color gradient indicates average expression, while size reflects the proportion of cells expressing a particular gene.



**Extended Data Figure 7. Overlap between cytotoxic signature of tumor-infiltrating T cells and super engager TEG gene expression.** (a,b) UMAP embedding color-coded for different populations of tumor-infiltrating lymphocytes (TILs) isolated from human breast cancer tumor samples from the Savas *et al.*<sup>41</sup> (a; 310 genes) or Azizi *et al.*<sup>40</sup> (b; 543 genes) study. (c,d) UMAP embedding of TILs showing relative expression of a cytotoxic gene signature identified in the Savas *et al.* (c) or Azizi *et al.* (d) dataset. (e) UMAP embedding of TEGs enriched for different behaviors (see Fig. 5c-e) showing normalized gene expression projection of the Savas *et al.* or Azizi *et al.* cytotoxic signature. Colors represent the log<sup>2</sup> transformed normalized counts of genes. (f) Violin plots for different TEG subtypes showing expression of the cytotoxic gene signature identified in Savas *et al.* (left panel) or Azizi *et al.* (right panel). Colors indicate different stages of targeting.



**Extended Data Figure 8. Behavior-guided transcriptomics of TEGs co-cultured with 13T and 10T organoids.** (a) Heatmap showing normalized gene expression of behavior-enriched TEG populations co-cultured with 10 T or 13 T organoids, or cultured without PDOs (*No target control*). Columns represent cells ordered by TEG populations and rows represent the expression of genes. Shown are 534 genes induced upon prolonged organoid engagement (*super engagers*) in both 10 T and 13 T co-cultures from Fig. 6b. (b) Functional enrichment analysis (conserved biological processes and pathways) of genes induced in both 10T- and 13T-co-cultured *super engager* TEGs (shown in A). (c) Functional enrichment analysis of genes differentially expressed between 10T- and 13T-co-cultured *super engager* TEGs. Top differentially regulated biological processes and pathways are shown. (d) IFN- $\beta$  concentration measured for the different organoid cultures in Fig. 6e-g.







# CHAPTER

# 5

## **Efficacy of $\alpha\beta$ T cell based immunotherapies relies on CCR5 expression in both CD4+ and CD8+ $\alpha\beta$ T cells**

A. Cleven<sup>1\*</sup>, A.D. Meringa<sup>1\*</sup>, L. Gasull-Celades<sup>1</sup>, C. Schwenzel<sup>1</sup>, P.K. Derevianko<sup>3</sup>, E. van Vliet<sup>3</sup>, M.A. Huisman<sup>4</sup>, T. Aarts-Riemens<sup>1</sup>, L.D.C.E. Gatti<sup>1</sup>, L.E. van der Wagen<sup>1</sup>, A. Rios<sup>3</sup>, H. Snippert<sup>4</sup>, J. Roodhart<sup>4</sup>, D.X. Beringer<sup>1</sup>, M. de Witte<sup>1</sup>, T. Straetemans<sup>1</sup>, P. Brazda<sup>1</sup>, H. G. Stunnenberg<sup>3</sup>, O. Heidenreich<sup>3</sup>, V. Peperzak<sup>1</sup>, J. Kuball<sup>1,2†</sup> and Z. Sebestyén<sup>1†</sup>

\* Shared first authorship

† Shared senior authorship

<sup>1</sup>Centre of Translational Immunology, University Medical Center Utrecht,  
Utrecht University, The Netherlands

<sup>2</sup>Department of Hematology, University Medical Center Utrecht, The  
Netherlands

<sup>3</sup>Princess Máxima Center for Pediatric Oncology, The Netherlands

<sup>4</sup>Center for Molecular Medicine, University Medical Center Utrecht,  
Utrecht University, The Netherlands

*Manuscript in preparation*

## Abstract

In this study we explore strategies to improve  $\alpha\beta$ T cell infiltration within the tumor microenvironment (TME) in order to boost the efficacy of adoptive  $\alpha\beta$ T cell therapies in various malignancies. Infiltration of tumor-reactive  $\alpha\beta$ T cells, especially CD8+  $\alpha\beta$ T cells, correlates with improved clinical outcomes and responses to immunotherapies. Using *in vitro* models, we examined the infiltration of BCMA-targeting CAR  $\alpha\beta$ T cells (BCMA-CART) and BTN2/3-targeting  $\gamma\delta$ TCR (TEG) engineered  $\alpha\beta$ T cells, finding that  $\alpha\beta$ T cell infiltration was limited; particularly in the CD8+ T lymphocyte compartment. Chemokines including CCL4 were found to be essential for  $\alpha\beta$ T cell migration in the TME, with blocking of these chemokines showing a reduction in  $\alpha\beta$ T cell migration and tumor-specific killing. Furthermore, overexpressing the corresponding chemokine receptor CCR5 in tumor-reactive  $\alpha\beta$ T cells significantly improved infiltration capacity and tumor targeting of engineered immune cells. This study highlights the importance of improving  $\alpha\beta$ T cell infiltration for  $\alpha\beta$ T cell therapies and argues for the potential of CCR5 overexpression in CD8+  $\alpha\beta$ T cells for improving clinical outcomes, particularly in the treatment of solid malignancies.

## Introduction

Chimeric antigen receptor (CAR) or T cell receptor (TCR) engineered  $\alpha\beta$ T cells therapies have demonstrated remarkable success in the treatment of hematological malignancies in recent years<sup>1</sup>. Nonetheless, translating the success of these engineered  $\alpha\beta$ T cell treatments to solid tumors has been proven to be more challenging<sup>2</sup>. Solid tumors construct immune-excluded, local microenvironments that block the infiltration and activation of endogenous  $\alpha\beta$ T cells. This while cytotoxic  $\alpha\beta$ T cell infiltration in the TME is associated with a good prognosis for multiple cancer types such as breast, colorectal and various hematological malignancies<sup>3-5</sup>. Furthermore, strong infiltration of specifically activated CD8+ T-cells correlate to favorable responses to checkpoint blockade treatments like targeting either PD-1 or CTLA-4<sup>6-7</sup>. In the case of TCR- or CAR - T cell therapies, similar correlations are observed where CD8+ T lymphocytes infiltration also correlates to better clinical responses and prognosis in patients<sup>8</sup>. These findings underscore the pivotal role of infiltrating, tumor-reactive  $\alpha\beta$ T cells play in providing effective clinical responses towards malignancies in patients.

However,  $\alpha\beta$ T cell infiltration in the tumor microenvironment is limited by an array of immunosuppressive mechanisms orchestrated by both the tumor and other cells residing in the surrounding TME<sup>9,10</sup>. Physical barriers such as a high-density extracellular matrix and irregular vasculature are frequently observed in TME of malignancies. Additionally, dysregulation in immune cell migration signalling; specifically the mismatch of the chemokine profile expressed in the TME and chemokine receptor expression profile of cytotoxic  $\alpha\beta$ T cells is a vital obstacle to overcome<sup>11</sup>. For instance, CCL2 expression by cancer-associated fibroblasts (CAF) has been reported to stimulate the proliferation of breast cancer cells<sup>12</sup> while CXCR2 and CXCR4 signalling in the metastatic lung niche allows for the recruitment of immunosuppressive MDSCs<sup>13</sup>. In contrast, clinical data of melanoma patients indicates that a lack of expression of the CCR5 ligands CCL4 and CCL5 correlates to limited infiltration of antigen-specific  $\alpha\beta$ T cells and thereby a reduced anti-melanoma immune response<sup>14</sup>. Presumably, the contribution of chemokines in the TME to pro- and anti-tumor immune responses will be context dependent, highlighting the overall complexity of chemokine receptor signaling in cancer. However, these findings provide a rationale for further investigating the role of chemokine receptors within the tumor microenvironment.

In this study,  $\alpha\beta$ T cell infiltration in the TME of both hematological and solid tumors was studied to identify pathways that could be engineered to boost  $\alpha\beta$ T cell infiltration. To this end, *in vitro* models of both tumor microenvironments were used to test BCMA-targeting CAR- $\alpha\beta$ T cells (BCM-CART) as well as BTN2/3-targeting  $\gamma\delta$ -TCR-engineered  $\alpha\beta$ T cells (TEG)<sup>15-17</sup>. Although partial tumor killing was observed in these models,  $\alpha\beta$ T

cell infiltration was limited. Specifically, CD8+ CAR and TEG cells were migrating to a lesser extent than their CD4+ counterparts. Upon overexpression of the CCR5 chemokine receptor on  $\alpha\beta$ T cells, CD8+ CAR and TEG  $\alpha\beta$ T cells were able to improve their infiltration in the TME of both solid and hematological malignancies. This improved  $\alpha\beta$ T cell infiltration led to a significant increase in tumor targeting in both hematological and solid tumor types.

## Materials and Methods

### Generation of engineered $\alpha\beta$ T cells

Primary PBMCs were isolated using Ficoll-Paque (GE Healthcare) from buffy coats of the Sanquin Blood Bank. Next,  $\alpha\beta$ T cells were isolated from primary PBMCs by activation via  $\alpha$ -CD3 (OKT3; Janssen-Cilag) and IL-2 (Clinigen).

$\alpha\beta$ T cells using the BCMA-CART or tumor-reactive  $\gamma\delta$ TCR were transduced according to previously published protocols<sup>18</sup>. In short, Gag-pol (HIT-60) and env (COLT-GALV) were transfected into Phoenix-Ampho cells combined with plasmids of either  $\gamma$  and  $\delta$ TCR chains<sup>18</sup> in the pMP71 vector or a previously described BMCA-CAR sequence<sup>19</sup> in the pBullet vector containing a neomycin resistance. Activated  $\alpha\beta$ T cells were transduced with the filtered viral supernatant produced by these phoenix-ampho cells combined with polybrene (Sigma-Aldrich).

After two transduction rounds,  $\alpha\beta$ T cells were selected under either neomycin (Merck) or puromycin (Merck) in the case of the BCMA-CART and CCR5 expressing cells respectively. Additionally, the  $\gamma\delta$ TCR transduced cells were magnetically depleted for non-transduced,  $\alpha\beta$ -TCR positive  $\alpha\beta$ T cells using the biotin-labeled anti- $\alpha\beta$ TCR antibody (BW242, Miltenyi Biotech) and  $\alpha$ -biotin magnetic beads (Miltenyi Biotech) on MD columns (Miltenyi Biotech) according to the manufacturer's protocol.

Subsequently, transduced  $\alpha\beta$ T cells were expanded on the rapid expansion protocol<sup>10</sup>. After expansion, cells were sorted for expression of either CD4 or CD8 by MACS selection using  $\alpha$ -CD4 and  $\alpha$ -CD8 microbeads (Miltenyi Biotech) and MS columns (Miltenyi Biotech) according to the manufacturer's protocol.

### Construction of the CCR5 construct

The DNA sequence of the wildtype CCR5 chemokine receptor<sup>20-21</sup> was synthesized by BaseClear and cloned into the pBullet vector containing a puromycin resistance. The restriction enzymes NcoI, BamHI and T4 ligase used for this cloning were provided by NEB. The CCR5-pBullet vector was included in the transfection mix of the phoenix-

ampho cells together with either plasmids containing the BCMA-CART or  $\gamma$  and  $\delta$ TCR chains for the BTN2/3-targeting  $\gamma\delta$ TCR as mentioned above<sup>10</sup>.

## Cell cultures

RPMI-8226, (ATCC), KG1a (ATCC) and patient-derived AML blasts were cultured in 10% FBS, 1% Penicillin Streptomycin containing RPMI(GlutaMax). HEK293F and  $\alpha\beta$ T cells were cultured in DMEM(GlutaMAX) with 10% FBS and 1% Pen-Strep. Mesenchymal stem cells were supplied by the Utrecht Cell Therapy Facility and cultured in 10% FBS, 1% Penicillin Streptomycin containing DMEM(GlutaMAX) supplemented with 0.2mM l-ascorbic acid (Bio-connect).

## Organoid cultures

Organoids derived from either breast or colon cancer were generated and cultured in Matrigel as previously described<sup>22-24</sup>. In short, organoids were cultured in Matrigel covered in DMEM(GlutaMAX) containing 10% FBS, 1% Pen-Strep and multiple growth factors. These organoids were isolated from the Matrigel using TrypLE Express and filtered through a 70  $\mu$ m cell strainer before being used in co-culture assays.

## *In vitro* malignant bone marrow niche models

The *in vitro* bone marrow models were generated as previously described<sup>15</sup>. In short, RPMI-8226 cells or patient-derived AML blasts were dyed using the Vybrant DiO dye and seeded together with Vybrant DiD (Thermo Fisher) dyed mesenchymal stromal cells (MSCs) in Matrigel in the bottom compartment of a 5.0  $\mu$ m pore transwell plate (3385, Corning). After a four day culture of the target  $\alpha\beta$ T cells with the MSCs,  $\alpha\beta$ T cells were added to the upper compartment of the transwell plate in 10  $\mu$ M Pamidronate (VWR international).

For the chemokine blocking experiments, neutralizing antibodies targeting CXCL1 (AF-310, Invitrogen), CCL4 (24006, Invitrogen) and CXCL10 (33036, Invitrogen) or the CCR5 inhibitor Maraviroc (HY-13004, Bio-connect) were administered at the manufacturers IC50 simultaneously with the engineered  $\alpha\beta$ T cells.

After a two days co-culture with of  $\alpha\beta$ T cells, supernatant of the model was used for Luminex (SigmaAldrich) analysis at the UMC Utrecht multiplex core. Recovery solution (Corning) was used to dissolve the Matrigel and retrieve a single cell suspension according to the manufacturers protocol. Next, cell suspensions of both compartments were stained for  $\alpha\beta$ T cell surface markers (see flow cytometry section). FACS Flow count Fluorospheres (Beckman Coulter) were added and samples were run on a Flow Cytometer to quantify the tumour load and  $\alpha\beta$ T cell infiltration.

### ***In vitro* organoid models**

Both colon and breast cancer organoids were seeded in Matrigel similar to the bone marrow models mentioned above but lack the presence of MSC<sup>17</sup>. After a four day culture in Matrigel in the lower compartment of the transwell plate,  $\alpha\beta$ T cells were administered to the upper part for a two day incubation. Subsequently, both compartments were isolated using cell recovery solution (Corning) according to the manufacturers protocol. Next, cells were stained for  $\alpha\beta$ T cell markers and FACS Flow count Fluorospheres (Beckman Coulter) were added to each sample. Samples were run on a Flow Cytometer to quantify  $\alpha\beta$ T cell infiltration and tumor targeting. Note; all breast cancer organoid experiments were performed in the Princess Maxima Centre.

### **Flow cytometry stainings**

The following antibodies were used according to the manufacturer instructions; CD3 (UCHT1, Biolegend), CD4 (RPA-T4, Biolegend), CD8 (RPA-T8, Biolegend), TCRpan  $\gamma\delta$  (IMMU510, Beckman Coulter), TCRpan  $\alpha\beta$  (IP26, eBioscience), CCR5 (HM-CCR5, Thermo fisher), CCR6 (R6H1, Thermo Fisher), CXCR2 (5E8-C7-F10, Thermo Fisher) and CXCR3 (CXCR3-173, Thermo Fisher).

Surface expression of the BCMA-CAR was determined by a primary staining of the  $\alpha\beta$ T cells with biotinylated BCMA (Bio-connect) followed by an secondary staining of Streptavidin-PE (AB\_10053328, BD Pharmingen) according to manufacturer's protocol.

### **3' single cell RNA library preparation and sequencing**

We prepared the harvested cells for the 3' scRNAseq by depleting them of dead cells using the Dead Cell Removal Kit (Miltenyi) and MS Columns (Miltenyi) according to the manufacturer's protocol, and straining them through a 70  $\mu$ m strainer. 12.000 live cells from each condition were taken for 3' scRNAseq. Libraries were prepared using the 10X Genomics v3.1 Single Index workflow and reagents (10X Genomics 1000127, 1000121, 1000213, 1000171), according to the manufacturer's protocol. The samples were sequenced on Illumina NovaSeq 6000 at depths of 13000–39500 read pairs per cell. FASTQ read files were generated from the raw intensity files using the built-in software of the NovaSeq 6000. The reads were then aligned onto the human genome and transcriptome using the Cell Ranger 6.0.1 software (10X Genomics) with GRCh38-2020-A (10X Genomics) as a reference. Demultiplexing of multiplets was done based on SNP deconvolution of donors within samples with the snp-dmx-cancer tool<sup>25</sup>. The successfully aligned reads, together with the demultiplexing data, were then analysed in R 4.0.1, primarily with the Seurat package<sup>26</sup>. Inference of the  $\alpha\beta$ T cell type (CD4+ or CD8+) was done with the scmap R package<sup>27</sup>.



## Software

GraphPad Prism 8, Microplate Manager (Bio-Rad), FACSDiva (BD Biosciences), R software (R foundation), Office 2016 (Microsoft).

## Results

### $\alpha\beta$ T cell migration towards the tumor site correlates with tumor targeting

We applied a 3D, multicellular system to model the malignant bone marrow niche<sup>15</sup> that allowed not only for physiological interaction between tumor cells and the healthy stroma, but also enabled to study the spatial dynamics of tumor specific  $\alpha\beta$ T cells. After establishing the 3D architecture of tumor cells and stroma in Matrigel<sup>15</sup>, we applied  $\alpha\beta$ T cells on the top of the 3D structure by using a transwell system that required active migration of  $\alpha\beta$ T cells to reach malignant targets below. This setup allowed for the monitoring of the efficacy of tumor killing, the role of healthy stroma and  $\alpha\beta$ T cell effector properties simultaneously<sup>16</sup> (**Figure 1A**). TEGs showed efficient killing of a range of tumors such as the multiple myeloma cell line RPMI-8226, leukemic cell lines KG1a and MV4-11 and primary multiple myeloma samples compared to  $\alpha\beta$ T cells containing a non-function/mock  $\gamma\delta$  TCR control (TEG-LM1) (**Figure 1B**), while the healthy stroma fraction of the co-culture system remained unharmed (**Supplementary Figure 1**). Killing capacity of TEG cells in the 3D bone marrow model however seemed suboptimal since we did not observe complete killing with any of the here-tested tumor targets in a two day window. In order to gain more insight in this heterogeneity in TEG targeting, we quantified the total number of  $\alpha\beta$ T cells present after treatment as well as the  $\alpha\beta$ T cell fractions that were either migrated to the lower (migrated) part of the transwell culture or remained in the upper part (non-migrated) (**Figure 1C**). We assumed that suboptimal killing of targets was not only the result of heterogenous target expression and therefore also tested BMCA- CAR-T efficacy in the same models system. BCMA-CART were administered to the leukemic bone marrow models containing either RPMI-8226 or patient-derived MM blasts (**Figure 1D-1E**), however BCMA-CART were unable to completely eradicate even the RPMI-8226 target.

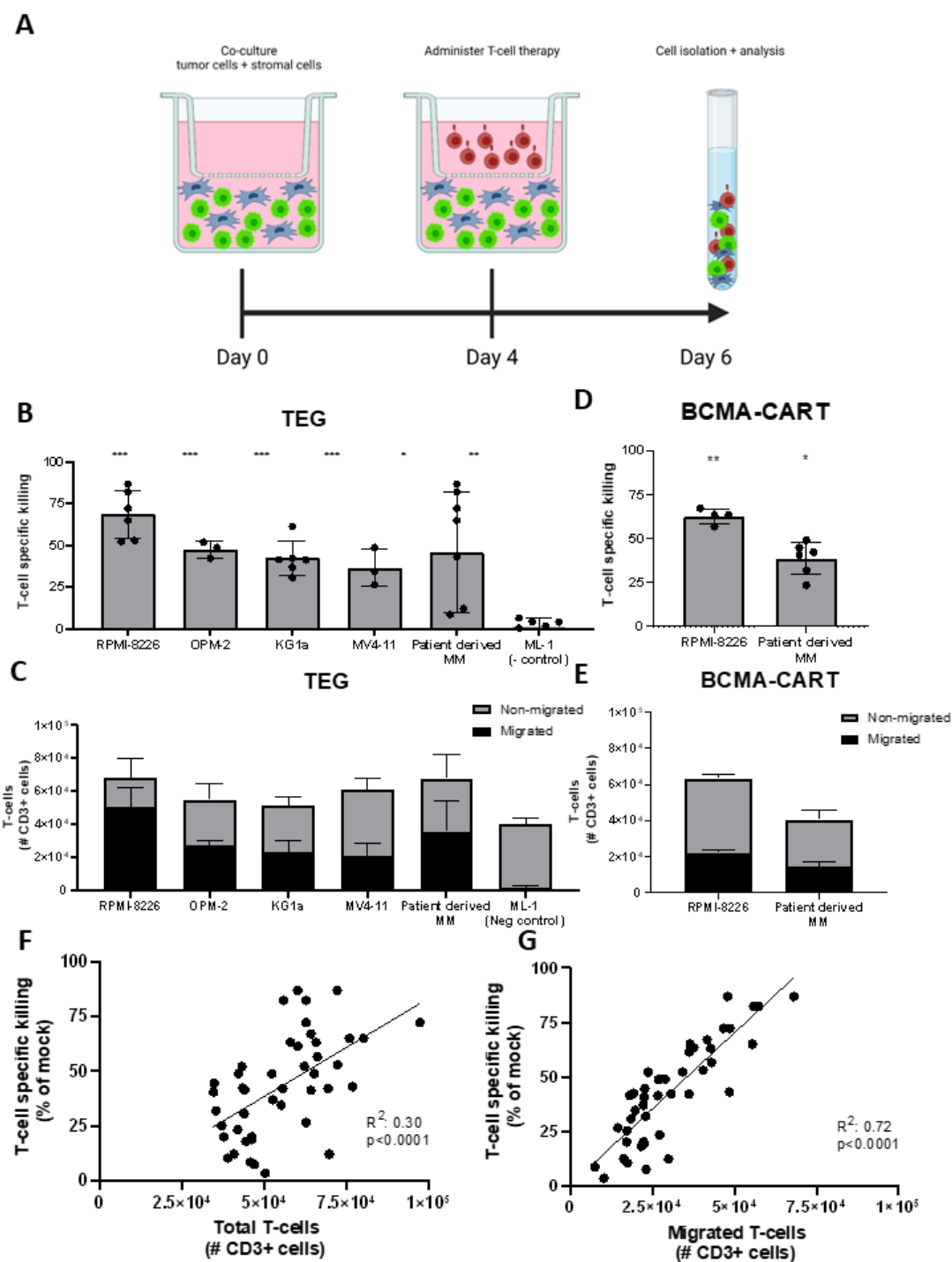


**Figure 1. Tumor killing is dependent on  $\alpha\beta$ T cell migration in the tumor microenvironment.** Schematic timeline of 3D TME model experiments; Tumor cells and stromal cell are dyed and co-cultured for 4 days in Matrigel.  $\alpha\beta$ T cells are administered on a transwell (A). TEG specific killing of tumor cells in the 3D TME model compared to mock  $\alpha\beta$ T cell control (B). Amount of TEG cells was determined by CD3 staining on cells isolated from both compartments (C). BCMA-CART specific killing of tumor cells in the 3D TME model compared to mock  $\alpha\beta$ T cell control TEG-LM1 (D). Amount of BCMA CART was determined by CD3 staining on cells isolated from both compartments (E). Correlation between total  $\alpha\beta$ T cells isolated on day 6 and  $\alpha\beta$ T cell specific killing of all tested tumors and  $\alpha\beta$ T cell therapies (F). Correlation between migrated  $\alpha\beta$ T cells isolated on day 6 and  $\alpha\beta$ T cell specific killing of all tested tumors and  $\alpha\beta$ T cell therapies (G). Error bars represent SD ( $n \geq 3$ ).

Next, the extent of TEG and BCMA-CART targeting of all tumor samples cultured in the *in vitro* transwell model was correlated to either persistence of all  $\alpha\beta$ T cells (migrated and non-migrated) or only to migrated  $\alpha\beta$ T cells observed two days post administration (**Figure 1F-G**). The persistence of total  $\alpha\beta$ T cells showed low predictive value for the level of T-cell specific tumor killing ( $R^2$ : 0,30) while only focusing on the migrating  $\alpha\beta$ T cells did show a higher correlation ( $R^2$ : 0,72). This emphasizes that rather the amount of  $\alpha\beta$ T cells that are able to migrate towards the tumor inside the TME than the total amount of  $\alpha\beta$ T cells persisting could be determinant for the efficacy of the  $\alpha\beta$ T cell therapy.

### **Blocking CXCL1, CCL4 or CXCL10 reduces $\alpha\beta$ T cell migration and thereby lowers $\alpha\beta$ T cell specific killing.**

Since tumor specific  $\alpha\beta$ T cells actively migrated to the tumor site through small transwell pores, we assumed that the presence of soluble factors facilitated target specific migration. To this end, we collected supernatants of 3D co-cultures and screened via Luminex technology for soluble molecules that might play a role in  $\alpha\beta$ T cell attraction to the tumor site. 3D co-cultures containing either primary patient-derived MM samples, the MM cell line RPMI-8226 or the AML cell line KG1a combined with donor-derived MSCs showed elevated levels of CXCL1, CCL4 and CXCL10 in tumor models only upon treatment with TEG cells, suggesting that these chemokines play a role in antigen-specific migration and tumor killing (**Figure 2A**).

To test whether these chemokines binding to receptors on the  $\alpha\beta$ T cells is needed for an effective  $\alpha\beta$ T cells migration towards the tumor micro-environment, neutralizing antibodies were used to block the function of these chemokines (**Figure 2B**). When blocking antibodies against CXCL1, CCL4 and CXCL10 were administrated simultaneously with the  $\alpha\beta$ T cells, we found that migration of either TEG or BCMA-CART was significantly reduced compared to blocking of the non-elevated chemokine CCL20 with identical antibody isotype. This reduction in  $\alpha\beta$ T cell migration also resulted in a significant lowering of the tumor killing of both TEG treatment as BCMA-CART treatment (**Figure 2C**). This indicates that binding of these chemokines to  $\alpha\beta$ T cells is needed for the migration of  $\alpha\beta$ T cells and that this migration plays an important role in killing capacity of these  $\alpha\beta$ T cells.

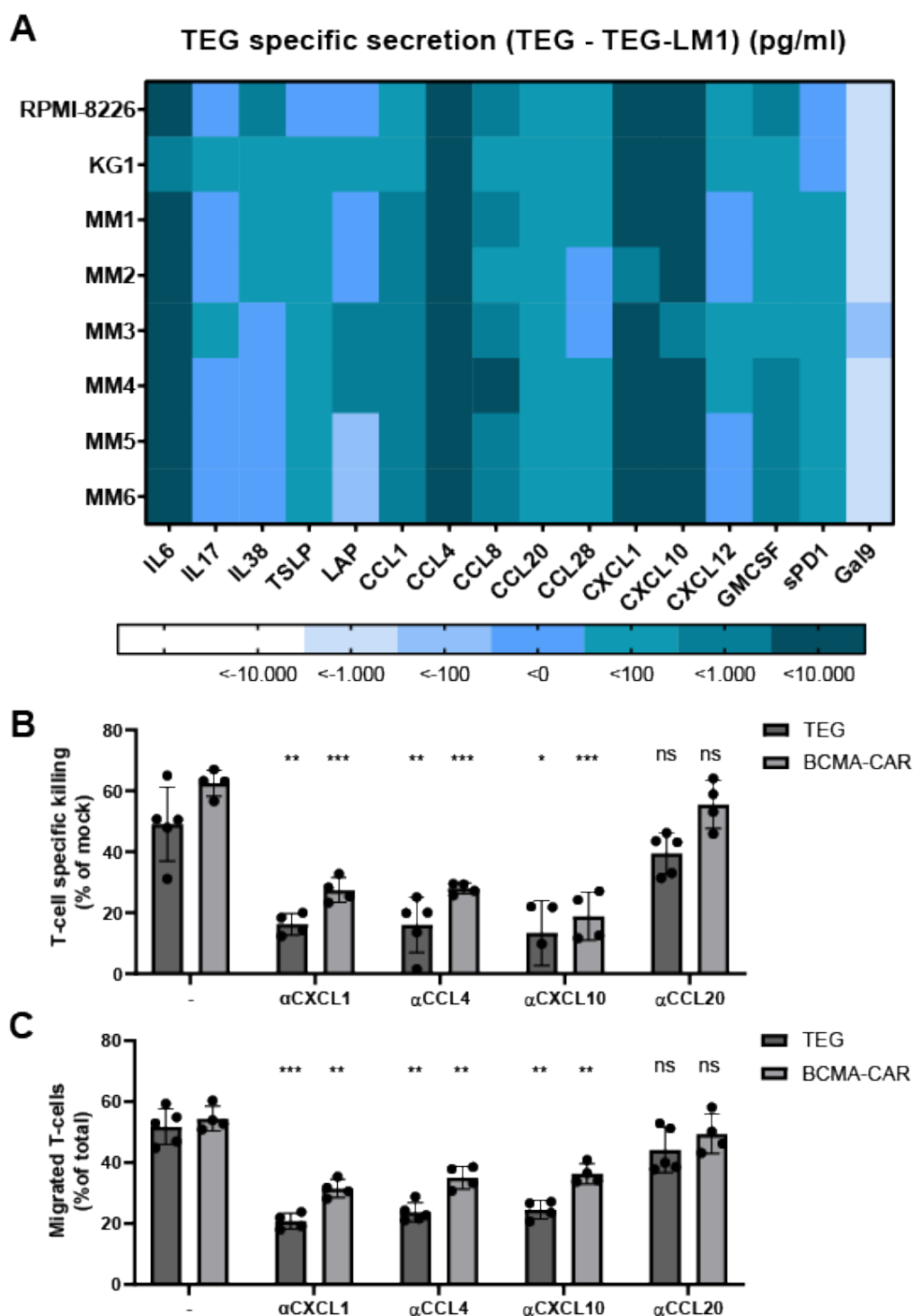


**Figure 2. CXCL1, CCL4 and CXCL10 gradients facilitate TEG cell migration in the tumor microenvironment.** Luminex analysis of 3D TME models treated with mock  $\alpha$  $\beta$ T cell (TEG-LM1) or TEG cells, cultured with primary MM or cell line RPMI-8226 or KG1a. Concentrations found in TEG-treated conditions are normalized to their TEG-LM1 control (A). Neutralizing antibodies were administered at the IC50 dose simultaneous with TEG administration. TEG cell migration (B) and RPMI-8226 tumor killing (C) was determined two days post administration. Error bars represent SD (n $\geq$ 3).

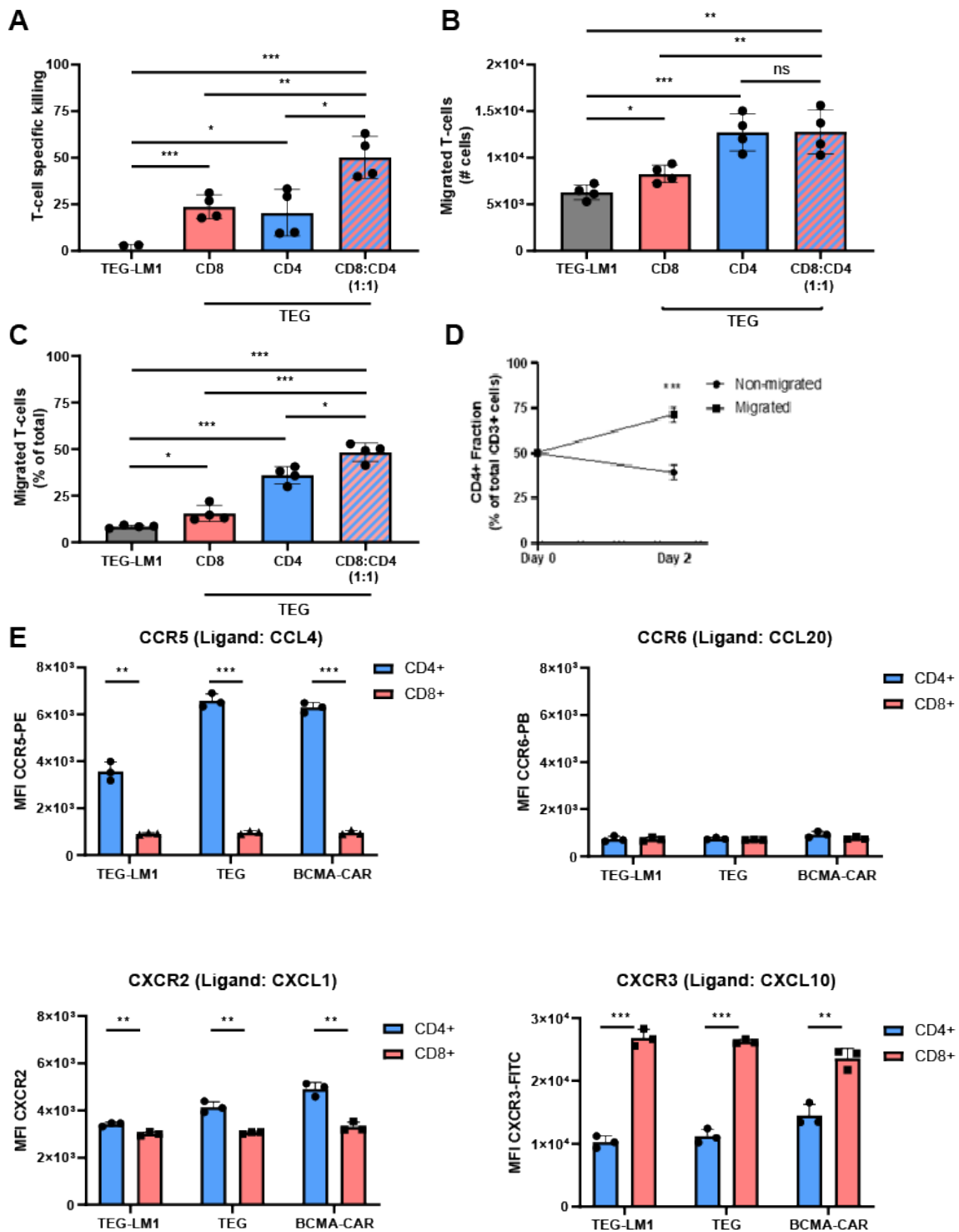


**Figure 3. Combined migration of CD4+ and CD8+  $\alpha\beta$ T cells leads to optimal tumor killing.** TEG killing of RPMI-8226 cells in the 3D TME model at either CD4 / CD8 alone or in a 1:1 ratio of CD4:CD8 compared to mock  $\alpha\beta$ T cell control (A). TEG and TEG-LM1 cell migration in the 3D TME model cultured with RPMI-8226 at either CD4 / CD8 alone or in a 1:1 ratio of CD4:CD8 (B,C). CD4 skewing in the migrated TEG fraction over time in RPMI-8226 3D TME models treated with a 1:1 ratio of CD4:CD8 (D). Chemokine receptor expression on isolated TEGs and BCMA-CART from 3D TME models cultured with RPMI-8226; see Figure 1B,D (E). Error bars represent SD (n $\geq$ 3).

## Both CD4+ and CD8+ $\alpha\beta$ T cell migration is necessary for optimal tumor reactivity

To further investigate which population of  $\alpha\beta$ T cells are migrating in the tumor microenvironment, CD4+ and CD8+ TEG cells were separated and administered separately or in a 1:1 ratio to 3D TME models cultured with RPMI-8226 (**Figure 3A**). Administering CD4+  $\alpha\beta$ T cells alone showed a reduced killing compared to administering CD4+ and CD8+  $\alpha\beta$ T cells in a 1:1 ratio as expected<sup>28</sup>. Similarly, treatment with CD8+ TEG cells alone demonstrated less efficient killing compared to the CD4+ and CD8+ combination confirming that the presence of both subsets is needed for an optimal anti-tumor response.

While CD8+  $\alpha\beta$ T cells applied alone resulted only in marginal levels of  $\alpha\beta$ T cell migration, both CD4+  $\alpha\beta$ T cells alone and a combination of CD4+ and CD8+  $\alpha\beta$ T cells in combination led to significantly higher numbers of migrated  $\alpha\beta$ T cells to the TME (**Figure 3B-C**). Furthermore, when CD4+ and CD8+  $\alpha\beta$ T cells were administered simultaneously, significantly more CD4+ than CD8+  $\alpha\beta$ T cells migrated into the TME (**Figure 3D**). This data combined indicates that CD4+  $\alpha\beta$ T cells are more capable to migrate into the tumor microenvironment than CD8+  $\alpha\beta$ T cells. Although migrated CD8+  $\alpha\beta$ T cell have a higher killing capacity than CD4+  $\alpha\beta$ T cells once migrated, the combination of both migrated CD4+ and CD8+  $\alpha\beta$ T cells provides the highest tumor killing. This highlights the importance of the presence of both  $\alpha\beta$ T cell subsets at the tumor site.

To further assess the dynamics in  $\alpha\beta$ T cell migration of CD4+ and CD8+  $\alpha\beta$ T cells, we isolated  $\alpha\beta$ T cells from the 3D tumor microenvironment (migrated  $\alpha\beta$ T cells) and measured surface expression of the chemokine receptors corresponding to the elevated chemokines CXCL1, CCL4 and CXCL10 via flow cytometry (**Figure 3E**). CCR5, the main chemokine receptor of CCL4 showed an approximately 5-fold higher expression in CD4+ than in CD8+  $\alpha\beta$ T cells, both in TEG and BCMA-CART. While CXCR2, the chemokine receptor binding CXCL1 also showed significantly higher surface expression in CD4+  $\alpha\beta$ T cells compared to the CD8+  $\alpha\beta$ T cells but to a lesser extent; approximately 1,5-fold. In contrast, CXCR3, the chemokine receptor binding CXCL10, showed higher expression in the CD8+ subset compared to the CD4+ subset. Finally, the receptor binding CCL20 (CCR6) did not show any differences in expression between CD4+ and CD8+ fractions in TEG-LM1 (Mock), TEG or BCMA-CART. This expression profile of CD4+ and CD8+  $\alpha\beta$ T cells suggests a unique role for CCR5 expression on CD4+  $\alpha\beta$ T cells in the ability to migrate better in the TME than CD8+  $\alpha\beta$ T cell.

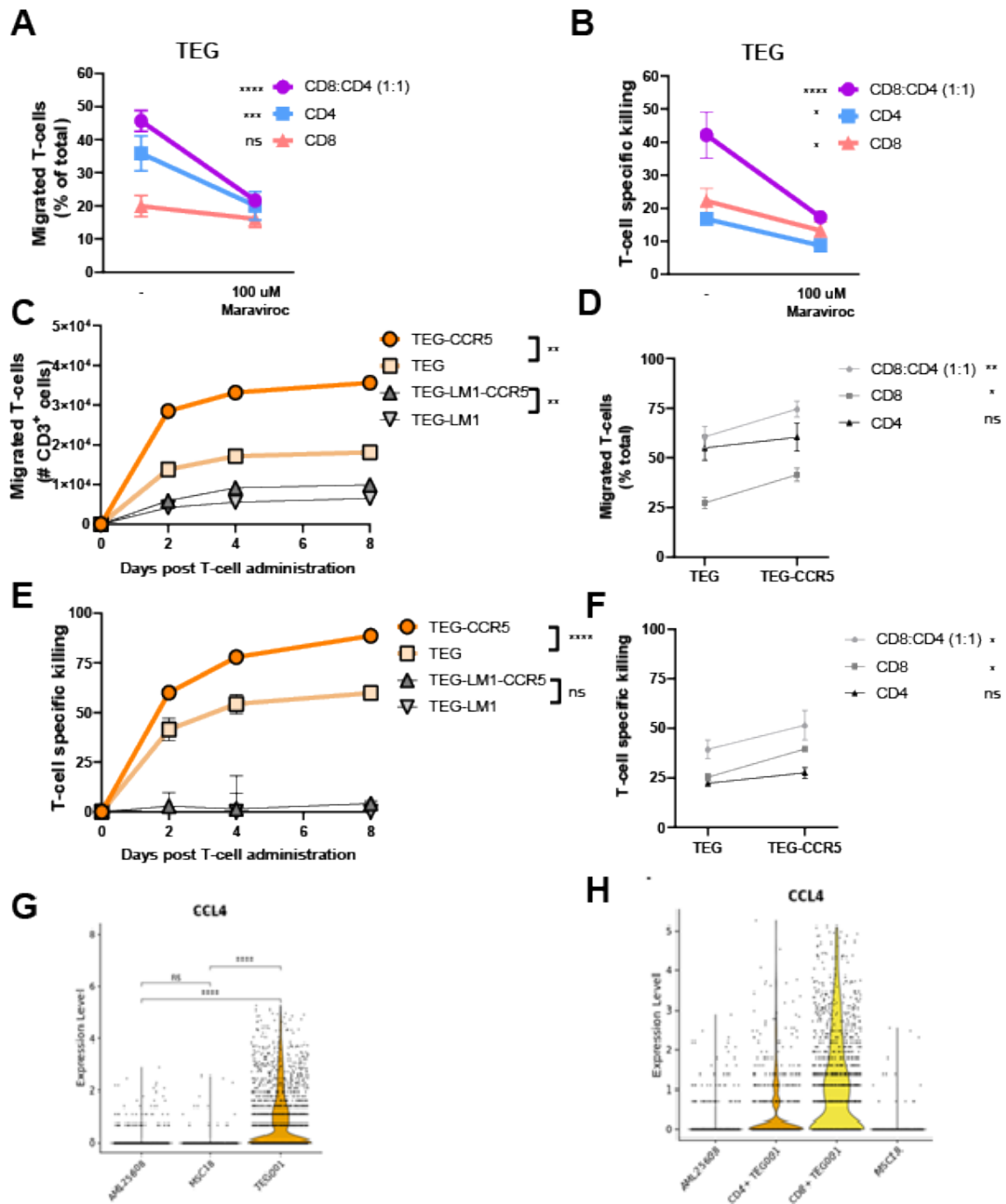


**Figure 4. CCR5 overexpression improves CD8+  $\alpha\beta$ T cell migration and thereby tumor killing.** Maraviroc blocking of CCR5 on TEG cell migration in RPMI-8226 3D TME models at either CD4+ or CD8+ engineered  $\alpha\beta$ T cells alone or in a 1:1 ratio of CD4:CD8 (A). Maraviroc blocking of CCR5 on TEG specific killing of RPMI-8226 cells in the 3D TME model at either CD4 / CD8 alone or in a 1:1 ratio of CD4:CD8 compared to mock  $\alpha\beta$ T cell control (B). Effect of CCR5 overexpression on TEG and TEG-LM1 migration in the 3D TME model in a 1:1 ratio of CD4:CD8 (C,E). Effect of CCR5 overexpression on CD4+ and CD8+ TEG cells and their killing capacity towards RPMI-8226 (D,F). scRNA sequencing of BM models with AML and MSCs followed by TEG treatment. CCL4 expression was plotted per cellular compartment (G,H). Error bars represent SD (n $\geq$ 3).

## Overexpression of CCR5 in CD8+ $\alpha\beta$ T cells enhances $\alpha\beta$ T cell migration and tumor killing via positive feedback loop

To confirm the role of CCR5 in the migration patterns of CD4+  $\alpha\beta$ T cells in the TME, we used *Maraviroc*, a clinically known inhibitor of CCR5 receptor<sup>29</sup> to block the chemokine receptor on TEG cells before administered to 3D *in vitro* BM models cultured with RPMI-8226 (**Figure 4A-B**). While administering *Maraviroc* did not affect CD8+  $\alpha\beta$ T cell migration, the amount of CD4+  $\alpha\beta$ T cells that migrated to the tumor site was significantly reduced when  $\alpha\beta$ T cells were administered in a 1:1 ratio of CD4+:CD8+. This indicates that CCR5 expressed on CD4+  $\alpha\beta$ T cells is an important factor for their migration towards their tumor target.

In order to boost CD8+  $\alpha\beta$ T cell migration to the tumor site, TEG-LM1 and TEG cells were genetically engineered to overexpress the CCR5 receptor via retroviral transduction<sup>18</sup> (**Supplementary Figure 2A-B**). As a result, TEG-CCR5  $\alpha\beta$ T cells showed increased migration in the 3D models cultured with RPMI-8226 when compared to wild type TEG cells and improved tumor targeting, which persisted up to 8 days (**Figure 4C**). Importantly, CCR5 overexpression exclusively improved the migration of the CD8+ T-cell subset while providing additional CCR5 to the CD4+  $\alpha\beta$ T cell subset did not further improve migration (**Figure 4D**). Consequently, the enhanced migration of CD8+ TEG-CCR5 did lead to increased tumor killing in both the CD8+  $\alpha\beta$ T cell alone condition as well as in the combination with CD4+  $\alpha\beta$ T cells (**Figure 4 E-F**).

To identify the source of the produced CCL4, scRNA sequencing of 3D TME models containing TEG cells, primary AML and donor-derived MSC was performed showing that upon TEG treatment, migrated  $\alpha\beta$ T cells are the main producers of CCL4 (**Figure 4G**, **Supplementary 3**). Interestingly, when dissecting CD4+ and CD8+ TEG cells, we found that the CD8+ TEG cells produce more CCL4 compared to the CD4+ TEG cells (**Figure 4H**). This all together suggests that CD8+  $\alpha\beta$ T cell presence in the TME is needed in order to initiate a positive feedback loop that will attract additional  $\alpha\beta$ T cells.

## CCR5 overexpression leads to increase $\alpha\beta$ T cell migration and tumor killing of solid tumors

To investigate whether supplementing engineered  $\alpha\beta$ T cells with CCR5 leads to increased  $\alpha\beta$ T cell infiltration and tumor killing also in solid tumor models, we tested TEG-CCR5  $\alpha\beta$ T cells in 3D tumor models containing either patient-derived breast cancer organoids and patient-derived colon cancer organoids (PDOs).

Overexpression of CCR5 in TEG significantly increased both  $\alpha\beta$ T cell migration (**Figure 5A**) and tumor killing (**Figure 5B**) in both tested breast cancer PDO-models, leading to



an approximately two-fold increase in tumor targeting. Importantly, overexpression of CCR5 in  $\alpha\beta$ T cells expressing a non-functional Vg9Vd2TCR (TEG-LM1) neither lead to more  $\alpha\beta$ T cell migration nor increased tumor killing. Targeting patient derived colon cancer organoids with either TEG or TEG-LM1 cells overexpressing CCR5 led to improved migration of the  $\alpha\beta$ T cells towards the tumor site (**Figure 5C**). However, only the TEG-CCR5 cells showed improved tumor killing while the TEG-LM1-CCR5 cells left tumor cells unharmed (**Figure 5D**). This increase in  $\alpha\beta$ T cell migration and tumor killing was mainly a result of a significant increased migration of CD8+ TEG-CCR5 cells when compared to the wild type TEG. This data shows that predominantly the CD8+  $\alpha\beta$ T cells benefit from gaining additional expression of the chemokine receptor (**Figure 5E-F**).

## Discussion

Clinical responses to immune cell based therapies partially rely on the ability of  $\alpha\beta$ T cells to infiltrate to the tumor microenvironment where low immune infiltration rates often leads to poor clinical responses<sup>30</sup>. Therefore, improving the  $\alpha\beta$ T cell infiltration of adoptively transferred  $\alpha\beta$ T cells such as CARTs and TCR-engineered  $\alpha\beta$ T cells can potentially exhibit future clinical benefits<sup>31</sup>. To this end, we used 3D models that enabled studying and modifying  $\alpha\beta$ T cell migration capacity towards the tumor microenvironment of both hematological and solid malignancies to demonstrate the benefits of overexpression of the chemokine receptor CCR5 in adoptive  $\alpha\beta$ T cell treatments to improve tumor clearance.

Chemokines and their chemokine receptors play a vital role in tumor progression by either restricting or promoting anti-tumor immunity<sup>32</sup>. Especially in a range of solid tumors, chemokine environment affecting  $\alpha\beta$ T cell infiltration has been identified as major cause of the lack of anti-tumor  $\alpha\beta$ T cell responses<sup>33</sup>. While  $\alpha\beta$ T cell infiltrating capability is has not been reported as limiting factor for the clinical outcome of CART therapies against bone marrow malignancies, we found that in 3D bone marrow niche models mainly the CD4+ fraction of tumor specific  $\alpha\beta$ T cells were infiltrating, while the CD8+  $\alpha\beta$ T cells were largely responsible for tumor clearance once infiltrated. This finding not only suggests that improving CD8+  $\alpha\beta$ T cell infiltration is key for improving the tumor clearance even in bone marrow residing malignancies but also provided an experimental tool to identify factors that influence the delicate dynamics of engineered  $\alpha\beta$ T cells in the TME.

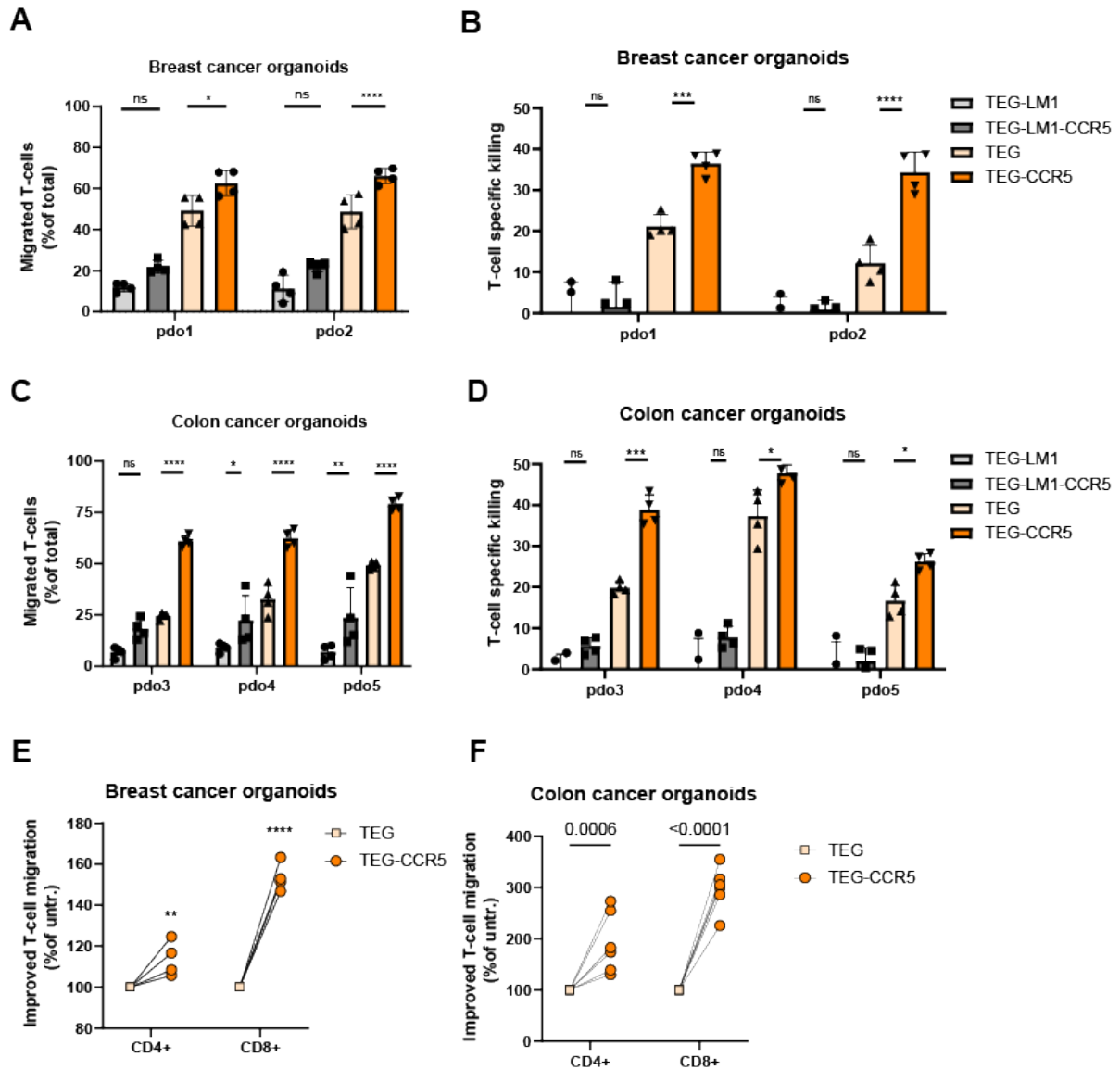


**Figure 5. CCR5 overexpression improves  $\alpha\beta$ T cell migration and thereby tumor killing of TEG cells in solid tumors.** Effect of CCR5 overexpression on TEG and TEG-LM1 cell migration towards two, patient-derived breast cancer organoids (PDO1,2) seeded in Matrigel (**A,B**). Effect of CCR5 overexpression on TEG and TEG-LM1 migration towards three, patient-derived colon cancer organoids (PDO3-5) seeded in Matrigel (**C,D**). Effect of CCR5 overexpression on CD4+ and CD8+ TEG cells targeting the two patient-derived breast cancer PDO1,2 (**E**) or the three colon cancer organoids PDO3-5 seeded in Matrigel (**F**). Error bars represent SD (n $\geq$ 2).

Luminex analysis of the TEG-treated leukemic microenvironment identified three chemokine gradients present in high concentrations namely CXCL1, CCL4 and CXCL10. We showed, furthermore, that blocking the interaction of these chemokines with the corresponding main chemokine receptors on  $\alpha\beta$ T cells such as CXCR2, CCR5 and CXCR3, respectively leads to decreased immune infiltration and tumor clearance. While these chemokines have been previously suggested to play a pivotal role in tumor specific  $\alpha\beta$ T cell infiltration in various solid tumor types<sup>34</sup>, we here show that largely differential surface expression of the CCR5 on the CD4+  $\alpha\beta$ T cell fraction of engineered  $\alpha\beta$ T cells could provide a potential advantage for these cells for their infiltration to the tumor site compared to CD8+  $\alpha\beta$ T cells. Preferential CD4+  $\alpha\beta$ T cell infiltration as a result of their better response to chemokine gradients has been described in various solid tumors where the migrated CD4+ regulatory  $\alpha\beta$ T cells negatively shaped the local immune environment<sup>35</sup>. Although we did not investigate the role of regulatory CD4+  $\alpha\beta$ T cell accumulation on the killing capacity of the adoptive  $\alpha\beta$ T cell therapy used, we primarily focused on whether equipping CD8+  $\alpha\beta$ T cells with CCR5 would overcome their limited capability to infiltrate. Although overexpression of CCR5 in tumor reactive CD8+  $\alpha\beta$ T cells improved their immune infiltration leading to a higher tumor clearance, the presence of both CD4+ and CD8+  $\alpha\beta$ T cells was required for optimal tumor clearance suggesting a limited role here for regulatory CD4+  $\alpha\beta$ T cells.

Clonally expanded, tumor specific CD8+  $\alpha\beta$ T cells have been previously suggested to produce CCL4 in oropharyngeal squamous cell carcinoma (OPSCC)<sup>36</sup>. Furthermore, we found that the majority of CCL4 mRNA in the TME is produced by tumor infiltrating CD8+  $\alpha\beta$ T cells. Supplementing CARTs and TCR engineered CD8+  $\alpha\beta$ T cells with CCR5 would therefore possibly lead to a positive feedback loop in which infiltration and tumor encounter induced CCL4 production would induce further CD8+  $\alpha\beta$ T cell migration towards the tumor microenvironment.

In conclusion, aiding the infiltration of adoptive  $\alpha\beta$ T cell therapies will improve their efficacy for the treatment of multiple malignancies. Mainly, improving the infiltrating rate of the cytotoxic, CD8+ fraction of the T lymphocytes will yield better clinical responses. Overexpression of the CCR5 receptor in this fraction increased their sensitivity to the CCL4 gradient present in the TME leading to increased infiltration and tumor targeting. These results indicate additional engineering on  $\alpha\beta$ T cell products can improve their clinical benefit.

## **Acknowledgements**

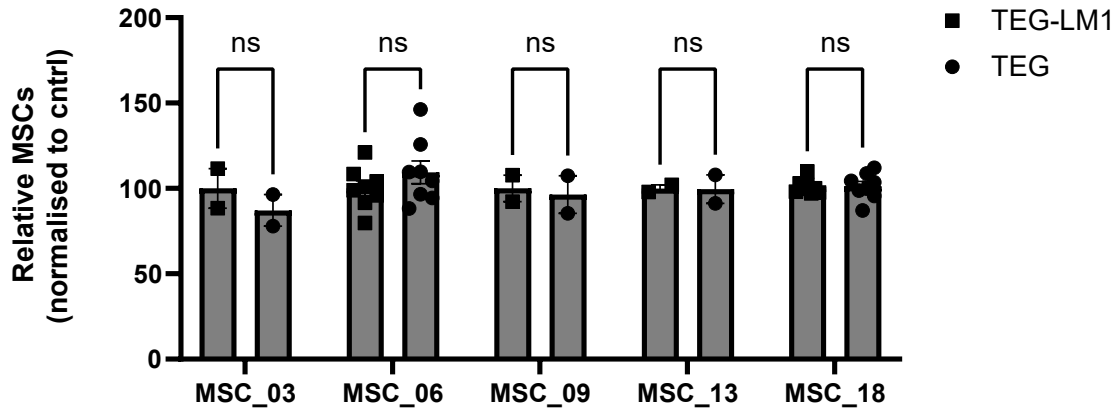
We thank the A. Rios group and the HUB of the Princess Máxima Center for Pediatric Oncology for providing the breast cancer PDOs. Note; all breast cancer organoid experiments were performed in the Princess Maxima Centre. We also thank the Snippert Group of the Center for Molecular Medicine in the UMC Utrecht for providing the colon cancer PDOs under the RASTRIC protocol. And finally we thank the Heidenreich group for providing the patient derived AML samples.

## References

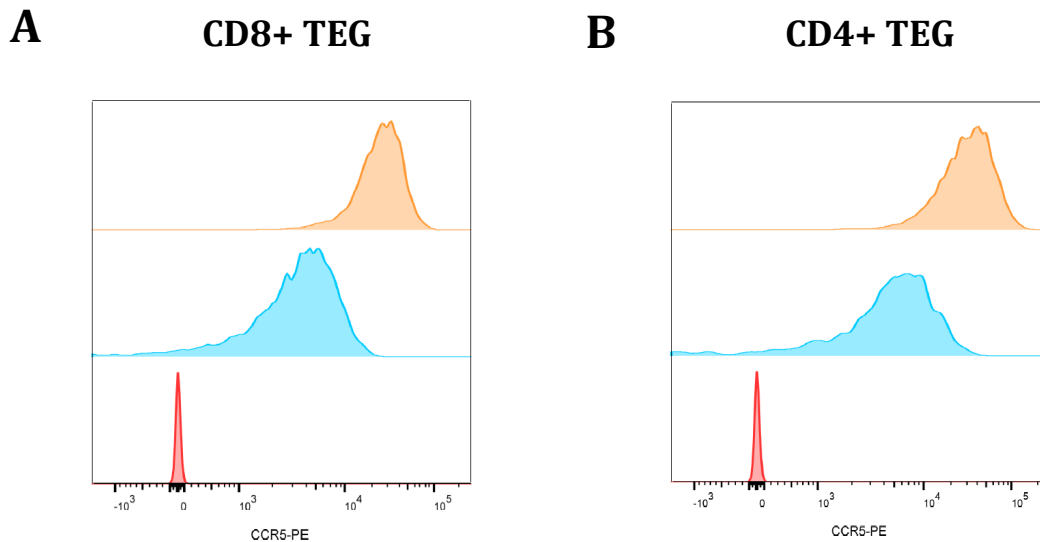
1. Chabannon C. et al. "Hematopoietic stem cell transplantation in its 60s: A platform for cellular therapies" *Sci Transl Med* (2018).
2. Finck A. et al. "Engineered cellular immunotherapies in cancer and beyond" *Nat Med* (2022).
3. Galon J. et al. "Type, density, and location of immune cells within human colorectal tumors predict clinical outcome." *Science* (1960).
4. Chen P. et al. "Analysis of Immune Signatures in Longitudinal Tumor Samples Yields Insight into Biomarkers of Response and Mechanisms of Resistance to Immune Checkpoint Blockade." *Cancer Discov* (2016).
5. Mahmoud, S et al. "Tumor-infiltrating CD8+ lymphocytes predict clinical outcome in breast cancer." *J Clin Oncol* (2011).
6. Rashidian, M. et al. "Predicting the response to CTLA-4 blockade by longitudinal noninvasive monitoring of CD8 T cells." *J Exp Med* (2017).
7. Tumeh, P. et al. "PD-1 blockade induces responses by inhibiting adaptive immune resistance." *Nature* (2014).
8. Li X. et al. "Infiltration of CD8(+) T cells into tumor cell clusters in triple-negative breast cancer." *Proc Natl Acad Sci* (2018)
9. Lamble A. "Targeting the Immune Microenvironment in Acute Myeloid Leukemia: A Focus on T Cell Immunity." *Front Oncol* (2018).
10. Marofi, F., et al. "CAR T cells in solid tumors: challenges and opportunities." *Stem Cell Res Ther* (2021).
11. Vilgelm A. et al. "Chemokines Modulate Immune Surveillance in Tumorigenesis, Metastasis, and Response to Immunotherapy" *Front Immunol.* (2019).
12. Tsuyada A et al. "CCL2 mediates cross-talk between cancer cells and stromal fibroblasts that regulates breast cancer stem cells." *Cancer Res.* (2012).
13. Yang L et al. "Abrogation of TGF beta signaling in mammary carcinomas recruits Gr-1+CD11b+ myeloid cells that promote metastasis." *Cancer Cell* (2008).
14. Weber LM et al. "Genetic demultiplexing of pooled single-cell RNA-sequencing samples in cancer facilitates effective experimental design" *GigaScience* (2021).
15. Braham, M. et al. "Cellular immunotherapy on primary multiple myeloma expanded in a 3D bone marrow niche model." *Oncoimmunology* (2018).
16. Hernandez-Lopez P et al. "Combining targeting of the cancer-metabolome with cancer-associated stress antigens impacts transcriptomic heterogeneity, dynamics, and efficacy of engineered T-cells" *Nature Immunology* (2023).
17. Dekkers F. et al. "Uncovering the mode of action of engineered T cells in patient cancer organoids" *Nature* (2023).
18. Marcu-Malina V. et al. "Redirecting  $\alpha\beta$ T Cells Against Cancer Cells by Transfer of a Broadly Tumor-Reactive  $\gamma\delta$ T-Cell Receptor." *Blood* (2011).
19. Raje N. et al. "Anti-BCMA CAR T-Cell Therapy bb2121 in Relapsed or Refractory Multiple Myeloma" *N Engl J Med* (2019).
20. Lopalco L et al. "CCR5: From Natural Resistance to a New Anti-HIV Strategy" *Viruses* (2010).
21. Esembl.org  
"ensembl.org/Homo\_sapiens/Gene/Summary?g=ENSG00000160791;r=3:46370946-46376206" Esembl.org (2023).
22. Driehuis, E. et al. "Establishment of patient-derived cancer organoids for drug-screening applications." *Nat Protoc*, (2020).

23. Sachs N. et al. "A living biobank of breast cancer organoids captures disease heterogeneity." *Cell* (2018).
24. Pleguezuelos-Manzano C. et al. "Establishment and culture of human intestinal organoids derived from adult stem cells." *Current Protocols in Immunology* (2020).
25. Weber L. et al. "Genetic demultiplexing of pooled single-cell RNA-sequencing samples in cancer facilitates effective experimental design" *GigaScience* (2021).
26. Hoan Y. et al. "Integrated analysis of multimodal single-cell data" *Cell* (2021).
27. Kiselev V. et al. "scmap: projection of single-cell RNA-seq data across data sets" *Nature Methods* (2018).
28. Boulch M et al. "A cross-talk between CAR T cell subsets and the tumor microenvironment is essential for sustained cytotoxic activity" *Sci Immunology* (2021).
29. Fätkenheuer G. et al. "Efficacy of short-term monotherapy with maraviroc, a new CCR5 antagonist, in patients infected with HIV-1" *Nature Medicine* (2005).
30. Wang L. et al. "Hot and cold tumors: Immunological features and the therapeutic strategies" *Medcomm* (2020).
31. Tian Y. et al. "CXCL9-modified CAR T cells improve immune cell infiltration and antitumor efficacy" *Cancer Immunol Immunother.* (2022).
32. Foeng J. et al. "Harnessing the chemokine system to home CAR-T cells into solid tumors" *Cell Rep Med.* (2022).
33. Nisar S. et al. "Chemokine–cytokine networks in the head and neck tumor microenvironment." *Int J Mol Sci.* (2021).
34. Cadilha B. et al. "Combined tumor-directed recruitment and protection from immune suppression enable CAR T cell efficacy in solid tumors" *Sci Adv.* (2021).
35. Plitas G. et al. "Regulatory T cells exhibit distinct features in human breast cancer." *Immunity* (2016).
36. Abdulrahman Z. et al. "Tumor-specific T cells support chemokine-driven spatial organization of intratumoral immune microaggregates needed for long survival" *J Immunother Cancer.* (2022).

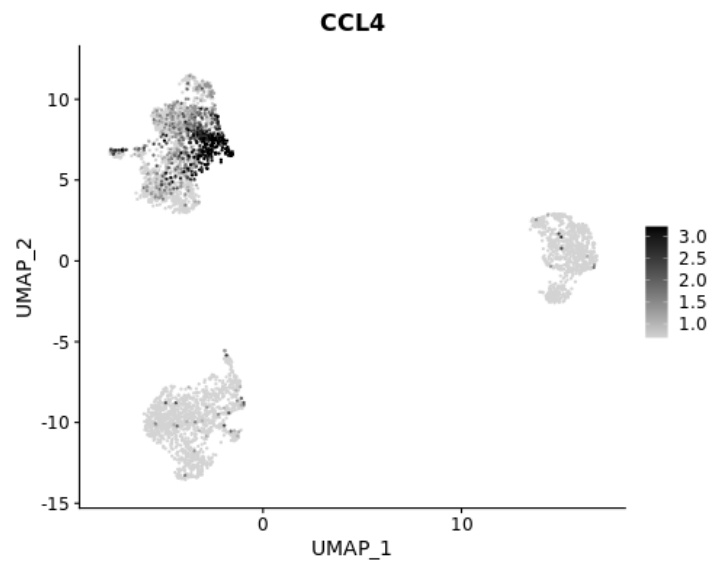
## Supplementary Figures



**Supplementary Figure 1. Mesenchymal stem cells from different donors are not targeted by TEG treatment.** 3D TME model experiments; Tumor cells and stromal cell are dyed and co-cultured for 4 days in Matrigel. Subsequently, either TEG or TEG-LM1 (mock) cells are administered on a transwell for a two-day treatment. On day 6, amount of MSCs was quantified on flow cytometry and normalized to the TEG-LM1 condition.



**Supplementary Figure 2. Overexpression of the CCR5 receptor in TEG cells.** CCR5 surface expression was measured on wildtype (green) and CCR5 transduced (blue) CD4+ TEG cells (A). Similarly, surface expression of CCR5 was measured on wildtype (green) and CCR5 transduced (blue) CD8+ TEG cells while showing unstained in red.



**Supplementary Figure 3. scRNA sequencing identifies  $\alpha\beta$ T cells as main producers of CCL4.** Principle component analysis of the scRNA data of TEG treated bone marrow models identifies three distinct cell populations. TEG cells in top left (CD3+, data not shown) show mRNA expression of CCL4 while the other cell populations; AML and MSCs show low to none expression of CCL4.







# CHAPTER

# 6

## The properties of mesenchymal stem cells in the tumor niche direct the outcome of engineered T cell therapy

A. Cleven<sup>1\*</sup>, A.D. Meringa<sup>1\*</sup>, P. Brazda<sup>1,2\*</sup>, P.K. Derevianko<sup>2\*</sup>,  
L. Gasull-Celades<sup>1</sup>, L. Hoorens van Heyningen<sup>1</sup>, C. Schwenzel<sup>1</sup>,  
T. Aarts-Riemens<sup>1</sup>, R. Paap<sup>1,4</sup>, L.C.D.E Gatti<sup>1</sup>,  
A. Miranda-Bedate<sup>1</sup>, M.I. Pascoal Ramos<sup>1,4</sup>,  
O. Heidenreich<sup>2</sup>, H. Stunnenberg<sup>2</sup>,  
L. Meyaard<sup>1,4†</sup>, J. Kuball<sup>1,3†</sup>, Z. Sebestyen<sup>1†</sup>

\*Shared first authorship  
†Shared senior authorship

<sup>1</sup>Center for Translational Immunology, University Medical Center Utrecht,  
Utrecht University, Utrecht, Netherlands

<sup>2</sup>Princess Máxima Center for Pediatric Oncology, Oncode  
Institute, Utrecht, The Netherlands

<sup>3</sup>Department of Hematology, University Medical Center Utrecht, Utrecht  
University, Utrecht, Netherlands

<sup>4</sup>Oncode Institute, Utrecht, The Netherlands

**Manuscript in preparation.**

## Abstract

Despite recent successes in adoptive T cell therapies against hematological malignancies, response rates remain variable, and patients often experience relapse post-treatment. This phenomenon is potentially influenced by the immunosuppressive tumor microenvironment within the bone marrow (BM), a complex niche where mesenchymal stem cells (MSCs) play a pivotal role, by producing extracellular matrix and immunomodulatory factors. However, the specific contribution of MSC-mediated immunomodulation to the outcome of adoptive T cell therapies is not understood.

We built an experimental and analysis pipeline that integrates single-cell functional data from a multicellular 3D BM model into single-cell RNA sequencing analysis. In this system we distinguished immunosuppressive (s-MSC) from permissive MSC (p-MSC). These MSC donor-intrinsic phenotypes differ in their capacity to support or suppress engineered T cell mediated tumor cell killing. Permissive MSCs (p-MSCs) display dynamic transcriptomic profiles that adapt to the surrounding cellular environment, particularly in the presence of tumor and immune cells, while the transcriptomic heterogeneity of immunosuppressive MSCs (s-MSCs) is more limited. Furthermore, we show that suppressive versus permissive MSCs differ in their collagen gene expression profile and suppress the migratory and cytolytic capacity of genetically engineered T cells, which is dependent on the inhibitory collagen receptor LAIR-1 on T cells.

In summary, using a 3D co-culture model we reveal donor-intrinsic differences in the capacity of MSC to suppress anti-tumor T cell activity in the bone marrow niche through extracellular matrix remodeling, possibly explaining patient-specific responses to engineered T cell therapy.

## Introduction

Adoptive T cell therapies (ACT) have risen, over the past few decades, as one of the most promising novel treatments against cancers, such as leukemia's or other hematological malignancies. Despite recent successes of immunotherapies in on-going clinical trials targeting several types of blood cancers[1-6], and the approval CART therapies by the Food and Drug Administration (FDA)[7-10], it is difficult to predict heterogenous responses of patients and the relatively high chance for relapse after treatment [11, 12].

The ACT most extensively studied and clinically tested are chimeric antigen receptor (CAR) T cells, which target highly specific antigens expressed in tumor cells [13]. However, the high dependency on the surface expression of these hyper specific antigens provides a window for the tumor to become resistant to the therapy via antigen escape, increasing relapse in patients [14, 15]. Hence, novel ACTs are being studied, such as  $\alpha\beta$  T cells engineered to express a defined  $V\gamma 9V\delta 2$  TCR (TEGs) [16, 17] and novel dual targeting TEGs[18].  $\gamma\delta$ TCRs recognize elevated levels of phosphoantigens (pAg) generated through the mevalonate pathway, allowing for MHC independent activation [19-21].

Despite considerable efforts put into improving these therapies, the major roadblock that all T cell immunotherapies face, the tumor microenvironment (TME), it's still largely unknown and misunderstood. The complexity of its cellular composition, the non-cellular factors involved, and the cross-talk with tumor cells all create an adverse hostile environment which hinders anti-tumor responses and support tumor growth [22]. The bone marrow (BM) microenvironment is a complex niche, comprised mostly of endothelial progenitor cells (EPCs) and mesenchymal stem cells (MSC), in which hematopoietic stem cells (HSCs) reside. These HSCs rely on local interaction and support of stromal cells within this niche to facilitate their regulation and hematopoietic function [23, 24], hence, it's the ideal environment for pathological hematopoietic cells proliferation and survival [25], acting as a tumorigenic driver for leukemia's.

BM-MSCs are a very heterogeneous population of cells with self-renewal capacity and the ability to differentiate to multiple lineages: osteocytes, adipocytes and chondrocytes [26]. In the tumor microenvironment, MSCs promote growth of tumor cells and possess immunosuppressive features which further allow the tumor to escape immune surveillance [27]. MSCs contribute substantially to the formation and remodeling of the extracellular matrix (ECM) of the TME, supporting tumor growth and metastasis [28]. To do so, MSC secrete components of the fiber network, such as collagens [29], as well as metalloproteinase and lysyl oxidases which are enzymes involved in the remodeling of the morphology, thickness and stiffness of the matrix [30]. Increasing our understanding

on the immunomodulatory role of MSCs, could shed light on the reason behind the variability in response rates between patients and how to intervene with these mechanisms for the improvement of T cell-based therapies and their clinical outcome. Thus, in this study, we performed an in-depth analysis of the immunomodulatory properties of MSCs. To this end, a single cell T cell function in a malignant 3D bone marrow model was combined with single-cell RNA sequencing for a full characterization of the role MSCs play in the tumor microenvironment.

## Results

### Donor-dependent MSC immunomodulation affects T-cell efficacy and migration

To assess the immunomodulatory effects of MSC from different individuals on T-cell immunotherapies, we designed a multifaceted 3D model with tumor cells, MSC, endothelial cells and different types of immune effector cells to mimic the malignant bone marrow niche [25]. (**Figure 1A**). When using TEGs as immune effector cells, killing efficacy differed in the presence of five randomly chosen MSC donors: When using MSC from donor 03, 06 and 09 TEGs were unable to kill RPMI-8226 tumor cells in the presence of Pamidronate while when using MSCs from donor 13 and 18 TEGs were able to kill up to 60% of all tumor cells (**Figure 1B**). Consequently, MSC donors were categorized accordingly into two primary groups based on their ability to influence T cell-specific tumor killing: immunosuppressive MSCs (s-MSC: donors 03, 06, and 09) and immunopermissive MSCs (p-MSC: donors 13 and 18). Migration of TEGs into the bottom compartment of the Transwell system was likewise significantly diminished when s-MSC were utilized in comparison to p-MSC (**Figure 1C and Supplemental Figure 1**). Immunomodulatory effects by s-MSC on TEGs was again seen when using various primary pediatric leukemia samples and leukemic cell lines as tumor targets, indicating the immunoregulation of TEGs by MSCs is donor-specific and independent of the tumor target (**Figure 1D**). Similarly, the immunosuppressive effect of s-MSC on T-cells compared to p-MSC was also observed when introducing BCMA CAR T-cells instead of TEGs to target RPMI-8226 (**Figure 1E**). Importantly, s- and p-MSCs did not differ in their proliferation capacity in culture neither in the co-cultures settings (**Figure 1F**). Together, these findings suggest that MSCs have a donor-dependent effect on tumor targeting by T-cells independent of the leukemic model or T-cell therapy implemented in the model.

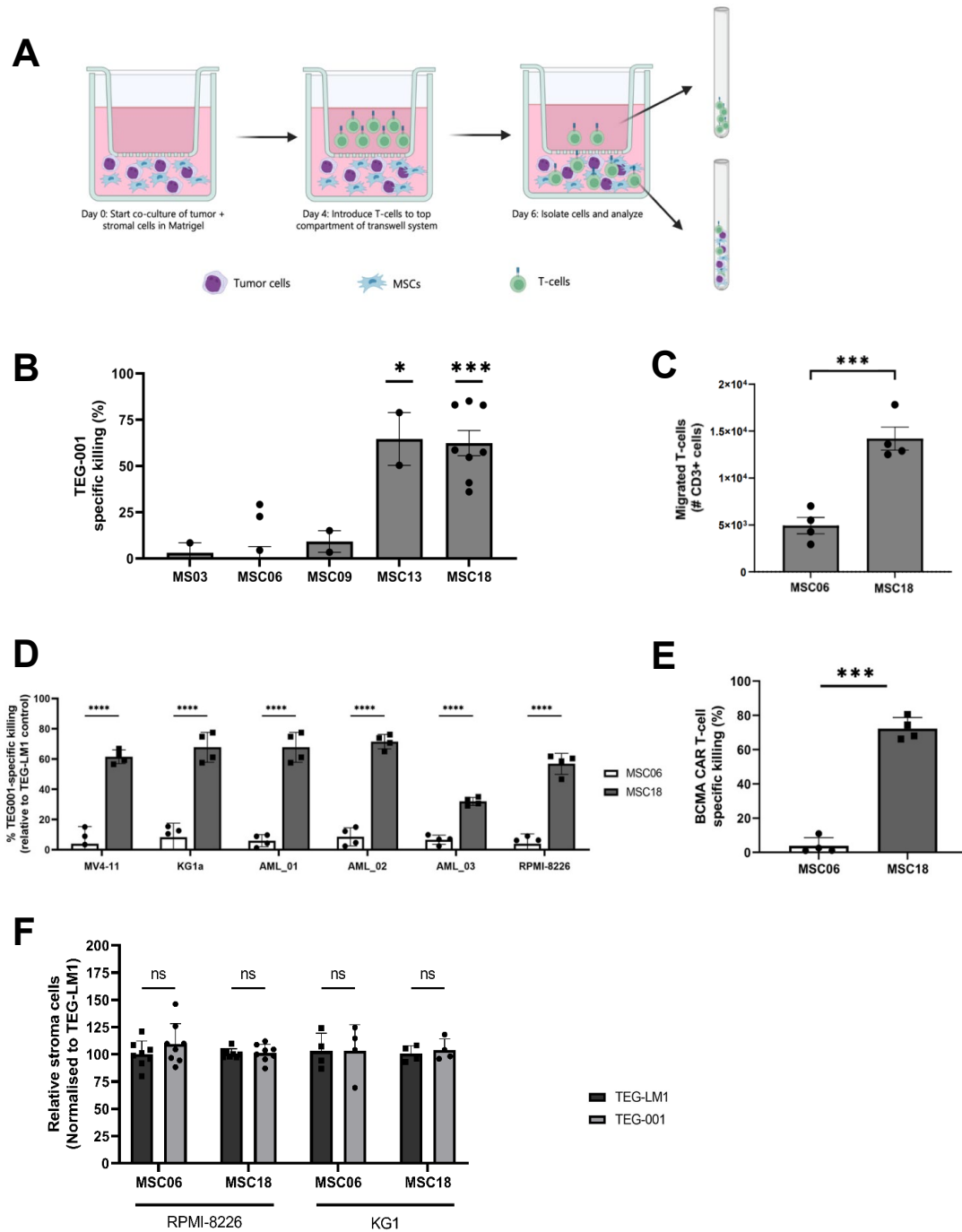


**Figure 1. 3D bone marrow model reveals donor-dependent MSC immunomodulation that affects migration, persistence, and tumor-killing capacity of T-cells. (A)** Schematic depicting the components and timeline of 3D in vitro model designed to mimic the bone marrow TME (designed with Biorender). **(B)** Killing of RPMI-8226 cells by TEG001 relative to TEG-LM1 control on day 6 when co-cultured with MSCs from 5 different healthy donors. **(C)** Total migrated TEG001 cells in bottom compartment of Transwell system on day 6 when co-cultured with RPMI-8226 and immunosuppressive (MSC06) or permissive (MSC18) stromal cells. **(D)** Killing of patient-derived AML cells (donors 01, 02, 03) and AML cell lines by TEG001 on day 6 when co-cultured with MSC06 or MSC18 (normalised to TEG-LM1 control). **(E)** Killing of RPMI-8226 by BCMA CAR T-cells on day 6 when co-cultured with MSC06 or MSC18 (normalized to TEG-LM1 control). **(F)** Total MSC cell counts on day 6 after co-culture with RPMI-8226 and TEG001 (normalised to TEG-LM1 control).

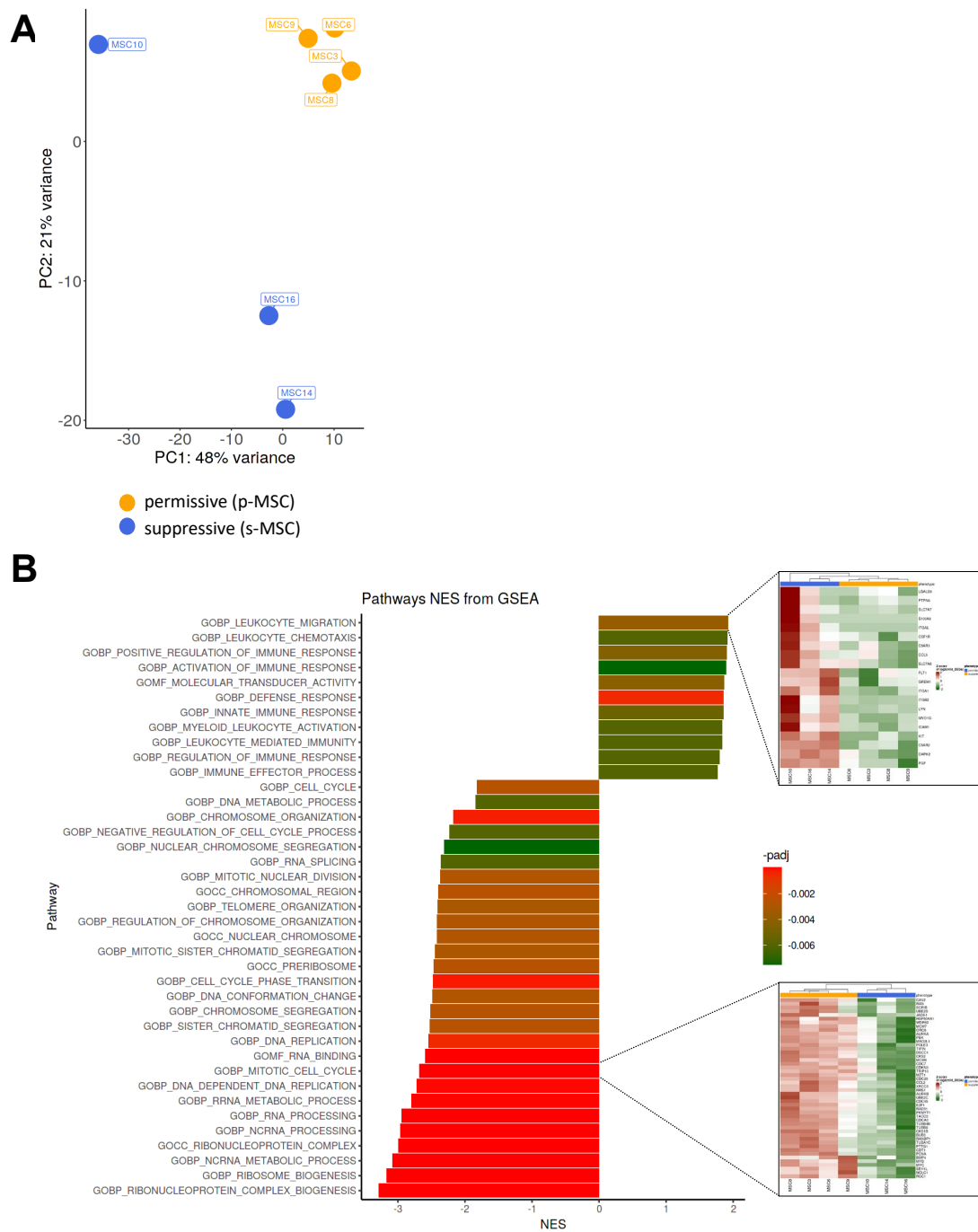


**Figure 2. Immunosuppressive MSCs display a more rigid transcriptomic profile at steady state with enriched transcription of cell division genes compared to the more variable profile of permissive MSCs. (A)** Principal component analysis (PCA) plot of RNAseq transcriptomic analysis done on immunosuppressive MSCs (donors 3, 6, 8, 9) and permissive MSCs (donors 10, 14, 16) cultured at steady state. The immunomodulation of these donors was previously characterized using the 3D BM model. **(B)** Gene set enrichment analysis (GSEA) plot depicting the statistically significant biological pathways for the immunosuppressive and permissive MSCs (left). Unsupervised clustering of the MSCs based on relevant genes from marked pathways supports the phenotypic split between the immunosuppressive and permissive MSCs (right).



## Transcriptomic profiles of p-MSCs and s-MSCs reflect distinct programs

To enhance our understanding of how mesenchymal stem cells (MSCs) with different capacities to modulate T cell-mediated tumor cytotoxicity are regulated at the transcriptomic level, we conducted RNA sequencing (RNAseq) on a panel of s-MSCs and p-MSCs. Analysis of the transcriptomic data via principal component analysis demonstrated that s-MSCs displayed a more compact cluster in the space defined by the first two principal components, indicating a more homogenous gene expression profile relative to p-MSCs (**Figure 2A**). Gene Set Enrichment Analysis (GSEA) showed that, p-MSCs had higher enrichment of terms such as ‘leukocyte migration’, ‘chemotaxis’, ‘immune effector process’, suggesting their role in fostering an immune-tolerant milieu even in the absence of T-cells or tumor cells. Conversely, s-MSCs had increased enrichment of biological pathways like ‘cell division’, ‘metabolic processes’, and ‘protein production’ (**Figure 2B**). Despite the increased enrichment of cell division related genes in the transcriptomic profiles, we did not detect higher numbers of s-MSCs in co-cultures, as shown in Figure 1F.

## s-MSC and p-MSC do not only have a different transcriptomic heterogeneity, but also different plasticity

To deepen our comprehension of the transcriptomic regulation in mesenchymal stem cells (MSCs) within a malignant bone marrow environment, particularly when these cells are in contact with tumor cells and T cells, we established co-cultures of either s-MSCs or p-MSCs with pediatric AML blasts (referred to as ‘cancer’ in our single cell RNA-sequencing (scRNA) experiments) embedded in Matrigel and TEGs (**Figure 3A**). We designed an experimental matrix that incorporated various cellular combinations to replicate incremental complexity levels of the bone marrow microenvironment. After co-culture, samples were processed per experiment into scRNA libraries and submitted for sequencing. The initial cell type separation per experiments was facilitated by single nucleotide polymorphism (SNP) profiles as the experimental components originated from distinct individuals. The separation was corroborated using uniform manifold approximation and projection (UMAP) alongside cell type annotation methodology, which divided the combined datasets into three major cluster groups corresponding to the expected cell types: cancer, TEGs, and MSCs, each identified by the expression of their canonical marker genes (**Figure 3B**). When we labelled the UMAP-plots according to the experiments cell phenotypes we noticed that s- and p-MSC types showed the highest levels of heterogeneity within cell types. Further, to investigate the interactions of MSCs with the components of our constructed bone marrow model, we examined the transcriptomic profiles of each element individually, but aggregated from all experimental runs.

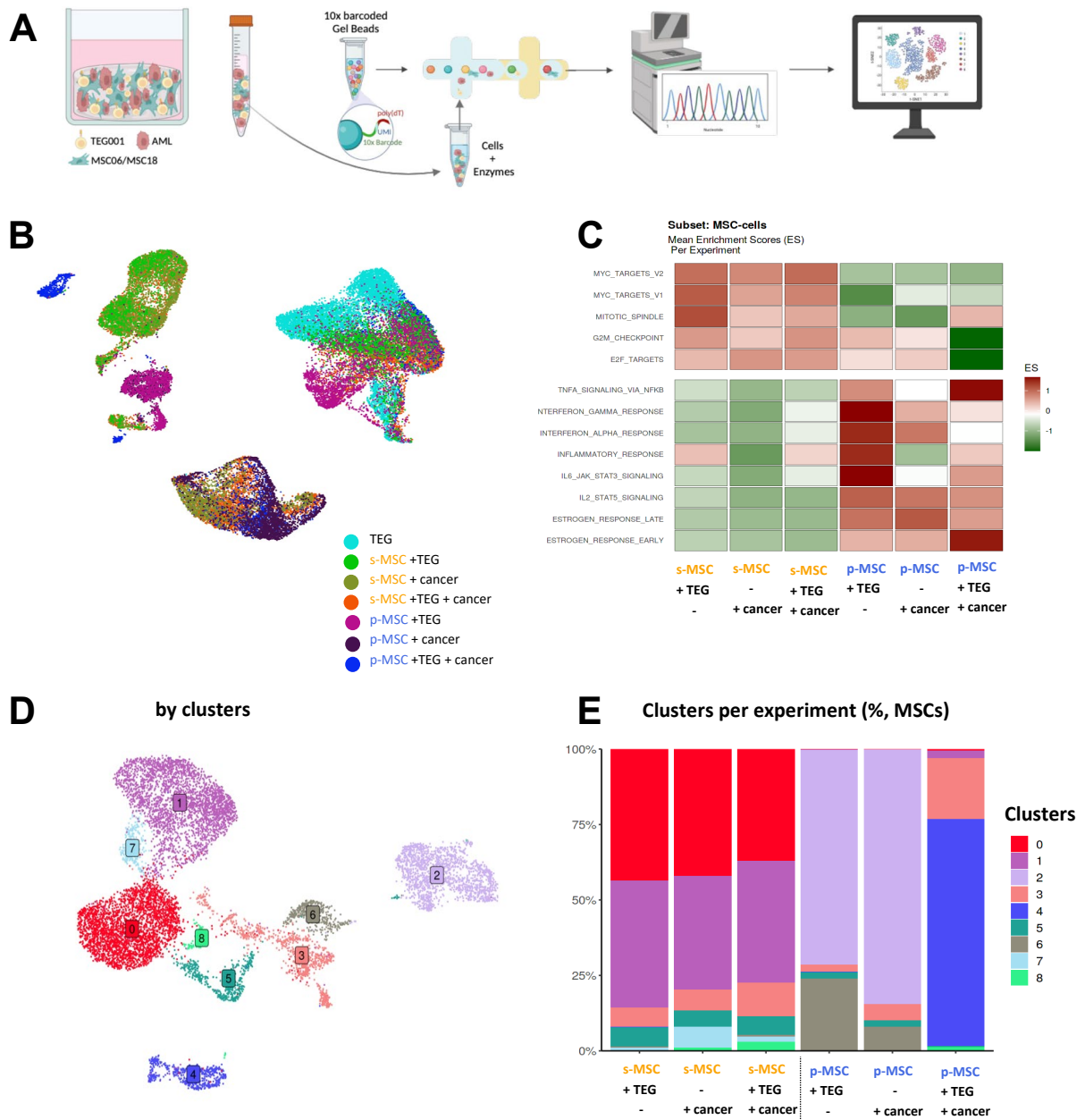


**Figure 3. Single-cell analysis reveals uniformity in the transcriptome of suppressive MSCs independent of TEG or tumor cell presence, while the transcriptomic activity of permissive MSCs is more susceptible to its environment. (A)** Process of single cell sequencing of the 3D co-cultures of the bone marrow niche **(B)** UMAP plot of unsupervised clustering of the combined dataset, annotated by experiment (cell type composition). **(C)** GSEA plot of a subset of HALLMARK genesets over the pseudobulk profiles of MSC subsets per experiment. **(D)** UMAP plot displaying the unsupervised clustering of MSC subsets from all experiment. **(E)** Cluster composition of the MSC population per experiments (%). The colors correspond to those of the clusters in (D).

Initiating our analysis, we conducted gene set enrichment analysis (GSEA) on the pseudobulk transcriptomes of MSC populations across our data collection, focusing on a selection of hallmark gene sets from molecular signature databases. This analysis reaffirmed the proliferative nature of s-MSCs and the pro-inflammatory milieu associated with p-MSCs, consistent across various experimental conditions (**Figure 3C**). To profile the cellular compositions of each dataset from our experimental conditions, we applied unsupervised clustering and identified eight distinct MSC clusters (**Figure 3D**).

After clustering we split the dataset per experiments to reveal the effect of conditions over the cluster compositions. In case of s-MSCs, cluster0 (top differential markers: KRT19, TIMP3, CHI3L1) and cluster1 (TOP2A, CENPF, MKI67) (Supplemental Data) were predominant, with their proportions remaining stable irrespective of whether cancer cells or TEGs were present alone or in combination (**Figure 3E, column 1-3**). GO-term analysis of cluster 0 revealed terms related to ossification and organ development, which led us to investigate the published references of the leading marker genes (**Supplemental Figure 2**). Both KRT19 (keratin 19) as an intermediate filament molecule [31], the metalloprotease inhibitor TIMP3 (TIMP metalloprotease inhibitor3) (<https://journals.aai.org/jimmunol/article/188/6/2876/85583/Stromal-TIMP3-Regulates-Liver-Lymphocyte>) and the secreted glycoprotein CHI3L1 (chitinase-3-like protein1) [32] have been associated with immunosuppression and extracellular matrix, hinting at a potential role in fostering immunoresistance within the tumor microenvironment (TME). Cluster 1 represented the cells with proliferative signatures, mirroring the proliferative profiles of s-MSCs in the (bulk) RNAseq experiments (**supplemental data**).

Contrariwise, p-MSCs displayed a different profile as compared to s-MSC in the presence of TEGs or cancer cells (**Figure 3E, column 4-6**). Under conditions with exclusively TEGs or cancer cells clusters 2 and 6 prevailed. These clusters were characterized by differential gene expression associated with hypoxia and apoptosis (cluster2 (BNIP3, HMOX1, LDHA)) and stress response pathways (cluster6 (PLCG2, PLK2, NFKBIZ)). In addition, in the presence of both TEGs and cancer cells, cluster 2 and 6 of p-MSCs showed in contrast to s-MSC a major shift towards cluster 3 and 4, reflecting an upregulation of genes implicated in extracellular matrix construction, (cluster3 (COL4A1, POSTN, THBS1)), and genes involved in immune cell infiltration, like CRYAB (cluster4) [33]. These findings suggest that the transcriptomic landscape of s-MSCs is not only different from p-MSCs but also comparatively stable, whereas p-MSCs exhibit an additional degree of plasticity in the presence of tumor and immune cells.

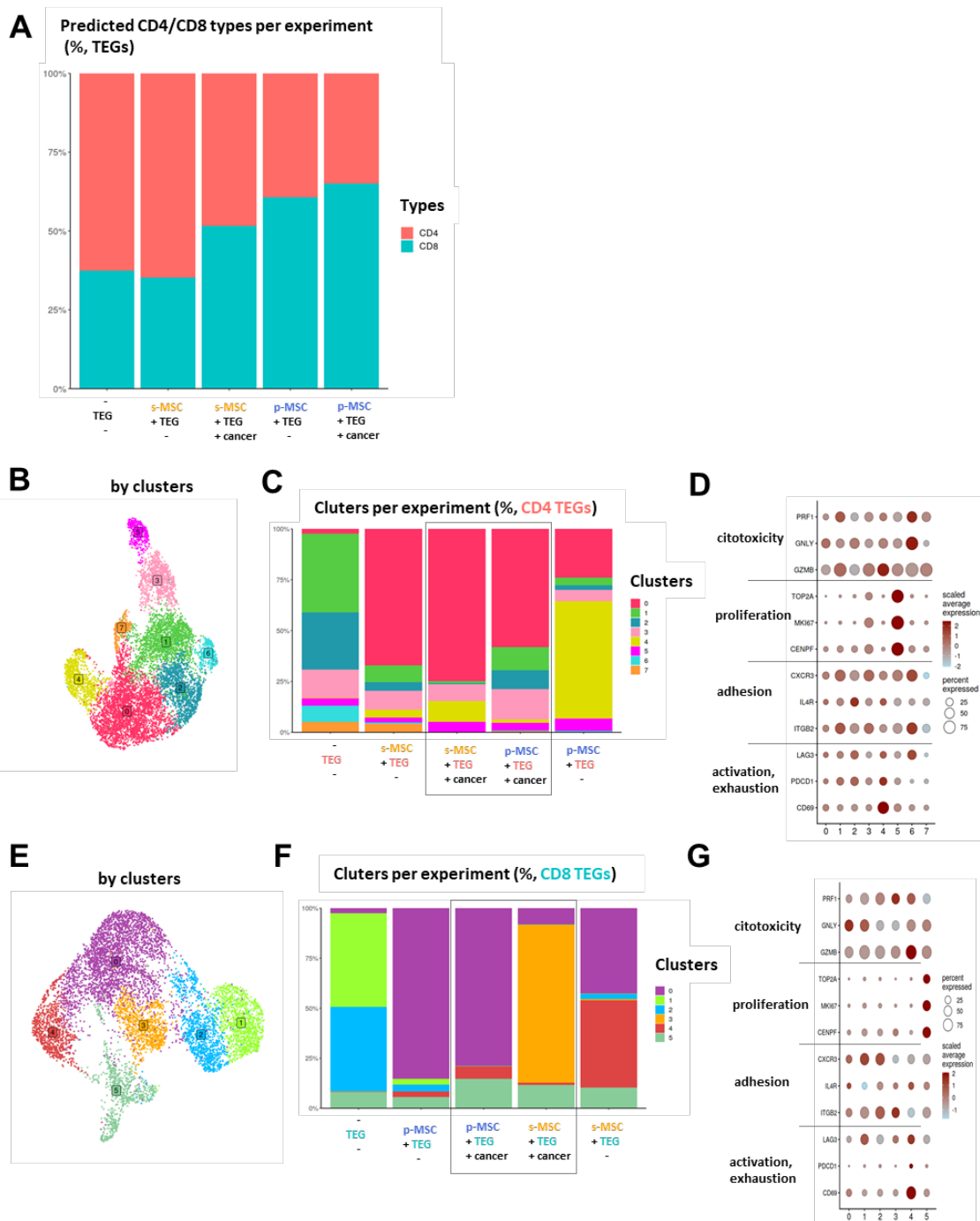


**Figure 4. Permissive MSCs allow for a transcriptomic shift primarily in the TEG population, while suppressive MSCs constrain TEG to a distinct, transcriptomic profile independent of tumor presence. (A)** CD4 / CD8 composition of the TEG subset from each experiment (%), according to our type prediction. **(B)** UMAP plot depicting the unsupervised cluster analysis of CD4+ TEGs. **(C)** Cluster composition of the CD4+ TEG population per experiments (%). The colors correspond to those of the clusters in (B). **(D)** Density dot plot of the percentage of cells from CD4+ TEG clusters (from B) that express a given gene ('percent expressed') and the scaled average expression of canonical marker representing the marked terms. **(E)** UMAP plot depicting the unsupervised cluster analysis of CD8+ TEGs. **(F)** Cluster composition of the CD8+ TEG population per experiments (%). The colors correspond to those of the clusters in (E). **(G)** Density dot plot of the percentage of cells from CD8+ TEG clusters (from B) that express a given gene ('percent expressed') and the scaled average expression of canonical marker representing the marked terms.

### s- and p-MSC impact transcriptomic heterogeneity of TEGs differently

Since s- and p-MSCs affected tumor targeting of T cells differently, we aimed to understand whether the s- and p-MSCs impact transcriptomic heterogeneity of TEGs. To this end, we dissected TEG transcriptomic data from all experiments and performed unsupervised clustering. First, we focused on the distinction of CD4<sup>+</sup> and CD8<sup>+</sup> TEGs. Given the absence of proteomic information for the single-cell transcriptomic profiles, we utilized a support vector machine (SVM) algorithm to predict the CD4/8 status of TEGs. This prediction was based on our earlier multiomic single-cell RNA sequencing experiment that provided us with profiles of FACS-sorted CD4<sup>+</sup> and CD8<sup>+</sup> TEG populations (**Supplemental Figure 3A-D, supplemental data**). Upon comparing the CD4/CD8 distribution across different experimental TEG populations, we observed a greater proportion of CD8<sup>+</sup> TEGs in the milieu containing p-MSCs (**Figure 4A**).

Firstly CD4<sup>+</sup> and CD8<sup>+</sup> TEGs cultured alone, had a different cluster composition when compared to transcriptomic composition of TEGs in the presence of MSC. For CD4<sup>+</sup> TEGs (**Figure 4B-C-D**), a predominantly GZMA and GZMA-related cytotoxicity cluster1 gave way to cluster0, characterized by GNLY-associated cytotoxicity along with genes implicated in 'response to external stimulation' and 'apoptosis' (Supplemental Figure 3E, supplemental data). The newly appeared cluster0 represented the majority of CD4<sup>+</sup> TEG cells in all co-culture setups involving s-MSCs, in the presence and absence of tumor cells (**Figure 4C and D**). In contrast, the combination of p-MSCs with TEGs spawned an additional cluster (cluster4) indicative of T-cell activity and exhaustion, distinguished by CCL3 and CCL4 expression. This cluster disappeared when tumor cells were introduced and CD4<sup>+</sup> TEGs in the presence s-MSCs or p-MSCs did not differ substantially, except for the lower representation of cluster0. (In **Figure 3 C and F** we ordered the two most complete co-culturing experiments, with different MSC-types, next to each other and squared them to guide the visual comparison.)

Similarly, CD8<sup>+</sup> TEG populations (**Figure 4E-F-G**) showed clusters 1 and 2 as dominant clusters in the absence of any additional components of the model, associated with TCR-binding (cluster1 (HLA-DRB1/5)), adhesion (cluster2 (CXCR6)). The clusters of the CD8 'TEG alone' condition were replaced by a GNLY-marked cluster that (unlike in CD4s) additionally expressed genes related to oxidative phosphorylation (NDUFA1, ATP5MD) (**Supplemental Figure 3F, supplemental data**). Again, p-MSCs alone induced the emergence of a new cluster (cluster4) expressing CCL3 and CCL4. In contrast to CD4<sup>+</sup> TEG in the presence of p-MSCs, the CD8<sup>+</sup> TEG cluster composition changed markedly with the addition of tumor cells when compared to comparable experimental conditions with s-MSCs (**Figure 4, marked with the square**). The exclusively identified cluster in this scenario (cluster3 in p-MSCs + CD8 TEG + cancer cells) was defined by terms such as 'response to stress' and 'apoptosis' (BTG1, BCL2L11). We conclude, that both s-MSCs and

p-MSCs changed transcriptomic heterogeneity of CD4+ and CD8+ TEGs, however only in the presence of p-MSCs did CD8+ TEGs show additional plasticity in transcriptomic heterogeneity once they encountered tumors.

### **Immunopermissive environments display higher number of potential cell-to-cell interactions**

While we established that s- and p-MSCs distinctly influence tumor-specific T cell functions within the 3D bone marrow niche, the question arose whether this modulation stemmed from specific receptor-ligand interactions. To explore this, we utilized the cell-chat algorithm, which predicts potential receptor-ligand interactions by calculating communication probabilities based on gene expression data, of a list of receptors and their ligands, and their overall representation throughout the compared groups.

Our analyses focused on comparing two separate experiments, each containing all three components (MSC + CD4 TEG + CD8 TEG + cancer cells (The CD4-CD8 annotations of the TEG cells were from our previous analysis.)), with the only variable being s- or p-MSCs. As such, each half of the analysis contains cells that could potentially interact (unlike when combining the cells from all experiments). We identified communication between every compartment of the model and also pathways within the same compartment. The MSC > MSC communication represented a prominent part of the complete list of potentially active channels (**Figure 5A**). Overall, in permissive conditions we detected higher number of different channels (**Figure 5B**).

We next compared the information flow (defined by the sum of communication probabilities among all pairs of cell groups in our analysis), for specific signaling pathways in suppressive versus permissive conditions.

Certain pathway groups, such as VISFANTIN and NOTCH prominently increased their information flow when s-MSCs were present, while with p-MSCs, pathways like BAG, GALECTIN and MHC-I were more prominent (**Figure 5C**). To further dissect these findings, we categorized the channels into sending (outgoing, green) and receiving (incoming, blue) pathways and compared their prevalence across the three cell types under both conditions (**Figure 5D, E**). Both s- and p-MSCs were highly represented both as senders and as receivers, underscoring the importance of MSC > MSC signaling within our models. The lower halves of these plots show channels that were detected in permissive but not in suppressive conditions. The higher number of detected channels at both the outgoing and the incoming sides in the permissive conditions is mirrored again on the lower halves of **Figure 5D and E**. The channels listed there are only detected on the permissive environments. The plasticity of CD8 TEGs that we described earlier in **Figure 4F** is now gaining an additional level of explanation as these cells did not only

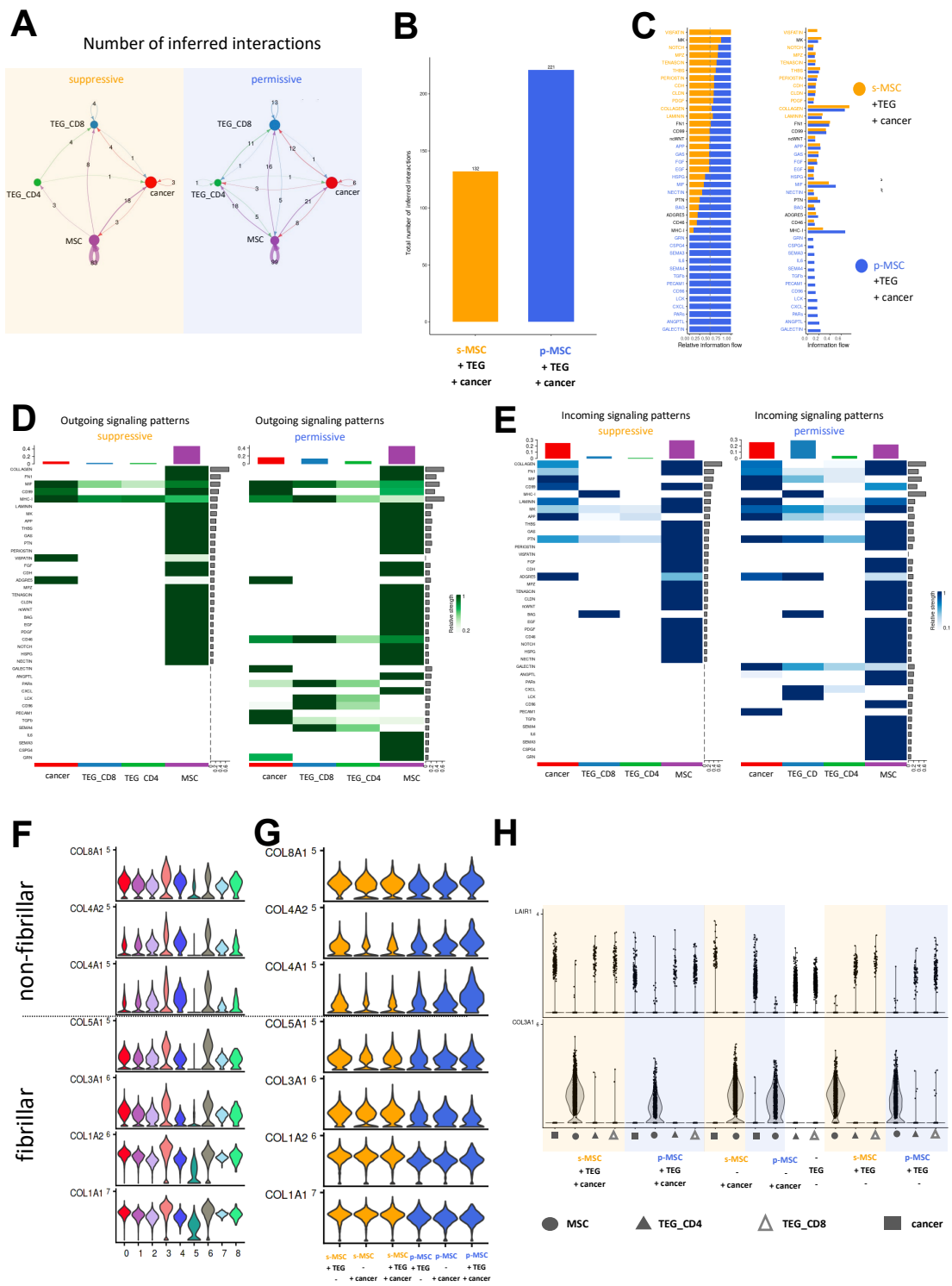


**Figure 5. MSCs represent an important cell-cell communication hub in the model marrow model. (A)** Comparison of numbers of interaction within the complete suppressive and permissive experiments. **(B)** Number of detected channels per experiment. **(C)** List of detected channel groups, marking their representation per experiment. **(D)** List of incoming channel groups, per cell type (source) per experiment. **(E)** List of outgoing channel groups, per cell type (receiver) per experiment. **(F)** Scaled expression of main detected collagen genes, per MSC-clusters (from Figure 3D). **(G)** Scaled expression of main detected collagen genes, in MSC cells per experiment (from Figure 3B). **(H)** Scaled expression of LAIR-1 and COL3A1, per cell types per experiment.

express higher number of ligand-receptor pairs compared to the CD4 TEGs, but also the number of their active channels were higher in the permissive environment (compared to the permissive).

This groups of channels in **Figure 5 D and E** contained potential points of interventions, leading us to initiate validation and exploratory studies. However, first we followed up the COLLAGEN pathway, a channel that was highly represented in both conditions (**Figure 5C**), and is biologically relevant considering the MSCs and the extracellular matrix.

We analyzed the data according to the fibrillar and non-fibrillar classification of collagens, attributing per-cluster annotations to identify the primary sources of various collagen types (**Figure 5F, as clusters from Figure 3D,E**). Cluster3 showed high levels of multiple types of collagens which reflected on the associated GO-terms (**es Supplemental Figure 2**), along with clusters 6 and 8. To draw comparative insights into the collagen production influenced by p- or s-MSCs under differing conditions, we combined the MSC profiles per each experiment (**Figure 4G**) and discerned that a fibrillar-type collagen signature (involving COL1A1, COL1A2, COL3A1, COL5A1) was more associated with s-MSCs, in contrast to the non-fibrillar types (COL4A1, COL4A2, COL8A1) prevalent in the permissive conditions. This prompted us is the idea to investigate the COLLAGEN pathway through the lens of a receptor that was not present in the original cell-chat reference dataset but is described to bind to collagen; LAIR-1 [34-36], an immunoinhibitory receptor. Specifically, COL3A1's link to adverse cancer prognosis potentially via LAIR-1 interaction garnered our attention [34-38]

Next, in a comparative analysis of LAIR-1 and COL3A1 expression across the entire dataset, grouping the cells per cell-type per experiment (Figure 5H) confirmed the MSCs as the primary source of collagen expression and both CD4 and CD8 TEGs as components that express the collagen-binding LAIR-1 receptors. We made several novel observations: firstly, not only TEGs, but also the cancer cells expressed LAIR-1. Secondly, this expression was more prominent when the cancer cells were co-cultured with s-MSCs, compared to the p-MSC condition. Lastly, LAIR-1 was induced in TEGs when co-cultured with MSCs.



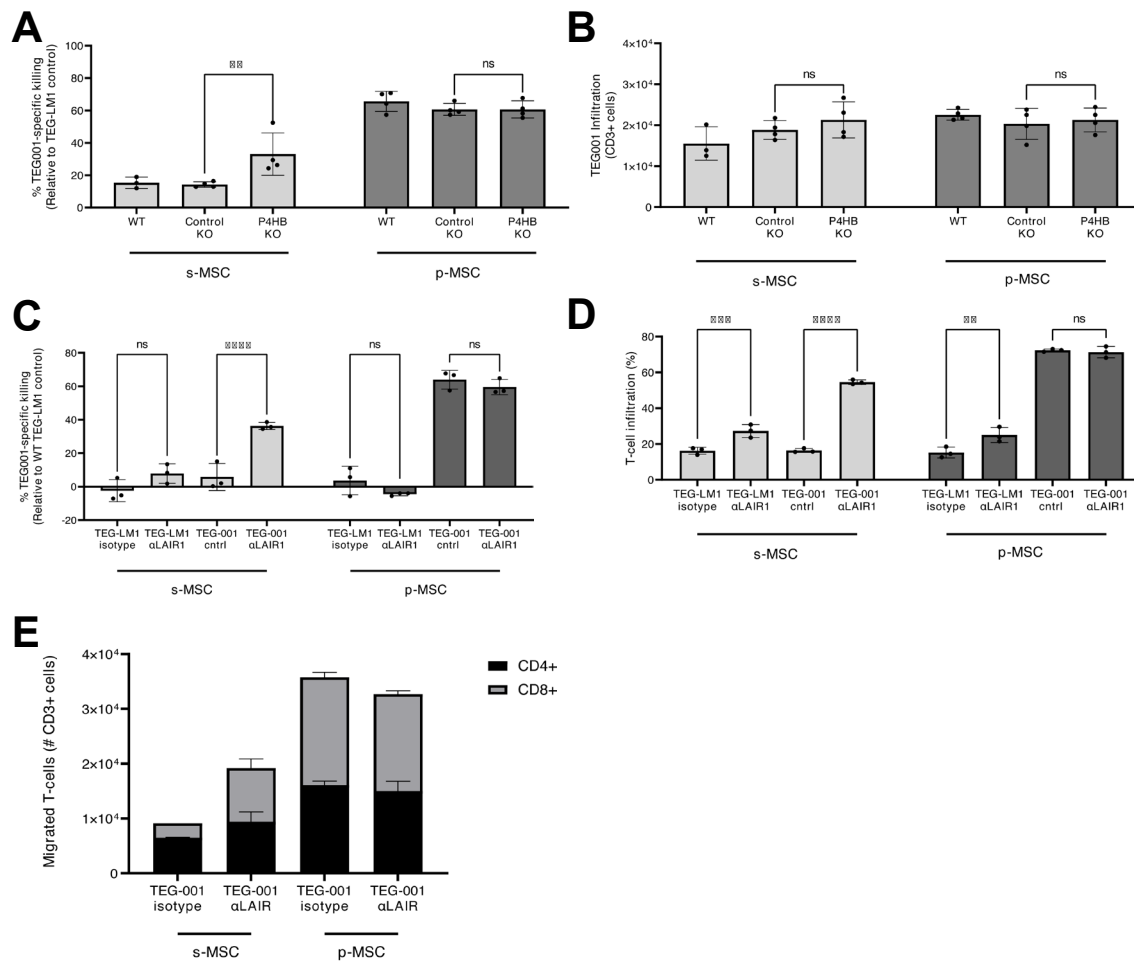


**Figure 6. Interference of collagen folding in MSCs and LAIR1-mediated binding to collagen in TEG001 both increase tumor killing in the suppressive microenvironment. (A)** TEG001-specific killing of RPMI-8226 and **(B)** TEG001 infiltration into bottom compartment of 3D model on day 6 after  $\beta$  subunit of prolyl 4-hydroxylase (P4HB) gene was knocked out in MSC06 and MSC18 on day 0. **(C)** TEG001-specific killing of RPMI-8226 and **(D)** TEG001 infiltration on day 6 after antibody blocking of LAIR1 on TEG001 (+ isotype control) prior to T-cell administration on day 4. **(E)** Total amount of migrated CD4+ and CD8+ TEG001 and TEG-LM1, treated with LAIR Isotype and LAIR1 blocking antibody, in the bottom compartment of the transwell system of an in vitro 3D RPMI-8226 model made with MSC18 and MSC06.

### Interference with LAIR1 increases cancer killing in the presence of s-MSC

To validate that collagen structures in s-MSCs play a role in modulating anti-cancer CD8+ T cell functions via cell-cell interactions and thus play a role in the immunosuppression of T cell-mediated cancer killing, we investigated whether collagen binding by LAIR-1 impacts T cell function. LAIR-1 was higher in expression on CD8+ as compared to CD4+ TEGs (**Supplemental Figure 4**). Furthermore, we knocked out the protein disulphid isomerase (P4HB), an enzyme responsible for collagen polymerization in cells [39], in both s-MSC and p-MSC using CRISPR Cas (MSC<sub>P4HB-KO</sub>). These s-MSC<sub>P4HB-KO</sub> were then

seeded in 3D bone marrow niches containing RPMI-8226 and treated with CD4<sup>+</sup> and CD8<sup>+</sup> TEGs in 1:1 ratio. Using s- $MSC_{P4HB-KO}$  instead of s- $MSC$  resulted in significant increase in cancer killing by TEG cells p- $MSC$  and p- $MSC_{P4HB-KO}$  did not affect cancer killing (Figure 6A). Migration capacity of TEGs in the 3D bone marrow niche was however not affected by s- $MSC_{P4HB-KO}$  (Figure 6B).

To further investigate the mechanism how collagens produced by MSCs could modulate T cell function, we inhibited LAIR-1, that binds to collagens [35] by using  $\alpha$ -LAIR-1 blocking antibodies. We pretreated TEGs with either  $\alpha$ -LAIR-1 or isotype control antibodies and used them as treatment in the 3D bone marrow niche. LAIR-1 blocking on TEGs rescued cancer killing only when s- $MSC$  was present but not in the presence of p- $MSC$  (Figure 6C), gain emphasizing the role of LAIR-1 in the context of s- $MSC$ . Altogether our data demonstrate that collagen expression by s- $MSC$ s play an important role in creating an immunosuppressive milieu in the malignant bone marrow impacting anti-cancer potential of cancer specific T cells.

## Discussion

In this study, we identified from healthy individuals s- $MSC$  and p- $MSC$  which differ in transcriptomic heterogeneity, transcriptomic plasticity, and function. While s- $MSC$  have been rigid in terms of transcriptomic heterogeneity, plasticity and were mainly immune suppressive, p- $MSC$  showed more transcriptomic plasticity not only themselves in the presence of cancer cells and engineered immune cells but were also able to induce transcriptomic plasticity in CD8<sup>+</sup> T cells and associated with an improved killing of leukemic blasts. P- $MSC$  created a milieu with more pro-inflammatory cytokine profiles. In addition, s- $MSC$  and p- $MSC$  rearranged the extracellular matrix differently with varying composition of collagens. This allowed to interfere in the presence of s- $MSC$  with either collagen polymerization or blocking collagen binding via LAIR1 which increased both killing and infiltration capacity of mainly cancer specific CD8<sup>+</sup> T cells.

Our data suggests that the differential  $MSC$  phenotypical profiles found are intrinsic to different individuals as distinct phenotypes grew out from different donors. This observation is in line with the observation that indeed  $MSC$  from different donors have different abilities to be immune suppressive when used for the treatment of acute graft versus host disease [40]. However, as we did not systematically compare multiple  $MSC$  clones from the very same donor we could not assess whether different individuals have exclusive s- $MSC$  or p- $MSC$  or whether both phenotypes are coexisting or one is dominant. Regardless of this consideration, we demonstrate that gene expression differences between s- and p- $MSC$ s are responsible for the immunomodulatory features. While s- $MSC$  have been stable in transcriptomic heterogeneity, p- $MSC$  further

changed profiles once T cells and cancer cells were added. However, functional consequences of s- and p-MSC have been maintained regardless of the cancer type present in the environment implying that this observation is not only relevant for the more extensively studied AML, but also other hematological cancer cell types like MM.

Transcriptomic heterogeneity in the infused engineered T cell product has been most recently described as major predictor for clinical outcome for various hematological malignancies [41]. We described that transcriptomic heterogeneity correlates with T cell behavior against solid cancers [42] and can be further modulated by different types of co-stimulation [18] against liquid and solid cancers. Our current data set implies that such 3D models might be too simplistic as simply the addition of MSC even in the absence of cancer cells further alters transcriptomic heterogeneity of engineered immune cells. Most importantly intrinsic abilities of MSC and the preference in s- or p-MSC has further major impact on shaping transcriptomic heterogeneity and most likely needs to be taken into consideration in individualized therapies. S-MSCs negatively affected the persistence and cancer killing capacity of CD8<sup>+</sup> T cells, which is in line with previous findings describing the immunomodulatory properties of MSC influencing effector cells. For instance, IFN $\gamma$  production by effector cells induces PD-L1 expression by MSCs, lead to T cell inactivation and exhaustion [43]. Furthermore, secretion of anti-inflammatory cytokines such as IDO1, TFG- $\beta$  and IL-4 among others [26, 27]. However, such studies did not dissect whether these properties are linked to all MSC or a property of s- or p-MSC. We showed now that the migration capacity of T cells to the cancer microenvironment was also strongly hindered by s-MSCs, while p-MSC induced pro-inflammatory genes in T cells.

Our data imply that s- and p-MSCs are able to remodel the extracellular matrix via expressing key proteins involved in matrix stiffening in line also other reports [44]. However, our data imply that different types of collagens are observed in either s- or p-MSC, suggesting that these may play an important role in the differential phenotype between MSCs. Assuming that different individuals favor either s-MSC or p-MSC this would argue for varying preferences in the extracellular matrix of healthy tissues and the cancer microenvironment. Here, we show that s-MSCs preferentially express type I, III and VI collagens, while p-MSC express type IV and XII collagens. Type I and III collagens are fibril-forming collagens that when highly expressed, lead to a dense fibrillary network which stiffens the ECM, a known hallmark of cancer [45]. Type I and III collagens have been also reported to be high affinity ligands for inhibitory receptor LAIR-1 [35, 36] and to inhibit the effector cytotoxic activity of CD8<sup>+</sup> T cells [46]. Our data now show that indeed CD8<sup>+</sup> TEGs expressed at the cell surface higher levels of LAIR-1, and thus, benefited the most from LAIR-1 blocking treatment in the suppressive MSC

environment. This effect is most likely due to an higher infiltration capacity of mainly CD8+ TEGs into the cancer microenvironment.

Altogether, we describe varying preferences for s- or p-MSK in different individuals, which associated most likely with different cell matrix already in healthy tissues. Intrinsic differences between s- and p-MSK derived from different individuals drive for many individuals a stronger suppressive phenotype through the modulation of the collagen composition. Once cancer develops cell matrix produced due to the presence of s-MSK can be detrimental for cancer immune surveillance and cancer immune therapies. Characterizing the individual preferences for MSK in patients' prior therapies might in the future allow to further individualize immune therapies through e.g. the addition of LAIR1-blocking antibodies.

## Methods

### Cell Culture

Bone marrow-derived mesenchymal stem cells (BM-MSCs) were isolated from healthy donors at the Utrecht University Medical Center. The BM-MSCs were cultured in DMEM medium (Fisher Scientific) containing 10% fetal bovine serum (FBS, Bodinco), 1% penicillin (100 U/mL) and streptomycin (100 µg/mL) (P/S) and 0.2 mM L-ascorbic acid-2-phosphate (Sanbio) and passaged once confluency reached ~80% using 0.5% trypsin-EDTA (Gibco). RPMI-8226 cells (ATCC) were maintained at a concentration of  $0.35 \cdot 10^6$  cells/mL in RPMI-1640 medium (Thermo Fisher Scientific) containing 10% FBS and 1% P/S.

All engineered T-cells (TEG-LM1, TEG001, HER2 CAR T-cells, BCMA CAR T-cells) were cultured using a two-week Rapid Expansion Protocol (REP) in which the T-cells are cultured with a mixture of irradiated Daudi cells (ATCC), human peripheral blood mononuclear cells (PBMCs, Sanquin Blood Bank, Amsterdam NL), and Lymphoblastoid Cell Line (LCL) cells (company). The T-cells and REP cell mixture are cultured with RPMI-1640 medium containing 2.5% human serum (UMC Utrecht, the Netherlands), 1% P/S, 2.5 mM beta-mercapotethanol (Gibco), IL-2 (50 U/mL), IL-15 (5 ng/mL), and PHA (1 µg/mL). Every 3-4 days within the two-week REP cycle, half of the media was refreshed, and IL-2 levels were replenished.

### Transfection and Lymphocyte Transduction

**Transfection of Retroviral Packaging Cells:** On Day 1, Phoenix-AMPHO cells (ATCC) are seeded and cultured at 37°C in DMEM media (Gibco) with 10% FCS and 1% P/S. On day 2, a transfection mixture of pHIT60 (gag, pol genes), pCOLT-GALV (env genes), FuGENE-HD Transfection Reaction (company), and the plasmid of interest (pMP71-TEGLM1, pMP71-TEG001, pBullet-BCMA-CAR, or pBullet-HER2 CAR) is prepared and incubated at room temperature for 20 minutes. The transfection mixture is then slowly added to the media of the Phoenix-AMPHO cells. On day 3, the DMEM media is replaced with complete huRPMI-1640 medium.

**T-cell Activation:** On day 2, PBMCs are selected for CD4+ and CD8+ T-cells using Human CD4 Microbeads (Miltenyi Biotec) and Human CD8 Microbeads (Miltenyi Biotec) according to the manufacturer's protocol. The isolated T-cells were then resuspended at a concentration of 2E6 cells/mL in complete RPMI-1640 medium and activated with Dynabeads T-Activator CD3/CD28 beads (30 ng/mL, Thermo Fisher Scientific, 11456D), IL-15 (154 U/mL), and IL-7 (1700 U/mL). The T-cells were plated in 6-well plates and incubated at 37°C.

**T-cell Transduction:** On day 4, retroviral supernatant from the Phoenix-AMPHO cells was collected, filtered using a 0.45  $\mu\text{m}$  syringe filter (Sastedt), and supplemented with IL-2 (50 U/mL) and Polybrene (5  $\mu\text{g}/\text{mL}$ , Sigma Aldrich). The activated T-cells were combined, magnetically depleted of Dynabeads, centrifuged, and resuspended in the retroviral supernatant. The T-cells were plated in 6-well plates, centrifuged at 25,000 rpm at 30°C for 60 minutes, and subsequently incubated overnight at 37°C. On day 5, the second transduction hit was performed as on day 4 with the exception of adding IL-2 to the retroviral supernatant. After centrifugation, the T-cells were restimulated with CD3/CD28 Dynabeads (30 ng/mL) and IL-2 (50 U/mL) and incubated at 37°C. When applicable, G418 neomycin (800  $\mu\text{g}/\text{mL}$ ) was added to select for the transduced T-cells. On day 10, IL-2 was added (50 U/mL). On day 11, magnetic Dynabead depletion was performed prior to placing the transduced T-cells on REP.

### 3D Bone Marrow *in Vitro* Model

Donor-derived primary mesenchymal stromal cells (MSCs) and either cancer cell lines or patient-derived samples were seeded in Matrigel in the bottom compartment of a Transwell system to allow for cell proliferation and structural resemblance of the cellular structure [25]. Two days later engineered T cells were subsequently administered to the top compartment, and through active migration, could reach and target cancer cells. After additional two days co-culture the top and bottom compartments were collected separately, and cellular components were separated from the extracellular matrix components. We were able to then quantify absolute number of cells of each cellular subset allowing us to assess cancer killing, T-cell migration, and the immunomodulatory effects of MSCs.

**Model Assembly (Day 1):** BM-MSCs and RPMI-8226 cells were stained with DiD and DiO dye (Thermo Fisher Scientific), respectively, according to the manufacturer's protocol. The cells were then combined (70,000 MSCs/well; 20,000 RPMI-8226 cells/well) and resuspended in growth-factor reduced Matrigel (Corning Life Sciences) that had previously been diluted to a concentration of 6.9 mg/mL using DMEM media. 75  $\mu\text{L}$  of cell suspension was then distributed to the bottom of wells of a Transwell plate with a 3.0  $\mu\text{m}$  pore membrane (Corning Life Science). Next, the plate was incubated at 37°C for 10 minutes. 125  $\mu\text{L}$  of media (1:1 ratio of complete RPMI-1640 and complete DMEM media) was added to both top and bottom compartments once the Matrigel solidified. The Transwell plate was left to incubate at 37°C for 4 days.

**T-cell Administration (Day 5):** Engineered T-cells were administered to the top compartments of the Transwell system (50,000 cells/well) using complete RPMI-1640 medium. When applicable, T-cells were pre-incubated with 5 $\mu\text{g}/\text{mL}$  blocking antibodies against NKp30 (Clone #210845; R&D Systems) for 1 hour prior to administration.

Pamidronate (Calbinochem) was added to all TEG conditions for a final concentration of 10  $\mu$ M. Plate was then left to incubate at 37°C for 2 days.

**Cell Isolation (Day 7):** Cell suspensions in the top compartments were collected and placed in FACS analysis tubes (company). The top compartments were then washed once with FACS buffer (Phosphate-buffered Saline (PBS) with 1% sodium azide and 1% bovine serum albumin (BSA)) and added to the analysis tubes accordingly. To isolate the cells from the Matrigel in the bottom compartments, two consecutive incubations of 20 minutes with Cell Recovery Solution (Corning Life Sciences) were performed prior to being placed in FACS analysis tubes. The samples were then washed, stained, and measured using flow cytometry. Equal amounts of Flow Count Fluorophores (Beckman Coulter) were added to all samples prior to measurement.

### Flow Cytometry

Samples were stained for 20 minutes at 4°C using the following antibodies where applicable: CD3-AF647 (UCHT1; Biolegend), CD4-PB (RPA-T4; Biolegend), CD8-PerCP-Cy5.5 (RPA-T8; Biolegend), pan  $\alpha\beta$  TCR – APC (IP26, Thermo Fisher Scientific), pan  $\gamma\delta$  TCR-PE-Cy7 (clone; company), LAIR1-PE (NKTA255; Thermo Fisher Scientific), NKp30-eFluor450 (AF29-4D12; Thermo Fisher Scientific). All samples were measured on the LSR Fortessa (BD) or Canto II (BD) using Diva Software (BD).

### Single-cell RNA Sequencing

**3D Model Preparation and Cell Isolation:** On day 0, various co-cultures were assembled as described under the section “3D Model” with the exception of the use of dye to label the stromal and cancer cells and of the use of the Transwell system. On day 4, TEG001 were administered to the co-culture. On day 6, cells were isolated using Cell Recovery Solution (Corning Life Sciences). The harvested cells were then depleted of dead cells with the Dead Cell Removal Kit (Miltenyi Biotec) according to the manufacturer’s protocol and strained with a 70  $\mu$ m strainer.

**3’ Single-cell RNA Library Preparation and Sequencing:** 12,000 living cells from each co-culture experimental condition were prepared for 3’ scRNA sequencing using the 10X Genomics v3.1 Single Index workflow and reagents (10X Genomics 1000127, 1000121, 1000213, 1000171) according to the manufacturer’s protocol with the following exception: 10% Tween-20, 50% glycerol, and Qiagen buffer EB (10 mM Tris-HCl, pH 8.5) were prepared in-house. Libraries were sequenced on Illumina NovaSeq 6000.

**Data Analysis:** The reads from FASTQ read files were aligned on the GRCh38-2020-A (10X Genomics) human genome and transcriptome reference using Cell Ranger 6.0.1 software (10X Genomics). Demultiplexing of components of co-cultures within shared

libraries was done based on single nucleotide polymorphism (SNP) deconvolution of donors within samples with the *vireo* and *cellsnp* R packages. The count matrices of the aligned reads were analyzed in R(4.0.1). Before dimensionality reduction and clustering, low-quality cells were excluded (based on gene counts, and percentage of mitochondrial genes). Data were normalized, scaled and log-transformed using the *NormalizeData* function of the *seurat* package. Principal component analysis (PCA) was performed on the scaled data with the 4000 most variable genes. The number of principal components used was determined using the *ElbowPlot* function. We calculated a UMAP representation of the data for visualization and calculated clusters, using the *FindNeighbors* and *FindClusters* functions. Marker genes that differentiated between clusters were identified using the *FindAllMarkers* function. We applied gene ontology (GO) over-representation test with *clusterProfiler*. We applied the *cellchat* package to map the possible cell-cell interactions.

### Bulk RNA Sequencing

MSC samples were prepared and sent to the Utrecht Sequencing Facility (USEQ) according to their guidelines. Raw counts were obtained. The dataset was filtered to remove all genes with less than 10 raw reads in total from all samples. DESeq2 R package (Love, M.I. et al, Genome Biology 2014) was then used to obtain a DEG list based on Log2 fold change analysis.

### Statistical Analysis

Experimental data was analyzed using GraphPad Prism 9 for Windows (GraphPad Software Inc., La Jolla, CA, USA). Statistical significances between groups were assessed with two-way ANOVA tests. Significant variance was determined with one-way ANOVA analysis. Standard error of the mean (SEM) is represented by error bars. P-values lower than 0.05 were considered statistically significant, with asterisks indicating the following P-value ranges: (\*)  $P < 0.05$ , (\*\*)  $P < 0.01$ , (\*\*\*)  $P < 0.001$ , (\*\*\*\*)  $P < 0.0001$ .

### Ethics declarations

MSCs were sourced from the GMP-licensed Cell Therapy Facility of the UMC Utrecht by expansion from bone marrow. Bone marrow aspirates were obtained from healthy donors according to the guidelines of the Dutch Central Committee on Research Involving Human Subjects (CCMO, Biobanking bone marrow for MSC expansion, NL41015.041.12). CCMO approved and informed consent was signed by either the bone marrow donor or the legal guardian of the donor.



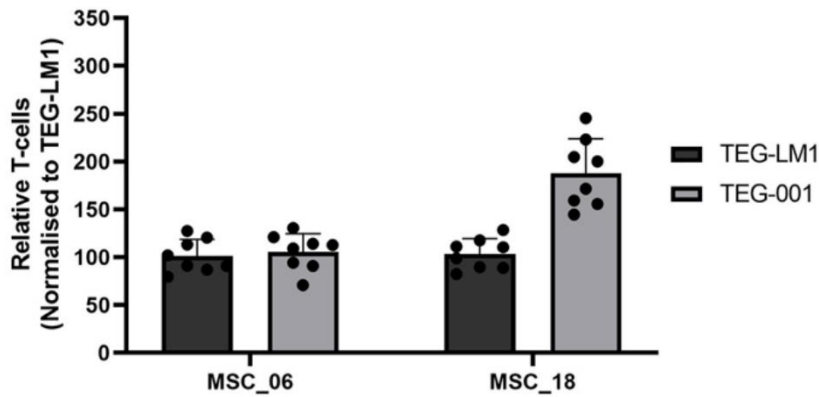
## References

1. Davids, M.S., et al., Ipilimumab for Patients with Relapse after Allogeneic Transplantation. *N Engl J Med*, 2016. 375(2): p. 143-53.
2. Berger, R., et al., Phase I safety and pharmacokinetic study of CT-011, a humanized antibody interacting with PD-1, in patients with advanced hematologic malignancies. *Clin Cancer Res*, 2008. 14(10): p. 3044-51.
3. Daver, N., et al., Efficacy, Safety, and Biomarkers of Response to Azacitidine and Nivolumab in Relapsed/Refractory Acute Myeloid Leukemia: A Nonrandomized, Open-Label, Phase II Study. *Cancer Discov*, 2019. 9(3): p. 370-383.
4. Ghorashian, S., et al., Enhanced CAR T cell expansion and prolonged persistence in pediatric patients with ALL treated with a low-affinity CD19 CAR. *Nat Med*, 2019. 25(9): p. 1408-1414.
5. Turtle, C.J., et al., CD19 CAR-T cells of defined CD4+:CD8+ composition in adult B cell ALL patients. *J Clin Invest*, 2016. 126(6): p. 2123-38.
6. Hay, K.A., et al., Factors associated with durable EFS in adult B-cell ALL patients achieving MRD-negative CR after CD19 CAR T-cell therapy. *Blood*, 2019. 133(15): p. 1652-1663.
7. Pasquini, M.C., et al., Real-world evidence of tisagenlecleucel for pediatric acute lymphoblastic leukemia and non-Hodgkin lymphoma. *Blood Adv*, 2020. 4(21): p. 5414-5424.
8. Martin, T., et al., Ciltacabtagene Autoleucel, an Anti-B-cell Maturation Antigen Chimeric Antigen Receptor T-Cell Therapy, for Relapsed/Refractory Multiple Myeloma: CARTITUDE-1 2-Year Follow-Up. *J Clin Oncol*, 2023. 41(6): p. 1265-1274.
9. Neelapu, S.S., et al., Axicabtagene Ciloleucel CAR T-Cell Therapy in Refractory Large B-Cell Lymphoma. *N Engl J Med*, 2017. 377(26): p. 2531-2544.
10. Schuster, S.J., et al., Tisagenlecleucel in Adult Relapsed or Refractory Diffuse Large B-Cell Lymphoma. *N Engl J Med*, 2019. 380(1): p. 45-56.
11. Sambhi, M., L. Bagheri, and M.R. Szewczuk, Current Challenges in Cancer Immunotherapy: Multimodal Approaches to Improve Efficacy and Patient Response Rates. *J Oncol*, 2019. 2019: p. 4508794.
12. Brown, C.E. and C.L. Mackall, CAR T cell therapy: inroads to response and resistance. *Nat Rev Immunol*, 2019. 19(2): p. 73-74.
13. Sterner, R.C. and R.M. Sterner, CAR-T cell therapy: current limitations and potential strategies. *Blood Cancer J*, 2021. 11(4): p. 69.
14. Xu, X., et al., Mechanisms of Relapse After CD19 CAR T-Cell Therapy for Acute Lymphoblastic Leukemia and Its Prevention and Treatment Strategies. *Front Immunol*, 2019. 10: p. 2664.
15. Maude, S.L., et al., Chimeric antigen receptor T cells for sustained remissions in leukemia. *N Engl J Med*, 2014. 371(16): p. 1507-17.
16. Gründer, C., et al., gamma9 and delta2CDR3 domains regulate functional avidity of T cells harboring gamma9delta2TCRs. *Blood*, 2012. 120(26): p. 5153-62.
17. Marcu-Malina, V., et al., Redirecting alphabeta T cells against cancer cells by transfer of a broadly tumor-reactive gammadeltaT-cell receptor. *Blood*, 2011. 118(1): p. 50-9.
18. Hernandez-Lopez, P., et al., Dual targeting of cancer metabolome and stress antigens affects transcriptomic heterogeneity and efficacy of engineered T cells. *Nat Immunol*, 2023.
19. Vyborova, A., et al., gamma9delta2T cell diversity and the receptor interface with tumor cells. *J Clin Invest*, 2020. 130(9): p. 4637-4651.

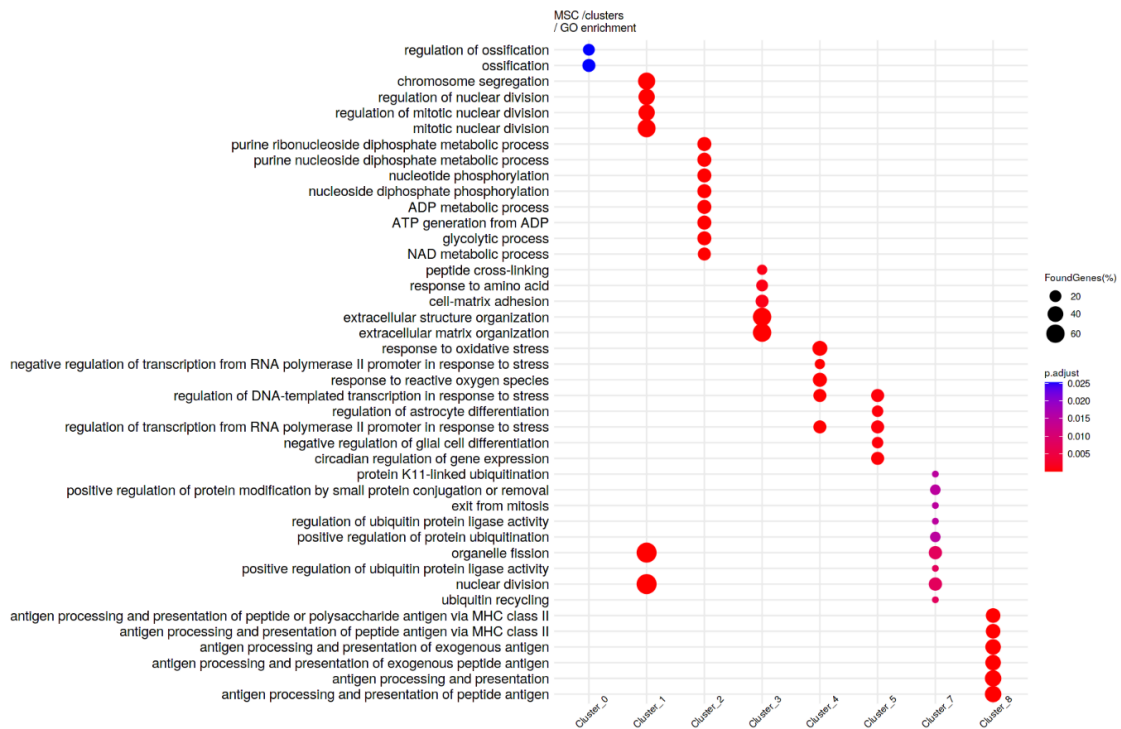
20. Mamedov, M.R., et al., CRISPR screens decode cancer cell pathways that trigger gammadelta T cell detection. *Nature*, 2023. 621(7977): p. 188-195.
21. Sebestyen, Z., et al., Translating gammadelta (gammadelta) T cells and their receptors into cancer cell therapies. *Nat Rev Drug Discov*, 2020. 19(3): p. 169-184.
22. Mancini, S.J.C., et al., Deciphering Tumor Niches: Lessons From Solid and Hematological Malignancies. *Front Immunol*, 2021. 12: p. 766275.
23. Goulard, M., C. Dosquet, and D. Bonnet, Role of the microenvironment in myeloid malignancies. *Cell Mol Life Sci*, 2018. 75(8): p. 1377-1391.
24. Mendez-Ferrer, S., et al., Bone marrow niches in haematological malignancies. *Nat Rev Cancer*, 2020. 20(5): p. 285-298.
25. Braham, M.V.J., et al., Cellular immunotherapy on primary multiple myeloma expanded in a 3D bone marrow niche model. *Oncoimmunology*, 2018. 7(6): p. e1434465.
26. Uccelli, A., L. Moretta, and V. Pistoia, Mesenchymal stem cells in health and disease. *Nat Rev Immunol*, 2008. 8(9): p. 726-36.
27. Papait, A., et al., The Multifaceted Roles of MSCs in the Tumor Microenvironment: Interactions With Immune Cells and Exploitation for Therapy. *Front Cell Dev Biol*, 2020. 8: p. 447.
28. Hass, R., Role of MSC in the Tumor Microenvironment. *Cancers (Basel)*, 2020. 12(8).
29. Amable, P.R., et al., Protein synthesis and secretion in human mesenchymal cells derived from bone marrow, adipose tissue and Wharton's jelly. *Stem Cell Res Ther*, 2014. 5(2): p. 53.
30. El-Haibi, C.P., et al., Critical role for lysyl oxidase in mesenchymal stem cell-driven breast cancer malignancy. *Proc Natl Acad Sci U S A*, 2012. 109(43): p. 17460-5.
31. Zhikai Wang, R.Y., Jiayun Li, Ya Gao, Philip Moresco, Min Yao, Jaclyn F. Hechtman, Matthew J. Weiss, Tobias Janowitz, Douglas T. Fearon, Pancreatic cancer cells assemble a CXCL12-keratin 19 coating to resist immunotherapy. *BioRxiv*, 2020.
32. Chen, A., et al., Chitinase-3-like 1 protein complexes modulate macrophage-mediated immune suppression in glioblastoma. *J Clin Invest*, 2021. 131(16).
33. Cheng, L., et al., The role of CRYAB in tumor prognosis and immune infiltration: A Pan-cancer analysis. *Front Surg*, 2022. 9: p. 1117307.
34. Vijver, S.V., et al., Collagen Fragments Produced in Cancer Mediate T Cell Suppression Through Leukocyte-Associated Immunoglobulin-Like Receptor 1. *Front Immunol*, 2021. 12: p. 733561.
35. Lebbink, R.J., et al., Collagens are functional, high affinity ligands for the inhibitory immune receptor LAIR-1. *J Exp Med*, 2006. 203(6): p. 1419-25.
36. Lebbink, R.J., et al., Identification of multiple potent binding sites for human leukocyte associated Ig-like receptor LAIR on collagens II and III. *Matrix Biol*, 2009. 28(4): p. 202-10.
37. Peng, D.H., et al., Collagen promotes anti-PD-1/PD-L1 resistance in cancer through LAIR1-dependent CD8(+) T cell exhaustion. *Nat Commun*, 2020. 11(1): p. 4520.
38. Joseph, C., et al., The ITIM-Containing Receptor: Leukocyte-Associated Immunoglobulin-Like Receptor-1 (LAIR-1) Modulates Immune Response and Confers Poor Prognosis in Invasive Breast Carcinoma. *Cancers (Basel)*, 2020. 13(1).
39. Wilhelm, D., et al., Tissue-specific collagen hydroxylation at GEP/GDP triplets mediated by P4HA2. *Matrix Biol*, 2023. 119: p. 141-153.
40. van der Wagen, L.E., et al., Efficacy of MSC for steroid-refractory acute GVHD associates with MSC donor age and a defined molecular profile. *Bone Marrow Transplant*, 2020. 55(11): p. 2188-2192.

41. Kirouac, D.C., et al., Deconvolution of clinical variance in CAR-T cell pharmacology and response. *Nat Biotechnol*, 2023. 41(11): p. 1606-1617.
42. Dekkers, J.F., et al., Uncovering the mode of action of engineered T cells in patient cancer organoids. *Nat Biotechnol*, 2023. 41(1): p. 60-69.
43. Jiang, W. and J. Xu, Immune modulation by mesenchymal stem cells. *Cell Prolif*, 2020. 53(1): p. e12712.
44. Ma, Z., et al., Bone Marrow Mesenchymal Stromal Cell-Derived Periostin Promotes B-ALL Progression by Modulating CCL2 in Leukemia Cells. *Cell Rep*, 2019. 26(6): p. 1533-1543 e4.
45. Zhang, J., et al., The role of network-forming collagens in cancer progression. *Int J Cancer*, 2022. 151(6): p. 833-842.
46. Meyaard, L., The inhibitory collagen receptor LAIR-1 (CD305). *J Leukoc Biol*, 2008. 83(4): p. 799-803.

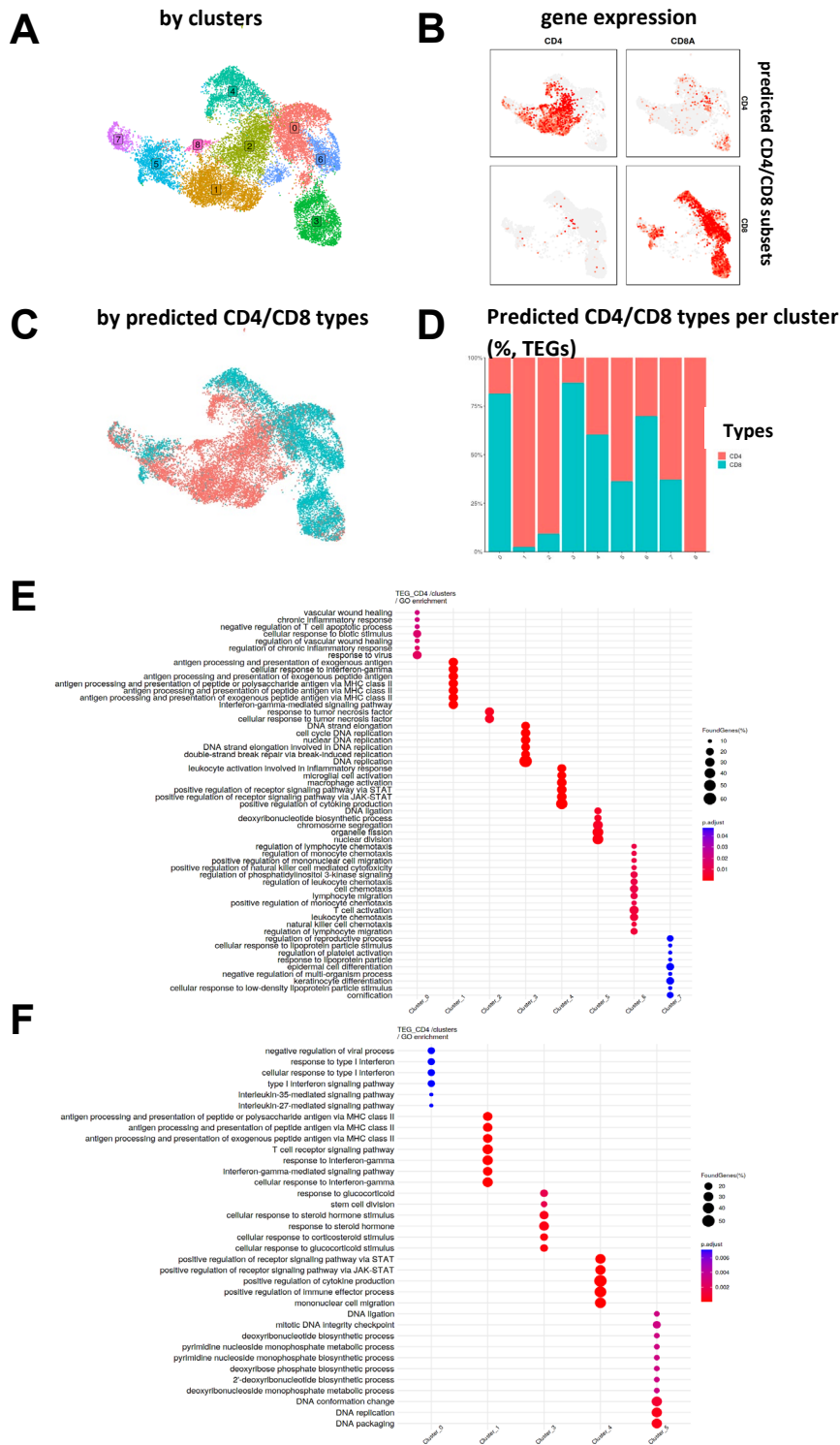
## Supplementary Figures



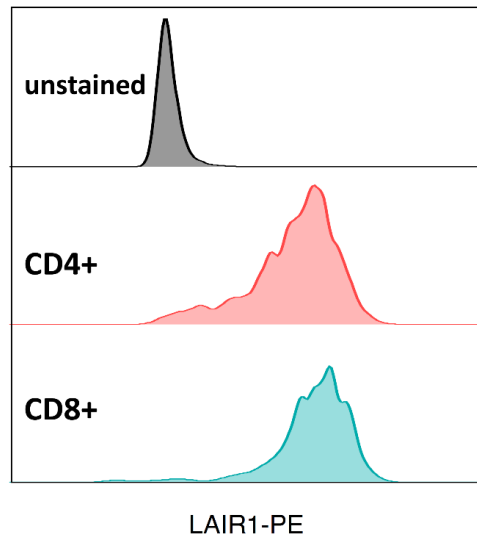
**Supplemental Figure 1.** Relative amount of T cells normalized to TEG-LM1 control in a co-culture with MSC donor 6 and 18 in matrigel after 2 days.



**Supplemental Figure 2.** GO-term analysis of MSC clusters.



**Supplemental Figure 3.** (A) UMAP plot displaying the unsupervised clustering of TEG subsets from all experiment. (B) CD4 and CD8A expression of the predicted CD4 and CD8 TEG subsets. Grey color mark lack of expression. (C) UMAP plot displaying the predicted CD4 and CD8 types of TEG cells from all experiment. (D) CD4 / CD8 composition of the TEG clusters in (A) (%), according to our type prediction. (E) GO-term analysis per CD4 TEG clusters. (F) GO-term analysis per CD8 TEG clusters.



**Supplemental Figure 4.** LAIR-1 expression and mean fluorescence intensity (MFI) of CD4+ (yellow) and CD8+ (blue) TEGs compared to unstained cells (grey).

**Supplementary Table 1. Fisher-tests.**

| MSC Cluster | p-values (Fisher-test)   |                          |                          |                          | cluster contributions (%) per contition |          |              |          |          |              |
|-------------|--------------------------|--------------------------|--------------------------|--------------------------|---|----------|--------------|----------|----------|--------------|
|             | P (+teg)_vs_P (+tum+teg) | P (+tum)_vs_P (+tum+teg) | S (+teg)_vs_S (+tum+teg) | S (+tum)_vs_S (+tum+teg) | P (+teg)                                | P (+tum) | P (+tum+teg) | S (+teg) | S (+tum) | S (+tum+teg) |
| 0           | 1,57E-01                 | 2,73E-01                 | 1,02E-04                 | 3,56E-05                 | 0,2                                     | 0,2      | 0,6          | 43,6     | 42,1     | 37,0         |
| 1           | 2,17E-07                 |                          | 3,77E-01                 | 1,77E-02                 | 0,1                                     |          | 2,5          | 42,0     | 37,6     | 40,5         |
| 2           |                          |                          |                          |                          | 71,1                                    | 84,3     |              |          |          |              |
| 3           | 3,43E-43                 | 1,03E-19                 | 6,14E-06                 | 3,84E-08                 | 2,4                                     | 5,5      | 20,1         | 6,5      | 7,1      | 11,1         |
| 4           | 0,00E+00                 |                          |                          |                          | 0,2                                     |          | 75,3         | 0,2      |          |              |
| 5           | 3,19E-04                 | 4,32E-04                 | 8,86E-01                 | 9,21E-02                 | 2,0                                     | 2,1      | 0,3          | 6,4      | 5,2      | 6,2          |
| 6           | 1,07E-70                 | 1,71E-18                 | 4,69E-01                 |                          | 24,0                                    | 7,7      | 0,1          | 0,3      |          | 0,6          |
| 7           |                          |                          | 4,29E-02                 | 2,16E-26                 |   |          |              | 0,9      | 7,1      | 1,7          |
| 8           |                          | 9,20E-03                 | 2,00E-11                 | 3,39E-09                 |   | 0,1      | 1,1          | 0,1      | 0,9      | 2,9          |

| TEG Cluster | p-values (Fisher-test) |                 |                          |                          | cluster contributions (%) per contition |              |          |              |      |
|-------------|------------------------|-----------------|--------------------------|--------------------------|---|--------------|----------|--------------|------|
|             | teg vs P (+teg)        | teg vs S (+teg) | S (+teg) vs S (+tum+teg) | P (+teg) vs P (+tum+teg) | P (+teg)                                | P (+tum+teg) | S (+teg) | S (+tum+teg) | teg  |
| 0           | 9,62E-214              | 2,32E-300       | 5,15E-24                 | 5,18E-91                 | 25,2                                    | 3,5          | 30,9     | 43,4         | 2,9  |
| 1           | 0                      | 9,13E-281       | 3,02E-52                 | 6,91E-03                 | 2,5                                     | 1,3          | 7,8      | 0,7          | 43,2 |
| 2           | 4,64E-51               | 0               | 5,24E-22                 | 1,04E-06                 | 9,2                                     | 5,2          | 41,8     | 30,0         | 1,9  |
| 3           | 0                      | 3,85E-301       | 1,73E-15                 | 4,20E-03                 | 1,5                                     | 0,5          | 2,3      | 0,2          | 35,1 |
| 4           | 0                      | 4,92E-60        | 2,91E-28                 | 4,82E-305                | 50,6                                    | 1,3          | 5,1      | 13,1         | 0,2  |
| 5           | 5,78E-13               | 2,76E-08        | 7,71E-01                 | 8,95E-04                 | 6,3                                     | 9,0          | 7,4      | 7,6          | 11,1 |
| 6           | 3,01E-05               | 1,00E+00        | 3,14E-01                 | 0                        | 0,5                                     | 76,2         | 0,1      | 0,2          | 0,1  |
| 7           | 1,97E-06               | 1,83E-01        | 6,47E-11                 | 4,75E-02                 | 4,2                                     | 3,0          | 1,9      | 4,9          | 2,3  |
| 8           |                        | 4,73E-01        | 5,01E-28                 |                          | 4,2                                     |              | 2,9      | 0,0          | 3,3  |

| CD4_TEG Cluster | p-values (Fisher-test) |                 |                          |                          | cluster contributions (%) per contition |              |          |              |      |
|-----------------|------------------------|-----------------|--------------------------|--------------------------|---|--------------|----------|--------------|------|
|                 | teg vs P (+teg)        | teg vs S (+teg) | S (+teg) vs S (+tum+teg) | P (+teg) vs P (+tum+teg) | P (+teg)                                | P (+tum+teg) | S (+teg) | S (+tum+teg) | teg  |
| 0               | 1,07E-100              | 0,00E+00        | 6,03E-07                 | 8,18E-42                 | 24,1                                    | 58,3         | 67,2     | 74,9         | 2,5  |
| 1               | 2,93E-132              | 1,65E-139       | 7,85E-27                 | 8,09E-09                 | 3,7                                     | 11,3         | 8,3      | 1,0          | 38,7 |
| 2               | 6,33E-93               | 5,59E-116       | 1,74E-13                 | 2,60E-09                 | 2,3                                     | 9,2          | 4,2      | 0,5          | 28,1 |
| 3               | 4,84E-15               | 5,58E-07        | 3,34E-01                 | 4,13E-10                 | 5,5                                     | 15,0         | 9,2      | 8,2          | 13,8 |
| 4               | 0                      | 1,96E-23        | 8,56E-14                 | 1,03E-136                | 57,8                                    | 1,7          | 3,9      | 10,3         | 0,3  |
| 5               | 6,22E-04               | 4,99E-02        | 1,28E-04                 | 5,80E-02                 | 5,9                                     | 3,7          | 2,5      | 5,0          | 3,5  |
| 6               | 6,43E-24               | 1,70E-37        | 3,54E-03                 | 5,03E-01                 | 0,7                                     | 0,3          | 0,7      | 0,1          | 8,0  |
| 7               |                        | 9,54E-02        |                          |                          |   | 0,5          | 4,1      |              | 5,1  |

| CD8_TEG Cluster | p-values (Fisher-test) |                 |                          |                          | cluster contributions (%) per contition |              |          |              |      |
|-----------------|------------------------|-----------------|--------------------------|--------------------------|---|--------------|----------|--------------|------|
|                 | teg vs P (+teg)        | teg vs S (+teg) | S (+teg) vs S (+tum+teg) | P (+teg) vs P (+tum+teg) | P (+teg)                                | P (+tum+teg) | S (+teg) | S (+tum+teg) | teg  |
| 0               | 3,76E-235              | 0,00E+00        | 2,83E-05                 | 1,06E-93                 | 42,8                                    | 8,1          | 85,3     | 78,9         | 2,6  |
| 1               | 4,03E-301              | 1,59E-165       |                          |                          | 0,2                                     |              | 2,9      |              | 46,9 |

**Supplementary Table 2. topDEGs\_MSC.**

| rank | Cluster_0 | Cluster_1 | Cluster_2 | Cluster_3 | Cluster_4 | Cluster_5 | Cluster_6 | Cluster_7 | Cluster_8 |
|------|-----------|-----------|-----------|-----------|-----------|-----------|-----------|-----------|-----------|
| 1    | KRT19     | HIST1H4C  | BNIP3     | MTRNR2L1  | HSPA1A    | GADD45B   | PLCG2     | H2AFZ     | HLA-DRA   |
| 2    | TIMP3     | HIST1H1B  | HMOX1     | THBS1     | CRYAB     | DDIT3     | MTRNR2L1  | RHOC      | CD74      |
| 3    | DCBLD2    | HIST1H1D  | LDHA      | NEAT1     | FOSB      | AL627171  | CSKMT     | SRM       | S100A4    |
| 4    | SULF1     | TOP2A     | IMP3      | COL4A1    | FOS       | RRAD      | PLK2      | UBE2S     | HLA-DPB1  |
| 5    | CHI3L1    | CENPF     | GAPDH     | POSTN     | RRAD      | SNAPC1    | PPP1R15A  | UBE2C     | HLA-DRB1  |
| 6    | PDLIM4    | H2AFZ     | NQO1      | CEMIP     | DUSP1     | SNHG8     | MTRNR2L1  | MYL9      | SERPINB1  |
| 7    | CXXC5     | TPX2      | PMAIP1    | CCN2      | JUN       | HES1      | NFKBIZ    | MRPL12    | HLA-DPA1  |
| 8    | TGM2      | UBE2C     | FGF5      | FN1       | ATF3      | ID2       | SLC38A2   | PFN1      | RGCC      |
| 9    | NREP      | PRC1      | CITED2    | COL12A1   | ACTA2     | GAS5      | MAFB      | LSM2      | PRSS57    |
| 10   | CTHRC1    | CKS2      | PGAM1     | GJA1      | HSPH1     | RSRC2     | MALAT1    | CKS2      | SPINK2    |
| 11   | MAP1A     | MKI67     | RND3      | SPARC     | DNAJB1    | BHLHE41   | SOD2      | NAA10     | H1FX      |
| 12   | MXD4      | CCNB1     | VASN      | MALAT1    | GADD45B   | HES4      | JUN       | KRT10     | RAB11FIP1 |
| 13   | NME3      | TYMS      | ENO1      | MEG3      | KLF6      | NR1D1     | RND3      | MLF2      | CYBA      |
| 14   | PENK      | ASPM      | PTX3      | TGFB1     | ANGPTL4   | SQSTM1    | CCNL1     | COX5A     | PYCARD    |
| 15   | ANKH      | PCLAF     | EMP3      | VCAN      | ID4       | GADD45A   | ABL2      | TUBA1C    | AIF1      |
| 16   | ID3       | PTTG1     | COTL1     | COL6A3    | CKB       | ATF3      | SOCS3     | PDLIM2    | SNHG29    |
| 17   | KRT10     | TMPO      | IGFBP6    | COL3A1    | KLF2      | FBXO32    | HEXIM1    | LSM7      | PLEK      |
| 18   | ARL1      | NUSAP1    | ALDOA     | APLP2     | TPM1      | HSPA1A    | PPP1R10   | CENPX     | TSC22D3   |
| 19   | HIF1A     | ANLN      | TMSB10    | FSTL1     | JUNB      | SNHG12    | PIK3R3    | ID3       | VAMP8     |
| 20   | APCDD1L   | DEK       | NUPR1     | COL1A2    | NNMT      | EGR1      | HYMAI     | CHI3L1    | H2AFY     |
| 21   | WWTR1     | RRM2      | PKD1      | PDIA3     | PRRX2     | CXCL3     | NABP1     | SVA1      | ATP5MC2   |
| 22   | MICAL2    | KIF23     | MIF       | ITGBL1    | HSPA1B    | PPP1R15A  | BRD2      | FHL2      | HLA-DMA   |
| 23   | CRABP2    | CENPW     | FTH1      | HSPA5     | JUND      | TAF1D     | STAT3     | GNG5      | PNRC1     |
| 24   | CTSK      | STMN1     | LGALS1    | FBN1      | NUPR1     | LMCD1     | AL627171  | BEX3      | CLEC2B    |
| 25   | ARFGAP3   | CKAP2     | PRDX1     | COL1A1    | CCN2      | GDF15     | TNFAIP3   | STUB1     | GAS5      |
| 26   | FAM114A   | UBE2T     | FAM180A   | COL4A2    | TSC22D3   | PIM3      | SLC2A3    | AURKAIP1  | ELF1      |
| 27   | S100A6    | SMC4      | ABL2      | PSAP      | DNAJA1    | SLC3A2    | SYNE1     | ATP5F1D   | RILPL2    |
| 28   | CNN3      | HMMR      | SNHG29    | HSP90B1   | EGR1      | SNHG15    | ANKRD11   | EVA1B     | ANKRD28   |
| 29   | CCL2      | CDK1      | TPT1      | LRP1      | SGK1      | PLK2      | COL6A2    | MRPL27    | EIF3E     |
| 30   | GALNT1    | CENPE     | EEF1G     | THBS2     | KRT18     | NFKBIA    | NFKBIA    | HINT1     | EIF3G     |
| 31   | MYO1B     | PBK       | BNIP3L    | COL5A1    | C11orf96  | EPB41L4A  | GLS       | COPZ2     | JUND      |
| 32   | LXN       | BIRC5     | FAM162A   | VMP1      | ANKRD1    | ANKRD1    | IRF1      | LY6E      | MXD4      |
| 33   | CLDN14    | CEP55     | AVP1      | LMAN1     | ZFAND5    | BBC3      | AC020916  | S100A16   | GIHCG     |
| 34   | RBPJ      | CKS1B     | PRSS23    | FAT1      | IER3      | ZFAS1     | CHD2      | LY6K      | SAT1      |
| 35   | RNF7      | SMC2      | IFITM3    | LOX       | TIPARP    | CHMP1B    | INTS6     | ATP5MC3   | ZEB2      |
| 36   | FAM98A    | UBE2S     | S100A10   | INHBA     | KCNE4     | SOX4      | NR1D1     | CUTA      | ID3       |
| 37   | VPS28     | DLGAP5    | TFPI2     | COL8A1    | TAGLN     | PMAIP1    | CEBPD     | EIF4EBP1  | NOP53     |
| 38   | PRRX1     | CLSPN     | TPI1      | COL6A1    | HSPB1     | HIST1H4H  | MYH9      | GABARAP   | TUBA1A    |
| 39   | MPG       | HIST1H1E  | TXNRD1    | COL5A2    | UBC       | CEBPD     | SMURF2    | YF1A      | EEF1A1    |
| 40   | BAALC     | CENPK     | SELENOM   | LTBP2     | NR4A1     | IER2      | NDRG1     | SH3BGRL   | SR        |

Supplementary Table 3. topDEGs\_TEG\_CD4.

| rank | Cluster_0 | Cluster_1 | Cluster_2 | Cluster_3 | Cluster_4 | Cluster_5 | Cluster_6 | Cluster_7 |
|------|-----------|-----------|-----------|-----------|-----------|-----------|-----------|-----------|
| 1    | IFI27     | C15orf48  | KLF2      | DUT       | CCL4L2    | HIST1H1B  | CD8A      | CD9       |
| 2    | GNLY      | GZMA      | KLRB1     | PCLAF     | CSF2      | HIST1H4C  | CTSW      | HPGDS     |
| 3    | TSC22D3   | BATF      | S100A4    | TYMS      | CCL3      | HIST1H1D  | GNLY      | PHLDA2    |
| 4    | STK17A    | MZB1      | SPOCK2    | HELLS     | IL13      | STMN1     | KLRK1     | ARG2      |
| 5    | ZFP36L2   | GZMB      | LTB       | CLSPN     | CCL4      | MKI67     | NKG7      | EGLN3     |
| 6    | S100A6    | HLA-DRA   | AQP3      | STMN1     | IFNG      | TUBA1B    | AIF1      | BACE2     |
| 7    | CXCR4     | HLA-DRB1  | CXCR4     | INS2      | IL4       | HIST1H3D  | CD8B      | KRT81     |
| 8    | LPIN2     | HLA-DPA1  | RORA      | PCNA      | IL5       | HIST1H1C  | GZMH      | FCER1G    |
| 9    | CCL5      | SIRPG     | GIMAP7    | NASP      | TNF       | HMGB2     | LIME1     | TRAV20    |
| 10   | PDCD4     | HLA-DPB1  | GIMAP4    | MCM4      | NR4A2     | HIST1H1E  | NCR3      | PTTG1     |
| 11   | CKAP2     | HLA-DRB5  | LIMS1     | MCM7      | NR4A3     | TOP2A     | GZMK      | PALLD     |
| 12   | MXD4      | CCR1      | RIPOR2    | TUBA1B    | CD69      | NUSAP1    | RCBTB2    | PTGDR2    |
| 13   | S1PR4     | ID2       | RNASET2   | CENPU     | DUSP2     | HIST1H3B  | MATK      | KRT7      |
| 14   | TNFAIP3   | PGK1      | TNFRSF25  | ATAD2     | CD40LG    | TUBB      | CD52      | CYSLTR1   |
| 15   | RABAC1    | HLA-DQA2  | SOS1      | DNAJC9    | GADD45B   | RRM2      | LAIR2     | KRT86     |
| 16   | RNASEK    | RGL4      | TRBC2     | FEN1      | PHLDA1    | PCLAF     | ITGA1     | TNFRSF18  |
| 17   | CCSER2    | ARG2      | LIME1     | CHEK1     | NR4A1     | TYMS      | CLEC2B    | B3GNT2    |
| 18   | HERC5     | CALHM6    | CORO1B    | MCM3      | BIRC3     | CENPF     | HCST      | LPCAT2    |
| 19   | TXNIP     | TMSB10    | PPP2R5C   | SNRNP25   | REL       | HIST1H2AI | CCL5      | CCDC71L   |
| 20   | NR3C1     | CKLF      | PCED1B-4  | MCM5      | PIM3      | ASPM      | LRRN3     | MIIP      |
| 21   | ISG20     | HLA-DMA   | NEAT1     | MSH6      | NFKBID    | H2AFZ     | TRBC1     | IL17RB    |
| 22   | PYHIN1    | CCL5      | TRAC      | GMNN      | SLA       | HIST1H2AI | GIMAP4    | CHCHD10   |
| 23   | ELK3      | NDFIP2    | PBXIP1    | DEK       | PTGS2     | UBE2C     | GABARAP   | BAG2      |
| 24   | ATP5ME    | CTSC      | GIMAP5    | ATAD5     | PRDX1     | HIST1H2A  | YBX3      | GLRX      |
| 25   | SQSTM1    | HLA-DQA1  | MAF       | NUDT1     | SDC4      | HMGN2     | LINC01871 | PMCH      |
| 26   | IGFLR1    | GPI       | RESF1     | TMPO      | MIR155HG  | DUT       | SPNS3     | EIF4G2    |
| 27   | GCC2      | LINC01943 | TC2N      | H2AFZ     | RNF19A    | TMPO      | PCED1B-4  | SPP1      |
| 28   | PFDN5     | STX3      | CCR4      | ORC6      | RILPL2    | HIST2H2A  | HOPX      | LAT       |
| 29   | DNPH1     | RSAD2     | ANKRD12   | BRCA1     | EVI2A     | CDK1      | PRMT2     | GLO1      |
| 30   | BTG1      | PLAAT3    | ITGA4     | CDT1      | TNFSF14   | TPX2      | ABI3      | SLFN5     |
| 31   | LEPROTL1  | ACTB      | NTRK2     | HMGB2     | KDM6B     | CKS1B     | GRAP2     | PGK1      |
| 32   | CD2       | PRF1      | S1PR4     | CENPX     | EGR3      | TUBB4B    | JAML      | GATA3     |
| 33   | ATP5F1E   | CD3E      | CYTIP     | SMC2      | RGCC      | BIRC5     | IGF1      | GPAT3     |
| 34   | EPST11    | PYCARD    | ADD3      | HNRNPAB   | MAP3K8    | CDKN3     | TESC      | CCNG2     |
| 35   | BCL11B    | SMCO4     | CDC42EP   | DHFR      | EGR2      | UBE2S     | APOBEC3   | BATF      |
| 36   | RALA      | BCL3      | PDCD4     | DNMT1     | DUSP5     | ATAD2     | ITGB1     | RTKN2     |
| 37   | PET100    | FAM89B    | CERK      | SLBP      | TNFSF9    | HIST1H3G  | LPAR6     | SNHG8     |
| 38   | ZBTB1     | MIIP      | LST1      | MCM6      | NFKBIA    | H2AFX     | KRT10     | ACER3     |
| 39   | SP100     | TRBC1     | TIPARP    | WDR76     | BTG2      | SMC4      | BIN1      | CDKN2D    |
| 40   | LGALS8    | LTA       | ZBTB38    | MKI67     | SIAH2     | PRC1      | PREX1     | MMP25     |
| 41   | NUB1      | LPCAT2    | TNFSF13E  | USP1      | NAMPT     | DLGAP5    | PRF1      | PDLIM5    |
| 42   | PCED1B-4  | CD48      | FKBP11    | FAM111B   | CREM      | KIF11     | CD37      | TPMT      |
| 43   | ARL14EP   | TPI1      | IF44      | CENPH     | SPRY1     | HIST1H3F  | SH3BGRL1  | GAS5      |
| 44   | N4BP2L2   | GAPDH     | TMEM167   | CHAF1A    | RAB11FIP  | FBXO5     | GNPTAB    | LMNA      |
| 45   |           | ACTG1     | GBP5      | E2F1      | DUSP6     | HIST1H2BI | GSTP1     | DENND1B   |
| 46   |           | ITM2A     | CD52      | SNRPB     | ARL5B     | CCNA2     | FAM126A   | TNFRSF4   |
| 47   |           | MAPKAPK   | HPGD      | RANBP1    | FASLG     | CENPW     | GYPC      | SMIM3     |
| 48   |           | CLIC1     | ZNRF1     | CDC6      | GZMB      | CDCA8     | MTRNR2L1  | LINC00667 |
| 49   |           | LAIR2     | GIMAP1    | DTL       | JUNB      | HMGB1     | BTG1      | CAPG      |
| 50   |           | TPST2     | JAML      | SIVA1     | FOSL2     | CLSPN     | GPI       | ECI2      |



**Supplementary Table 4. topDEGs\_TEG\_CD8.**

| rank | Cluster_0 | Cluster_1 | Cluster_2 | Cluster_3 | Cluster_4 | Cluster_5 |
|------|-----------|-----------|-----------|-----------|-----------|-----------|
| 1    | GNLY      | TRBC1     | KRT86     | TSC22D3   | IFNG      | HIST1H1B  |
| 2    | ISG15     | LINC01871 | CXCR6     | FKBP5     | CSF2      | STMN1     |
| 3    | IER2      | HLA-DRB1  | TRAC      | ZFP36L2   | IL13      | TUBA1B    |
| 4    | GZMK      | GPI       | ID2       | CXCR4     | XCL2      | PCLAF     |
| 5    | S100A6    | RCBTB2    | TXNIP     | PIK3IP1   | CCL4L2    | TYMS      |
| 6    | STAT1     | LPAR6     | KRT81     | DDIT4     | XCL1      | HIST1H4C  |
| 7    | MX1       | ITGB1     | GIMAP7    | TXNIP     | CCL3L1    | MKI67     |
| 8    | IL27RA    | HLA-DRB5  | CD48      | BTG1      | CCL3      | HMGB2     |
| 9    | RNASEK    | CD52      | KLRG1     | SMAP2     | CCL4      | DUT       |
| 10   | ATP5ME    | CD2       | PDLIM2    | ZBTB16    | IL4       | HIST1H1D  |
| 11   | NDUFA3    | FAM126A   | TRG-AS1   | BBC3      | TNF       | CLSPN     |
| 12   | ATP5F1E   | HLA-DRA   | GAS5      | BCL2L11   | NR4A2     | TUBB      |
| 13   | IGFLR1    | RGL4      | EIF3E     | LPIN2     | NR4A3     | H2AFZ     |
| 14   | ZRANB2    | CASP1     | EVL       | TRMO      | IL5       | HELLS     |
| 15   | LYSMD2    | HLA-DPB1  | AGTRAP    | PDCD4     | CRTAM     | PCNA      |
| 16   | OTULIN    | PGK1      | SEPHS2    | CCSER2    | GZMB      | TOP2A     |
| 17   | EML4      | HLA-DQA2  | RGL4      | CREBRF    | PIM3      | NUSAP1    |
| 18   | SNX10     | ABI3      | NCR3      | LBH       | PHLDA1    | NASP      |
| 19   | OST4      | GZMH      | RFLNB     | RCSD1     | REL       | HIST1H1C  |
| 20   | CLDND1    | IGF1      | FKBP11    | SYTL3     | EVI2A     | TMPO      |
| 21   | IL2RG     | RNF167    | RASSF1    | AKAP13    | NFKBID    | HMG2      |
| 22   | LIMA1     | HLA-DMA   | TPT1      | ERN1      | MIR155HG  | CENPF     |
| 23   | CCL5      | CAMK1     | LSP1      | UBC       | SDC4      | ATAD2     |
| 24   | TMEM258   | ANKRD12   | PLCG2     | BPTF      | RGCC      | RRM2      |
| 25   | TMA7      | BCL11B    | CDKN2A    | HERPUD1   | NR4A1     | GIN2      |
| 26   | SNHG6     | CD6       | GIMAP5    | ETS1      | KDM6B     | SMC2      |
| 27   | PAXX      | LPCAT2    | ZNRD1     | KLF13     | DUSP2     | MCM7      |
| 28   | SEC62     | SIRPG     | IL16      | PPP1R2    | CD69      | ASPM      |
| 29   | BHLHE40   | PTTG1     | TRAF3IP3  | YPEL2     | GADD45B   | MCM4      |
| 30   | PET100    | APOBEC3   | RHOC      | CNOT6L    | TNFSF14   | HIST1H3D  |
| 31   | MRPL52    | LINC02694 | SIT1      | PARP8     | RILPL2    | CENPU     |
| 32   | C12orf57  | HLA-DQA1  | ATF7IP2   | RESF1     | BIRC3     | DNAJC9    |
| 33   | HCST      | BCL2      | CD3E      | CDV3      | RNF19A    | GMNN      |
| 34   | ATP5MD    | GIMAP4    | NCAM1     | NIBAN1    | EGR3      | HIST1H1E  |
| 35   | NDUFA1    | PREX1     | TRGC2     | FAM102A   | DUSP5     | MCM3      |
| 36   | NDUFC1    | HLA-DPA1  | SLAMF7    | HERC5     | EGR2      | DEK       |
| 37   | DSTN      | JAML      | CSTB      | MYH9      | FASLG     | FEN1      |
| 38   | ANXA2     | THEMIS    | SYNRG     | UGP2      | MAP3K8    | CENPM     |
| 39   | COX7C     | IER5L     | PNN       | SLFN5     | CD40LG    | SNRNP25   |
| 40   | NDUFB1    | LAT       | NDFIP2    | SMIM3     | NAMPT     | CHEK1     |
| 41   | DDHD1     | GRAP2     | CCDC85B   | IL10RA    | TNFSF9    | BRCA1     |
| 42   | RAB8B     | JUN       | EEF1A1    | PPM1K     | IL23A     | ORC6      |
| 43   | MRPS36    | CD3E      | GIMAP1    | GABARAP   | BCL2A1    | DHFR      |
| 44   | SON       | SH3BGR1   | C4orf3    | CASP8     | ZBED2     | CENPK     |
| 45   | SAMD3     | HLA-DQB1  | TP1       | PRDM1     | PRDX1     | ANP32B    |
| 46   | NECAP2    | RASGRP1   | SRSF9     | IKZF1     | SLA       | SMC4      |
| 47   | EIF2S2    | STX3      | EIF4B     | GPATCH8   | SPRY1     | MCM5      |
| 48   | LBR       | PPDPF     | UBE2F     | CD8B      | CREM      | CKS1B     |
| 49   | NA        | AIF1      | PGK1      | OGA       | NFKBIA    | RANBP1    |
| 50   | NA        | CD3G      | HTATSF1   | FAM3C     | IER3      | NUDT1     |

**Supplementary Table 5. Collagen genes**

| HGNC ID (gene)             | Approved symbol         | Approved name                     | Previous symbols | Chromosome |            |
|----------------------------|-------------------------|-----------------------------------|------------------|------------|------------|
| <a href="#">HGNC:2197</a>  | <a href="#">COL1A1</a>  | collagen type I alpha 1 chain     |                  | 17q21.33   | fibrillar  |
| <a href="#">HGNC:2198</a>  | <a href="#">COL1A2</a>  | collagen type I alpha 2 chain     | OI4              | 7q21.3     | fibrillar  |
| <a href="#">HGNC:2200</a>  | <a href="#">COL2A1</a>  | collagen type II alpha 1 chain    | SEDC,<br>EDS4A   | 12q13.11   | fibrillar  |
| <a href="#">HGNC:2201</a>  | <a href="#">COL3A1</a>  | collagen type III alpha 1 chain   |                  | 2q32.2     | fibrillar  |
| <a href="#">HGNC:2209</a>  | <a href="#">COL5A1</a>  | collagen type V alpha 1 chain     |                  | 9q34.3     | fibrillar  |
| <a href="#">HGNC:2210</a>  | <a href="#">COL5A2</a>  | collagen type V alpha 2 chain     |                  | 2q32.2     | fibrillar  |
| <a href="#">HGNC:14864</a> | <a href="#">COL5A3</a>  | collagen type V alpha 3 chain     |                  | 19p13.2    | fibrillar  |
| <a href="#">HGNC:2186</a>  | <a href="#">COL11A1</a> | collagen type XI alpha 1 chain    | COLL6,           | 1p21.1     | fibrillar  |
| <a href="#">HGNC:2187</a>  | <a href="#">COL11A2</a> | collagen type XI alpha 2 chain    | DFNA13,          | 6p21.32    | fibrillar  |
| <a href="#">HGNC:20821</a> | <a href="#">COL24A1</a> | collagen type XXIV alpha 1 chain  |                  | 1p22.3     | fibrillar  |
| <a href="#">HGNC:22986</a> | <a href="#">COL27A1</a> | collagen type XXVII alpha 1 chain |                  | 9q32       | fibrillar  |
| <a href="#">HGNC:2202</a>  | <a href="#">COL4A1</a>  | collagen type IV alpha 1 chain    |                  | 13q34      | networking |
| <a href="#">HGNC:2203</a>  | <a href="#">COL4A2</a>  | collagen type IV alpha 2 chain    |                  | 13q34      | networking |
| <a href="#">HGNC:2204</a>  | <a href="#">COL4A3</a>  | collagen type IV alpha 3 chain    |                  | 2q36.3     | networking |
| <a href="#">HGNC:2206</a>  | <a href="#">COL4A4</a>  | collagen type IV alpha 4 chain    |                  | 2q36.3     | networking |
| <a href="#">HGNC:2207</a>  | <a href="#">COL4A5</a>  | collagen type IV alpha 5 chain    | ASLN,            | Xq22.3     | networking |
| <a href="#">HGNC:2208</a>  | <a href="#">COL4A6</a>  | collagen type IV alpha 6 chain    |                  | Xq22.3     | networking |
| <a href="#">HGNC:2215</a>  | <a href="#">COL8A1</a>  | collagen type VIII alpha 1 chain  | C3orf7           | 3q12.1     | networking |
| <a href="#">HGNC:2216</a>  | <a href="#">COL8A2</a>  | collagen type VIII alpha 2 chain  | FECD             | 1p34.3     | networking |
| <a href="#">HGNC:2185</a>  | <a href="#">COL10A1</a> | collagen type X alpha 1 chain     |                  | 6q22.1     | networking |





# CHAPTER

# 7

## Summarizing Discussion

## T cell therapy for cancer

In the past decade cancer therapy has shifted from generalized standard treatments, such as chemotherapy, to more personalized approaches. Adoptive T cell therapy (ACT) and the idea of harnessing the anti-tumor capability of the patient's own immune system in the form of tumor infiltrating lymphocytes (TILs) and checkpoint inhibitors have revolutionized the opportunities for cancer treatment<sup>1,2</sup>. The approval of engineered T cells expressing a chimeric antigen receptor (CAR-T cells) by both the FDA and EMA finally has resulted in overwhelming clinical successes of treating hematological malignancies, in particular acute lymphoblastic leukemia (ALL), diffuse large B-cell lymphoma (DLBCL) and myeloma. Targeting solid tumors with ACT, however, remains a challenge. In **chapter 1**, we described the main roadblocks of targeting solid tumors<sup>3</sup> – antigen dilemma, T cell fitness and an immune-suppressive tumor microenvironment – and provide in this thesis potential solutions.

### Overcoming the “antigen dilemma” by V $\gamma$ 9V $\delta$ 2TCR based T-cell therapies

One of the major pitfalls of the appliance of CAR-based immunotherapies in solid tumors is their reliance on a widely expressed yet tumor-specific antigen. Often, chosen antigens are also expressed on healthy tissue, resulting in on-target off-tumor effects by the CAR-T cells<sup>4</sup>. One strategy to overcome this limitation is by using V $\gamma$ 9V $\delta$ 2TCR instead of an antibody-based CAR<sup>5</sup>. As opposed to  $\alpha\beta$ TCRs and CAR-T cells they specifically target malignantly transformed cells<sup>6</sup> in an HLA-independent manner. In addition, V $\gamma$ 9V $\delta$ 2TCR target a broad range of hematopoietic and solid tumors *in vitro*<sup>7</sup>. Despite the promising features of V $\gamma$ 9V $\delta$ 2T cell based therapies, they have yet to be successfully transferred into clinical applications, mainly due to the high diversity in affinity and avidity of the TCRs in bulk V $\gamma$ 9V $\delta$ 2T cells<sup>8,9</sup>. To overcome diversity V $\gamma$ 9V $\delta$ 2T cells regarding V $\gamma$ 9V $\delta$ 2TCR-affinity and co-receptors expression, our group has developed so called TEG ( $\alpha\beta$  T cells engineered to express a defined  $\gamma\delta$  TCR) over the past decade<sup>10-12</sup>. In this approach  $\alpha\beta$  T cells are being engineered to express a specific, high affinity V $\gamma$ 9V $\delta$ 2TCR to combine the broad but tumor-specific killing capacity of V $\gamma$ 9V $\delta$ 2T cells with the high proliferation capacity of ab T cells. This therapy is currently undergoing evaluation in a phase I clinical trial (NTR6541)<sup>13,14</sup>, where we recently reported that a patient suffering from acute myeloid leukemia achieved a complete remission after administration of one infusion of TEG001 (TEGs with the specific V $\gamma$ 9V $\delta$ 2TCR clone 5)<sup>15</sup>.

## A major dilemma of V $\gamma$ 9V $\delta$ 2TCR based therapies: poor definition of the target

A major challenge in the application of V $\gamma$ 9V $\delta$ 2TCR-based therapies is the incomplete knowledge of the functional mechanism of this cell type, which has a direct impact on selection of eligible patients and further directed improvement of the therapy. V $\gamma$ 9V $\delta$ 2TCR recognize stress-induced intracellular accumulations of phosphoantigens (pAg)<sup>16</sup> and subsequent changes in the BTN2A1-BTN3A-RhoB-complex<sup>17-23</sup>. From this complex, butyrophilin BTN2A1 has been identified as direct ligand of the V $\gamma$ 9V $\delta$ 2TCR<sup>21,22</sup>, and in 2023 the crystal structure of BTN2 with BTN3 allowed to hypothesize that pAg glue BTN2 with BTN3 to activate V $\gamma$ 9V $\delta$ 2T cells<sup>24</sup>. Also the transcriptional regulation of BTN2 and BTN3 has been elucidated by a CRISPR screen<sup>25</sup>, however still letting many important pieces of the puzzle open, for instance additional involved intracellular players as well as at what stage of cancer development this pathway is activated. Within this context we describe in **chapter 3** in two independent, step-wise mutagenesis models of colorectal cancer (CRC)<sup>26</sup> and breast cancer (BC), that as little as a single oncogenic mutation is sufficient to fully activate the BTN-pathway and consequently trigger targeting by V $\gamma$ 9V $\delta$ 2T cells. While the normal human small intestinal organoid stem cells remained untargeted, single mutations in either APC, KRAS and p53, respectively, lead to increased IFN $\gamma$  production by V $\gamma$ 9V $\delta$ 2TCR T cells. Similarly, non-tumorigenic epithelial breast cell line MCF10a only became recognized by V $\gamma$ 9V $\delta$ 2TCR T cells upon an introduced mutation in the tyrosine-kinase domain of HER2/ErbB2. This is in stark contrast to other forms of ACT and immune checkpoint inhibition (ICI), where a high mutational burden has been shown to correlate with efficacy of the treatment<sup>27-29</sup> and is underlining the important role of V $\gamma$ 9V $\delta$ 2T cells in early immunosurveillance and their great potential in cancer therapy. Moreover, we could link multiple specific commonly occurring mutations in known oncogenes, namely KRAS<sup>G12D</sup> (shown in CRC)<sup>26</sup>, ErbB2/HER2<sup>V777E/L</sup> (shown in BC)<sup>30</sup>, that indicate a positive response to treatment with TEG or other V $\gamma$ 9V $\delta$ 2TCR based therapies. Notably, a mutation on position V777 of HER2 was associated with resistance to monoclonal antibody therapy with trastuzumab<sup>31</sup>, rendering V $\gamma$ 9V $\delta$ 2TCR based therapies a valid option for alternative treatment. Furthermore, we not only provided evidence that the oncogenic mutations allowing for recognition of a tumor cell are activating the PI3K/AKT/mTOR pathway, but also that BTN2A1 surface upregulation is a direct consequence of this, and in reverse blocking of PI3K diminished BTN2A1 surface expression and targeting by V $\gamma$ 9V $\delta$ 2TCR T cells in various cell lines. Interestingly, not all PI3K-activating HER2/ErbB2 mutations triggered activation of TEG001, suggesting a different downstream activation cascade for distinct mutations. Previous studies have found evidence for a transcriptional upregulation of BTN2A1 and BTN3A by the AMPK

activating compound AICAR<sup>25</sup> or as a consequence of EBV-induced activation of the JNK pathway<sup>32</sup>, followed by enhanced targeting by V $\gamma$ 9V $\delta$ 2T cells. While JNK is a downstream signaling pathway of PI3K<sup>33</sup>, AMPK and AKT pathways are often observed to regulate the cellular mechanisms autophagy and apoptosis in opposing directions<sup>34,35</sup>. However, AICAR specifically has been found to not only activate AMPK, but also AKT<sup>35,36</sup> and mTORC2<sup>37</sup>, and the AMPK-inhibitor compound C simultaneously reduced AKT activity<sup>36</sup>, respectively. Hence, the mechanism we discovered might trigger the same downstream effects than JNK and AICAR-activated AMPK signaling and further investigation to their identification will be necessary.

Hallmarks of V $\gamma$ 9V $\delta$ 2TCR tumor recognition, such as relocalization of BTN2A1 and RhoB to the cell membrane were found to occur already in the absence of targeting-boosting aminobisphosphonates (ABP). Full activation of V $\gamma$ 9V $\delta$ 2T cells, however, required elevated pAg levels, suggesting a two-step activation process. We could link ABP-treatment to two novel phosphorylation sites in the juxtamembrane region of BTN3A1, potentially promoting heterodimerization of BTN2A1 and BTN3A1 and therefore stabilizing surface expressed BTN2A1. Finally, by applying an innovative proximity proteomics approach we uncovered an ABP-dependent interactome of BTN3A1-proximate proteins and identified with PHLDB2, SYNJ2 and CARMIL1 three novel proteins that are involved in regulating targeting by V $\gamma$ 9V $\delta$ 2TCRs. Those proteins are potentially fostering cytoskeletal spatial rearrangements together with RhoB<sup>17</sup> to allow and maintain BTN2A1 and BTN3A1 surface expression, heterodimerization and stabilization of the immunological synapse. Although we found evidence of the involvement of PHLDB2, SYNJ2 and CARMIL1 in the regulation of V $\gamma$ 9V $\delta$ 2TCR targeting, further research is necessary to clarify their role in the signaling cascade leading to tumor killing by V $\gamma$ 9V $\delta$ 2T cells.

Our findings in this chapter enhance our understanding of V $\gamma$ 9V $\delta$ 2T cell targeting, hopefully improving the identification of patients susceptible to treatment with V $\gamma$ 9V $\delta$ 2TCR-based immunotherapies and allow next generation engineering strategies like TEGs<sup>7,11</sup> and Gamma delta TCR anti-CD3 bispecific molecules (GABs)<sup>38</sup> to unfold their full potential. Moreover, the outcomes of this chapter resulted in a patent application, and as motivating as it is that signatures of cell activation have been patented it caused at the very same time delay in the publication process.

## Characterizing heterogeneity of engineered immune cells

Depending on the ACT, some crucial criteria for release of the final cell product, like cell viability and cell purity are strictly regulated. In contrast, the final composition of CD4+ and CD8+ and their subsets is often very heterogeneous when administered to patients,



even though their capacity in terms of proliferation, persistence, and their anti-tumor effect despair significantly. Hence, we introduce in **chapter 4** BEHAV3D, a 3D-live-imaging tool for assessing the heterogeneity in behavioral and phenotypic traits among cellular immunotherapies with potential to contribute to the optimization of personalized cell-based therapies for targeting solid tumors<sup>39</sup>. In this study, interactions between TEG and patient-derived breast cancer organoids (BC PDOs) were live-tracked on a single cell level by 3D-imaging. To allow comparisons and conclusions on efficacy and changes in the cellular composition over the duration of co-culture, the TEG product composition was kept within specific definitions (>90%  $\gamma\delta$ TCR+, <5% endogenous  $\gamma\delta$ T cells, 50% CD4+:50% CD8+). BEHAV3D identified and differentiated nine classifications of TEG001 subtypes, that varied in their tumor engagement from static/dying to highly engaged (“super-engagers”) T cells. Interestingly, the composition of the subsets over time varied between differentially targeted PDOs, as the percentage of engaging T-cells increased in co-cultures with effectively killed PDOs compared to healthy or untargeted PDOs, although the starting TEG product was equal among all conditions. This observation emphasizes the importance of striving to apply defined ratios of CD4 and CD8 TEG/CAR-T cells to *in vitro* experiments and finally to patients to allow conclusions over differentiation and enrichment of subtypes of the cells during treatment. Implementing defined ratios of subsets of cellular therapy would also allow better comparability among patients and even among types of therapies (e.g. CAR-T and TEG) and therefore potentially higher chances to detect shortcomings or risks of certain treatments earlier. Furthermore, a synergistic effect of a defined CD4:CD8 ratio in B-ALL patients treated with CAR-T cells targeted against CD19 *in vitro* and *in vivo* has been described<sup>40</sup>. Hence, although properties such as killing of entire PDOs by single effector cells as well as serial killing capacity, a characteristic that has been shown favorable for CD8+ CAR-T cells previously<sup>41</sup>, were features observed for CD8+ TEG, also CD4+ TEG and the interaction between the subsets appear to be crucial for scanning, persistence and finally killing. The importance of CD4+ CAR-T cells for the latter has been described in a recent observation of long-term persisting CAR-T cells in leukemia patients, which were found to be exclusively CD4+<sup>42</sup>.

Moreover, the insights gained in this study will allow for a better characterization of cellular therapy products even during their development, and for identification of interesting novel targets for improvement. For instance, transcriptomic analysis of TEG by single cell RNA sequencing (scRNAseq) revealed differential expression of neural cell adhesion molecule 1 (NCAM1) in activated CD8+ T cells. These NCAM1+CD8+ T cells more often showed super-engager behavior and higher killing capacity compared to NCAM1-CD8+ T cells, and NCAM1 surface expression was elevated in TEGs expanded in the presence of IL-15. Zou et. al have shown that simultaneous decrease of inhibitory receptors PDL-1, Tim-3 and Lag-1 on HER2 CAR-T cells resulted in increased expression

of NCAM1, accompanied by prolonged CAR-T cell survival, increased tumor infiltration and IFN $\gamma$  production<sup>43</sup>. Yet, further research is required to assess whether the functional characteristics of super-engager cells can be artificially induced by arming TEG or CAR-T cells with NCAM1. Another option to increase this and other potent phenotypes would be selection of TEGs during the engineering and production process. This, however would pro-long the already time-consuming manufacturing process and the heterogenous apheresis material among patients<sup>44</sup> would potentially lead to higher rates of failed production.

## Enhancing migration and circumventing a hostile tumor environment

Infiltration of the tumor microenvironment (TME) by cytotoxic T cells is associated with good prognosis in a variety of cancer types, among others colorectal<sup>45</sup>, breast<sup>46</sup>, and multiple hematological malignancies<sup>47</sup>, as well as the infiltration of CD8+ T lymphocytes in the context of ACTs such as CAR-T cell therapy<sup>48</sup>. However, it has been shown that the tumor itself and the surrounding TME itself harbors multiple factors to create a tumorigenic and environment hostile for anti-tumor immune cells<sup>49,50</sup>. These factors include the cellular composition of the TME (e.g. mesenchymal stromal cells, immunosuppressive myeloid-derived cells and regulatory T cells) as well as the dense extracellular matrix in solid tumors<sup>51,52</sup>. In **chapters 5 and 6** we aimed to overcome these factors by actively modifying T cells for increased tumor infiltration. These modifications of T cells include genetically removing expression of specific proteins and arming T cells with additional proteins. In these chapters we conduct experiments in a complex 3D multicellular co-culture setting in which the engineered T cells have to actively migrate to the tumor site and into a 3D structure of tumor cells and stroma in Matrigel, mimicking tumor infiltration<sup>53</sup>. We investigated both, hematological and solid malignancies using cell lines, patient-derived tumor cells as well as patient-derived organoids (PDO).

In **chapter 5**, we investigated the discrepancy we observed in T cell migration among CD8+ and CD4+ engineered T cells in a TME infiltration model. Even when administered in an equal ratio, CD8+ T lymphocytes migrated less efficiently to the TME than CD4+ T cells. A screening for soluble molecules uncovered increased levels of chemokines CXCL1, CCL4 and CXCL10 correlated with efficient tumor targeting in 3D tumor models and blocking of these chemokines significantly reduced the capacity of TEG and CAR-T cells to infiltrate and target tumor cells. Analysis of the corresponding surface receptors for these chemokines revealed significantly lower expression of CCL4-receptor CCR5 in CD8+ cells. A more in-depth investigation by scRNAseq identified CD8+ T cells as main

source of CCL4 expression. In this thesis we therefore propose to armor T cell based immunotherapies with the chemokine receptor CCR5, as we found it to enhance tumor migration of cytotoxic CD8+ T cells, infiltration as well as T cell killing of both, breast cancer and colorectal cancer PDOs in a 3D multicellular TME model. Armoring T cells engineered to express a non-functional V $\gamma$ 9V $\delta$ 2TCR called TEG-LM1<sup>11</sup> did increase migration of the T cells, however their killing capacity remained unaffected, nor did we observe targeting of healthy stromal cells by the modified T cells. While we need to collect further proof in *in vivo* studies, these are first indications for the safety of this strategy. Furthermore, CCR5 is not exclusively binding to CCL4, its ligands include CCL3 and CCL5<sup>54,55</sup>. These chemokines are described to be mostly secreted by tumor-associated cells, including various activated immune cells<sup>56</sup>. Therefore, arming T cells with CCR5 might result in a positive feedback-loop and potentially recruiting additional T cells, enhancing efficacy of the treatment. Drug resistance of acute lymphoblastic leukemia has been described as response to increased expression of both, CCL3 and CCL4 upon treatment with anticancer drugs<sup>57</sup>. In such a situation, CCR5-armored T cell-based therapies would possess a unique advantage of increased tumor targeting even when anticancer drugs fail. Nevertheless, CCL4 secretion is clearly tumor-associated and has been shown to factor angiogenesis by increased expression of VEGF in cancer cells<sup>58</sup>, therefore the advantage of increased recruitment of TEGs to the tumor site needs to be carefully balanced to a potential pro-tumor effect of the increase of CCL4 secretion by CD8+ T cells. However, it remains unclear whether CCR5 is the only potential interesting receptor, many other chemokine receptors have been suggested for genetic engineering such as CXCR2<sup>59</sup> and more systematic studies will be needed to explore the optimal co-engineering.

In **chapter 6**, we laid the focus on analyzing immunosuppressive characteristics of the TME in the malignant bone marrow niche and identifying mechanisms to modify the interaction with T cells to allow a more effective tumor infiltration. We used *in vitro* multicellular 3D models to analyze the immunomodulatory effect of Mesenchymal stromal cells (MSC) on the efficacy of T cell based immunotherapies, like TEG and CAR-T, and observed a strong MSC donor dependency. Further analysis by bulk and single cell RNA sequencing (scRNAseq) revealed these differences between immunosuppressive and immunopermissive MSCs to be intrinsic and independent of the cellular environment. Our findings furthermore suggest a difference in collagen expression between the types of MSCs, with permissive MSCs expressing preferentially type IV and XII collagens, and suppressive MSCs preferentially type I, III and VI collagens. The here-identified signatures are presenting a potential option as prognostic markers for patient screening upfront immunotherapy. While patients with an immunopermissive profile seem suitable for treatment with regular T cell based immunotherapy, patients that present an immunosuppressive profile might profit from

additional treatments, such as collagen-blocking options. For instance, we provide evidence that blocking of the collagen-receptor LAIR-1 on T cells partially overcomes the suppressive effect of MSCs and increases killing, providing more evidence of the importance of collagens in the immunosuppressive characteristics of the tumoral extracellular matrix and the role of MSCs in the formation of this collagen matrix. The immune inhibitory receptor LAIR-1 is widely expressed on peripheral blood leukocytes<sup>60</sup> and blocking of interaction of LAIR-1 and its ligands has been previously proposed to be of advantage for T cell targeting<sup>61</sup>. In an ongoing phase 1/2 clinical trial, blocking of LAIR-1 ligands by a LAIR-2 fusion protein (NC410)<sup>62</sup>, is being tested (clinical trial NCT04408599), and especially combinational blockade of TGF- $\beta$ , PD-L1 and LAIR-1 was found to have a strong anti-tumor effect *in vitro*<sup>63</sup>. While one advantage of a broad treatment like this might be the additional effect on other LAIR-1 expressing immune cells besides T cells<sup>61</sup>, the risk of side-effects and toxicities needs to be taken seriously. Another, more directed approach might be the generation of a LAIR-1<sup>KO</sup> T cell therapy product. There is ongoing research on applying the technology of CRISPR-Cas9-based gene editing in the context of engineered T cells, and first results seem promising<sup>64</sup>, as it appeared to be safe in a phase 1 human pilot study<sup>65</sup>. However, the feasibility to implement an extra step into the manufacturing protocol needs to be considered with care. More *in vitro* and *in vivo* studies will be needed to investigate the potential value of our engineering strategy. Instead of genetically removing protein expression by CRISPR-Cas9 technology, the armored CAR-T cells describe engineered T cells expressing additional chemokines or receptors for advanced efficacy, persistence or attraction of other anti-tumor immune cells<sup>66</sup>. Previous designs of armored CAR-T cells include cytokine-secreting CARs, designed to self-stimulate, improve persistence or local proliferation of the CAR-T cells in the TME, or attract other cytotoxic immune cells. While some modifications, for instance secretion of IL-18<sup>67-69</sup>, have been found safe for patient infusion, others such as IL-15 resulted in severe toxicities<sup>70</sup>. Advanced modifications like inducible secretion might help to develop further combinations of interleukin-armored CAR-T cells and might be beneficial to implement in our designs as well<sup>71,72</sup>. Overall, in all of these promising concepts adverse effects of arming T cells need to be carefully accounted for and the safety of the patient needs to be priority over increased efficacy at all times.

## Concluding remarks

Overall, the findings of this thesis prove that there is still a multitude of possibilities to improve T cell based therapies as well as the advantage of the analysis of complex co-culture and screening systems in the quest of discovering new strategies to improve T cell based therapies in general, and V $\gamma$ 9V $\delta$ 2TCR-based therapies specifically. V $\gamma$ 9V $\delta$ 2TCR based T cell engineering therapies are promising future therapies for a variety of tumors, both, hematological and solid malignancies. In this thesis, we contributed to clarify crucial parts of the functional mechanism of this type of  $\gamma\delta$  T cells to exploit their full potential. We provided proof of specific and commonly occurring mutations in cancer cells that trigger recognition through a V $\gamma$ 9V $\delta$ 2TCR, and can hopefully assist in providing more personalized cancer care and allow for selection of patients that will be most likely to respond to treatment with V $\gamma$ 9V $\delta$ 2TCR based immune therapies.

## References

- 1 Finck, A. V., Blanchard, T., Roselle, C. P., Golinelli, G. & June, C. H. Engineered cellular immunotherapies in cancer and beyond. *Nat Med* **28**, 678-689, doi:10.1038/s41591-022-01765-8 (2022).
- 2 Rui, R., Zhou, L. & He, S. Cancer immunotherapies: advances and bottlenecks. *Front Immunol* **14**, 1212476, doi:10.3389/fimmu.2023.1212476 (2023).
- 3 Meringa, A. D. *et al.* Strategies to improve gammadeltaTCRs engineered T-cell therapies for the treatment of solid malignancies. *Front Immunol* **14**, 1159337, doi:10.3389/fimmu.2023.1159337 (2023).
- 4 Wagner, J., Wickman, E., DeRenzo, C. & Gottschalk, S. CAR T Cell Therapy for Solid Tumors: Bright Future or Dark Reality? *Mol Ther* **28**, 2320-2339, doi:10.1016/j.ymthe.2020.09.015 (2020).
- 5 Sebestyen, Z., Prinz, I., Déchanet-Merville, J., Silva-Santos, B. & Kuball, J. Translating gammadelta ( $\gamma\delta$ ) T cells and their receptors into cancer cell therapies. *Nat Rev Drug Discov* **19**, 169-184, doi:10.1038/s41573-019-0038-z (2020).
- 6 Johanna, I. *et al.* Evaluating in vivo efficacy - toxicity profile of TEG001 in humanized mice xenografts against primary human AML disease and healthy hematopoietic cells. *J Immunother Cancer* **7**, 69, doi:10.1186/s40425-019-0558-4 (2019).
- 7 Marcu-Malina, V. *et al.* Redirecting alphabeta T cells against cancer cells by transfer of a broadly tumor-reactive gammadeltaT-cell receptor. *Blood* **118**, 50-59, doi:10.1182/blood-2010-12-325993 (2011).
- 8 Saura-Esteller, J. *et al.* Gamma Delta T-Cell Based Cancer Immunotherapy: Past-Present-Future. *Front Immunol* **13**, 915837, doi:10.3389/fimmu.2022.915837 (2022).
- 9 Dolgin, E. Unconventional gammadelta T cells 'the new black' in cancer therapy. *Nat Biotechnol* **40**, 805-808, doi:10.1038/s41587-022-01363-6 (2022).
- 10 Straetemans, T. *et al.* Untouched GMP-Ready Purified Engineered Immune Cells to Treat Cancer. *Clin Cancer Res* **21**, 3957-3968, doi:10.1158/1078-0432.Ccr-14-2860 (2015).
- 11 Grunder, C. *et al.* gamma9 and delta2CDR3 domains regulate functional avidity of T cells harboring gamma9delta2TCRs. *Blood* **120**, 5153-5162, doi:10.1182/blood-2012-05-432427 (2012).
- 12 Vyborova, A. *et al.* gamma9delta2T cell diversity and the receptor interface with tumor cells. *J Clin Invest* **130**, 4637-4651, doi:10.1172/JCI132489 (2020).
- 13 Straetemans, T. *et al.* TEG001 Insert Integrity from Vector Producer Cells until Medicinal Product. *Mol Ther* **28**, 561-571, doi:10.1016/j.ymthe.2019.11.030 (2020).
- 14 Straetemans, T. *et al.* GMP-Grade Manufacturing of T Cells Engineered to Express a Defined gammadeltaTCR. *Front Immunol* **9**, 1062, doi:10.3389/fimmu.2018.01062 (2018).
- 15 de Witte, M. A. *et al.* Activity of ex vivo graft and DLI Engineering within the last decade increases, a survey from the EBMT Cellular Therapy & Immunobiology Working Party. *Bone Marrow Transplant* **58**, 719-722, doi:10.1038/s41409-023-01953-1 (2023).
- 16 Poupot, M. & Fournie, J. J. Non-peptide antigens activating human Vgamma9/Vdelta2 T lymphocytes. *Immunol Lett* **95**, 129-138, doi:10.1016/j.imlet.2004.06.013 (2004).
- 17 Sebestyen, Z. *et al.* RhoB Mediates Phosphoantigen Recognition by V $\gamma$ 9V $\delta$ 2 T Cell Receptor. *Cell Rep* **15**, 1973-1985, doi:10.1016/j.celrep.2016.04.081 (2016).
- 18 Gu, S. *et al.* Phosphoantigen-induced conformational change of butyrophilin 3A1 (BTN3A1) and its implication on Vgamma9Vdelta2 T cell activation. *Proc Natl Acad Sci U S A* **114**, E7311-E7320, doi:10.1073/pnas.1707547114 (2017).

- 19 Harly, C. *et al.* Key implication of CD277/butyrophilin-3 (BTN3A) in cellular stress sensing by a major human gammadelta T-cell subset. *Blood* **120**, 2269-2279, doi:10.1182/blood-2012-05-430470 (2012).
- 20 Palakodeti, A. *et al.* The molecular basis for modulation of human V $\gamma$ 9V $\delta$ 2 T cell responses by CD277/butyrophilin-3 (BTN3A)-specific antibodies. *J Biol Chem* **287**, 32780-32790, doi:10.1074/jbc.M112.384354 (2012).
- 21 Rigau, M. *et al.* Butyrophilin 2A1 is essential for phosphoantigen reactivity by gammadelta T cells. *Science* **367**, doi:10.1126/science.aay5516 (2020).
- 22 Karunakaran, M. M. *et al.* Butyrophilin-2A1 Directly Binds Germline-Encoded Regions of the Vgamma9Vdelta2 TCR and Is Essential for Phosphoantigen Sensing. *Immunity* **52**, 487-498 e486, doi:10.1016/j.immuni.2020.02.014 (2020).
- 23 Hsiao, C. C., Nguyen, K., Jin, Y., Vinogradova, O. & Wiemer, A. J. Ligand-induced interactions between butyrophilin 2A1 and 3A1 internal domains in the HMBPP receptor complex. *Cell Chem Biol* **29**, 985-995 e985, doi:10.1016/j.chembiol.2022.01.004 (2022).
- 24 Yuan, L. *et al.* Phosphoantigens glue butyrophilin 3A1 and 2A1 to activate Vgamma9Vdelta2 T cells. *Nature*, doi:10.1038/s41586-023-06525-3 (2023).
- 25 Mamedov, M. R. *et al.* CRISPR screens decode cancer cell pathways that trigger gammadelta T cell detection. *Nature* **621**, 188-195, doi:10.1038/s41586-023-06482-x (2023).
- 26 Drost, J. *et al.* Sequential cancer mutations in cultured human intestinal stem cells. *Nature* **521**, 43-47, doi:10.1038/nature14415 (2015).
- 27 Lin, C. *et al.* Tumor Mutation Burden Correlates With Efficacy of Chemotherapy/Targeted Therapy in Advanced Non-Small Cell Lung Cancer. *Front Oncol* **10**, 480, doi:10.3389/fonc.2020.00480 (2020).
- 28 Goodman, A. M. *et al.* Tumor Mutational Burden as an Independent Predictor of Response to Immunotherapy in Diverse Cancers. *Mol Cancer Ther* **16**, 2598-2608, doi:10.1158/1535-7163.MCT-17-0386 (2017).
- 29 Sha, D. *et al.* Tumor Mutational Burden as a Predictive Biomarker in Solid Tumors. *Cancer Discov* **10**, 1808-1825, doi:10.1158/2159-8290.CD-20-0522 (2020).
- 30 Bose, R. *et al.* Activating HER2 mutations in HER2 gene amplification negative breast cancer. *Cancer Discov* **3**, 224-237, doi:10.1158/2159-8290.CD-12-0349 (2013).
- 31 Hirotsu, Y. *et al.* Intrinsic HER2 V777L mutation mediates resistance to trastuzumab in a breast cancer patient. *Med Oncol* **34**, 3, doi:10.1007/s12032-016-0857-2 (2017).
- 32 Liu, Y. *et al.* EBV latent membrane protein 1 augments gammadelta T cell cytotoxicity against nasopharyngeal carcinoma by induction of butyrophilin molecules. *Theranostics* **13**, 458-471, doi:10.7150/thno.78395 (2023).
- 33 Zhao, H. F., Wang, J. & Tony To, S. S. The phosphatidylinositol 3-kinase/Akt and c-Jun N-terminal kinase signaling in cancer: Alliance or contradiction? (Review). *Int J Oncol* **47**, 429-436, doi:10.3892/ijo.2015.3052 (2015).
- 34 Kovacic, S. *et al.* Akt activity negatively regulates phosphorylation of AMP-activated protein kinase in the heart. *J Biol Chem* **278**, 39422-39427, doi:10.1074/jbc.M305371200 (2003).
- 35 Zhao, Y. *et al.* ROS signaling under metabolic stress: cross-talk between AMPK and AKT pathway. *Mol Cancer* **16**, 79, doi:10.1186/s12943-017-0648-1 (2017).
- 36 Leclerc, G. M., Leclerc, G. J., Fu, G. & Barredo, J. C. AMPK-induced activation of Akt by AICAR is mediated by IGF-1R dependent and independent mechanisms in acute lymphoblastic leukemia. *J Mol Signal* **5**, 15, doi:10.1186/1750-2187-5-15 (2010).
- 37 Kazyken, D. *et al.* AMPK directly activates mTORC2 to promote cell survival during acute energetic stress. *Sci Signal* **12**, doi:10.1126/scisignal.aav3249 (2019).

- 38 van Diest, E. *et al.* Gamma delta TCR anti-CD3 bispecific molecules (GABs) as novel immunotherapeutic compounds. *J Immunother Cancer* **9**, doi:10.1136/jitc-2021-003850 (2021).
- 39 Dekkers, J. F. *et al.* Uncovering the mode of action of engineered T cells in patient cancer organoids. *Nat Biotechnol* **41**, 60-69, doi:10.1038/s41587-022-01397-w (2023).
- 40 Sommermeyer, D. *et al.* Chimeric antigen receptor-modified T cells derived from defined CD8+ and CD4+ subsets confer superior antitumor reactivity in vivo. *Leukemia* **30**, 492-500, doi:10.1038/leu.2015.247 (2016).
- 41 Davenport, A. J. *et al.* CAR-T cells are serial killers. *Oncoimmunology* **4**, e1053684, doi:10.1080/2162402X.2015.1053684 (2015).
- 42 Melenhorst, J. J. *et al.* Decade-long leukaemia remissions with persistence of CD4(+) CAR T cells. *Nature* **602**, 503-509, doi:10.1038/s41586-021-04390-6 (2022).
- 43 Zou, F. *et al.* Engineered triple inhibitory receptor resistance improves anti-tumor CAR-T cell performance via CD56. *Nat Commun* **10**, 4109, doi:10.1038/s41467-019-11893-4 (2019).
- 44 Cuffel, A. *et al.* Real-world characteristics of T-cell apheresis and clinical response to tisagenlecleucel in B-cell lymphoma. *Blood Adv* **6**, 4657-4660, doi:10.1182/bloodadvances.2022007057 (2022).
- 45 Galon, J. *et al.* Type, density, and location of immune cells within human colorectal tumors predict clinical outcome. *Science* **313**, 1960-1964, doi:10.1126/science.1129139 (2006).
- 46 Mahmoud, S. M. *et al.* Tumor-infiltrating CD8+ lymphocytes predict clinical outcome in breast cancer. *J Clin Oncol* **29**, 1949-1955, doi:10.1200/JCO.2010.30.5037 (2011).
- 47 Chen, P. L. *et al.* Analysis of Immune Signatures in Longitudinal Tumor Samples Yields Insight into Biomarkers of Response and Mechanisms of Resistance to Immune Checkpoint Blockade. *Cancer Discov* **6**, 827-837, doi:10.1158/2159-8290.CD-15-1545 (2016).
- 48 Li, X. *et al.* Infiltration of CD8(+) T cells into tumor cell clusters in triple-negative breast cancer. *Proc Natl Acad Sci U S A* **116**, 3678-3687, doi:10.1073/pnas.1817652116 (2019).
- 49 Marofi, F. *et al.* CAR T cells in solid tumors: challenges and opportunities. *Stem Cell Res Ther* **12**, 81, doi:10.1186/s13287-020-02128-1 (2021).
- 50 Lambie, A. J. & Lind, E. F. Targeting the Immune Microenvironment in Acute Myeloid Leukemia: A Focus on T Cell Immunity. *Front Oncol* **8**, 213, doi:10.3389/fonc.2018.00213 (2018).
- 51 Hou, A. J., Chen, L. C. & Chen, Y. Y. Navigating CAR-T cells through the solid-tumour microenvironment. *Nat Rev Drug Discov* **20**, 531-550, doi:10.1038/s41573-021-00189-2 (2021).
- 52 Verma, N. K. *et al.* Obstacles for T-lymphocytes in the tumour microenvironment: Therapeutic challenges, advances and opportunities beyond immune checkpoint. *EBioMedicine* **83**, 104216, doi:10.1016/j.ebiom.2022.104216 (2022).
- 53 Braham, M. V. J. *et al.* Cellular immunotherapy on primary multiple myeloma expanded in a 3D bone marrow niche model. *Oncoimmunology* **7**, e1434465, doi:10.1080/2162402X.2018.1434465 (2018).
- 54 Raport, C. J., Gosling, J., Schweickart, V. L., Gray, P. W. & Charo, I. F. Molecular cloning and functional characterization of a novel human CC chemokine receptor (CCR5) for RANTES, MIP-1beta, and MIP-1alpha. *J Biol Chem* **271**, 17161-17166, doi:10.1074/jbc.271.29.17161 (1996).
- 55 Combadiere, C., Ahuja, S. K., Tiffany, H. L. & Murphy, P. M. Cloning and functional expression of CC CKR5, a human monocyte CC chemokine receptor selective for MIP-



- 1(alpha), MIP-1(beta), and RANTES. *J Leukoc Biol* **60**, 147-152, doi:10.1002/jlb.60.1.147 (1996).
- 56 Menten, P., Wuyts, A. & Van Damme, J. Macrophage inflammatory protein-1. *Cytokine Growth Factor Rev* **13**, 455-481, doi:10.1016/s1359-6101(02)00045-x (2002).
- 57 Chen, Y. L. *et al.* Blocking ATM-dependent NF-kappaB pathway overcomes niche protection and improves chemotherapy response in acute lymphoblastic leukemia. *Leukemia* **33**, 2365-2378, doi:10.1038/s41375-019-0458-0 (2019).
- 58 Hua, F. & Tian, Y. CCL4 promotes the cell proliferation, invasion and migration of endometrial carcinoma by targeting the VEGF-A signal pathway. *Int J Clin Exp Pathol* **10**, 11288-11299 (2017).
- 59 Idorn, M. *et al.* Chemokine receptor engineering of T cells with CXCR2 improves homing towards subcutaneous human melanomas in xenograft mouse model. *Oncoimmunology* **7**, e1450715, doi:10.1080/2162402X.2018.1450715 (2018).
- 60 Meyaard, L. *et al.* LAIR-1, a novel inhibitory receptor expressed on human mononuclear leukocytes. *Immunity* **7**, 283-290, doi:10.1016/s1074-7613(00)80530-0 (1997).
- 61 Xie, J. *et al.* Blocking LAIR1 signaling in immune cells inhibits tumor development. *Front Immunol* **13**, 996026, doi:10.3389/fimmu.2022.996026 (2022).
- 62 Ramos, M. I. P. *et al.* Cancer immunotherapy by NC410, a LAIR-2 Fc protein blocking human LAIR-collagen interaction. *Elife* **10**, doi:10.7554/eLife.62927 (2021).
- 63 Horn, L. A. *et al.* Remodeling the tumor microenvironment via blockade of LAIR-1 and TGF-beta signaling enables PD-L1-mediated tumor eradication. *J Clin Invest* **132**, doi:10.1172/JCI155148 (2022).
- 64 Dimitri, A., Herbst, F. & Fraietta, J. A. Engineering the next-generation of CAR T-cells with CRISPR-Cas9 gene editing. *Mol Cancer* **21**, 78, doi:10.1186/s12943-022-01559-z (2022).
- 65 Stadtmauer, E. A. *et al.* CRISPR-engineered T cells in patients with refractory cancer. *Science* **367**, doi:10.1126/science.aba7365 (2020).
- 66 Hawkins, E. R., D'Souza, R. R. & Klampatsa, A. Armored CAR T-Cells: The Next Chapter in T-Cell Cancer Immunotherapy. *Biologics* **15**, 95-105, doi:10.2147/BTT.S291768 (2021).
- 67 Robertson, M. J. *et al.* A dose-escalation study of recombinant human interleukin-18 using two different schedules of administration in patients with cancer. *Clin Cancer Res* **14**, 3462-3469, doi:10.1158/1078-0432.CCR-07-4740 (2008).
- 68 Avanzi, M. P. *et al.* Engineered Tumor-Targeted T Cells Mediate Enhanced Anti-Tumor Efficacy Both Directly and through Activation of the Endogenous Immune System. *Cell Rep* **23**, 2130-2141, doi:10.1016/j.celrep.2018.04.051 (2018).
- 69 Chmielewski, M. & Abken, H. CAR T Cells Releasing IL-18 Convert to T-Bet(high) FoxO1(low) Effectors that Exhibit Augmented Activity against Advanced Solid Tumors. *Cell Rep* **21**, 3205-3219, doi:10.1016/j.celrep.2017.11.063 (2017).
- 70 Conlon, K. C. *et al.* Redistribution, hyperproliferation, activation of natural killer cells and CD8 T cells, and cytokine production during first-in-human clinical trial of recombinant human interleukin-15 in patients with cancer. *J Clin Oncol* **33**, 74-82, doi:10.1200/JCO.2014.57.3329 (2015).
- 71 Chmielewski, M., Kopecky, C., Hombach, A. A. & Abken, H. IL-12 release by engineered T cells expressing chimeric antigen receptors can effectively Muster an antigen-independent macrophage response on tumor cells that have shut down tumor antigen expression. *Cancer Res* **71**, 5697-5706, doi:10.1158/0008-5472.CAN-11-0103 (2011).
- 72 Liu, Y. *et al.* Armored Inducible Expression of IL-12 Enhances Antitumor Activity of Glypican-3-Targeted Chimeric Antigen Receptor-Engineered T Cells in Hepatocellular Carcinoma. *J Immunol* **203**, 198-207, doi:10.4049/jimmunol.1800033 (2019).



# Appendix

**Nederlandse Samenvatting**

**Acknowledgements**

**List of publications**

**Curriculum vitae**

## Nederlandse Samenvatting

### T cel therapie tegen kanker

Bij kanker vindt er ongecontroleerde deling van cellen plaats. Tot voor kort bestonden de meest gebruikte behandelmethoden tegen kanker uit opereren, chemotherapie of bestraling. Deze behandelingen zijn echter niet heel specifiek en zorgen voor veel bijwerkingen in de patiënten.

De afgelopen decennia is ontdekt dat het menselijke immuunsysteem niet alleen in staat is ziekteverwekkers, zoals virussen en bacteriën, te bestrijden maar dat deze ook een belangrijke rol speelt in het detecteren en opruimen van gemuteerde (kanker) cellen. Sindsdien is er veel onderzoek gedaan waarbij gebruikgemaakt wordt van het immuunsysteem om een meer gepersonaliseerde en preciezere kankertherapie te ontwikkelen, in de vorm van immunotherapie.

Vandaag de dag bestaan er veel vormen van immunotherapie, waaronder gemodificeerde T cellen die een chimeer antigeen receptor tot expressie brengen (CAR-T cellen). De goedkeuring van CAR-T cellen door de FDA en de EMA heeft gezorgd voor een overweldigend klinisch succes in de behandeling van hematologische aandoeningen, in het bijzonder tegen acute lymfatische leukemie (ALL), diffuus grootcellig B cel lymfoom (DLBCL) en myeloma. CAR-T cellen herkennen kwaadaardige cellen door bepaalde stukjes eiwitten op het oppervlak, antigenen geheten, door middel van hun antigeen-receptor. Ondanks het succes in de behandeling van hematologische aandoeningen blijft het aanpakken van solide tumoren met celtherapie een uitdaging. In **hoofdstuk 1** worden de belangrijkste hindernissen voor het aanpakken van solide tumoren beschreven - antigeen dilemma, T cel fitness en een immuun-onderdrukkende tumor micro omgeving - en zullen mogelijke oplossingen in deze thesis benoemd worden.

### Oplossing voor het “antigeen dilemma” door gebruik van V $\gamma$ 9V $\delta$ 2TCR gebaseerde T-cel therapieën

Een van de grootste nadelen van het gebruik van CAR-gebaseerde immunotherapie in solide tumoren is hun afhankelijkheid van een breed tot expressie gebracht en tumor-specifiek antigeen. Vaak komen gekozen antigenen ook tot expressie in gezond weefsel, welke vervolgens herkend kunnen worden door de CAR-T cellen, wat tot (ernstige) bijwerkingen leidt. Een mogelijke oplossing voor dit probleem is het gebruik van een V $\gamma$ 9V $\delta$ 2TCR. V $\gamma$ 9V $\delta$ 2T cellen zijn een subset van T cellen, die in plaats van de meer gebruikelijke  $\alpha\beta$ TCR een bepaald type TCR genaamd  $\gamma\delta$ TCR bij zich dragen op het oppervlak. Ondanks dat deze cellen maar een kleine fractie van ongeveer 5% van alle T

cellen in menselijk bloed uitmaken, zijn ze erg interessant voor onderzoekers in het veld van immunotherapie. Dit komt door de manier waarop ze tumorcellen herkennen. Ze zijn in staat subtiele verschillen in het metabolisme van kwaadaardige cellen te detecteren.

Deze V $\gamma$ 9V $\delta$ 2TCR herkent een breed scala van hematopoietische en solide tumoren *in vitro*, oftewel in het lab. Ondanks de veelbelovende kenmerken van op V $\gamma$ 9V $\delta$ 2T-cell gebaseerde therapieën, zijn deze nog niet succesvol toegepast in de kliniek. Dit komt voornamelijk doordat in de mix van V $\gamma$ 9V $\delta$ 2TCRs er grote verschillen zijn in hoe goed deze in staat zijn om zich aan hun doel te binden. Als oplossing voor dit probleem heeft onze groep in het afgelopen decennium TEGs ontwikkeld;  $\alpha\beta$  T cellen aangepast om een bepaalde  $\gamma\delta$  TCR tot expressie te brengen. Bij deze methode introduceren we een tumor-specifieke en sterk bindende  $\gamma\delta$ TCR in  $\alpha\beta$ T cellen, waardoor de twee voordelen van beide type T cellen benut worden. Namelijk de brede maar tumor-specifieke herkenning van de  $\gamma\delta$ TCR en de mogelijkheid om snel uit te groeien van  $\alpha\beta$ T cellen.

### **Een groot dilemma van V $\gamma$ 9V $\delta$ 2TCR gebaseerde therapie: slechte definitie van het target**

Alhoewel V $\gamma$ 9V $\delta$ 2T cellen een grote groei in onderzoek focus hebben doorgemaakt de afgelopen jaren, en ze in het middelpunt staan van meerdere nieuwe aanpakken van immunotherapie, is hun directe ligand BTN2A1 pas onlangs ontdekt. Ook is het herkennings mechanisme van V $\gamma$ 9V $\delta$ 2TCR T cellen nog niet helemaal bekend. In **hoofdstuk 3** beschrijven we het onbekende mechanisme van transformatie in kwaadaardige cellen waardoor V $\gamma$ 9V $\delta$ 2TCRs tumorcellen herkennen en aanvallen. Om de vroegste transformaties in kankercellen na te bootsen, hebben we enkelvoudige oncogene mutaties genetisch aangebracht in gezonde borstcellen en darm organoïden – simpel gezegd, 3-dimensionale mini-versies van een orgaan. Dit is gedaan om te laten zien dat deze enkelvoudige mutaties genoeg zijn om herkenning door V $\gamma$ 9V $\delta$ 2TCR T cellen te induceren. Verder onderzoeken we de betrokken cellulaire pathways en identificeren we nieuwe betrokken eiwitten.

### **Karakteriseren van heterogeneity of gemodificeerde immuuncellen**

In **hoofdstuk 4** introduceren we een 3D-live-imaging platform, BEHAV3D, die het live volgen en karakteriseren van T cellen en hun dynamische interactie met van patiënten afkomstige borstkanker organoïden mogelijk maakt. We beschrijven hoe we cellulaire anti-kanker immunotherapie kunnen verbeteren door verschillende types van T cellen in dit systeem te identificeren. Dit geeft de mogelijkheid om te verrijken voor een bepaalde potente transcriptomische handtekening in effector cellen voor het toedienen aan patiënten.

## Vergroten van migratie en circumventing een hostile tumor omgeving

Naast de  $\alpha\beta$  receptor, dragen  $\alpha\beta$  T cellen meerdere andere receptoren op hun oppervlakte, waaronder de co-receptoren CD4 en CD8. T cellen die CD8 op hun oppervlakte dragen, de zogenoemde cytotoxische T cellen, zijn in staat om geïnfekteerde of gemuteerde cellen te elimineren. T cellen die een CD4 receptor bij zich dragen scheiden verschillende stofjes uit, zogenoemde cytokines, die indirect het doden van tumorcellen tot stand brengen.

In **hoofdstuk 5** tonen we aan dat TEGs het beste zijn in het doden van tumorcellen als zowel CD4+ als CD8+ TEGs aanwezig zijn. Echter, zelfs als deze toegediend worden in gelijke delen zijn de CD4+ cellen beter in staat om naar de tumor plek te bewegen. In dit hoofdstuk hebben we CD8+ TEGs en CAR-T cellen genetisch aangepast om een extra receptor tot expressie te brengen op hun oppervlak, CCR5. Dit stelt hen in staat om beter naar de plek van de tumor te migreren voor een meer gestuurd anti-tumor effect.

In **hoofdstuk 6** hebben we een poging gewaagd de vijandige micro omgeving van de kwaadaardige beenmerg tumor te begrijpen en te overwinnen. We ontdekten dat mesenchymale stamcellen (MSC), cellen die een groot deel van de beenmerg tumor micro omgeving uitmaken, gemodificeerde immuuncellen zowel kunnen stimuleren als remmen in de aanpak van kwaadaardige cellen als deze samen gekweekt worden met tumorcellen. Verder laten we zien dat het erg donor afhankelijk is of deze cellen een remmende of stimulerende invloed hebben. We bevestigden de rol van MSCs in het vormen van een immunosuppressieve collageen matrix, een netje van collageen-draden. LAIR-1 is een receptor die tot expressie komt op T cellen, die remmende signalen naar de T cell stuurt na binding met collageen. We laten zien dat het verstoren van deze binding, door LAIR-1 te blokkeren op T cellen, zorgt voor een toename in tumorinfiltratie in de aanwezigheid van immuunonderdrukkende MSCs.

In het laatste hoofdstuk, **hoofdstuk 7**, worden de resultaten van deze thesis samengevat en bediscussieerd in de context van recente literatuur in het veld van Vg9V $\delta$ 2T cel biologie en modificering van T cell immunotherapieën.

## Acknowledgements

Dear **Jürgen**, you're both the busiest and yet most approachable professor I have ever worked for. To me it's truly amazing that you are still as involved in daily research as you are, besides all your other positions and responsibilities, and always make a small spot available for your employees if they are running into problems. I still remember sending my CV for the research technician position at 21h and I think it's telling that I got a reply from you within 20 min. Thank you for giving me the opportunity to still change my path to become a PhD student, for your rational but enthusiastic mentality. Vielen Dank auch für die Möglichkeit zwei Konferenzen mit dir zu besuchen, und für den gemütlichen Abend in Berlin! Ich drücke die Daumen für TEGs in der Zukunft!

Dear **Zsolt**, during my time under your supervision it felt that the group and accompanied with that your responsibilities grew exponentially. I always felt comfortable to knock on your door with problems or new results (and sometimes those were the same). Thank you for giving me the opportunity to become a PhD student in your group and for your support, guidance and enthusiasm throughout that time. I've enjoyed the many discussions in meetings, "very straight forward" plans, shared sweets and chats. Please continue hosting your garden barbeques, it's always been a pleasure being in your beautiful garden and enjoying your cooking skills. Thanks for buying overpriced Moscow Mules in Lisbon on my birthday, they were actually very delicious! Finally, thanks for helping me arrange to stay a member in the CTI and to shadow in your group for my Postdoc.

Dear **Trudy**, thanks for being a role model and all your input and knowledge that helped our progress and manuscripts. I wish you all the best for your projects!

**Dennis**, Dr. Beringer, thank you so much for all your valuable input and critical thoughts on our articles and experiments! Your door was always open for my questions and you would always think along and try to help out. I always enjoyed meeting you in the protein or VMT lab (back when you were there a bit more often) and have a little chat. Thanks for all your funny stories in the many meetings we shared, and for a fun party night in Lisbon! Good luck on your future path!

Dear **Pierre**, thanks for giving me some extra time to finish my thesis before I started my postdoc with you. I'm very excited to continue our research!

Dear **Sanne** and **Froso** (Froowsoow), we started as research technicians in the group almost at the same time, and we quite immediately hit it off as friends as well. Long culturing sessions in the ML2, Doppios at the "secret spot", borrels and of course Monday's pubquiz at Mick O'Connells with Nachos, Coke zeros, sisterhood of the travelling pants and other dinner outings will always be on my mind when I think of us three. **Sanne**, thank god you always keep on reminding us that you're nice and we like you. I'm very impressed with your broad range of interests and skills. I'm beyond grateful

to call you my friend and to know that I can literally call you at all times for an emergency or a renovation! Special thanks to you and Guido for helping with the Dutch translation of this thesis' summary. **Froso**, you were a constant in the Kuball group for a good while, and I always knew that I could come to you, when I needed an extra hand, help with a protocol, or just an ear to vent to. Thank you for being in our lives, being a great friend, for your help in both house renovations and for being involved with the girls (and for bringing mostly non-annoying presents). To far more years of friendship for the three of us and, who knows, maybe we all end up working together again at some point in our lives.

**Thomas**, with some short breaks we shared our whole time in the CTI and I already miss having you around! We share lots of fun memories at work and besides: From discussing work over a coffee, a weekend trip to Hamburg, pubquiz, and watching football to you helping us renovate and move. You're truly a person that I can count on (if I have the time to wait for you, Slowmas)! Not missing the bike content, though..

I am so grateful to all current and former members of the **Kuball labs** for eight lovely years and their direct or indirect contribution to this thesis. It's been fun to see the group grow over the past years. Best of luck for your future paths to everybody and please continue to meet up and do fun things and great science!

**Tineke**, I can't thank you enough for being such a huge help in the lab and for simply being the person that you are. Whether it was for performing stimulation assays, culturing TEGs or placing urgent orders, I could always count on you. All your funny stories always lightened up meetings and borrels. Enjoy your last years in the lab and especially the time outside of the lab in your garden and with your family. **Patricia**, first off, thank you so much with all your tips regarding formatting and submission infos for this boekje! I hope our conversations can soon go back to the normal and nicer things. Thank you for lunches and coffees and all the nice chats in and outside of the lab, about science, projects and other things and your endless bafflement about the Dutch weather. I'm very glad you're sticking around as Postdoc! **Sabine**, fellow pieper-survivor and master of the mice. Thanks for always being open to help others out, your contributions to the *in vivo* experiments and for chats during the washing steps of my ELISAs. I always enjoy meeting you in the lab, the hallway or at the liftplein for a small (and sometimes longer) chat. **Caterina**, team "late" lunches, thanks for the nice lunch and coffee conversations, playing beach house in the ML2 and for helping us out with TEGs if ours decided not to grow well. **Ivana**, I enjoyed the lunch breaks and chats in the lab with you. Best of luck on your future path! **Lucrezia**, glad that you've joined me on the one specific CAR-project so that we could share the many frustrations.. Glad that we still won in the end! Thanks for nice chats and delicious chocolates from Switzerland. **Anniek**, thanks for the great days and nights in Lisbon! Glad you will take over hosting the "Glühwein-Abend" after I left. **Annet**, I love your calm and funny character, I think it's truly impossible to stress you. Thanks for nice chats. **Angelo**, thanks for working



together on multiple great manuscripts! Good luck for your defence in June! **Peter**, thank you for all your expertise and knowledge in data analysis, and for your contribution to almost all papers in this thesis! **Caro**, was für ein Glücksgriff dass du in meinem letzten PhD Jahr als Studentin zu uns gekommen bist. Danke für deine Mitarbeit an Chapter 6 und wie schön dass du dich entschieden hast in der Gruppe zu bleiben. Viel Freude und Erfolg auf deinem PhD Weg! **Mara**, it's funny that we are more involved scientifically now compared to when I was still an active member in the group. Thanks for organizing CTI drinks! **Konstantinos**, thanks for bringing some fun and chaos into the group during the time you were here! **Laia**, you're such a cheerful person, it's always a pleasure meeting you in the hallway or lab. **Jiali**, thanks for still helping me with an assay, although it turned out you've also never done it before. **Monique**, I'm endlessly impressed how you manage Jürgen's agenda and thankful for all your help in arranging flights and trains and for always sharing a nice word in your mails to me!

**Eline**, it's truly fascinating that we never shared a project or meeting, since you've been working in the group for most of my time as well. I enjoyed the talks in the protein lab and ML2 and it's nice to still sometimes run into you! **Inez**, if I had to think of a morning person, you probably would be the last person on my mind. Thanks for funny Monday morning meetings, help with mouse experiments, and times for little rants. **Domenico**, I loved sharing an office with you, being in meetings with you and seeing you running around the lab stressed and being dramatic in Italian ("It's a disaster!!"). Thanks for all the chats about weird things kids do and all the laughs we shared. Your expertise helped us in so many ways and I enjoyed discussing my project with you. See you at the playground! **Lovro**, although in reality you've only been here for a year, it felt so much longer. Game nights, pubquiz, city and beach day trips in the weekend, and coffees will always be in good memories and I'm looking forward to our summer holiday in Slovenia! **Anna**, you're truly a fascinating person, nice, funny, so driven and caring for other people. Thanks for karaoke at the sushi festival, weird questions while working at the flow bench and self-baked food! Good luck finishing your PhD.

**Aram**, first and most special student to me. You hit me up with lots of "fun facts". Your agarose gels were amongst the ugliest I've ever seen. Thanks for the many Tivoli parties we've joined together and your dramatic "Take on me" performances. Looking forward to the next coffee date! Good luck finishing your own PhD and your dream to go to space. I'm sure you'll make it! All other students who helped us in all stories that make up this thesis, especially **Jelle**, **Nikos** and **Lauren**, thank you so much and good luck for your future! **Noa**, you definitely set new standards for future bachelor students for me. I'm certain you will end up doing great things!

**Mitchell**, it was and still is inspiring to see how enthusiastic you are about science. Thanks for still catching up every now and then, for game nights, Game of Thrones watching events. "We should get a coffee soon!" **Coco**, although it wasn't for long, I really enjoyed sharing the office with you, we had so many things in common and to talk

and discuss about! **Leon**, great company in our little private office! Thanks for the discussions and giving a doctor's view on things. All your bike talk with Thomas was definitely insufferable and I think my ears only didn't start to bleed thanks to my noise-cancelling headphones. **Marta**, thank you for being a lovely person, it's always a pleasure running into you in the corridor! **Maria**, I always enjoy the little catch-up chats whenever we meet in the corridor. It feels so good to have someone in the same situation and to share frustrations over flawed systems.

I want to thank all **research technicians** in the CTI for the nice chats, help with ordering, finding things, and so much more. You're truly the backbone of each lab and it's so nice to see the special bond you! All the best for your futures!

**Tomo** and **Sangho**, thanks a lot for culturing the colorectal organoids for us and answering our endless questions regarding culturing, medium composition and age of the organoids. Good luck on your further journey. **Florijn**, I believe the collaboration with you and your colleagues in the PMC was the most driven one I have ever been involved in. Good luck for your new mission! **Thijs** and **Annick**, I wished the collaboration with you could have come along earlier, since it really boosted our chapter 3 and I wished I had more time left to follow it up myself. Thanks for nice meetings, chats in the lab and on the hallway and sharing the enthusiasm about the project!

**Rabea, Jana, Judith, Lisa, Johannes, Willi, Lucas, Jan, Martin, Sven, Caro, Petra, Matthias**, Freunde seit Kindheit, Schulzeit und Studium! Danke fürs Begleiten von so vielen Lebensstationen, Zuhören und der tollen und wichtigen Freundschaften!

**Marén** und **Micha**, seit inzwischen 13 Jahren in meinem Leben, und ich könnte mir keine besseren Schwiegereltern vorstellen. Ich habe mich bei euch direkt wohl gefühlt und bin euch für so viele Dinge dankbar, allen voran dafür, dass ihr wunderbare Großeltern für Elin und Mina seid. Micha, danke für deine Hilfe beim Renovieren von unserer Wohnung, dein aufrichtiges Interesse an so vielen Dingen und deiner ansteckenden Begeisterung beim Sport-gucken. Marén, danke für deine herzliche Art, all die Zeit die du mir freigemacht hast damit ich arbeiten konnte wenn wir bei euch waren, für den unendlichen Vorrat an Sekt und quatschen am Abend. **Celine**, danke dass du ausnahmslos jedes Mal Zeit investiert um uns zu sehen wenn wir „im Osten“ sind, für Spaziergänge mit Rocko, lustige Abende und veganes Kochen. **Jan** und **Katharina**, Qualität und Zusammenhang unserer Gespräche verläuft definitiv anti-proportional zur Anzahl an Kindern im Raum. Zum Glück gibt es abends Zeit das nachzuholen und es ist immer schön euch zu sehen!

**Oma Marlies**, danke für den unendlichen Vorrat an selbstgestrickten Socken, Gurken, Erdbeeren, Himbeeren, Salat und Zucchini. **Martin**, die Wochenendtrips nach Barcelona fehlen mir zwar, aber ich bin froh, dass ihr wieder näher bei uns wohnt! Wissenschaftlich gesehen natürlich ein Vorbild (glaube ich zumindest, selbstverständlich habe ich von deiner Thesis auch nur das Dankwort ~~gelesen~~ verstanden), aber es ist noch

viel wunderbarer zu sehen, was für ein toller Papa du bist und dass wir uns trotz der 7 Jahren Altersunterschied heute so nah sind wie selten zuvor. **Vierka**, zum Glück warst du zur gleichen Zeit wie Martin in Barcelona und bist jetzt auch Teil unserer Familie. Danke für die vielen Gespräche, Spieleabende und einen unvergesslichen Sommerurlaub in deiner Heimat Slowakei. **Anke**, Schwester, Mitbewohnerin, Freundin. Ohne den Urlaub in Groningen mit Martin, dir und Janne wäre ich wahrscheinlich nie in Utrecht gelandet und du hast mir in den letzten Jahren in so vieler Hinsicht geholfen. Du bist ein riesiges Vorbild für mich, und zeigst mir immer wieder dass man mit einer starken Familie im Rücken alles schaffen kann. **Janne**, gefühlt warst du gestern noch ein Baby und bist in meiner Wohnung in Utrecht rumgekrabbelt. Es ist wundervoll zu sehen, was für ein toller Mensch aus dir wird und wie sehr Elin, Mina, Anna und Rieke zu dir aufschauen. **Philipp**, danke dass du immer daran denkst schöne Momente auf Fotos festzuhalten! Auf viele weitere gemeinsame Familienjahre!

**Mama** und **Papa**, ich weiß nicht, wo ich anfangen soll euch zu danken, ihr seid tolle Vorbilder für mich. Daher jetzt eine nicht gewichtete und sehr unvollständige Aufzählung: Danke für eure Unterstützung beim Studium. Fürs opfern eurer Freizeit in der Rente für eure Kinder (bzw Enkelkinder). Für all eure Hilfe beim Renovieren und der Gartenarbeit. Für das Übernehmen vom Mama-Tag in den letzten Monaten. Für das Organisieren von (Kurz)Urlaube mit der ganzen Familie, die uns so wichtig sind und ein Grund, dass unsere Familie so eng ist. Dass ich immer anrufen kann. Für das Auffüllen von unserem Tee-Vorrat und selbstgebackenes Brot und Brötchen und Kuchen. Dass wir uns wirklich immer auf euch verlassen können. Ohne euch wäre ich nicht wo ich bin. Vielen Dank für wirklich alles!

**Marcus**, ich bin unendlich froh, dich an meiner Seite zu haben, ganz besonders in dieser doch sehr intensiven Zeit. Auch wenn du nicht immer Verständnis für Abläufe im Labor hattest, hast du immer dafür gesorgt, dass ich Zeit bekomme um etwas mehr zu arbeiten. Danke für das Planen von Wochenendtrips, Konzerte und fürs Ablenken, fürs gemeinsame Lachen und bedingungslose Unterstützung (und das Umsetzen meiner endlosen Ideen im Haus und Garten). Danke für alles!

**Elin** und **Mina**, ihr habt meine PhD Zeit stressiger und komplizierter gemacht als sie sowieso schon ist, und ich hatte oft das Gefühl weder der Arbeit noch euch gerecht zu werden. Und trotzdem seid ihr mit Abstand das Beste und Wichtigste was ich in dieser Zeit geschaffen habe und ich müsste nicht eine Sekunde nachdenken was ich wählen würde wenn ich müsste. Ich freue mich auf viele weitere Erinnerungen mit euch und bin stolz euch weiter begleiten zu dürfen und so gespannt wo eure Reise euch hin führt.

## List of publications

### This thesis

Meringa AD\*, Hernández-López P\*, Cleven A\*, de Witte M, Straetemans T, Kuball J, Beringer DX, Sebestyén Z. Strategies to improve  $\gamma\delta$ TCRs engineered T-cell therapies for the treatment of solid malignancies. *Front Immunol.* 2023 Jun 27;14:1159337. doi: 10.3389/fimmu.2023.1159337. PMID: 37441064; PMCID: PMC10333927.

Cleven A\*, Meringa AD\*, Fasci D, Koorman T, Brazda P, Aarts-Riemens T, Johanna I, Beringer DX, Hernandez-Lopez P, Heijhuurs S, Mizutani T, Lim S, Huismans M, Bernink , Vargas-Dias D, Wu W, San Jose E, Schipper J, Tskakirakis N, Hoorens van Heyningen L, Nouwens A, Gatti L, Straetemans T, Snippert H, Roodhart J, Derksen P, Drost J, Altelaar M, Heck A, Clevers H, Kuball J#, Sebestyén Z#. PI3K-AKT1-mTOR activity and BTN3A1 phosphorylation are required for early cancer immune surveillance via V $\gamma$ 9V $\delta$ 2TCR T cells. Manuscript in preparation.

Dekkers JF\*, Alieva M\*, Cleven A, Keramati F, Wezenaar AKL, van Vliet EJ, Puschhof J, Brazda P, Johanna I, Meringa AD, Rebel HG, Buchholz MB, Barrera Román M, Zeeman AL, de Blank S, Fasci D, Geurts MH, Cornel AM, Driehuis E, Millen R, Straetemans T, Nicolassen MJT, Aarts-Riemens T, Ariese HCR, Johnson HR, van Ineveld RL, Karaiskaki F, Kopper O, Bar-Ephraim YE, Kretzschmar K, Eggermont AMM, Nierkens S, Wehrens EJ, Stunnenberg HG, Clevers H#, Kuball J#, Sebestyén Z# and Rios AC#. Uncovering the mode of action of engineered T cells in patient cancer organoids. *Nat Biotechnol.* 2023 Jan;41(1):60-69. doi: 10.1038/s41587-022-01397-w. Epub 2022 Jul 25. PMID: 35879361; PMCID: PMC9849137.

Cleven A\*, Meringa AD\*, Gasull-Celades L, Schwenzel C, Derevianko PK, van Vliet E, Huismans MA, Aarts-Riemens T, Gatti LDCE, van der Wagen LE, Rios A, Snippert H, Roodhart J, Beringer DX, de Witte M, Straetemans T, Brazda P, Stunnenberg HG, Heidenreich O, Peperzak V, Kuball J# and Sebestyén Z#. Efficacy of  $\alpha\beta$ T cell based immunotherapies relies on CCR5 expression in both CD4+ and CD8+  $\alpha\beta$ T cells. Manuscript in preparation.

Cleven A\*, Meringa AD\*, Brazda P\*, Derevianko PK\*, Gasull-Celades L, Hoorens van Heyningen L, Schwenzel C, Aarts-Riemens T, Paap R, Gatti LCDE, Miranda-Bedate A, Pascoal Ramos MI, Heidenreich O, Stunnenberg H, Meyaard L#, Kuball J#, Sebestyén Z#. The properties of mesenchymal stem cells in the tumor niche direct the outcome of engineered T cell therapy. Manuscript in preparation.

\*These authors share first authorship

#These authors share senior authorship

## Other

Hernández-López P\*, van Diest E\*, Brazda P, Heijhuurs S, Meringa A, Hoorens van Heyningen L, Riillo C, Schwenzel C, Zintchenko M, Johanna I, Nicolassen MJT, Cleven A, Kluiver TA, Millen R, Zheng J, Karaiskaki F, Straetemans T, Clevers H, de Bree R, Stunnenberg HG, Peng WC, Roodhart J, Minguet S, Sebestyén Z, Beringer DX#, Kuball J#. Dual targeting of cancer metabolome and stress antigens affects transcriptomic heterogeneity and efficacy of engineered T cells. *Nat Immunol.* 2023 Nov 27. doi: 10.1038/s41590-023-01665-0. Epub ahead of print. PMID: 38012415.

Sebestyén Z, Scheper W, Vyborova A, Gu S, Rychnavska Z, Schiffler M, Cleven A, Chéneau C, van Noorden M, Peigné CM, Olive D, Lebbink RJ, Oostvogels R, Mutis T, Schuurhuis GJ, Adams EJ, Scotet E, Kuball J. RhoB Mediates Phosphoantigen Recognition by V $\gamma$ 9V $\delta$ 2 T Cell Receptor. *Cell Rep.* 2016 May 31;15(9):1973-85. doi: 10.1016/j.celrep.2016.04.081. Epub 2016 May 19. PMID: 27210746; PMCID: PMC5035041.

Nickel N, Cleven A, Enders V, Lisak D, Schneider L, Methner A. Androgen-inducible gene 1 increases the ER Ca(2+) content and cell death susceptibility against oxidative stress. *Gene.* 2016 Jul 15;586(1):62-8. doi: 10.1016/j.gene.2016.03.055. Epub 2016 Mar 31. PMID: 27040980.

## Curriculum vitae

Astrid Cleven was born on the 22<sup>nd</sup> of June 1990 in Geldern, Germany. In 2012 she completed her bachelor's degree in Biology at the University of Düsseldorf. For her bachelor thesis, she undertook a five-month internship at the Life Science Center/Neurology under supervision of Prof. Dr. Axel Methner, studying the effect of androgen-inducible gene 1 (AIG1) on the cell's calcium homeostasis and cell survival. Subsequently, Astrid started a master's degree in Biology at the University of Düsseldorf with focus on cell physiology and cell signaling. The nine-month internship for her master thesis she spend in the group of Prof. Dr. Sebastian Wesselborg and Prof. Dr. Björn Stork at the institute for molecular medicine studying cell death and autophagy in rituximab-treated B-lymphoma cells. After obtaining her MSc in 2015, Astrid worked as research technician in the Center for Translational Immunology (CTI) at the University Medical Center Utrecht in the group of Prof. Dr. Jürgen Kuball and Dr. Zsolt Sebestyén, where she then started her PhD in 2019. During this time she investigated the underlying mechanisms of recognition by V $\gamma$ 9V $\delta$ 2TCRs and new strategies to improve T cell-based immunotherapies. The results of this work are discussed in this thesis. Since 2023, Astrid is working as a postdoctoral researcher in the group of Prof. Dr. Pierre Robe in the department of Neurology and Neurosurgery at the UMC Utrecht, investigating the role of NK cells in glioblastoma.

